

## ABSTRACT

Title of Dissertation: QUASI-STATIC ACOUSTIC MAPPING OF  
HELICOPTER BLADE-VORTEX  
INTERACTION NOISE

Gaurav Gopalan, Doctor of Philosophy, 2004

Dissertation directed by: Martin Professor Fredric H. Schmitz  
Department of Aerospace Engineering

This research extends the applicability of storage-based noise prediction techniques to slowly maneuvering flight. The quasi-static equivalence between longitudinal decelerating flight and steady-state longitudinal descent flight, and its application to the estimation of BVI noise radiation under slow longitudinal maneuvering flight conditions, is investigated through various orders of flight dynamics modeling. The entire operating state of the helicopter is shown to be similar during equivalent flight conditions at the same flight velocity. This equivalence is also applied to the prediction of control requirements during longitudinal maneuvers. Inverse simulation based flight dynamics models of lower order are seen to capture many important

trends associated with slow maneuvers, when compared with higher order modeling. The lower order flight dynamics model is used to design controlled maneuvers that may be practically flown during descent operations or as part of research flight testing. A version of a storage-based acoustic mapping technique, extended to slowly maneuvering longitudinal flight, is implemented for helicopter main rotor Blade-Vortex Interaction (BVI) noise. Various approach trajectories are formulated and analytical estimates of the BVI noise radiation characteristics associated with a full-scale two-bladed rotor are mapped to the ground using this quasi-static mapping approach. Multi-segment decelerating descent approaches are shown to be effective in ground noise abatement. The effects of steady longitudinal winds are investigated on radiated and ground noise. Piloting trim choices are seen to dominate the noise radiation under these flight conditions.

QUASI-STATIC ACOUSTIC MAPPING OF HELICOPTER  
BLADE VORTEX INTERACTION NOISE

by

Gaurav Gopalan

Dissertation submitted to the Faculty of the Graduate school of the  
University of Maryland, College Park in partial fulfillment  
of the requirements for the degree of  
Doctor of Philosophy  
2004

Advisory Committee:

Martin Professor, Fredric H. Schmitz, Chairman/Advisor  
Alfred Gessow Professor, Inderjit Chopra  
Associate Professor, James D. Baeder  
Assistant Professor, Ella M. Atkins  
Professor, Tobias von Petersdorff (Dean's Representative)

© Copyright by

Gaurav Gopalan

2004

# DEDICATION

To my family

## ACKNOWLEDGEMENTS

I begin by expressing my immense gratitude and appreciation for my advisor of six years, Dr. Frederic H. Schmitz, whose benevolent mentorship and patronage made this experience possible and successful. His vast professional experience, his industry and humility, his fairness and his diligent perfectionism have been very important lessons for me. I admire his creativity and inventiveness, his resourcefulness and his ever fresh ideas.

Dr. Inderjit Chopra has always been a role model for me. His astute scholarship, his technical brilliance, leadership and advising skills are an inspiration. I am indebted by his belief in my abilities and his continued support and guidance. I thank Dr. Baeder for his technical guidance, his support and his encouragement. Dr. Ella Atkins has also been a source of much encouragement and unflinching support. Dr. von Petersdorff was always helpful, and I thank him for his willingness to be part of my Dissertation Committee.

A very special thanks to Dr. Celi for his technical help with the flight dynamics simulation. Your timely help and approachability were lifesavers. Dr. Ben Sim has been my colleague for six years and I have learnt much from him. His trademark willingness to help and his professionalism are admirable. Other colleagues at the

rotorcraft center, have also been very helpful. Aerospace Researchers, all over the world have also, at several levels impacted my work and life in very positive ways, and aided my sometimes reluctant transition from interloper to insider.

On a more personal note, to my family, that continues to amaze me by their humanity, their dignity and courage, and their utter and unquestioning faith in me, even at times when I myself am in doubt, I give thanks. I am proud to be a part of you and hope that someday I can make you proud.

My friends are an integral part of my family. Through times thick and thin, they have been by my side, often taking the oars from my exhausted arms, and allowing me rest and much joy. Your love, your help, your presence in my life, your faith in me and your unquestioning embrace of my choices, always startles me and I thank you for my continued bewilderment, for without it, without comrades and allies, life would have less meaning. Thank you for your company in our joint quest for love, meaning, truth, beauty and personal success.

Lastly, to this great country, the United States of America, I humbly and proudly give my thanks. Your beauty is breathtaking and your ideals inspiring. May God bless you and protect you.

# TABLE OF CONTENTS

<b>Acknowledgements .....</b>	<b>iii</b>
<b>Table of Contents .....</b>	<b>v</b>
<b>List of Tables .....</b>	<b>xi</b>
<b>List of Figures.....</b>	<b>xii</b>
<b>Nomenclature .....</b>	<b>xxiii</b>
<b>Chapter 1 .....</b>	<b>1</b>
<b>Introduction.....</b>	<b>1</b>
1.1    The Importance of Reducing Helicopter Noise in Terminal Area Operations .....	1
1.2    Major Sources of Helicopter Noise During Landing Approach .....	4
1.3    Review of BVI Noise Research and Control .....	9
1.3.1    Experimental Investigations.....	9
1.3.2    BVI Noise Predictions .....	13
1.3.3    BVI Noise Reduction Techniques .....	18
1.3.3.1    Low BVI Noise Design (Passive Control).....	20
1.3.3.2    Active HHC and IBC Control.....	20

1.3.3.3	X-Force Control.....	22
1.3.3.4	Flight Trajectory Management .....	24
1.4	Rotorcraft Noise & Performance Modeling for Flight Trajectory Management.....	28
1.4.1	BVI & Loading Noise During Steady Descents .....	30
1.4.1.1	Theoretical Modeling.....	30
1.4.1.2	Rotorcraft Noise Model .....	30
1.4.2	BVI Noise During Steady Descents with Wind.....	32
1.4.3	Loading Noise During Maneuvering Flight.....	32
1.4.4	BVI Noise During Maneuvering Flight .....	33
1.5	Thesis Objectives .....	34
1.5.1	General Focus .....	34
1.5.2	Specific Research Objectives.....	35
1.5.3	Dissertation Road-map.....	36
<b>Chapter 2</b>	<b>.....</b>	<b>40</b>
<b>Steady-State BVI Noise Estimation</b>	<b>.....</b>	<b>40</b>
2.1	Steady State BVI Noise: .....	40
	Governing Factors and Functional Dependencies .....	40
2.2	Steady-State Main-Rotor BVI Noise Estimation.....	51
2.2.1	BVI Modeling Methodology.....	53
2.2.2	Steady State BVI Noise: Representation .....	60

2.2.3	Steady-State BVI Noise Radiation Trends for the Bell206-B Helicopter.....	62
<b>Chapter 3</b>	.....	<b>69</b>
<b>Tip Path Plane Formulation and Methodology</b>	.....	<b>69</b>
3.2	Equations Governing Tip Path Plane Performance .....	78
3.3	Levels of Tip Path Plane Modeling During Longitudinal Maneuvers.....	85
3.2.1	First-Order Longitudinal Performance, Dynamics and Control Model.. .....	86
3.2.2	Second-Order Longitudinal Performance, Dynamics and Control Model	94
3.2.3	Third and Fourth Order Longitudinal Flight Dynamics Analysis .....	97
3.4	Higher Order Trim and Flight Dynamics Modeling.....	103
3.5	Sample Longitudinal Maneuvers: Mathematical Functional Representations .....	110
<b>Chapter 4</b>	.....	<b>115</b>
<b>Tip Path Plane Performance and Dynamics: Results</b>	.....	<b>115</b>
4.1	Higher order Model Results.....	116
4.1.1	Trim Results.....	117
4.1.1.1	Effect of Flight Velocity .....	117
4.1.1.2	Effect of Flight Path Angle .....	122
4.1.2	Higher Order Model – Maneuver Implementation .....	126
4.1.3	Level Flight Deceleration Maneuvers.....	132

4.1.3.1	Baseline Deceleration Maneuver Description .....	135
4.1.3.2	Deceleration Maneuver Results: Higher Order Model .....	136
4.3	Longitudinal Maneuver Results : Lower Order Modeling .....	156
4.3.1	Slow Deceleration Maneuver Results: Lower Order Modeling .....	157
4.3.2	Flight Path Angle Transition Maneuver Results: Lower Order Modeling .....	162
4.2.3	Constant “ $\gamma$ -effective” maneuver results: Lower level modeling .....	164
<b>Chapter 5</b>	.....	<b>168</b>
<b>Flight Trajectory Management of Helicopter BVI Noise</b>	.....	<b>168</b>
5.1	The Quasi-Static Acoustic Mapping (Q-SAM) Technique .....	168
5.1.1	Major Assumptions.....	173
5.1.2	Steady State BVI noise: Storage and Representation .....	176
5.1.3	Reduction of BVI Noise Radiation.....	186
5.1.4	Landing Trajectories: Description and Assumptions.....	188
5.2	Flight Trajectory Management without Wind Effects .....	190
5.2.1	Effects of Flight Path Angle & Flight Velocity .....	191
5.2.2	Effect of Vehicle Deceleration.....	206
5.2.3	Effect of Vehicle Drag Changes .....	208
5.2.4	Sample Noise Abatement Profiles .....	209
5.2.5	Piloting Implications.....	211
5.3	Flight Trajectory Management with Steady Headwinds and Tailwinds...	214
5.3.1	Modeling Methodology .....	214

5.3.2 Major Assumptions.....	216
5.3.3 Piloting Strategies .....	217
5.3.3.1 Approach Procedure 1 (Piloting Strategy 1) : Holding airspeed and flight path in the ground reference frame .....	220
5.3.3.2 Approach Procedure 2 (Piloting Strategy 2): Holding Rate of Sink and Flight Path in the ground reference frame .....	233
5.3.4 Noise Abatement Profiles and the Effect of Wind.....	238
5.3.5 Noise Exposure and Piloting Implications.....	246
<b>Chapter 6 .....</b>	<b>249</b>
<b>Summary and Conclusions.....</b>	<b>249</b>
6.1 Major Conclusions.....	250
6.2 Recommendations for Future Work.....	256
<b>Appendix A.....</b>	<b>260</b>
<b>Tip path plane Estimation in Trim .....</b>	<b>260</b>
<b>Appendix B.....</b>	<b>268</b>
<b>Force Balances and Coordinate Systems .....</b>	<b>268</b>
<b>Appendix C.....</b>	<b>275</b>
<b>Implementing the Q-SAM Method: Some Details .....</b>	<b>275</b>
Aero-Acoustic module .....	277

Performance and Trajectory-Specification Module.....	280
The Sphere Selection module .....	286
Ground Noise Module.....	288
<b>Appendix D .....</b>	<b>297</b>
<b>Development of Approach Trajectories that Minimize BVI Noise Exposure on the Ground.....</b>	<b>297</b>
 BIBLIOGRAPHY.....	 313

## LIST OF TABLES

Table 3.1	Characteristic parameters associated with three sample deceleration cases. ....	113
Table 4.1	Relevant design and operational parameters for the UH-60 model.....	118
Table 4.2	Control correction factor values used for the trim and maneuver study, along with the associated units. ....	132
Table 5.1	AH-1 helicopter geometry and flight parameters. ....	178
Table A.1	Bell206-B Operational Parameters. ....	261

## LIST OF FIGURES

Figure 1.1	Sources of main rotor noise and vibration [5]. .....	2
Figure 1.2	Simultaneous non-interfering (SNI) trajectories for runway- independent aircraft (RIA).....	3
Figure 1.3	Helicopter BVI geometry for a two-bladed rotor: top and side view [9]. .....	7
Figure 1.4	Schematic showing the BVI phenomenon and the radiated noise directivity [5]. .....	8
Figure 1.5	In-Flight acoustic measurement technique with “flying acoustic platform” by Schmitz and Boxwell [9].....	11
Figure 1.6	A schematic of a possible “X-force Controller” for BVI noise suitable for some helicopter design, proposed by Schmitz [44].....	23
Figure 1.7	Measured cabin noise levels as a function of helicopter flight conditions [50]. .....	25
Figure 1.8	Typical ground noise measurement set up for flight test [50]. .....	26
Figure 1.9	A descending decelerating noise abatement approach [52]. .....	28
Figure 1.10	Three different steps of aeroacoustics predictions for ground noise studies: blade aerodynamics, acoustics radiation on radiation sphere and propagation factors.....	29
Figure 2.1	Blade-vortex intersection locations as a function of advance ratio for an undistorted epi-cycloidal wake of a two-bladed rotor.....	43

Figure 2.2	Tip-Path Plane geometry of the BVI problem for a two bladed rotor in forward flight. ....	46
Figure 2.3	Rotor Tip-path plane, Inflow and Inflow angle. ....	51
Figure 2.4	Schematic depicting the BVI noise estimation model. ....	59
Figure 2.5	Radiation sphere geometry. ....	60
Figure 2.6	Flight velocity vector and the tip-path-plane relative to the radiation sphere. ....	62
Figure 2.7	A 2-D representation of BVI radiation characteristics ....	64
Figure 2.8	Computed trends of sound pressure levels radiated on a 3R sphere around the Bell206-B helicopter for varying inflow angles. $\mu = 0.172$ . ....	65
Figure 2.9	Average radiated noise level estimates for the Bell206-B as a function of the advance ratio and a) tip-path plane angle, b) inflow angle (wake skew angle - $\pi/2$ ) and c) the effective inflow angle. ....	67
Figure 3.1	Euler angles and rotation rates of a general right-handed coordinate system (subscripts “ <i>N</i> ” have been dropped). ....	71
Figure 3.2	Ground fixed (inertial), gravity and body-fixed coordinate systems. .	73
Figure 3.3	“Wind” coordinate system referenced to gravity coordinates. ....	73
Figure 3.4	The tip-path plane coordinate system and the flight velocity vector. .	77
Figure 3.5	Lateral tilt of the tip-path plane : $\phi_{TPP}$ . ....	80
Figure 3.6	Longitudinal Force balance of a helicopter, shown for a descending decelerating condition. ....	81
Figure 3.7	Schematic showing the inverse simulation scheme for slowly maneuvering flight. ....	101

Figure 3.8	Velocity profile along three sample deceleration cases.....	113
Figure 3.9	Acceleration profile along three sample deceleration cases. ....	114
Figure 3.10	Rate of change of acceleration profile along three sample deceleration cases. ....	114
Figure 4.1	Component wise drag to weight terms and the tip-path plane angle at a flight velocity of 40 knots.....	119
Figure 4.2	Fixed frame flapping angles and vehicle acceleration as a function of time at a trim condition of 40 knots.....	120
Figure 4.3	Component wise drag to weight terms and the tip-path plane angle as a function of flight velocity. ....	121
Figure 4.4	Effect of flight path angle on Tip-path plane angle and fixed-frame flapping angles at a flight velocity of 70 knots.....	123
Figure 4.5	Effect of flight path angle on tip-path plane angle, longitudinal flapping angle and fuselage pitch attitude, at a flight velocity of a) 50 knots and b) 70 knots.....	125
Figure 4.6	Control input requirements as a function of flight path angle, at a flight velocity of 50 knots and 70 knots. ....	126
Figure 4.7	Baseline slow deceleration or “Slow Stop” maneuver showing: a) velocity profile, b) acceleration profile and c) rate of change of acceleration profile. ....	134
Figure 4.8	Variation of effective trim and quasi-static control inputs along the baseline slow stop maneuver. ....	136
Figure 4.9	Velocity profile along the baseline slow deceleration maneuver. ....	138

Figure 4.10	Variation of Control input requirements along the baseline slow stop maneuver.....	138
Figure 4.11	Variation of tip-path plane angle, deceleration in g's and flight path angle along the baseline slow stop maneuver.....	139
Figure 4.12	Variation of non-dimensional dynamic inflow (induced velocity) coefficients along the slow deceleration maneuver.....	139
Figure 4.13	Variation of Euler angles along the baseline slow stop maneuver. ..	141
Figure 4.14	Variation of main rotor flapping angles relative to the hub plane along the baseline slow stop maneuver.....	141
Figure 4.15	Variation of body and tip-path plane rotation rates along the baseline slow stop maneuver.....	142
Figure 4.16	Variation of effective trim and quasi-static control inputs along the “quick stop” maneuver.....	146
Figure 4.17	Velocity profile along the “quick stop” maneuver.....	150
Figure 4.18	Variation of Control input requirements along the “quick stop” maneuver.....	150
Figure 4.19	Variation of body and tip-path plane rotation rates along the “quick stop” maneuver.....	151
Figure 4.20	Variation of tip-path plane angle, deceleration in g's and flight path angle along the “quick stop” maneuver.....	151
Figure 4.21:	Errors in tip path plane estimation based on the quasi-static assumption, for the “quick stop” maneuver results.....	152

Figure 4.22	Variation of Euler angles along the “quick stop” maneuver, along with the corresponding level flight trim and quasi-static values of fuselage pitch attitude. ....	152
Figure 4.23	Variation of main rotor flapping angles along the “quick stop” maneuver. Corresponding level flight trim and quasi-static values are also shown. ....	153
Figure 4.24	Variation of non-dimensional dynamic inflow (induced velocity) coefficients along the “quick stop” maneuver. The corresponding level flight trim and quasi-static values are also shown. ....	155
Figure 4.25	The “Slow Deceleration” Maneuver: Variation of performance and control parameters. ....	159
Figure 4.26	The “Slow Deceleration” Maneuver: variation of effective inflow angle. ....	160
Figure 4.27	The “Quick Stop” Maneuver: Variation of performance and control parameters. ....	161
Figure 4.28	Performance parameter variations during the flight path angle transition maneuver at 70 knots. ....	163
Figure 4.29	The “Flight-Path Angle Transition” Maneuver: variation of effective inflow angle. ....	164
Figure 4.30	The “ $\gamma$ -effective” maneuver. ....	165
Figure 4.31	The “ $\gamma$ -effective” maneuver – variation of performance parameters. ....	166
Figure 4.32	The “ $\gamma$ -effective” Maneuver: variation of effective inflow angle. ....	167
Figure 5.1	Schematic of the Quasi-Static Acoustic Mapping Technique. ....	169

Figure 5.2	An illustration of the storage based acoustic mapping approach to the evaluation of ground noise metrics associated with flight trajectories. ....	173
Figure 5.3	Radiation sphere used in the Q-SAM method .....	179
Figure 5.4	A 2-D representation of BVI radiation characteristics. ....	181
Figure 5.5	Variations of sound pressure levels on radiation spheres with: (a) tip-path-plane angle, (b) advance ratio. ....	182
Figure 5.6	Average radiated sound power as a function of: a) $\mu$ and $\alpha_{TPP}$ ; b) $\mu$ and $R/S$ ; c) $\mu$ and $\gamma$ . ....	185
Figure 5.7	Effective Inflow Angle as a function of advance ratio and effective flight path angle for the AH-1 helicopter. ....	187
Figure 5.8	Helicopter trajectory and ground observer plane. ....	189
Figure 5.9	Predicted SEL ground noise contours and acoustic time histories for $\mu = 0.165$ at different flight path angles: (a) $\gamma = -2^\circ$ , (b) $\gamma = -4^\circ$ , (c) $\gamma = -6^\circ$ , (d) $\gamma = -8^\circ$ . ....	196
Figure 5.10	The effect of descent angle on miss-distances and the location of the wake relative to the rotor disk. ....	197
Figure 5.11	Predicted SEL ground noise contours for $\gamma = -6^\circ$ at different advance ratios: (a) $\mu = 0.10$ , (b) $\mu = 0.11$ , (c) $\mu = 0.12$ . ....	198
Figure 5.12	Predicted SEL ground noise contours for $\gamma = -6^\circ$ at different advance ratios: (a) $\mu = 0.13$ , (b) $\mu = 0.14$ , (c) $\mu = 0.15$ . ....	199
Figure 5.13	Predicted SEL ground noise contours for $\gamma = -6^\circ$ at different advance ratios: (a) $\mu = 0.16$ , (b) $\mu = 0.17$ , (c) $\mu = 0.18$ . ....	200

Figure 5.14	Predicted SEL ground noise contours for $\gamma = -6^\circ$ at different advance ratios: (a) $\mu = 0.19$ , (b) $\mu = 0.20$ , (c) $\mu = 0.21$ .	201
Figure 5.15	Predicted SEL ground noise contours for $\gamma = -6^\circ$ at different advance ratios: (a) $\mu = 0.22$ , (b) $\mu = 0.23$ , (c) $\mu = 0.24$ .	202
Figure 5.16	Predicted $SEL_{av}$ ground noise contours as a function of: a) $\mu$ and R/S; b) $\mu$ and $\gamma$ .	205
Figure 5.17	SEL contours for a deceleration approach (0.05g) at a flight path angle of $-6^\circ$ .	207
Figure 5.18	SEL contours for a deceleration approach (0.025g) at a flight path angle of $-6^\circ$ .	207
Figure 5.19	Effect of X-force on SEL contours on the ground plane: a) without X-force and b) with X-force.	209
Figure 5.20	A 2-segmented approach at 70 knots.	210
Figure 5.21	A decelerating 2-segmented approach.	211
Figure 5.22	Geometrical relationships between air mass and ground fixed frames with wind.	218
Figure 5.23	Flight parameter adjustments to maintain fixed ground flight path with headwinds	219
Figure 5.0.24	Variation of tip-path-plane angle, sink rate and aerodynamic flight path angle for Piloting Strategy 1 in the presence of a 20 knot head/tailwind compared to the no-wind values at an inertial descent angle of $-6^\circ$ .	222
Figure 5.25	Variation of sink rate and for Piloting Strategy 1 in the presence of a 20 knot head/tailwind compared to the no-wind values at a sink rate of 700 fpm.	226

Figure 5.26	Effect of Piloting Strategy1 on ground noise exposure (SEL) contours at $\mu = 0.165$ and $\gamma_g = -6^\circ$ : a) 20 knot headwind, b) no wind and c) 20 knot tailwind. ....	227
Figure 5.27	Effect of Piloting Strategy 1 on ground noise exposure (SEL) contours at $\mu = 0.165$ and $\gamma_g = -3^\circ$ : a) 20 knot headwind, b) no wind and c) 20 knot tailwind. ....	229
Figure 5.28	Effect of Piloting Strategy 1 on $SEL_{av}$ for constant speed descent at $\mu = 0.165$ , $\gamma_g = -3^\circ$ and $-6^\circ$ at different wind speeds. ....	231
Figure 5.29	Effect of Piloting Strategy1 on $SEL_{av}$ as a function of 1) $\gamma_g$ ; 2) $\gamma_a$ and 3) Sink Rate in FPM under a) 20 knot headwind, b) no wind and c) 20 knot tailwind conditions.....	232
Figure 5.30	Variation of tip-path-plane angle and aerodynamic flight path angle as a function of non-dimensionalized ground speed in the presence of a 20 knot head/tailwind compared to the no-wind values during a $-6^\circ$ descent for Piloting Strategy 2. ....	234
Figure 5.31	Variation of tip-path-plane angle and aerodynamic flight path angle as a function of non-dimensionalized ground speed in the presence of a 20 knot head/tailwind compared to the no-wind values at a sink rate of 700 fpm for Piloting Strategy2.....	236
Figure 5.32	Effect of Piloting Strategy 2 on $SEL_{av}$ for constant speed descent at $\mu = 0.165$ , $\gamma_g = -3^\circ$ and $-6^\circ$ at different wind speeds. ....	238
Figure 5.33	Changes in average radiated sound power in the presence of a 20 knot head/tailwind for approach procedure 2 at $\gamma_g = -3, -6$ and $-9$ and $\mu_g = 0.165$ . ....	239

Figure 5.34	Effect of Piloting Strategy 2 on $SEL_{av}$ as a function of $\gamma_g$ under a) 20 knot headwind, a) no wind and a) 20 knot tailwind conditions. ....	240
Figure 5.35	Effects of wind on steep decelerating descents: a) 20 knot headwind; b) no wind; c) 20 knot tailwind.....	242
Figure 5.36	Effects of wind on shallow descents: with X-Force, a) 20 knot headwind; b) no wind; c) 20 knot tailwind; d) no X-Force, no wind .....	245
Figure 5.37	Effect of Approach Procedures 1 and 2 on the average radiated sound power. ....	248
Figure 6.0.1	In-flight test set-up – Bell206-B with spray boom. ....	256
Figure A.1	Predicted performance parameters for the Bell-206B in trimmed steady-state forward flight: tip-path plane angle, thrust to weight ratio, collective pitch, longitudinal cyclic pitch, helicopter pitch attitude and longitudinal flapping. ....	265
Figure A.2	Predicted performance parameters for the Bell-206B in trimmed steady-state forward flight: a) thrust coefficient, b) tip-path plane angle, c) thrust, d) main-rotor H force, e) collective pitch, f) longitudinal cyclic pitch, g) helicopter pitch attitude and h) longitudinal flapping.....	267
Figure B.1	Euler angles and rotation rates of a general right-handed coordinate system with respect to the inertial system.....	271
Figure B.2	Euler angles and rotation rates of the wind coordinate system with respect to the inertial system.....	271
Figure C.1	The four modules used in the implementation of the Q-SAM method... ..	276

Figure C.2	Radiation sphere geometry. ....	278
Figure C.3	Flight velocity vector and the tip-path-plane relative to the radiation sphere. ....	280
Figure C.4	Trajectory components: Segments, Elements and Control Points. ....	281
Figure C.5	Orientation of the flight velocity vector. ....	284
Figure C.6	Trajectory segments, segment interfaces and “switching points”. ....	285
Figure C.7	Linear Interpolation over small changes in $V$ and $\alpha_{TPP}$ . ....	286
Figure C.8	Interpolation Schemes used in the sphere selection module. ....	287
Figure C.9	Correct positioning and orientation of the radiation sphere, along with propagation geometry. ....	289
Figure C.10	Acoustics mapping in the Q-SAM method. ....	291
Figure C.11	Atmospheric absorption mapping factors as a function of one-third octave band center-frequencies. ....	292
Figure C.12	A-weighting filter factors as a function of one-third octave band center-frequencies. ....	293
Figure C.13	A schematic representation of noise extrapolation from the sphere to the ground. ....	296
Figure D.1	$SPL_{av}$ over the ground plane for steady flight conditions as a function of tip-path plane angle for advance ratios 0.12, 0.143 0.165, 0.188 and 0.21. ...	300
Figure D.2	Curve-fit for the average radiated BVI sound power on the ground plane, as a function of main-rotor tip-path plane angle, for advance ratio 0.165. ...	301

Figure D.3 The variation of the mean-trend for the radiated main-rotor BVI sound power averaged over a representative ground plane plotted as a function of height above the ground plane center. .... 302

Figure D.4 Several low-noise solutions for a 2-segmented trajectory with a range of 50000 feet, obtained using gradient descent. The maximum noise trajectories corresponding to 5° approaches are also shown for comparison..... 311

Figure D.5 Several low-noise solutions for a 2-segmented trajectory with a range of 20000 feet, obtained using gradient descent. The maximum noise trajectories corresponding to 5° approaches are also shown for comparison..... 312

## NOMENCLATURE

$A$	Total ground plane area, $ft^2$
$A_s$	Total radiation sphere area, $ft^2$
$A_x$	Acceleration parallel to flight path
$a_o$	Speed of sound ( $1125\text{ ft/sec}$ )
$C_f$	Atmospheric absorption mapping factor, $dB\text{ per }ft$
$C_T$	Thrust coefficient
$c$	Rotor blade chord, $ft$ ; rate parameter in sigmoidal functions
$\cos$	Trigonometric cosine function
$\cosh$	Hyperbolic cosine function
$D_F$	Fuselage drag, $lb$
$D_{F,0}$	Fuselage drag based on equivalent flat plate area, $lb$
$D_{EFF}$	Equivalent/effective helicopter drag, in the “wind” coordinate system, $lb$
$dB$	decibel
$dB-A$	A-weighted dB value
$dS$	Elemental surface area
$dV$	Volume element
$d\bar{l}$	Vortex element

$dV/dt$	Helicopter acceleration along the flight path, $ft\ sec^{-2}$
$E$	Beddoe's wake factor
$e$	Exponential function
$F$	Objective function used in optimization procedure
$\bar{F}$	Total external forces acting on the helicopter fuselage
$\bar{F}_{NI}$	Total external forces acting on the helicopter fuselage, expressed along non-inertial coordinate directions
$F()$	System of coupled non-linear equations
$F_x$	Auxiliary X-Force
$f$	Equivalent flat plate area ( $ft$ )
$f$	Frequency ( $Hz$ )
$f=0$	Radiation source surface
$f()$	Non-linear function
$f_x$	Equivalent flat plate area of X-Force device, $ft^2$
$f_\lambda$	Inflow factor
$G$	"Guidance" correction factor in flight dynamics simulation
$g$	acceleration due to gravity ( $32.2\ ft/sec^2$ )
$H$	Main rotor "H-Force" or drag, $lb$
$H_{TPP}$	Main rotor "H-Force" in the tip-path plane (tip-path plane coordinates), $lb$
$I_y$	Fuselage pitching moment of inertia, $slug\ ft^2$
$i$	blade number or index
$i, j, k$	unit vectors along x, y, z respectively

$\hat{i}, \hat{j}, \hat{k}$	unit vectors along x, y, z axes respectively of reference frame denoted by subscript
$k$	parameter
$L_{EFF}$	Effective lift acting on the helicopter, apart from main-rotor thrust, in the “wind” coordinate system, $lb$
$l_i$	Radiation surface lift component along $i^{th}$ coordinate direction, $lb$
$ln$	Natural Logarithmic function
$M$	Pitching moment, $lb-ft$
$M_{AT}$	Advancing-tip Mach number
$M_H$	Hover-tip Mach number, $\Omega R/a_0$
$M_r$	Mach number of acoustic source in radiation direction
$M_{tr}$	Trace Mach number (Trace Velocity of BVI intersection point with respect to the medium divided by sonic velocity)
$m$	Helicopter mass ( <i>slug</i> ); number of retained main rotor modes in flight dynamics analysis
$N_b$	Number of main rotor blades
$P_{av}$	Average acoustic power on sphere, $dB$
$P_{ij}$	Compressive stress, or pressure, tensor
$p$	Rotation rate about x axis; Fuselage roll rate, <i>rad per sec</i>
$p'$	Acoustic pressure, $Pa$
$p'_L$	Acoustic pressure due to lift dipoles, $Pa$
$p_{NI}$	Rotation rate about x axis (non-inertial coordinate system)

$q$	Rotation rate about y axis; Fuselage pitch rate, <i>rad per sec or deg per sec</i>
$q_{NI}$	Rotation rate about y axis (non-inertial coordinate system)
$R$	rotor blade radius, <i>ft</i>
$R_{AM}$	coordinate system fixed to air-mass or medium
$R_F$	ground-fixed inertial coordinate system
$R_{obs}$	Sphere center-to-observer distance, <i>ft</i>
$R_{oh}$	hub-to-observer distance, <i>ft</i>
$R_s$	radius of radiation sphere, <i>ft</i>
$RPM$	rotation rate ( <i>revolutions per min</i> )
$R/S$	helicopter sink rate, $dz/dt$ , <i>ft per min</i>
$r$	Fuselage yaw rate, <i>rad per sec or deg per sec</i>
$r$	radiation or propagation distance, <i>ft</i>
$\hat{r}$	unit vector along radiation direction (acoustics formulation)
$\hat{r}_i$	component of unit radiation vector along $i^{th}$ coordinate
$\hat{r}$	unit direction vector from vortex element to point of interest (Biot-Savart Law)
$r_{NI}$	Rotation rate about z axis (non-inertial coordinate system)
$r_b$	non-dimensional position along blade span
$r_{core}$	vortex core radius
$r_h$	position vector of the hub/sphere-center in frame $R_F$
$r_o$	position vector of the observer in frame $R_F$

$S$	“Stability Augmentation” correction factor in flight dynamics simulation
$SEL$	Sound Exposure Level, $dB-A$
$SEL_{av}$	average SEL on ground plane, $dB-A$
$SPL$	Sound Pressure Level, $dB$
$s$	distance traveled along the trajectory, in reverse order
$\sin$	Trigonometric sine function
$\sinh$	Hyperbolic sine function
$T$	Main rotor thrust ( $lb$ ); rotor revolution period ( $sec$ ); elements of transformation matrix
$T_{ij}$	Lighthill Stress Tensor
$t$	time, in seconds; observer time
$t_{obs}$	Observer time, $sec$
$u$	velocity along x axis (body coordinate system), $ft\ per\ sec$
$u$	Control vector in flight dynamics analysis
$u_{NI}$	velocity along x axis (non-inertial coordinate system)
$u_n$	Local flow velocity normal to radiation source surface (acoustics formulation)
$V$	Flight velocity, $ft\ per\ sec$
$V_W$	Wind velocity, $ft\ per\ sec$
$v_I$	Main-rotor induced velocity
$v_{NI}$	Velocity along y axis (non-inertial coordinate system)
$v_n$	Velocity normal to radiation source surface (acoustics formulation)

$W$	Helicopter weight, $lb$
$w_{NI}$	velocity along $z$ axis (non-inertial coordinate system)
$w_{tip,i}$	Elastic tip displacement for $i^{\text{th}}$ main rotor blade
$X$	Force along $x$ axis, in force balance equations
$X_{NI}$	Force along $x$ axis of non-inertial coordinate system, in force balance equations
$x_b$	non-dimensional “ $x$ ” location of point on blade in the tip-path plane coordinate system
$x_v$	non-dimensional “ $x$ ” location of vortex element in the tip-path plane coordinate system
$x_i^j$	non-dimensional “ $x$ ” location of $i^{\text{th}}$ intersection point along $j^{\text{th}}$ blade-vortex interaction, in the tip-path plane
$\bar{x}$	Observer location in the medium
$x, y, z$	coordinate axis directions
$Y$	Force along $y$ coordinate, in force balance equations
$Y_{NI}$	Force along $y$ axis of non-inertial coordinate system,, in force balance equations
$Y_{TPP}$	Main rotor “ $Y$ -Force” in the tip-path plane (tip-path plane coordinates)
$y$	Body-axis coordinate, points starboard
$y$	State vector in flight dynamics analysis
$y_b$	non-dimensional “ $y$ ” location of point on blade in the tip-path plane coordinate system

$y_v$	non-dimensional “y” location of vortex element in the tip-path plane coordinate system
$y_i^j$	non-dimensional “y” location of $i^{\text{th}}$ intersection point along $j^{\text{th}}$ blade-vortex interaction, in the tip-path plane
$Z$	Force along z coordinate, in force balance equations
$Z_{NI}$	Force along x axis of non-inertial coordinate system, in force balance equations
$\alpha$	Angle of attack (positive nose up), qualified by subscript, <i>rad or deg</i>
$\alpha_F$	Fuselage angle of attack (positive nose up) , <i>rad or deg</i>
$\alpha_{TPP}$	Tip-path-plane angle (positive nose up) , <i>rad or deg</i>
$\beta_0$	Coning angle in the hub plane, <i>rad or deg</i>
$\beta_{1C}$	Longitudinal flapping in the hub plane, positive for nose-down, <i>rad or deg</i>
$\beta_{1S}$	Lateral flapping in the hub plane, positive for nose-down, <i>rad or deg</i>
$\beta_F$	Sideslip angle of fuselage
$\beta_d$	Differential Coning angle in the hub plane, <i>rad or deg</i>
$\beta_i^j$	Rotating frame generalized displacement for $j^{\text{th}}$ mode and $i^{\text{th}}$ blade, <i>rad or deg</i>
$\chi$	Wake skew angle, <i>rad or deg</i>
$\chi'$	Inflow Angle, $\chi - \pi/2$ , <i>rad or deg</i>
$\chi''$	Effective Inflow Angle, <i>rad or deg</i>

$\Delta A_i$	Elemental ground area, $\text{ft}^2$
$\Delta A_j$	Elemental sphere area, $\text{ft}^2$
$\Delta t$	Numerical Integration time-step, sec
$\Delta V$	Total change in flight velocity during deceleration maneuver, ft per sec
$\Delta \gamma$	Total change in flight path angle during flight path transition maneuver, deg
$\delta$	Pilot control inputs, qualified by subscript
$\delta(f)$	Dirac delta function
$\varepsilon$	Ordering analysis parameter ( $\approx 0.1$ )
$\phi$	Helicopter roll angle , <i>deg</i>
$\phi_{NI}$	“Roll” Euler angle associated with non-inertial coordinate system
$\phi_{TPP}$	“Roll” angle associated with the tip-path plane
$\Gamma_v$	Vortex strength
$\gamma$	Flight path angle (negative in descent), <i>rad or deg</i>
$\gamma_{EFF}$	Effective flight path angle, <i>rad or deg</i>
$\varkappa$	Angle between tangent to vortex in the tip-path plane and blade span at blade-vortex intersection location
$\lambda$	Average main-rotor inflow (positive for upwash), <i>ft per sec</i>
$\lambda'$	Effective main-rotor inflow (positive for upwash), <i>ft per sec</i>
$\bar{\lambda}$	Uniform/average main-rotor inflow ratio (positive for upwash), $\lambda/\Omega R$
$\mu$	Advance ratio, $V \cos(\alpha_{TPP}) / \Omega R$
$\mu$	micro, as in $\mu Pa$

$\Omega$	Angular rotation of the main rotor, <i>rad per sec</i>
$\overline{\Omega}_{NI}$	Angular velocity of non-inertial coordinate system relative to an inertial system
$\theta$	Helicopter fuselage pitch attitude; radiation sphere elevation angle, <i>rad or deg</i>
$\theta_o$	Main rotor collective pitch input, <i>rad or deg</i>
$\theta_{IC}$	Main rotor longitudinal cyclic pitch input, <i>rad or deg</i>
$\theta_{IS}$	Main rotor lateral cyclic pitch input, <i>rad or deg</i>
$\theta_{NI}$	“Pitch” Euler angle associated with the non-inertial coordinate system
$\theta_S$	Inherent shaft tilt, positive for tilt aft, <i>deg</i>
$\theta_{TPP}$	Pitch Attitude of tip-path plane relative to horizon, positive nose up, <i>rad or deg</i>
$\theta_v$	Angle between vortex element and direction vector to the point of interest (Biot-Savart Law)
$\rho$	Density of air ( <i>0.002378 slugs/ft<sup>3</sup></i> )
$\rho_o$	density of quiescent medium (acoustics formulation)
$\tau$	Retarded or source time, <i>sec</i>
$\tau_{source}$	Source time, <i>sec</i>
$\psi$	Helicopter yaw angle; radiation sphere azimuth angle, <i>deg</i>
$\psi$	Reference or blade azimuth angle, in the tip-path plane
$\psi_{NI}$	“Yaw” Euler angle associated with the non-inertial coordinate system

$\psi_V$	Yaw or azimuth angle of the flight velocity vector relative to gravity axis system
$\psi_o$	Reference azimuth associated with the “formation” of any vortex element
$\psi_v$	Wake age associated with vortex element
$\partial$	Partial differential operator
$\tilde{\partial}$	Partial differential operator, acting on generalized functions
$(\dot{\phantom{a}})$	Time derivative
$(\ddot{\phantom{a}})$	Double time derivative
$(\vec{\phantom{a}})$	Vector
$(\hat{\phantom{a}})$	Double time derivative
$(\prime)$	Symbol qualifier or distinguisher
$\bar{\square}^2$	Wave operator

## Subscripts

$0$	reference, initial or baseline; collective; steady (“DC”) component
$1,2$	Non-linear function indices, to distinguish between different functions

<i>I<sub>c</sub></i>	First harmonic cosine
<i>I<sub>s</sub></i>	First harmonic sine
<i>AM</i>	air-mass
<i>a</i>	aerodynamic, in the air-mass system or medium reference frame
<i>avg</i>	average value, averaged over one rotor revolution
<i>B</i>	Body coordinate system
<i>B</i>	Beddoe's wake induced velocity formulation
<i>des</i>	desired
<i>EFF</i>	effective, resultant
<i>eff</i>	effective, resultant
<i>F</i>	Fuselage
<i>G</i>	Gravity coordinate system
<i>HS</i>	Horizontal Stabilizer
<i>I</i>	Interference (forces); induced (velocity); inertial (coordinate system)
<i>i</i>	general index - blade number or index; point on ground plane, time step along flight trajectory
<i>j</i>	Point on radiation sphere, state variable index
<i>lat</i>	lateral (pilot control input)
<i>level</i>	level flight
<i>level flight</i>	level flight
<i>lon</i>	longitudinal (pilot control input)
<i>max</i>	maximum
<i>MR</i>	Main-rotor

<i>NI</i>	Non-inertial coordinate system
<i>NW</i>	under no wind conditions
<i>ped</i>	pedal (pilot control input)
<i>ret</i>	At the correct retarded time
<i>SS</i>	Steady state
<i>t</i>	Tail rotor
<i>TPP</i>	Tip-path plane or tip-path plane coordinate system
<i>TR</i>	Tail rotor
<i>trim</i>	Under trim conditions
<i>v</i>	Associated with vortex element
<i>VT</i>	Vertical Tail
<i>W</i>	Wind or velocity coordinate system

### **Superscripts**

<i>i</i>	time-step number
<i>EFF</i>	effective
<i>SS</i>	steady-state

### **Acronyms, Abbreviations, Units and Titles**

<i>1-D</i>	One-dimensional
<i>2-D</i>	Two-dimensional

<i>3-D</i>	Three-dimensional
<i>AH-1</i>	Attack Helicopter – 1, “Cobra”
<i>Bell206-B</i>	Bell Helicopter, “JetRanger”
<i>BVI</i>	Blade-Vortex Interaction
<i>DGPS</i>	Differential global positioning system
<i>DNW</i>	Duits-Nederlandse Windtunnel
<i>dB</i>	decibel
<i>dB-A</i>	A-weighted decibel
<i>deg</i>	degrees
<i>FFT</i>	Fast Fourier Transform
<i>ft</i>	feet
<i>Hz</i>	Hertz
<i>lb</i>	Pounds
<i>min</i>	minute
<i>Q-SAM</i>	Quasi-Static Acoustic Mapping
<i>Pa</i>	Pascal
<i>RNM</i>	Rotorcraft Noise Model
<i>rad</i>	radians
<i>SEL</i>	Sound exposure level
<i>SPL</i>	Sound pressure level
<i>sec</i>	second
<i>UH-60</i>	Sikorsky “BlackHawk” Helicopter

# Chapter 1

## Introduction

Noise, or undesirable sound, is often the byproduct of operating propulsive aerodynamic systems, of which aircraft are a prime example. Fixed-wing aircraft, for instance, generate both engine noise and airframe noise, which typically increase with thrust level and vehicle velocity. In addition to these sources, helicopters are equipped with a complex rotor system which is the primary source of thrust, control and, usually, the associated noise as well [1], [2], [3]. Figure 1.1 highlights the complex aeromechanical environment of the main rotor, including transonic flow on the advancing side and dynamic stall on the retreating side, blade aeroelasticity, an azimuthally varying flow field, a complex unsteady wake structure, and vortex impact. Some of these pressure disturbances are radiated to the far-field as noise.

### **1.1 The Importance of Reducing Helicopter Noise in Terminal Area Operations**

Excessive noise around heliports has been one of the key impediments to the use of rotorcraft for commercial air transportation. Helicopters can radiate significantly

high noise levels to the surrounding communities when operating at low altitudes, where the sound decay with distance from the noise source is small, or during an approach to an airport. Although the noise generated and radiated by rotorcraft is not loud by large commercial fixed-wing aircraft standards, rotorcraft often serve smaller airports or vertiports where ambient or background noise levels are also lower than large commercial airports [4]. When the rotorcraft noise levels exceed the ambient or acceptable levels of the surrounding communities they are to serve, rotorcraft operations are limited or prohibited altogether.

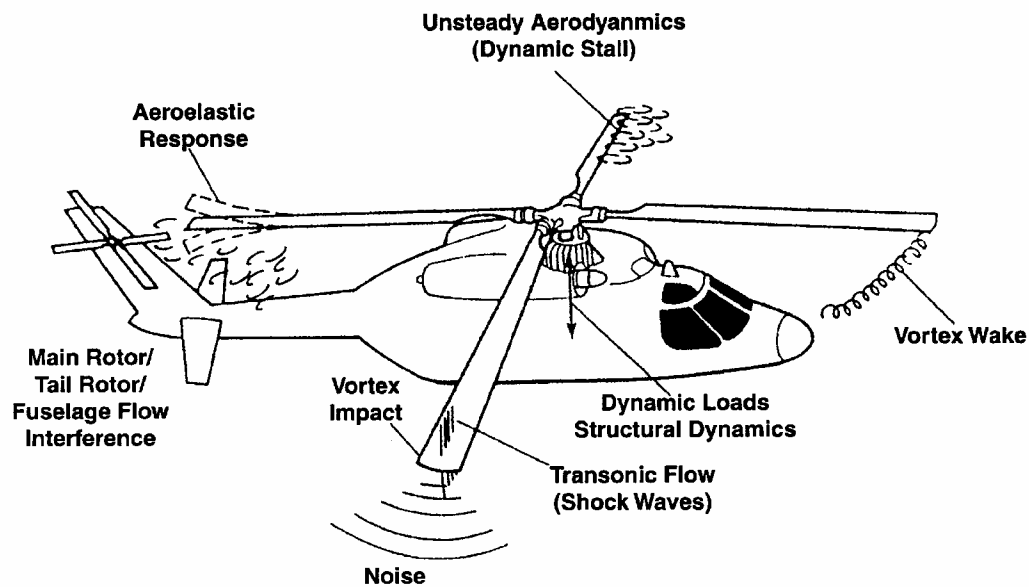


Figure 1.1 Sources of main rotor noise and vibration [5].

To date, civilian helicopter use has been restricted mainly to specialized purposes. Applications include medical or emergency evacuations, law enforcement, tourism and short-haul business transport. To meet the increasing need for public transport,

the introduction of rotorcraft into mainstream civilian air transportation networks has been proposed. Soaring demands for air travel are likely to result in increased delays as traffic queues bottleneck at runways with fixed capacity. Because few new airports are being planned, many airports operate at or near capacity with many others approaching a similar state. It has been proposed that the short to medium haul traffic may be offloaded by the use of Runway Independent Aircraft [6], including helicopters and tilt-rotor aircraft (Fig. 1.2). This allows the shorter fixed-wing traffic slots to be filled by longer-range, higher-passenger high-revenue flights, thus substantially increasing the overall capacity of the airport. If rotorcraft are to replace fixed-wing aircraft over these shorter route segments, they must not increase the noise radiated to the communities surrounding the airport. This consideration makes noise abatement a priority in rotorcraft operations and design.

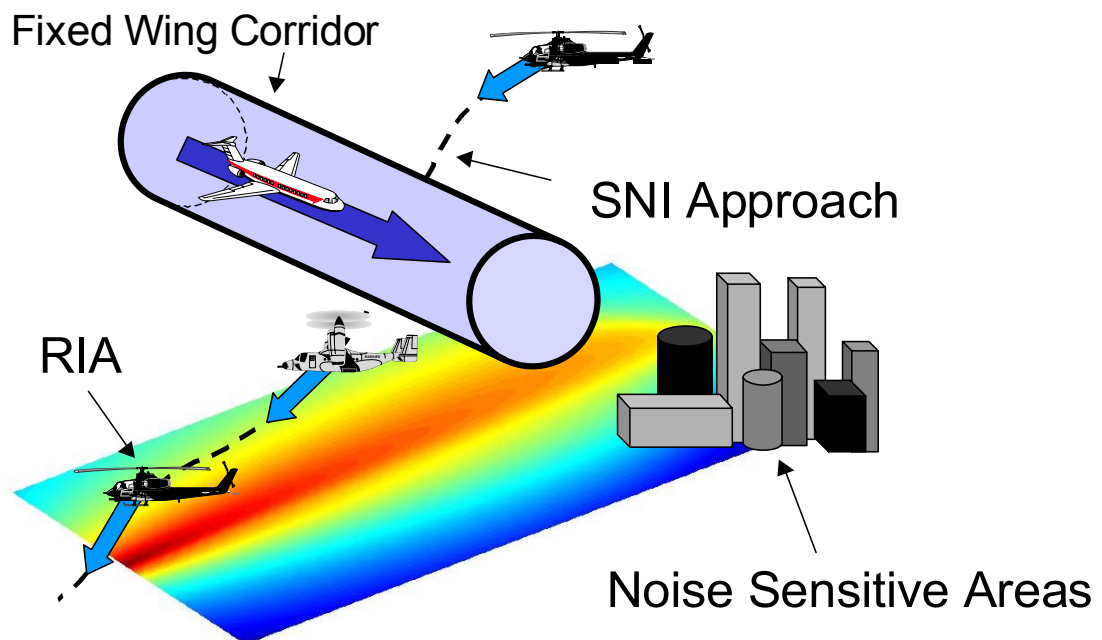


Figure 1.2 Simultaneous non-interfering (SNI) trajectories for runway-independent aircraft (RIA).

The distinctive nature of rotorcraft noise often calls attention to operations even when the radiated noise levels are, by community standards, quite low [7]. The characteristic pulsating nature of noise generated by the main rotor, the propeller-like sound of the tail rotor, or the characteristic whine of the “Fenestron” cause an awareness to rotorcraft operations that is often synonymous with non-acceptance. Several metrics have been used to assess the undesirable quality of sound based on the associated frequency content, level and duration. For terminal area aircraft operations, the Sound Exposure Level (SEL) and the Effective Perceived Noise Level (EPNL) [8], both expressed in dB, are the most commonly employed metrics used to quantify the “noisiness” associated with a flyby or approach procedure. Such metrics apply weights or filters to the frequency spectrum of the radiated sound, based on human annoyance considerations.

## **1.2 Major Sources of Helicopter Noise During Landing Approach**

Fixed wing aircraft mainly suffer from engine noise and airframe noise. In addition to these conventional noise sources, different components of the helicopter system are associated with distinct sources of noise emission. The main and tail rotors, engine, airframe and gear box all produce noise when in operation [1], [2]. In terms of noise annoyance on the ground, it is the main and tail rotors that produce the most significant noise sources.

The important main rotor noise sources can be classified broadly into three classes. These are linear harmonic noise (thickness and loading), impulsive noise (BVI and HSI) and broadband noise (turbulence generated noise, blade-wake interaction noise and self-noise) [3], [5]. Loading noise arises because of blade pressures in motion. Harmonic loading noise is associated with the non-vibratory component of blade loads. Periodic impulsive loading and vibration occurs during vortex impact. This results in a particularly strong, impulsive and annoying noise source called blade-vortex interaction (BVI) noise. Thickness noise is a result of air-volume displacement due to blade thickness. At or above certain tip advance Mach numbers, the thickness-associated noise becomes highly impulsive. This is a result of shock waves that connect to the far-field, rather than remaining localized to the blade surface. Harmonic thickness and loading noise occur at the lower harmonics of blade passing frequency, while impulsive noise occurs in the medium frequency range – 200 Hz to 2000 Hz.

Two of the most prominent sources of helicopter main rotor noise are High Speed Impulsive (HSI) Noise and Blade-Vortex Interaction (BVI) Noise [9]. These noise sources have received more attention from researchers, operators and the public, than all other noise sources, because of their distinctly offensive and annoying nature.

High Speed Impulsive (HSI) Noise, which occurs in high speed forward flight, is associated with transonic effects and “delocalization” of blade surface shock waves at the advancing tip of the blade [10], [11], [12]. This noise source is predominantly

related to the thickness of the blade airfoil, and is mainly radiated directly ahead along the helicopter's flight path, near the plane of the rotor disk. For this reason it is especially important from the standpoint of detection of high speed military helicopters. Since the noise is radiated directly ahead and is not heard in the cabin, pilots and passengers are usually oblivious to the radiated noise. For conventional helicopters, during an approach to a landing HSI noise is usually not a major contributor to terminal area noise exposure. This is because HSI noise occurs at high flight velocities and is radiated more in-plane of the rotor disk rather than below it.

BVI noise occurs mostly during low/moderate speed descent flight, and sometimes in turning or maneuvering flight, when the rotating blades pass in close proximity to the previously shed rotor tip vortices [9], [13]. These vortices induce sharp periodic aerodynamic disturbances on the blades (high frequency blade loading), which then generate BVI noise. BVI noise is known to be highly directional and quite sensitive to flight condition. Its particularly annoying nature comes from the fact that BVI acoustic energy is usually concentrated in the mid frequency range of 200 Hz to 2000 Hz. The human ear is highly sensitive to the higher harmonics of BVI noise.

Blade-Vortex Interaction (BVI) noise occurs at moderate flight velocities and rates of sink, typical of nominal civilian approach operations, and is radiated primarily out-of-plane of the rotor disk. During an approach to a landing, several helicopters radiate BVI noise, below and around their flight paths, to the communities near the heliport as they descend. When it occurs, BVI noise, is one of the most distinct and

objectionable sounds emitted from rotorcraft. It's typical popping or slapping sound radiates large amounts of acoustic energy in distinct patterns far from its source. BVI noise reduction is the primary focus of this research.

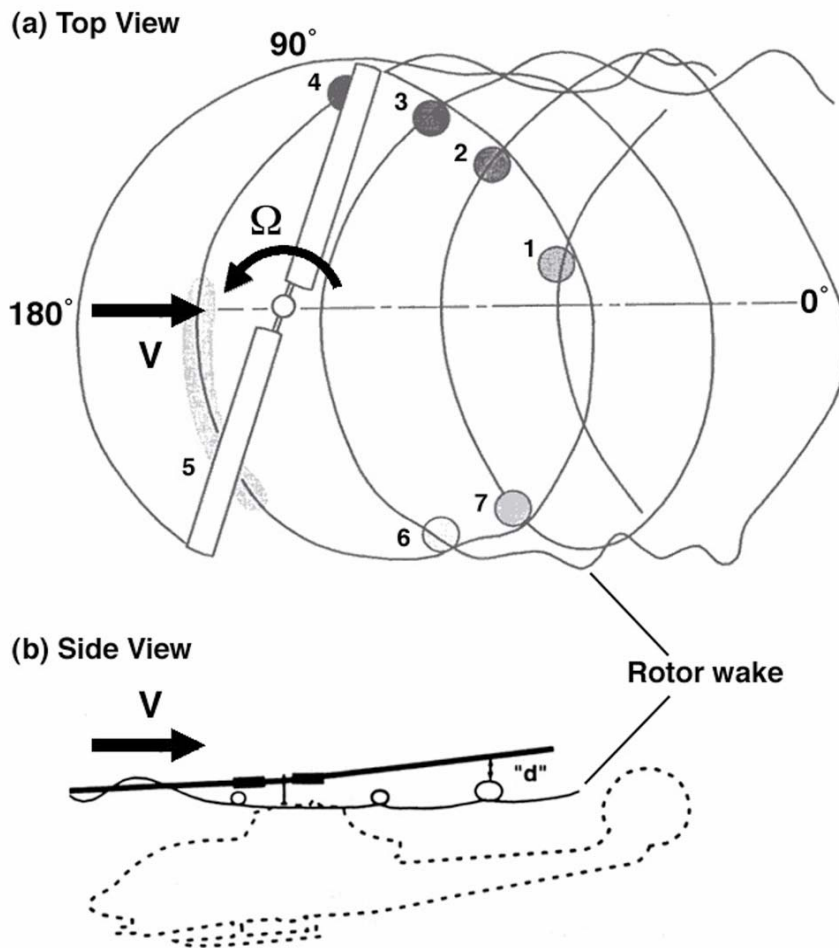


Figure 1.3 Helicopter BVI geometry for a two-bladed rotor: top and side view [9].

The geometry of the BVI problem is sketched in Fig. 1.3a for a two-bladed helicopter as seen from a “top” view [9]. In the top view, rotor blades appear to intersect the

vortices that were previously shed from the tips of the rotor at earlier times. Even for a two-bladed rotor, several blade-vortex intersections are seen possible. The “miss-distance”, which is the vertical distance of separation between the vortex elements and the rotor blade during the interaction, is illustrated in a “side view” sketch of Figure 1.3b. Highly impulsive BVI noise are radiated as a result of the unsteady aerodynamic blade pressures induced when the rotor blades pass close to, or intersect previously shed tip vortices (Fig. 1.4). One way of reducing BVI noise radiation is to increase these characteristic miss-distances associated with important blade-vortex interactions.

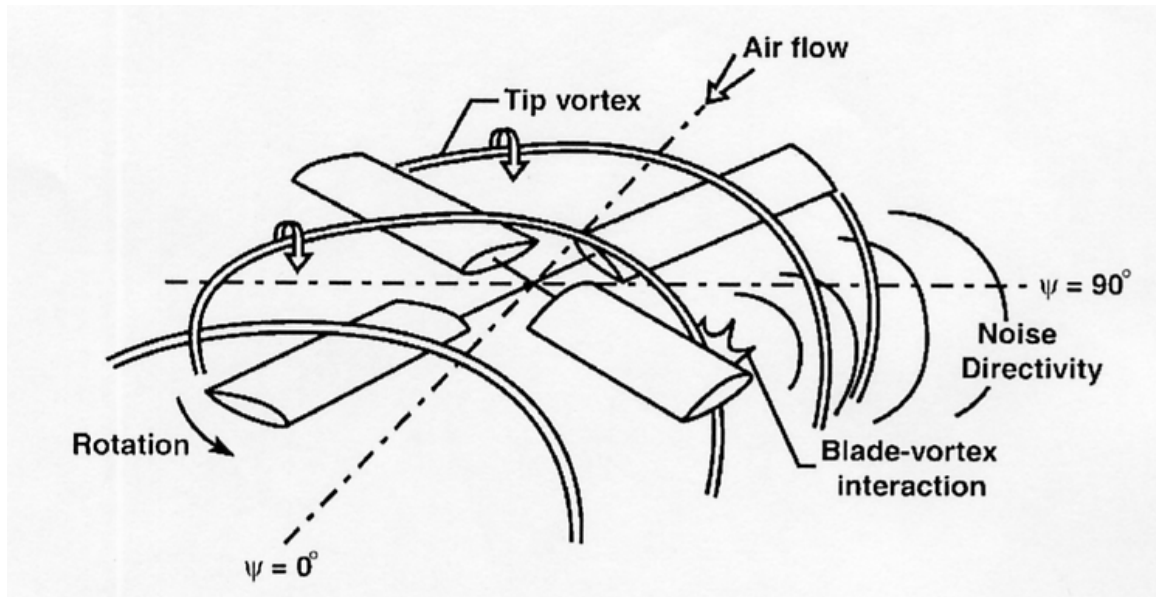


Figure 1.4 Schematic showing the BVI phenomenon and the radiated noise directivity [5].

## 1.3 Review of BVI Noise Research and Control

Steady-state BVI noise has been a subject of intensive research, experimental and analytical, over the past three decades [9], [13]. This dedicated effort on the part of several researchers has led to a fundamental physical understanding into some of the basic underlying mechanisms through observations, measurements and theoretical-analytical techniques.

### 1.3.1 Experimental Investigations

Wind tunnel tests as well as flight tests have been conducted as part of numerous research efforts to characterize the acoustics of model-scale and full-scale rotors. The now-classic AH-1/OLS wind-tunnel test conducted at the Duits-Nederlandse Windkanal (DNW) measured blade-vortex interaction noise characteristics associated with a model-scale two-bladed rotor. Geometrically scaled AH-1 blades were run in an anechoic wind-tunnel and the associated noise characteristics were measured [9], [14]. Under trimmed steady-state conditions, Schmitz et al [14] showed that for a given rotor design (specified blade geometry, number of blades etc.) BVI noise is governed by four helicopter non-dimensional operational parameters; rotor thrust coefficient,  $C_T$ ; rotor advance ratio,  $\mu$ ; rotor tip-path-plane angle,  $\alpha_{\text{TPP}}$ ; and hover-tip Mach number,  $M_{\text{HT}}$ .

These wind tunnel tests were complemented with full-scale acoustic in-flight testing of the same main rotor system. The in-flight testing technique, developed by Schmitz and Boxwell [9], [15], [16] consists of an aircraft flying in formation with the helicopter being tested (Fig. 1.5). The additional aircraft acts as an instrumented “flying platform” for making acoustic measurements. The first tests consisted of a Mohawk (OV-1C) instrumented with a microphone flown in formation with a UH-1H helicopter (Fig. 1.5). Microphone locations representing observer locations of interest in terms of main-rotor impulsive noise radiation were flown. This program was the first successful effort in clearly establishing the full-scale impulsive noise characteristics of this helicopter. It was also shown that cabin noise measurement is a sufficient but not necessary indicator of noise radiation. This was especially true of HSI noise which could not be heard in the cabin. In general, it was shown that BVI noise radiated mostly forward of and below the main rotor. Flight conditions corresponding to high BVI noise radiation included low to moderate flight velocities and moderate rates of sink. Subsequently a much quieter aircraft, the Y0-3A was used as the instrumented aircraft and the noise characteristics of the AH-1S, AH-1G and the UH-1H were studied, along with other helicopters [17].

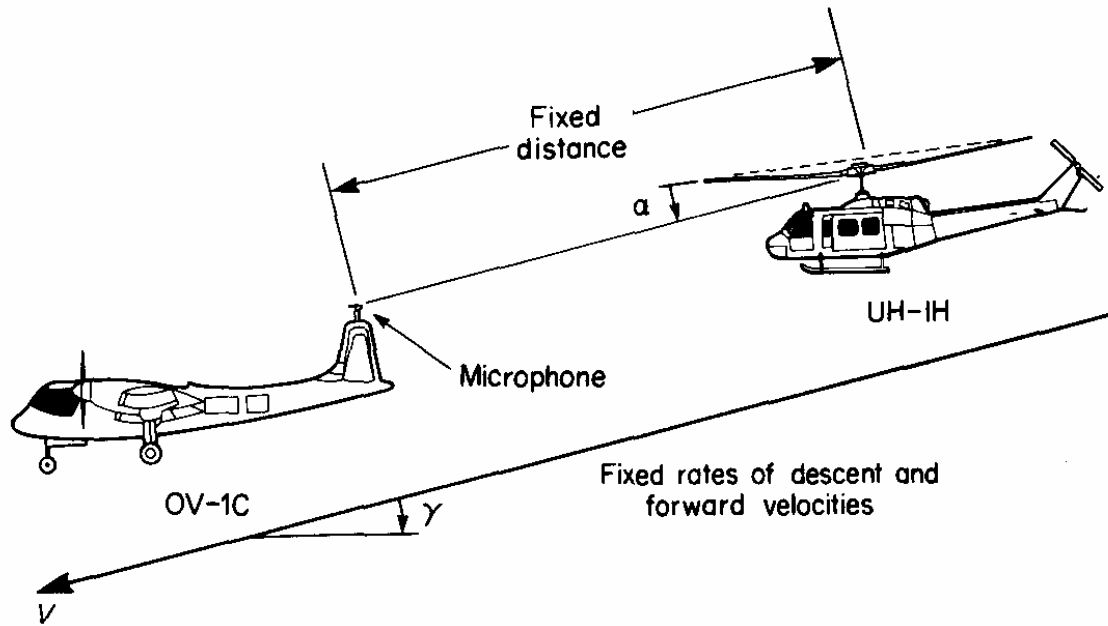


Figure 1.5 In-Flight acoustic measurement technique with “flying acoustic platform” by Schmitz and Boxwell [9].

A comparison of wind-tunnel and in-flight acoustic data was conducted. While wind-tunnel test acoustic measurements showed qualitative agreements with full-scale in-flight data, strict scalability was questionable, especially at advance ratios higher than 0.2 [9]. The corresponding wind-tunnel acoustic pulses in general exhibited lower amplitude but larger pulse widths. This seemed to indicate that the impulsiveness of the acoustic event was perhaps somewhat underrepresented in the scaled model experiment. Scalability at low and moderate advance ratios was shown to be reasonable, as long as the four aforementioned governing non-dimensional parameters are matched. These studies justified the use of less expensive scale-model wind-tunnel testing of rotors rather than full-blown flight testing.

Several wind tunnel tests have further explored the effects of design and operational parameters on BVI noise radiation. Burley and Martin [18] presented detailed time history results of BVI noise associated with a model BO-105 rotor in the German-Dutch wind-tunnel, DNW. The effects of changes in tip-path plane angle and advance ratio were assessed. It was observed that peak BVI noise radiation occurred at a specific tip-path plane angle, which was seen to be a function of advance ratio. This tip-path plane angle corresponding to peak BVI noise radiation was seen to decrease as advance ratio increased. It was also shown that BVI noise is highly directional [19], and that directivity characteristics are strongly dependent on the tip-path plane angle and advance ratio. These observations highlight the tremendous potential of controlling BVI noise through the control of advance ratio and tip-path plane angle.

The in-flight measurement technique was revisited by Yamauchi [20] et al in 1991 as part of the IRAP (In-Flight Rotorcraft Acoustics Program). This program is an ongoing effort to enhance fundamental understanding of BVI noise. The main objective of this test was to conduct in-flight testing of the S-76 4-bladed rotor system and to compare the acoustic radiation characteristics with full-scale wind-tunnel measurements. Comparisons between the flight test and wind tunnel were reasonable at low to moderate advance ratio but poor at high advance ratios ( $> 0.25$ ). The wind tunnel measurements actually showed higher blade-to-blade and revolution-to-revolution variability than the in-flight data. The noise measurements made in-flight were studied in terms of variations in the tip-path plane angle and advance ratio. The effects of changes in thrust coefficient and hover tip Mach number were not studied.

Tip-path plane angle was estimated using the measured flight path angle and an estimate of vehicle drag to weight based on the equivalent flat plate area of the helicopter. It was observed that peak BVI noise radiation increased with increasing tip-path plane angle until it reached a maximum value for a particular advance ratio. Further increases in the tip-path plane angle resulted in a reduction in peak BVI noise. This characteristic tip-path plane angle corresponding to peak BVI noise radiation was shown to be a function of advance ratio, as was shown in previous wind tunnel tests. Subsequently, in-flight tests were also conducted with the BO-105 [21] and the UH-60A [22] and compared with wind-tunnel results. These experimental tests highlighted the complex directional nature of main rotor BVI noise, and its strong dependence on operational parameters, especially the tip-path plane angle and advance ratio, as well as on main rotor design.

### **1.3.2 BVI Noise Predictions**

BVI noise prediction is usually a combined experimental and theoretical effort. The role of experiment and theory depend on the specific methodology adopted for the noise prediction procedure. An entirely theoretical first principles approach would still rely on experimental data for validation.

Acoustic pressure in the far-field is simply the perturbation aerodynamic pressure. Aeroacoustics is governed by the fundamental conservation laws of mass, momentum and energy. Therefore, a full solution to the Navier-Stokes equations over the entire

flow field would, in theory, provide the desired solution. This approach is currently beyond existing computing capacity, and will be so in the near foreseeable future for most rotor problems [23].

Rather than solving the aeroacoustics equations associated with the entire flow field, the problem is usually divided into two parts – a determination of the aerodynamic pressure, velocity and aerodynamic stress fields around the rotor blade (near-field) is followed by an application of acoustic propagation equations to determine the acoustic pressures at the observer location (far-field) [24].

Lighthill [25] rewrote the exact Navier-Stokes equations, to extract acoustic propagation terms on one side of the equation, leaving effective acoustic source terms on the other side. This subtle equation, called the “acoustic analogy” was derived primarily for jet noise and is usually not applied directly in analytical or computational work for rotor problems.

Ffowcs Williams and Hawkings [26] followed the same general derivation methodology used by Lighthill and recast the continuity equation and the Navier-Stokes equations into the form of a non-homogenous wave equation with three sources terms. Using the method of generalized variables, and applying it to general surfaces in arbitrary motion, a much more widely applicable governing acoustics equation, than the Lighthill equation, was developed.

$$\bar{\square}^2 p'(\bar{x}, t) = \underbrace{\frac{\tilde{\partial}}{\partial t} [\rho_o v_n \delta(f)]}_{\text{mass term}} - \underbrace{\frac{\tilde{\partial}}{\partial x_i} [l_i \delta(f)]}_{\text{force term}} + \underbrace{\frac{\tilde{\partial}^2}{\partial x_i \partial x_j} [T_{ij} \delta(f)]}_{\text{Stress Term}} \quad (1.1)$$

where  $\bar{\square}^2$  is the wave operator. It was assumed in this classic derivation that the aerodynamic surface was impenetrable, though the application of this methodology to more general surfaces was also clear to the authors. An integral solution to this equation is obtained through the application of the free-space Green's theorem, and utilizing the fact that through the use of the generalized functions, the FW-H equation is valid over unbounded space. This is the form adopted by most deterministic acoustics formulations in use today:

$$4\pi p' = \underbrace{\int_s \left[ \frac{\rho_o}{r(1-M_r)} \frac{\partial}{\partial t} \left( \frac{v_i n_i}{1-M_r} \right) \right]_{ret} dS}_{\text{thickness integral}} + \underbrace{\int_s \left[ \frac{r_i}{a_o r^2 (1-M_r)} \frac{\partial}{\partial t} \left( \frac{p_{ij} n_j}{1-M_r} \right) \right]_{ret} dS}_{\text{loading integral}}$$

$$+ \underbrace{\int_V \left[ \frac{r_i r_j}{a_o^2 r^3 (1-M_r)} \frac{\partial}{\partial t} \left( \frac{1}{1-M_r} \frac{\partial}{\partial t} \frac{T_{ij}}{1-M_r} \right) \right]_{ret} dV}_{\text{quadrupole integral}}$$

(1.2)

This equation has been written in the “far-field” radiation form. The acoustic pressure “p” in the far-field is given as the sum of three integrals: a thickness integral, a loading integral and a “quadrupole” integral. The thickness integral is conducted over the blade surface and accounts for the air-mass displacement effect due to blade thickness. The loading integral, is also a surface integral over the blade, and accounts

for pressure forces on the blade surface. The last term, is a volume integral term, over the aerodynamic stresses produced in the flow-field around the blade.

Much progress has been made in rotor aeroacoustics predictions since the FW-H equations were first presented in 1969, especially in the last 20 years [9]. This equation has been recast and reinterpreted by several researchers [27] into forms that can be implemented in analyses and computer programs [28, 29]. A popular acoustics prediction analysis code, WOPWOP [29], uses Farassat's formulation 1A [27], and essentially ignores the quadrupole term.

Caradonna et al [30] presented a study to compare prediction methods ranging from full CFD to indicial-aerodynamics based blade-element methods, and also using the blade pressures as inputs to compute the aeroacoustics associated with an idealized and controlled parallel vortex interaction experiment [31]. This experiment consisted of an idealized isolated parallel BVI at the acoustically treated NASA Ames 80×120 foot wind tunnel. A two-bladed NACA 0012 rotor blade system was studied. The vortex was independently created with an upstream NACA0015 airfoil. Comparisons between experiment and theory were encouraging. It was concluded that most prediction methods predict BVI noise fairly well when vortex parameters and blade motions are accurately known. Another favorable factor was the fact that a “parallel” interaction is primarily a 2-D problem, which is simpler to treat analytically compared to oblique 3-D interactions.

Unfortunately, accurately predicting helicopter BVI noise from first principles is a difficult challenge that has yet to be accomplished in a general sense. BVI noise is caused by high frequency impulsive blade loading due to close passage of the main rotor blades with previously shed tip vortices. Besides a good estimation of the helicopter trim state, accurate prediction of the strength, structure, and position of the vortices, unsteady blade aerodynamics and blade aeroelasticity is essential for accurate prediction of high frequency BVI impulsive loading and hence BVI noise.

When additional modeling assumptions are employed to make the problem more tractable, the theoretical methods do seem to capture many of the noise level trends of BVI noise radiation. Hassan, Taghichi and Charles [32] predicted BVI noise with WOPWOP using predicted pressures. They coupled the aerodynamics code CAMRAD [33] with a full-potential analysis to obtain blade loads. This method requires some prior knowledge of the rotor wake as well as specific details of the vortices involved in the interaction. Comparisons with experiment were reasonable but it is noted that the prediction of airloads needs improvement. Better agreements with experimental data have been obtained recently using more sophisticated first-principles representations of both the wake [34] and blade motions [35].

It is widely believed that problems in estimating noise radiation arise mainly due to inadequacies in the prediction of the aerodynamic field to the requisite resolution and accuracy rather than in modeling the equations representing the acoustic propagation itself. The scenario of being provided detailed information regarding the pressure and

velocity distribution over the blade, and then being required to compute the associated acoustics has been referred to as an “acoustician’s dream” [9]. This second method of acoustic prediction, through the use of measured blade pressures, has also been attempted by various researchers. Earlier prediction attempts with the AH1-OLS main rotor test results, from the DNW, by Nakamura [36], by Joshi and Liu [37] using WOPWOP, by Schultz and Spletstoesser [38] using a solution to the FW-H equations including the quadrupole term, and other efforts [39], for instance Visintainer et al [40], pointed out the need for higher resolution in measured data for complete and better correlation [40, 41].

### **1.3.3 BVI Noise Reduction Techniques**

Helicopter noise reduction is possible through both design changes and operational techniques [4, 7], and a combined approach is usually most effective. Noise reduction, though not a traditional design driver, is gaining increasing prominence as various engineering technologies advance in sophistication. Conventional metrics of performance have almost always superceded concerns of noise emission in past design efforts, but acoustics has become an increasingly important design and operational consideration for aircraft manufacturers and operators in the past few decades [42, 43]. This evolutionary change in design philosophy has been facilitated by years of technical experience and physical understanding [9], and necessitated by military requirements, increasing civilian awareness and sensitivity to aircraft noise, as well as competitive market forces. Three major drivers for helicopter noise

reduction from a design point of view are certification requirements, local community noise standards, and the fact that fixed wing aircraft noise has steadily reduced [5].

To some degree, BVI noise reductions can be realized by reducing the rotor disk loading and by lowering the main rotor tip speed [4]. From a design/performance standpoint, low disk loading rotors are, however, not efficient for larger rotorcraft envisioned for commercial operations. Many modern quiet helicopters incorporate a lower main rotor tip speed and a modest blade area increase to reduce BVI noise, and to allow a higher cruise speed by minimizing the compressibility effects on the advancing side of the rotor disk. However, stalled flow on the retreating side of the rotor disk and/or the reduced hover performance often limits this design solution. For rotor hovering tip Mach numbers of  $\sim 0.65$  and above, BVI noise, when it occurs, is still considered to be the dominant noise source for rotorcraft operations.

Most helicopters in commercial use today have either two or four rotor blades. Increasing the number of rotor blades from two to four, five or even seven results in lower individual blade loading and hence lower trailed vortex strength. This reduces the severity of individual blade-vortex interactions, but possibly introduces many more interactions compared to a two-bladed rotor. Even for four bladed helicopters, blade-vortex interaction noise continues to be a critical operational issue.

Most BVI noise reduction strategies have essentially focused on either reduction of the associated vortex strength, increasing the “miss-distance”, or modification of aerodynamic response of the blade during the interaction.

### **1.3.3.1 Low BVI Noise Design (Passive Control)**

Passive control [44] through innovative planform designs, like serrated leading edges, and new blade shapes like wavy planforms, forward swept planforms, focus on changing the BVI acoustic wave collection process (“phasing”), and reducing acoustic efficiency. It is also attempted to favorably alter the aerodynamic response of the blade to the BVI through leading edge design like porous leading edges. New tip shapes have been suggested to reduce the strength of individual blade vortices, and thus reduce BVI noise.

### **1.3.3.2 Active HHC and IBC Control**

Active rotor control includes Higher Harmonic Control (HHC) [45, 46], Individual Blade Control (IBC) [47], active blade twist [48], fluidic control of the trailed vortex through trailing edge air-jets, active leading edge modification. Higher Harmonic Control has been reported to achieve noise reduction through local increase in miss distance associated with the BVI. With these methods, it is also attempted to reduce BVI noise by locally reducing the vortex strength at appropriate wake ages,

corresponding to important BVIs. Fluidic control attempts to diffuse the tip vortex, reducing its strength and increasing its core size.

The HART (Higher Harmonic Control Aeroacoustic Rotor Test) program at the German-Dutch wind-tunnel DNW, tested an instrumented model of the BO-105 main rotor at several operating conditions and HHC settings [46]. This comprehensive effort has spawned several research papers analyzing and presenting the measured blade loads, blade motion and acoustics. The wake geometry and vortex strength were also measured using laser techniques. Several analyses codes have used these data to make acoustics predictions, and the results compared with each other and with acoustics data. Three different flight conditions were studied in detail – a nominal descent at a flight path angle of  $-6^\circ$ , a low vibration case with higher harmonic control (HHC) inputs and a low BVI case with higher harmonic control inputs. Increase in miss-distance was identified as the cause of noise reduction due to HHC. The low vibration case was associated with an increase in BVI noise and the low BVI noise case as associated with an increase in low frequency noise and vibration. The vortex structure and trajectory, blade deflections and motion as well as blade airloads have been identified as the most important parameters for the accurate prediction of BVI noise radiation. Increase in miss-distance is deemed to be the major cause of BVI noise reduction due to HHC.

### 1.3.3.3 X-Force Control

For longitudinal straight line flight, Schmitz [49] suggested the possible control of tip-path plane angle and hence main rotor inflow by controlling X-forces acting on the helicopter in the wind axis system. It is when the inflow through the rotor disk is close to zero that vortices remain close to the rotor tip-path plane, which increases the likelihood of vortex impact. It was suggested that these X-force controls can be used to control and possibly reduce the likelihood of strong BVI noise radiation, by avoiding near-zero inflow conditions.

Several simplifying assumptions were made in the analysis. Main rotor thrust was assumed equal to helicopter weight. Only the X-force balance equation in the wind axis system was considered. Helicopter drag was assumed to be a function of flight velocity alone and based on an equivalent flat plate area of the fuselage. The main rotor H force in the tip-path plane was assumed to be small.

Three possible X-forces were identified: additional aerodynamic drag force due to deployable drag devices (Fig. 1.9), non-aerodynamic propulsive or drag forces acting along the flight path and vehicle acceleration or deceleration parallel to the flight path. By treating the acceleration parallel to the flight path as a static control parameter, it was suggested that the effect, on the value of the tip-path plane angle, of

a small change in flight path angle in radians was equivalent to the effect of vehicle acceleration in g's.

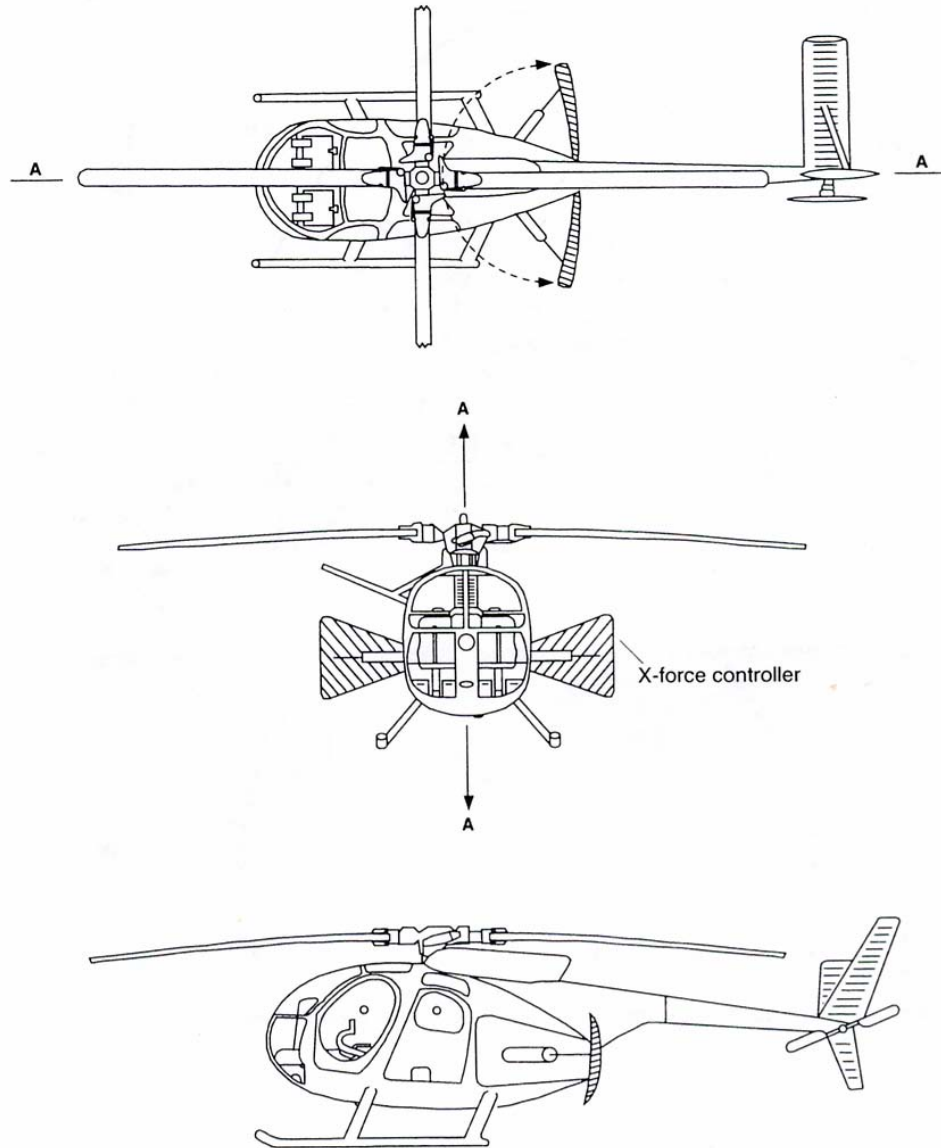


Figure 1.6 A schematic of a possible “X-force Controller” for BVI noise suitable for some helicopter design, proposed by Schmitz [44].

#### **1.3.3.4 Flight Trajectory Management**

An alternative means of reducing BVI noise is through flight path management and control. Because the separation distances between the rotor and the previously shed tip vortices is a consequence of the vehicle flight state, which governs its inflow distribution, it alludes to the possibility of reducing BVI noise signatures by directing the helicopter to approach/land under more acoustically-favorable and safe operating conditions. Changes in main-rotor operational state can also be used to change BVI directivity patterns, and potentially focus noise radiation to less noise sensitive areas. Wind tunnel tests and in-flight testing have demonstrated the strong dependence of BVI noise radiation and directivity on main-rotor operational conditions.

Some of the first experimental attempts at using flight path control to reduce the noise exposure to the surrounding community were done by Hawles [50]. Using cabin noise measurements and subjective evaluations of those measurements, a high-noise “fried egg” region, characterized by “loud blade slap”, was approximated for particular helicopters on a rate of sink versus forward velocity plot shown in Figure 1.6. It was observed that peak “blade-slap” or BVI noise radiation occurred during nominal descent conditions. For the helicopter represented in Fig. 1.6, maximum noise radiation occurred at flight velocities of 60 knots to 80 knots and a rate of descent of about 300 fpm to 500 fpm. The pilot was to avoid this region, and in so doing, would minimize BVI noise radiation (or blade slap”) to the surrounding community. These procedures were developed, by the Helicopter Association

International (HAI), into the “Fly Neighborly Program” [51] which has helped minimize BVI noise radiation for certain helicopters.

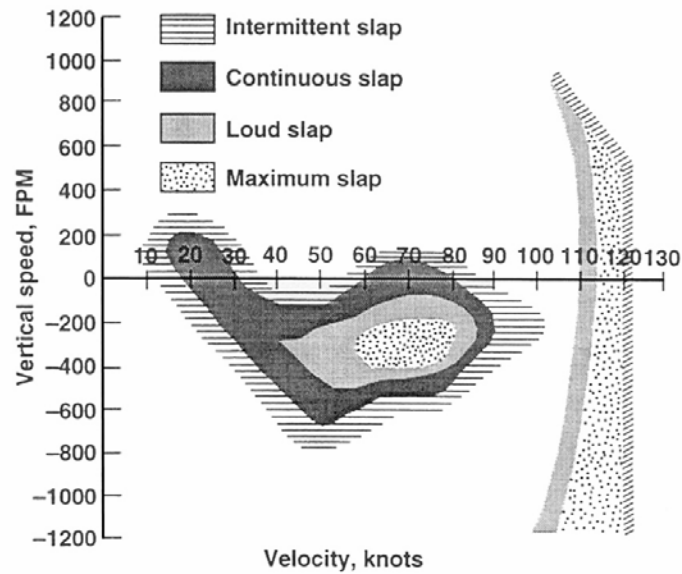


Figure 1.7 Measured cabin noise levels as a function of helicopter flight conditions [50].

Flight tests were conducted by the FAA in an effort to gather an extensive database of acoustic characteristics and flight information associated with typical enroute and heliport operations [52]. This effort was called the FAA/HAI Helicopter Flight Operations Noise Test Program. Level flyovers, normal and constant-glideslope approaches as well as noise abatement approaches were flown. Ground noise was measured using an array of microphones. The measured ground noise levels associated with the flight runs indicated that flight trajectory management could indeed be used to attain noise reductions during landing approaches.

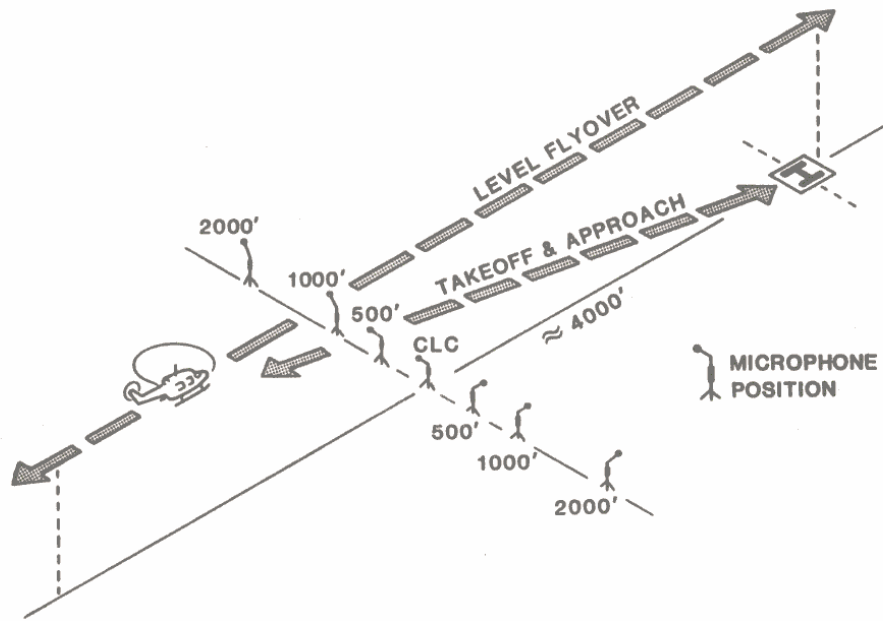


Figure 1.8 Typical ground noise measurement set up for flight test [50].

Experimental flight testing using GPS tracking and guidance has shown that flight trajectory control can alter helicopter noise exposure to the surrounding community [53], [54]. Using an S-76 helicopter equipped with a DGPS flight director several approach trajectories were flown [54]. Noise measurements were taken using a ground microphone array. Decelerating approaches were shown to have a significantly different noise level compared to steady state flight runs conducted at the same descent angle (Fig. 1.9). A multi-segment decelerating noise abatement approach was seen to be associated with a 5 dB noise level reduction compared to the certification approach.

A UH-60 research helicopter was used in a BVI noise abatement study in January 1995 [55]. Precision guided multi-segment decelerating approaches were flown and their noise impact on the ground assessed. A Local Differential Global Positioning System (LGPS) was used for precision navigation and cockpit display guidance. A laser based rotor state measurement system onboard was used to measure rotor blade flapping angles. The main rotor fixed-frame (shaft axis) flapping was obtained using a Fourier Coordinate Transform (FCT), and the tip-path plane angle was determined using the helicopter flight path angle, shaft tilt, fuselage pitch attitude. The static effect of vehicle acceleration parallel to the flight path was accounted for in the analysis of the data but not during the development of the approaches themselves. From handling qualities considerations, vehicle decelerations of 0.7 to 1 knot per sec (0.035g to 0.05g) were considered. It was pointed out that the effect of deceleration must be explicitly included in tip-path plane calculations. Ground based microphones, similar to that used in standard ICAO/FAA certification tests, were used for acoustic measurements. A methodology for the development and design of low BVI multi-segment decelerating approaches was developed based on a database of measured wind tunnel and flight data. However, because the effect of deceleration was ignored in the development of the noise abatement approach, it showed no reduction in BVI noise from standard 6° and 9° decelerating approaches. It was also pointed out that steeper approaches are more favorable when deceleration is employed, because during shallow approaches the use of deceleration could possibly “push” the helicopter into more BVI intensive regions of flight operation.

## DGPS Profile Reduces Noise Footprint By 5 dB

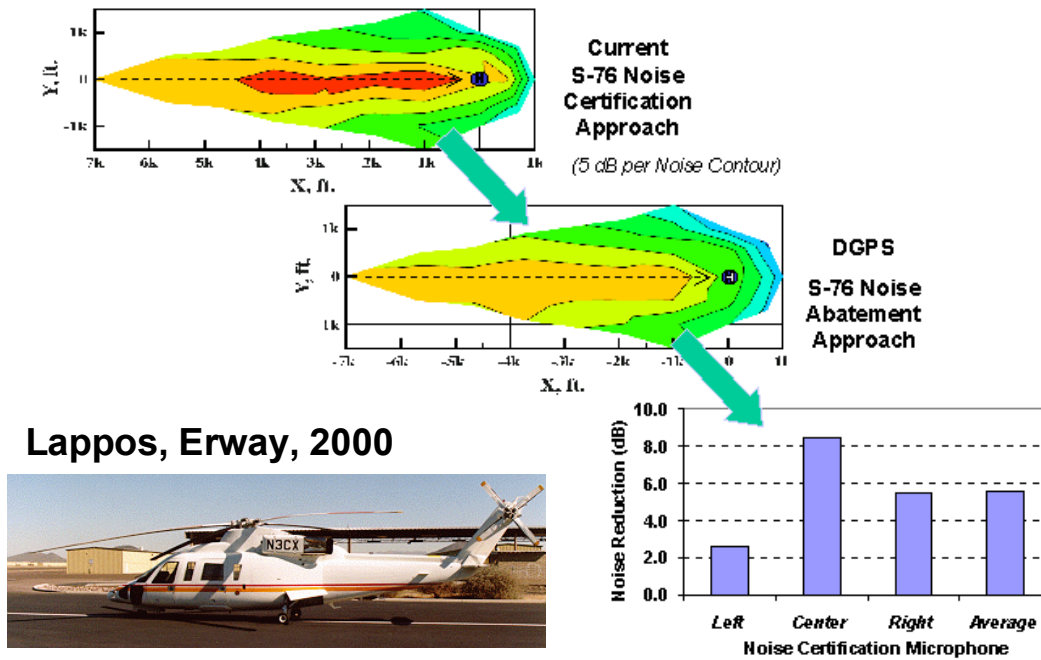


Figure 1.9 A descending decelerating noise abatement approach [52].

## 1.4 Rotorcraft Noise & Performance Modeling for Flight Trajectory Management

Flight trajectory management studies of radiated noise require the evaluation of ground noise metrics associated with different helicopter operations. It is usual to think of the ground noise prediction problem in three stages (Fig. 1.10) – the aerodynamic source field around the helicopter (unsteady pressure and velocity fields surrounding the rotor blades, for main-rotor noise) and its prediction or measurement; an intermediate acoustic surface, in the acoustic far-field, where acoustic predictions

are conducted; and the ground plane where these acoustic signatures are measured or propagated, using standard propagation tools and software.

Two general approaches [56] to predict ground noise exist – a direct approach that computes the noise radiation from the source to the ground from first principles, and a storage-based mapping approach that selects the appropriate noise radiation characteristics from a database at various instances along a trajectory and then propagates the noise levels to the ground.

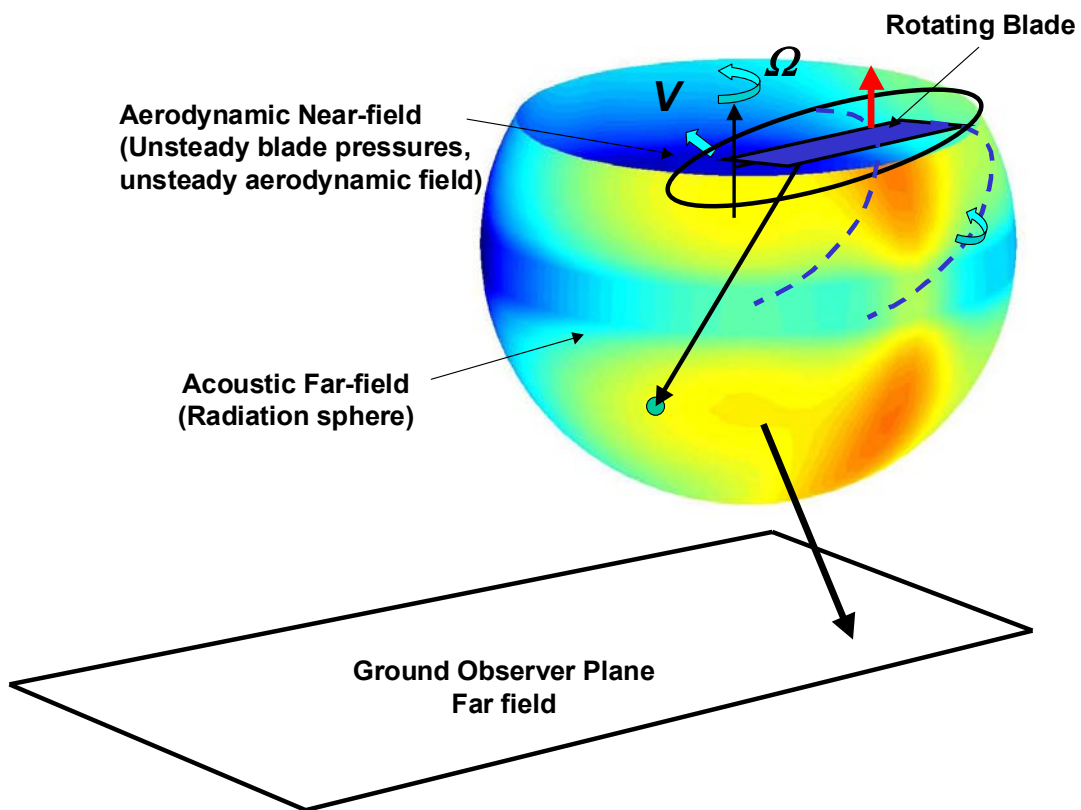


Figure 1.10 Three different steps of aeroacoustics predictions for ground noise studies: blade aerodynamics, acoustics radiation on radiation sphere and propagation factors.

## **1.4.1 BVI & Loading Noise During Steady Descents**

### **1.4.1.1 Theoretical Modeling**

Early theoretical attempts at using flight path management to minimize noise radiation for Vertical Take-Off and Landing (VTOL) aircraft showed that trajectories did exist that could help mitigate the noise problem [57], [58], [59]. Mathematical models of aircraft performance and noise generation/radiation were developed and used to project noise exposure to the surrounding communities. In these early studies, it was also discovered that BVI aerodynamic and noise modeling did not have the necessary mathematical fidelity to adequately represent the physics of the BVI phenomena.

Analytical flight trajectory management studies of helicopter have focused on BVI noise radiation. As stated earlier, the accurate, first-principles based prediction of BVI noise during steady-state flight still eludes researchers. The key issues have been identified. Accurate prediction of BVI noise would require a knowledge of wake structure and behavior, blade aeroelastic deformations and time-accurate blade-loads.

### **1.4.1.2 Rotorcraft Noise Model**

The “Rotorcraft Noise Model” (RNM) [60, 61], is a storage based acoustic mapping approach to helicopter ground noise prediction. It builds a radiation sphere that contains the spectral characteristics of the radiated noise for a given steady-state flight

condition, based on ground noise measurements. The main purpose of this research is to develop low noise approach trajectories for existing rotorcraft and to assess community noise impact during descent operations. Instead of directly calculating the noise from first principles, this approach maps acoustic data that has been stored as a function of steady-state flight conditions of the helicopter, to observers on the ground. Since measured data is the basis of such a method, the acoustic data does represent an accurate depiction of the generating physics of helicopter noise sources, thus avoiding the limitations of the first-principles approach.

The acoustic data to build each sphere is obtained from ground-based microphones in specially flown flight tests. Microphones are either mounted on stands near the ground or on poles or cranes to get near in-plane directivity information [60]. The effect of atmospheric absorption is intrinsically captured in this approach. The procedure, of developing radiation spheres from ground noise data is called the Acoustic Repropagation Technique, or ART [62], an entirely apt acronym. The desired ground noise estimates are then constructed by theoretically projecting these stored levels to the ground from a trajectory that is composed of a sequence of steady-state flight conditions.

Flight tests were conducted at Crows Landing for steady state and decelerating descent flight conditions using an MD-900 helicopter [63]. The results were analyzed using the RNM approach and compared with a first-principles based approach. The ground noise measurements were back-propagated to a radiation sphere surrounding

the helicopter using ART and then propagated to the ground using RNM. Several problems and areas of improvement were identified. For instance, difficulties of extrapolating these noise sources along long path lengths in both the storage and projection phases of the procedure introduce their own inaccuracies.

#### **1.4.2 BVI Noise During Steady Descents with Wind**

Wind can have a significant effect on noise radiation. While research testing has often alluded to the important effect of wind on helicopter trim, noise radiation and atmospheric propagation, a systematic study of the effect of wind on landing approaches, especially its effect on the radiated BVI noise, has not been conducted.

#### **1.4.3 Loading Noise During Maneuvering Flight**

Flight dynamics analysis of maneuvering flight has been the subject of extensive research over the past decades. Maneuver predictive capabilities based on first principles analyses are a subject of active research today. Higher order flight dynamics analyses have been developed by several researchers [33], [64]. Perhaps most challenging is the accurate prediction of the wake structure and behavior during these unsteady flight conditions [65]. This, coupled with unsteady aerodynamics and flexible blade motions results in an extremely complex problem that is difficult to study at a fundamental cause and effect level. When focusing on a special aspect of

this formidable problem, it is usually preferable to make some key assumptions that are valid within the domain of the particular sub-problem being addressed. For instance, it is reported [66] that unless the cross-coupling dynamic behavior is the focus of study, the use a dynamic inflow model [67], [68], as opposed to a full-blown time-accurate free wake model, for the main rotor wake would suffice for slow maneuver performance and flight dynamics studies.

Brentner et al have recently investigated the effect of transient maneuvers on loading and thickness noise [69], [70], [71]. Using a flight dynamics and aerodynamics code, with a dynamic inflow model, coupled to a modified version of the acoustics code WOPWOP adapted to maneuvering flight, the radiated loading and thickness noise during some simulated maneuvers was computed. Transitions to roll maneuvers and arrested descents are shown to be associated with considerable transient maneuver noise effects. Validation of maneuvering flight noise has not been conducted yet. BVI noise has not been addressed because a dynamic inflow model is used, which does not predict the high frequency loading response to blade-vortex interactions.

#### **1.4.4 BVI Noise During Maneuvering Flight**

Slowly decelerating flight is intrinsic to helicopter landing approaches. Deceleration has been experimentally observed to have a significant effect on the radiated BVI noise during flight testing. Wind also has a significant effect on noise radiation.

However, prediction of BVI noise during maneuvering flight is currently beyond the state of the art of analytical prediction capability. First-principles based noise prediction approaches currently lack the capability to accurately predict blade airloads during maneuvering flight. While maneuvering free wake models have been developed by some researchers, they have not been rigorously validated with experiments. The coupled aeroelastic analysis of the main rotor during maneuvering flight, required for the accurate prediction of BVI noise, is currently beyond the state of the art. This poses a limitation in the prediction of the associated acoustics.

## **1.5 Thesis Objectives**

### **1.5.1 General Focus**

While storage based-mapping approaches to BVI noise prediction and flight trajectory management studies show tremendous promise, they are currently limited to steady state flight conditions only. Extending such mapping techniques to slowly maneuvering flight will greatly improve their usefulness and applicability.

Currently, the RNM method [60, 61] does not account for any wind effects. Only straight-line propagation of sound is assumed. In addition, the RNM method is only valid for straight, steady-state flight in the longitudinal plane. Acceleration/deceleration along the flight path during the landing phase of flight

strongly affects BVI ground noise levels but is not included in this approach. Turning flight and changes in the design operating state are also not captured by this combined experimental/theoretical approach.

The focus of the present research is flight trajectory management to reduce helicopter BVI noise radiation during the landing phases of civilian flight operations. The employment of deceleration along the flight path to control BVI noise is emphasized. The acoustic mapping approach is extended to include the consideration of longitudinal maneuvering flight and steady wind conditions.

### **1.5.2 Specific Research Objectives**

The main objectives of this research are:

1. To study tip-path plane behavior and characteristics during slow longitudinal maneuvers, especially slow decelerating flight, and its implications to the radiated main rotor BVI noise. To investigate the quasi-static equivalence between deceleration and descent in longitudinal flight using analytical flight dynamic modeling.
2. To explore and validate the use of lower order flight dynamics modeling in the estimation of tip-path plane performance characteristics during slow longitudinal maneuvers.

3. To develop a general acoustic mapping approach that is based on the physical parameters that govern BVI noise and that is valid for nominal civilian descent operations including slow maneuvering flight.
4. To explore the use of deceleration and other flight and control parameters along the flight path as a means of BVI noise abatement.
5. To identify pilot cues and gain practical insights into slow maneuvering flight, especially slow decelerating flight. To design flight trajectories that can be flown to validate the acoustic equivalence between descent and deceleration.
6. To investigate the first order effect of steady longitudinal wind on BVI noise radiation.

### **1.5.3 Dissertation Road-map**

Chapter 2 presents steady-state noise estimates for a two-bladed helicopter, and the underlying analytical model is described. The noise radiation characteristics are presented as a function of advance ratio and tip-path plane angle. The trends are discussed in relation to the governing parameters.

Chapter 3 begins with developing equations governing tip-path plane performance – the tip-path plane angle and main rotor thrust. These expressions are derived from the X- and Z-force balance equations expressed in a wind or velocity coordinate system. This formulation is followed by the development of analytical models of helicopter flight dynamics to study the behavior and characteristics of the tip-path plane during slow maneuvering longitudinal flight. A brief analysis of lower order systems is presented. These lower order models serve as simple design tools for the study of tip-path plane behavior during longitudinal maneuvers. The equivalence between deceleration and descent is also explored using these analyses. A higher order coupled flight dynamics simulation is also adapted for use in the present research. A brief description of existing features is followed by modifications implemented for the present study. Finally idealized mathematical functional representations of longitudinal flight maneuvers are presented.

Chapter 4 presents the results obtained using the flight dynamics models developed in the previous chapter. Models of the UH-60 helicopter and the Bell206-B are studied. The effect of flight velocity and flight path angle on the tip-path plane and main rotor thrust are presented for trimmed steady-state flight, and their relations to the radiated BVI noise are discussed. This is followed by a study of tip-path plane behavior and characteristics during longitudinal maneuvers. Both decelerating flight and flight path transitions are studied along with combination maneuvers.

In chapter 5, a Quasi-Static Acoustic Mapping (Q-SAM) approach for the flight trajectory management of helicopter BVI noise is developed and implemented. The quasi-static acoustic equivalence between deceleration and descent is applied to storage based mapping techniques. Analytical estimates of the ground noise exposure trends associated with landing trajectories are presented and discussed. Some noise abatement strategies are presented. The Q-SAM technique is then used to investigate the effect of steady headwinds and tailwinds on radiated ground noise. Possible piloting strategies and their effect on BVI noise radiation are discussed. The effect of wind on representative noise abatement trajectories is presented.

Chapter 6 summarizes and concludes the thesis. Recommendations for future work in this research area are made. This is followed by a Bibliography and Appendices.

Three different helicopter models are used in this research – the Bell206-B (Chapter 2 and 4), UH-60 (Chapter 4) and the AH-1 (Chapter 5). A full-scale AH-1 model is used for the flight trajectory management and flight profile development section of this thesis (Chapter 5). There were several reasons for this choice. Two blades simplify the BVI problem because there are a lesser number of interactions to model. This results in reduced interference between vortices. A two-bladed rigid teetering main rotor system lends itself more easily to a simple treatment of its acoustics and performance compared to more modern helicopters. A simple analysis is therefore more likely to capture the trends associated with the BVI noise radiation of the AH-1 helicopter. A prescribed wake for a two bladed rotor in forward flight (low to

moderate flight velocities) fitted to experimental measurements has been used. Also its acoustics radiation characteristics have been extensively reported in the open literature. An experimental in-flight investigation of BVI noise radiation in slowly maneuvering flight conditions was started as part of this research effort, but no AH-1 helicopter was available. The Bell206-B was used for these tests. This explains the use of the Bell206-B in chapters 2 and 4. The higher order flight dynamics model adapted for use in the present research has been developed and partially validated for four bladed rotors, the UH-60 and BO-105. Because the study and understanding of tip-path plane angle behavior during maneuvers was considered to be for the most part platform independent, the UH-60 model was adopted in chapter 4.

## **Chapter 2**

### **Steady-State BVI Noise Estimation**

This chapter begins with a study of the factors governing BVI noise in steady state flight. This is followed by a description of an analytical model that has been previously developed [72], [73] to estimate the trends associated with BVI noise radiation. The results for a model of the full-scale Bell206-B helicopter are presented and discussed in the light of the current research. The main purpose of this chapter is to present typical BVI noise radiation characteristics of a two-bladed helicopter using a simplified analytical model, which is used in chapter 5 to study the flight path management of BVI noise associated with a full-scale two-bladed helicopter.

#### **2.1 Steady State BVI Noise:**

##### **Governing Factors and Functional Dependencies**

BVI noise generation is a complex coupled aeroacoustic, aerodynamic and aeroelastic physical phenomenon [13]. BVI noise radiation is primarily influenced by the strength and geometry of the near-wake structure and inflow field near the rotor

blades and the coupled aerodynamic and aeroelastic response of the blade to the interaction.

Steady-State main-rotor BVI noise is governed by several key physical parameters:

1. the spatio-temporal BVI interaction geometry - the geometry of the blade-vortex interaction in the tip path plane as well as the “miss distances” along each interaction,
2. the blade dynamic pressures,
3. blade design, which governs its aeromechanical response to the interaction,
4. the vortex strength and vortex core size, and
5. atmospheric conditions and properties like temperature and density.

The interaction geometry in the tip path plane is primarily defined by the advance ratio. This can be simply illustrated by assumed a tip-vortex structure that is undistorted in the  $x$ - $y$  rotor plane (tip-path plane). The equations representing blade motion and the tip-vortex geometry in the tip-path plane are:

*Blade Geometry for reference blade in the tip-path plane:*

$$\begin{aligned}x_b &= r_b \cos \psi \\ y_b &= r_b \sin \psi\end{aligned}\tag{2.1}$$

Undistorted Tip-vortex Geometry in the tip-path plane:

$$\begin{aligned}x_v &= \cos\left(\psi + (i-1)\frac{2\pi}{N_b} - \psi_v\right) + \mu\psi_v \\y_v &= \sin\left(\psi + (i-1)\frac{2\pi}{N_b} - \psi_v\right)\end{aligned}\tag{2.2}$$

The above equations (2.2) denote the vortex geometry associated with the  $i^{\text{th}}$  blade. The blade and vortex locations have been non-dimensionalized by the rotor radius  $R$ . In the above simplified equations, it is assumed that a single tip-vortex is trailed from each blade-tip and that the wake does not undergo any contraction. The in-plane tip-vortex geometry is assumed to be an undistorted epi-cycloid. The location of any vortex element, designated by the particular blade and blade azimuth associated with its “formation”, is a function of time, or blade azimuth angle ( $\psi$ ). The angle  $\psi$  refers to the current azimuth angle of the reference blade and is used to denote time.  $\psi_v$  is called the “wake age”, which, for any vortex element, denotes the time elapsed since its issue:

$$\psi_v = \psi_o - \psi\tag{2.3}$$

where  $\psi_o$  denotes the time that the particular vortex element was formed, in terms of the azimuth angle of the reference blade. Equation 2.2 can be used to determine the entire vortex geometry at a given time or to trace the time-history associated with a particular vortex element.

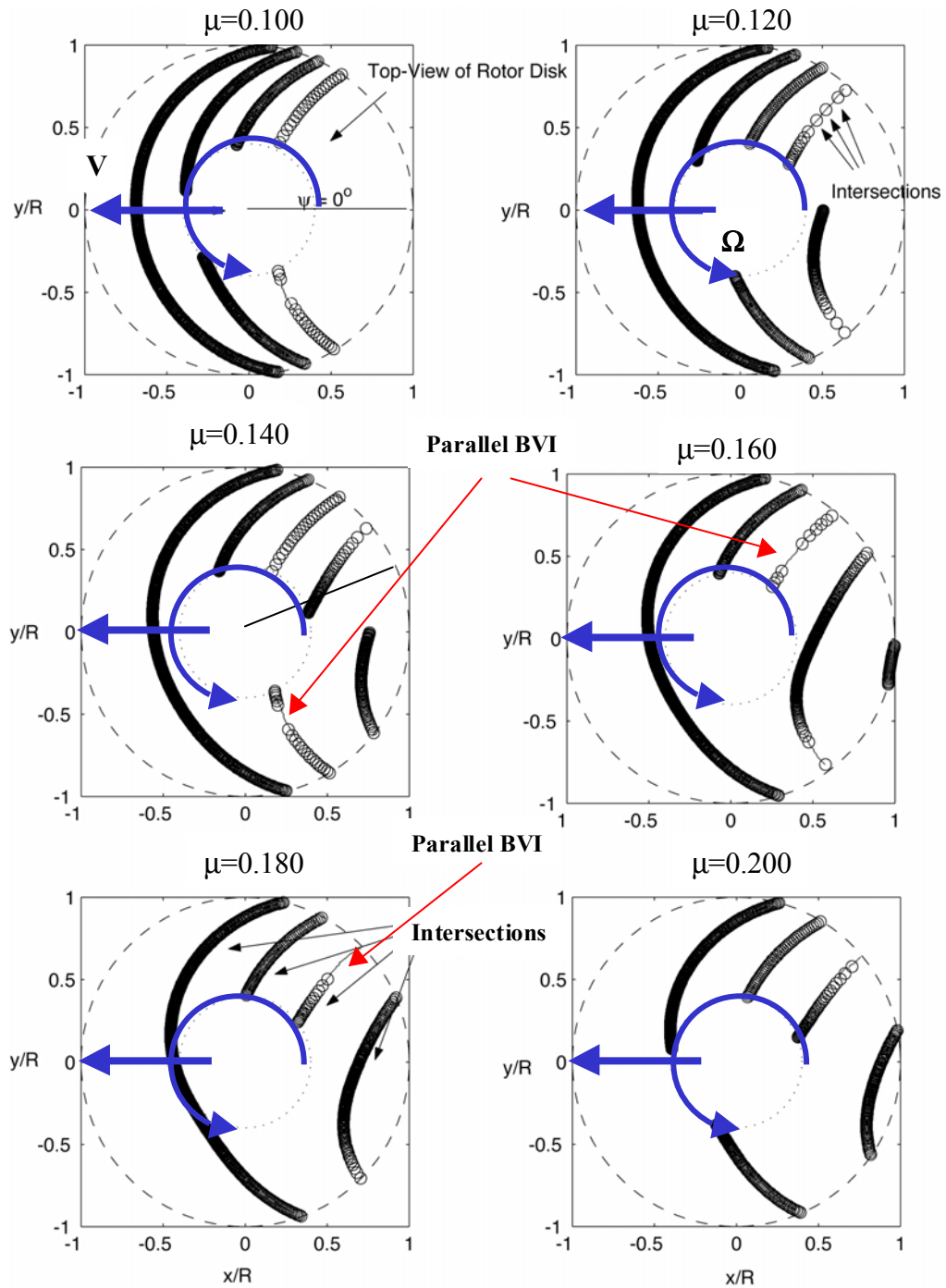


Figure 2.1 Blade-vortex intersection locations as a function of advance ratio for an undistorted epi-cycloidal wake of a two-bladed rotor.

BVI intersection locations for a given advance ratio and number of blades can be estimated by finding the intersection of these two curves [74, 75], or:

$$\begin{aligned}x_b &= x_v \\y_b &= y_v\end{aligned}\tag{2.4}$$

As a function of the reference azimuth angle, the values of  $r_b$  that satisfy the above condition are obtained [75]. Multiple solutions at each azimuth angle are obtained in general. This results in a family of curves,  $(x_i^j, y_i^j)$  that represents the intersection trajectory associated with the  $j^{\text{th}}$  interaction over one rotor revolution for a given flight condition (fixed advance ratio). This method has been used to plot the BVI intersection locations for a two bladed rotor as a function of advance ratio in Fig. 2.1. Several interactions are observed even for a two bladed rotor. The geometry of these interactions in the tip-path plane is seen to be a strong function of the advance ratio. The intersection locations are sampled at a constant azimuthal spacing and so the distance between two intersection locations along a given interaction gives an idea of the relative velocity associated with the effective BVI source or intersection location. “Parallel” interactions are observed in both the advancing and retreating side of the rotor disk. These parallel interactions are associated with very widely spaced intersection locations. These “parallel” interaction locations are seen to move out toward the tip of the rotor disk as advance ratio increases.

If an operational rotor tip-speed is now selected, the velocity profile of the intersection locations along each interaction trajectory can be obtained. This velocity of the effective BVI locations, divided by the sonic velocity, is called the trace Mach number [76, 77]:

$$M_{tr} = \frac{\mu \sin \psi + r_b}{\sin \gamma_i} M_H \quad (2.5)$$

where,  $\gamma_i$  (Fig. 2.2) is the angle between the blade and the tangent to interaction trajectory ( $\gamma_i = \tan^{-1} \frac{\partial y_i}{\partial x_i} - \psi$ ) and  $M_H$  is the hover tip Mach number,  $\Omega R / a_o$ . The trace Mach number profile along any BVI, which governs its “phasing” characteristics, or “acoustic efficiency”, is primarily set by the hover tip Mach number and the advance ratio, as seen in the above equation.

One method of studying the trends associated with BVI noise involves the identification of the effective BVI source locations in the tip-path plane and then using wavelets to estimate the directivity of the associated noise radiation. These source locations can be determined either experimentally or using different levels of wake modeling, from rigid or prescribed to free wake models. Wave tracing concepts have been used by several researchers (Widnall [76], Sim [73], [78], Lowson [75], Leishman [79], [80]) to investigate BVI directivity. These simple studies pointed out the highly directional nature of BVI noise and presented simple methods of studying BVI noise trends. Schmitz and Sim [78], [81] showed the effect of advance ratio and

hover tip Mach number on the directivity characteristics of a two bladed rotor. BVIs were classified according to trace Mach number variation along the interaction. As the advance ratio was increased for a fixed hover tip Mach number, the directivity of any BVI was shown to sweep across from directly ahead of the rotor to the advancing side.

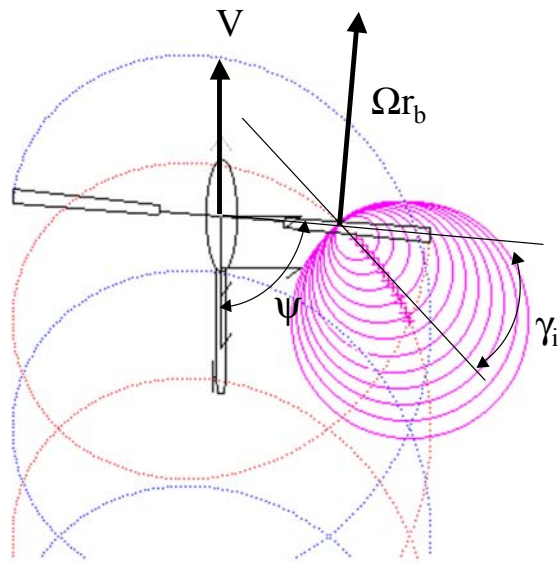


Figure 2.2 Tip-Path Plane geometry of the BVI problem for a two bladed rotor in forward flight.

The blade dynamic pressures are primarily a function of the hover tip Mach number and the advance ratio. The strength of the tip vortices is determined primarily by the thrust coefficient and the advance ratio.

Miss distances along a particular interaction are governed by the tip-path plane angle or the wake skew angle, and the advance ratio. The wake skew angle [82, 83, 74] is

the angle the wake makes with the normal to the rotor disk, defined to be zero at hover and 90° when the wake is in-plane:

$$\chi = \tan^{-1}\left(\frac{V \cos \alpha_{TPP}}{-\lambda}\right) \approx \tan^{-1}\left(\frac{V}{-\lambda}\right) \quad (2.6)$$

where,  $\lambda$  is the uniform inflow through the rotor disk, from momentum theory [84, 85, 74]. The inflow is defined positive “up” through the rotor disk in the current analysis.

The uniform inflow, from momentum theory, can be expressed as a function of disk loading ( $T/A$ ), velocity of the free-stream parallel to the rotor disk ( $V \cos \alpha_{TPP}$ ) and the tip-path-plane angle ( $\alpha_{TPP}$ ) of the rotor,

$$\lambda = -v_I + V \sin \alpha_{TPP} \quad (2.7)$$

$$\text{where, } v_I = \frac{T/A}{2\rho\sqrt{(V \cos \alpha_{TPP})^2 + \lambda^2}}.$$

In the above expression, the tip-path plane angle is defined positive “pitched-up” relative to the free-stream velocity vector (Fig. 2.3). The inflow is therefore a function of the main rotor thrust  $T$ , flight velocity  $V$  and the tip-path plane angle ( $\alpha_{TPP}$ ).

From the above discussion it can be deduced, as has been shown experimentally [14], that for a given main rotor system, steady-state BVI noise is governed by: Thrust Coefficient,  $C_T$ , Advance Ratio,  $\mu$ , Hover Tip Mach Number,  $M_H$  and the tip-path plane angle  $\alpha_{TPP}$ :

$$\text{Steady-State BVI Noise} = f(C_T, \alpha_{TPP}, \mu, M_H) \quad (2.8)$$

The inflow angle,  $\chi'$  [86], defined as the wake skew angle minus  $\pi/2$ , is the effective angle made by the main-rotor wake relative to the tip path plane (Fig. 2.3):

$$\chi' = \chi - \frac{\pi}{2} = \tan^{-1}\left(\frac{\lambda}{V}\right) \approx \tan^{-1}\left(\sin \alpha_{TPP} - \frac{v_I}{V}\right) \quad (2.9)$$

This expression relates the wake skew angle to the uniform inflow based on momentum theory. The inflow angle (or wake skew angle) can be viewed as the parameter that sets the miss-distances for the individual BVI's at a given advance ratio.

Under high positive or negative inflow conditions the wake remains below or above the rotor disk, which has the effect of keeping the miss-distances associated with important BVIs quite large ensuring low BVI noise radiation. High BVI noise radiation may be expected when the uniform inflow through the rotor disk is close to zero. This results in a wake that remains close to the rotor disk. In reality the induced

velocity across the rotor disk is not uniform. It is largest at the rear of the rotor disk and small or even negative (up through the rotor disk) over the front. A widely used prescribed wake model, the Beddoe's wake [82], illustrates this non-uniform variation. This model is valid for two bladed main rotor systems operated at low disk loading and at advance ratios between 0.1 to 0.2. According to this model, and assuming that the vortex is trailed from the tip of the rotor blades, the induced velocity  $v_i$  over the main rotor disk is given by:

$$v_{I,B} = v_I \left( 1 + E \cos \psi - E |\sin \psi|^3 \right) \quad (2.10)$$

where the subscript “ $B$ ” refers to the Beddoe's induced velocity and  $\psi$  refers to rotor azimuth angle. The classic expression for  $E$  in the original Beddoe's wake model is  $E = |\chi|$ . A slightly modified version of this wake, due to Leishman [74], assumes  $E = \frac{|\chi|}{2}$ . It is this modified Beddoe's wake model that is used in the present research.

To account for this non-uniform inflow and its effect on the miss distances associated with important BVIs, Schmitz [49] showed that, using a factor  $k$  to weight the induced velocity term in the expression for uniform inflow, a simple and reasonable estimation of the condition of high BVI noise radiation may be obtained. It is to be noted that the factor “ $k$ ” has the form of an induced power factor [74]. Therefore the effective inflow is defined below as:

$$\lambda' = -kv_I + V \sin \alpha_{TPP} \quad (2.11)$$

and the condition for the likelihood of high BVI noise radiation is given by the zero effective inflow condition. While this is a simplification of the complex BVI problem, it nonetheless is an indicator for high noise radiation. In Ref. [49] a value of 0.5 was assumed and found to correlate reasonably with some experimental data.

The tip-path plane angle corresponding to this zero effective inflow condition may be derived by linearizing the dependence of the induced velocity on the tip-path plane angle [49]. The changes in tip-path plane angle are assumed to be “small” (less than 10°), which is justified for nominal flight conditions. This linearization about the zero tip-path plane angle condition, is shown below:

$$\lambda' = -kv_{I,0} - \left. \frac{\partial v_i}{\partial \alpha_{TPP}} \right|_{\alpha_{TPP}=0} \alpha_{TPP} + V\alpha_{TPP} + O(\alpha_{TPP}^2) \approx -kv_{I,0} + V\alpha_{TPP} f_\lambda \quad (2.12)$$

where,

$$v_{I,0} = \sqrt{\frac{\sqrt{V^4 + \left(\frac{T/A}{2\rho}\right)^2} - V^2}{2}}$$

$$\text{and } f_\lambda = \left( 1 - \frac{k}{V} \left. \frac{\partial v_I}{\partial \alpha_{TPP}} \right|_{\alpha_{TPP}=0} \right) = \frac{1}{2} \left( 2 + k \left\{ 1 / \sqrt{1 + \left(\frac{T/A}{2\rho}\right)^2 / V^4} - 1 \right\} \right)$$

The tip-path plane angle that corresponds to zero effective inflow through the rotor disk is now given by:

$$\alpha_{TPP, \lambda'=0} = k \frac{\sqrt{\sqrt{V^4 + \left(\frac{T/A}{2\rho}\right)^2} - V^2}}{2} = k \frac{v_{I,0}}{\frac{1}{2} V f_\lambda} \quad (2.13)$$

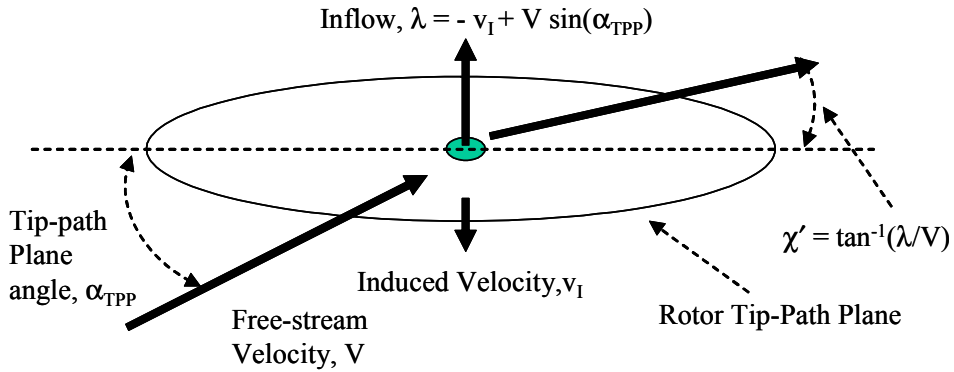


Figure 2.3 Rotor Tip-path plane, Inflow and Inflow angle.

## 2.2 Steady-State Main-Rotor BVI Noise Estimation

To make the analysis of the BVI problem more tractable and to better understand the associated physical mechanisms, idealizations of the actual complicated problem are

often constructed. Assuming an undistorted prescribed wake structure, and a lifting line rigid representation of the rotor blade, allows a simple physical understanding of the geometry, nature and “strength” of the important interactions. This method was used in Ref. [56] and [72] for the full-scale AH-1 helicopter main rotor. A modified Beddoe’s wake model was used [82, 74]. Reasonable qualitative agreement of the BVI noise radiation trends was obtained as compared with scale-model experimental wind-tunnel data using this analytical model in Ref. [73].

It should also be noted that accurate absolute-based predictions of the unsteady BVI air-loads and noise depend on the type of interaction [81] and detailed rotor wake geometry. These factors determine the relative importance of the three-dimensional and transonic flow effects that modify the BVI air-loads. For parallel interactions, two-dimensional compressible, indicial aerodynamics indicates that quasi-steady aerodynamics substantially over-predicts the unsteady loading [87, 88].

A Bell206-B helicopter main rotor system is first selected to study its BVI noise radiation trends. A two-bladed main-rotor system was selected for the BVI noise estimation study for several reasons. Firstly, a simple analytical model is more likely to predict acoustic trends and radiation characteristics for a teetering two-bladed main-rotor system than for other more complex, flexible, multi-bladed rotor systems. A two-bladed rotor is an ideal starting point for academic acoustic studies, because it is relatively simple to treat. There are lesser number of BVI’s and they do not interfere as much as they might for a four-bladed rotor. This facilitates the study of

individual BVI's and their trends as a function of various governing parameters. Also experimental wake measurements for two bladed rotors have been measured and reported in the literature and have been used to develop empirical prescribed wake models. For the present study the helicopter is modeled as a rigid main rotor system. Some relevant rotor geometry and operational parameters for this study of the Bell206-B helicopter are summarized in Table A.1 (Appendix A).

### 2.2.1 BVI Modeling Methodology

The formulation for the estimation of BVI noise has been adopted from previous research work, and has remained unchanged in the present work. The features and implementation of this model are discussed below.

Farassat's formulation 1A [89], based on the Ffowcs Williams and Hawkings [26] equation (Equations 1.1, 1.2) for noise generated by bodies in motion, is used to model BVI noise. Only the surface pressure term of the FW-H equation is considered (Equation 1.2, second term on the right hand side, with "near-field" effect) and BVI noise sources are modeled as linear chord-wise compact lift dipoles. The effect of drag forces is ignored. The governing BVI acoustics equation for surface pressures (or lift dipoles) in motion, used in the present formulation, is:

$$p'_L = -\frac{1}{4\pi a_o} \left\{ \frac{\partial}{\partial t} \int_{f=0} \left[ \frac{\hat{r}_i F_i}{r(1-M_r)} \right]_{ret} dS + \int_{f=0} \left[ \frac{a_o \hat{r}_i F_i}{r^2(1-M_r)} \right]_{ret} dS \right\} \quad (2.14)$$

The square braces in the above equation are a reminder that the expression must be evaluated at the correct retarded time. In the above equation  $p'_L$  refers to acoustic pressure at an observer location at time  $t$  due to lift dipole sources (connoted by the subscript “ $L$ ”),  $a_o$  refers to the sonic velocity assumed constant, “ $F$ ” refers to lift per unit area,  $r$  refers to distance of propagation of the acoustic pressures, along the direction of propagation,  $\hat{r}$ . The subscript “ $r$ ” refers to a component along the direction vector  $\hat{r}$ , the radiation direction.  $M$  refers to the Mach number associated with the motion of the source relative to the medium. The subscript “ $i$ ” refers to coordinate direction,  $x$ ,  $y$  and  $z$ . A medium fixed coordinate system is assumed, and aligned along the tip-path plane coordinate system axes. The tip-path plane angle remains constant during steady state flight conditions. The coordinate system and its relation to the rotor disk in the medium is described in the next section.  $dS$  refers to an elemental blade area associated with the point source;  $t$  refers to observer time. The integration limit “ $f = 0$ ” signifies that the integration is carried out over the blade surface. This equation is based on the impermeable form of the Ffowcs Williams and Hawkings equation (Equation 1.1).

The first term in the above equation decays as  $1/r$  and is referred to as the far-field term, while the second term decays more rapidly and is referred to as the near field term. Both terms are evaluated, but for observers in the acoustic far field, it is the first far-field term that predominates.

Blade element theory is used to model the quasi-steady aerodynamics associated with the blade-vortex interaction. Only the additional lift due to the BVI is considered. A linear aerodynamics model is used. The main-rotor trim condition is specified by a combination of advance ratio and tip-path plane angle. The aerodynamic blade loads over only the outer 40% of the blade is considered. The induced velocity contribution from the tip-vortices [74] are determined by integrating the contribution from each vortex element using the Biot-Savart Law and a Scully vortex model [90] to include the effect of a finite vortex core radius. Thus, the induced velocity contribution from each tip-vortex is obtained by the following integral expression:

$$\bar{v}_{I,v} = \int_0^l \frac{\Gamma_v}{4\pi} \frac{r^2 \sin^4 \theta_v}{(r^2 \sin^2 \theta_v + r_{core}^2)^2} d\bar{l} \times \hat{r} \quad (2.15)$$

$$\text{or simply, } \bar{v}_{I,v} = \int_0^l \frac{\Gamma_v}{4\pi} \frac{d\bar{l} \times \hat{r}}{(r^2 + r_{core}^2)} .$$

$$\text{where } \sin \theta_v = \frac{d\bar{l} \times \hat{r}}{|d\bar{l} \times \hat{r}|} .$$

In the above expressions,  $\bar{v}_{I,v}$  represents the induced velocity at a point in the medium due to a vortex of length “ $l$ ”. The vortex is divided into elements of length  $dl$ . “ $\bar{r}$ ” is the vector joining the vortex element to the point of interest (location along the blade), and  $\hat{r}$  is the associated unit vector. The vortex element is associated

with vortex strength “ $\Gamma_v$ ” and a vortex core of size “ $r_{core}$ ”. The BVI acoustics model utilizes a prescribed wake model (modified Beddoe’s wake [74, 82]). The current formulation allows the strength of the trailed vorticity to change as a function of advance ratio [85]. As advance ratio increases, the trailed vorticity decreases reflecting the fact that the rotor blade loading has been reduced to balance the roll moment about the hub of the teetering two-bladed rotor. This simple effect is represented in equation 2.16:

$$\frac{\Gamma_v}{2\pi\Omega R^2} = \frac{C_T}{N_b} \left\{ \frac{1 - \frac{3}{2}\mu \sin \psi_o}{1 - \frac{3}{2}\mu^2} \right\} \quad (2.16)$$

A vortex core growth model is also included [72]. The core of the shed tip vortex is known to be influenced by the wake age of the vortex and by the pressure field that the vortex passes through [74, 91, 92]. It is assumed that the vortex core size is 5% of main rotor blade chord initially when it is shed from the blade tip. The net acoustic effect of modeling the increase in core size of the vortices for BVI that occur at older wake ages is to reduce the peak BVI noise level associated with these interactions when the vortices pass close to the rotor tip-path-plane. Although it may be important, no attempt was made to model vortex core size changes due to changes in the local pressure field that might occur during the time that the rotor blades pass in close proximity to the vortices.

$$\frac{r_{core}}{c} = 0.05 \sqrt{1 + \left(\frac{\psi_v}{70}\right)} \quad (2.17)$$

Because it is assumed that the contributing aerodynamic BVI pressures are localized at the quarter chord of the blade, at a series of points along the span, the governing equation can be simplified to be an integral over the blade radius over one complete rotor revolution. For numerical implementation, the integrals in the governing equation (2.14) are replaced by summations over the blade span. The time derivative is also brought inside the summation [93]:

$$p'_L = -\frac{1}{4\pi a_o} \sum_{n=1}^N \left\{ \frac{\partial}{\partial t} \left[ \frac{\hat{r}_i F_i}{r(1-M_r)} \right]_{ret,n} + \left[ \frac{a_o \hat{r}_i F_i}{r^2(1-M_r)} \right]_{ret,n} \right\} \quad (2.18)$$

Equation 2.8 is interpreted as the sum of acoustic pressure contributions from a sequence of triggered rotating point sources arranged along the blade span and moving with the blade (Fig. 2.4). “ $F$ ” refers to the aerodynamic lift force associated with each “point source”, denoted by the index “ $n$ ”. Thus each “point-source” along the blade span is evaluated as an independent source in motion. If the time derivative is taken inside the retarded time brackets [94], and transformed to “source time”, equation 2.18, that represents the acoustic pressure contribution of these dipole point sources in motion, becomes:

$$p'_L = -\frac{1}{4\pi a_o} \sum_{n=1}^N \left[ \frac{\hat{r}_i \cdot \left( \frac{\partial F_i}{\partial \tau} + \frac{F_i}{(1-M_r)} \cdot \frac{\partial M_r}{\partial \tau} \right)}{r(1-M_r)^2} + \frac{a_o \left( \frac{F_i \hat{r}_i (1-M^2)}{(1-M_r)} - F_i M_i \right)}{r^2 (1-M_r)^2} \right]_{ret} \quad (2.19)$$

where, the relation between the source time “ $\tau$ ” and the observer time “ $t$ ” is :

$$t = \tau + \frac{r}{a_o} \quad (2.20)$$

This relation between the source and observer time is sometimes referred to as the “retarded” time equation. Equation 2.19 is now used to evaluate the far-field BVI acoustic pressure based on blade pressures and their time derivatives.

A forward-in-time formulation or source-time dominant formulation is used for the acoustics calculations. The blade location at zero rotor azimuth is taken to be time  $\tau = 0$  sec. A rotor azimuth step-size of  $0.3^\circ$  is assumed to ensure that the parallel BVI is adequately represented. Acoustic pressure contributions from each radial station over the entire rotor revolution are first computed at any observer location at the correct time. This partial acoustics time history is interpolated on to a uniform time spacing grid, using cubic spline interpolation. This process is repeated over the entire span of the blade, and for all observer locations. This results in an acoustics time history at each observer location. Two rotor revolutions of the rotor blades are considered to

account for differences in reception time of acoustic pressures from the entire lengths of the two blades. A one rotor revolution time period at each observer is taken to correspond to the time difference between an acoustic signal from the rotor hub to reach the observer at the beginning and end of one rotor revolution.

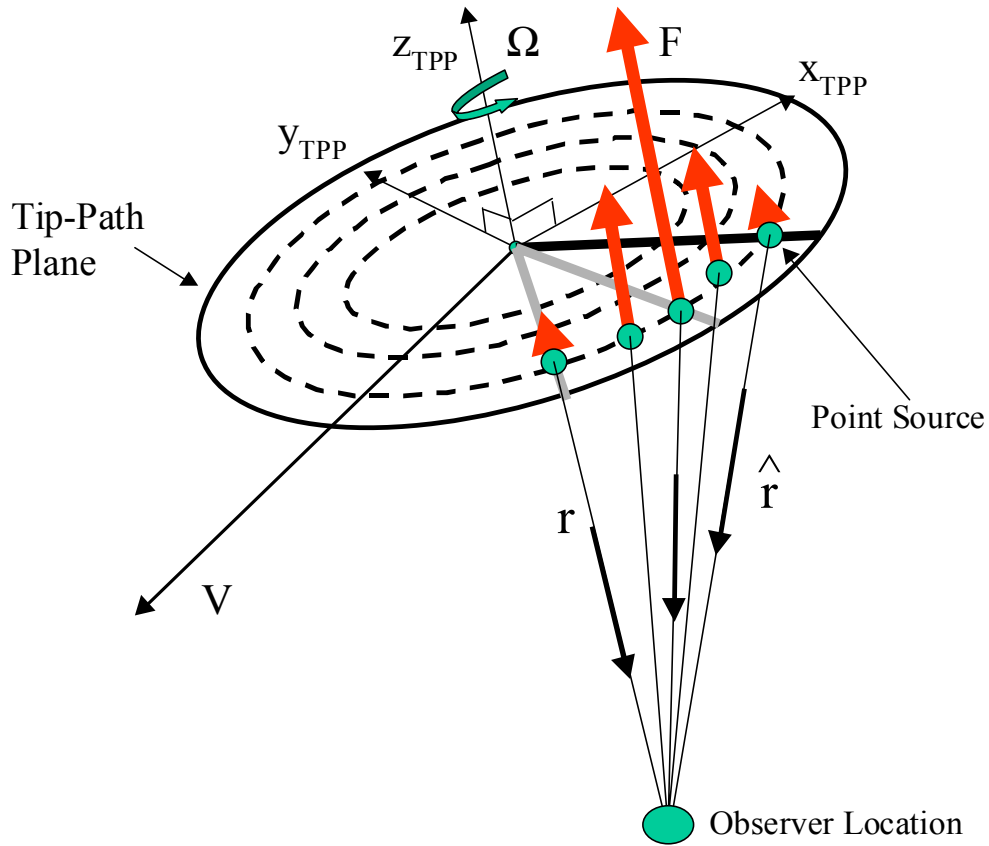


Figure 2.4 Schematic depicting the BVI noise estimation model.

The observer locations are arranged on a sphere surrounding the main rotor. This sphere is held fixed relative to the medium while the main rotor hub moves at the flight velocity  $V$ . The details of the radiation sphere are discussed in the next section.

Finally an FFT (Fast Fourier Transform) is performed over a one rotor revolution period time history at each observer location. The frequency spectrum is represented in dB (Reference pressure 20  $\mu$ Pa). The amplitudes are summed up on an energy basis to obtain the Sound Pressure Level (SPL) at each observer location.

### 2.2.2 Steady State BVI Noise: Representation

The observer locations are arranged over a sphere around the main rotor, a “radiation sphere”. This acoustic radiation sphere essentially represents a spherical map of the acoustic energy radiated by the helicopter over one rotor revolution. In the current work, radiation spheres or the mapping surfaces are assumed to be fixed to the medium.

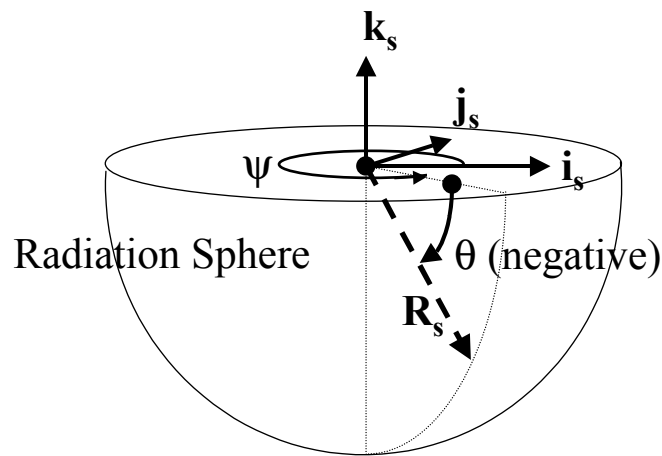


Figure 2.5 Radiation sphere geometry.

The radiation spheres used are briefly described next. A point on the radiation sphere is described using spherical coordinates by specifying the radius,  $R$ , the azimuth angle,  $\psi$ , and the elevation angle,  $\theta$ , as shown in Fig. 2.5. For a specified choice of trim parameters  $(\mu, \alpha_{\text{TPP}})$ , the helicopter is assumed to perform one rotor revolution along a trajectory element, thus traversing a distance  $2\pi\mu R$  along the velocity vector. The center of the sphere is located at the mid-interval hub location, i.e. at the midpoint of this element (Fig. 2.6). The median plane ( $\theta = 0^\circ$ ) is defined parallel to the tip-path plane. The elevation angle is taken to be negative below, and positive above this median plane. For instance, the flight velocity vector is oriented at an elevation angle of  $-\alpha_{\text{TPP}}$  relative to the median plane. All spheres used are defined with an elevation angle range of  $-90^\circ$  to  $30^\circ$ . The choice of  $0^\circ$  for the azimuth angle follows normal helicopter convention. It lies in the tip-path-plane (or median plane) and points opposite to the direction of the flight velocity of the helicopter. The azimuth angle is considered to be positive in the direction of blade rotation, counter-clockwise when viewed from above. A cartesian coordinate system (with unit vectors  $\mathbf{i}_s, \mathbf{j}_s, \mathbf{k}_s$  along the  $x_s, y_s, z_s$  axis directions), with its origin at the center of the radiation sphere is also defined in addition to the spherical reference coordinates described above. The  $x_s$ - $y_s$  plane of this reference system lies in the median plane  $\theta = 0^\circ$ , with the  $x_s$ -axis pointing along  $\psi = 0^\circ$ ,  $y_s$ -axis pointing along  $\psi = 90^\circ$ , and the  $z_s$  axis pointing in the  $\theta = 90^\circ$  direction.

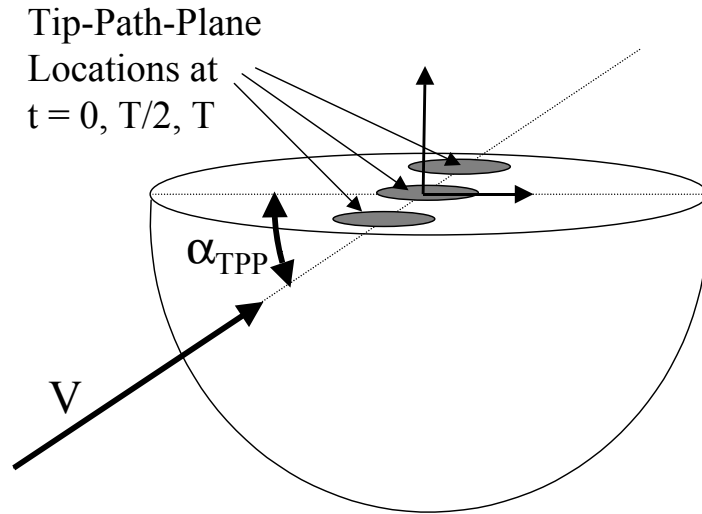


Figure 2.6 Flight velocity vector and the tip-path-plane relative to the radiation sphere.

### 2.2.3 Steady-State BVI Noise Radiation Trends for the Bell206-B Helicopter

The steady state BVI noise radiation trends for the Bell206-B are calculated numerically as a function of the tip path plane angle and advance ratio in this section, for a fixed thrust coefficient and hover-tip Mach number. Noise radiated by the helicopter over a one-rotor revolution period is estimated over a sphere fixed relative to the stationary medium. The 2-D surface representation of the radiation spheres is shown in Fig. 2.7 using a transformation that preserves area of surface elements formed by the latitudes and longitudes, but not orthogonality of latitude-longitude intersections. Note that  $\psi = \text{constant}$  contours on the surface of the sphere are referred to as longitudes and  $\theta = \text{constant}$  contours are referred to as latitudes.

Figure 2.8 shows the noise radiation maps for the Bell206-B as a function of the inflow angle at an advance ratio of 0.172. At an inflow angle of  $-5.3^\circ$  the noise levels are seen to be relatively low. This is because the inflow “down” through the rotor disk insures that the wake operates away from rotor blades. The miss-distances associated with the important interactions are relatively high. This approximately corresponds to level flight conditions at 70 knots for the Bell206-B, and a tip-path plane angle of  $-2.2^\circ$ . As the helicopter descends, inflow angle is increased from negative to positive values, miss-distances associated with the important BVIs reduce, and the maximum BVI noise level radiated over the sphere peaks close to the zero inflow or zero inflow angle condition. The BVI noise radiation is seen to be highly directional. Two preferred directions are one directly ahead and one more towards the advancing side of the main rotor. The advancing side BVI is due to the broadside or “parallel” interaction, and is seen to radiate its peak levels at an azimuth angle of  $135^\circ$  and an elevation angle of  $-40^\circ$ . This “hotspot” has been observed for other two-bladed main rotor configurations as well, and is well documented. Peak BVI noise radiation is seen to occur between an inflow angle of  $-1.5^\circ$  and  $+0.4^\circ$  and tip-path plane angles of between  $1.6^\circ$  and  $3.4^\circ$ . This figure illustrates the strong dependence of BVI noise radiation on the tip-path plane angle, at a specified advance ratio (and hover tip Mach number and thrust coefficient).

The noise over the entire sphere can be summed up on an energy basis and represented in dB by the average radiated sound pressure level over the sphere,  $P_{av}$ .

$$P_{av} = 10 \log_{10} \left[ \sum_j \left( 10^{\frac{SPL_j}{10}} \cdot \frac{\Delta A_j}{A_s} \right) \right] \quad (2.21)$$

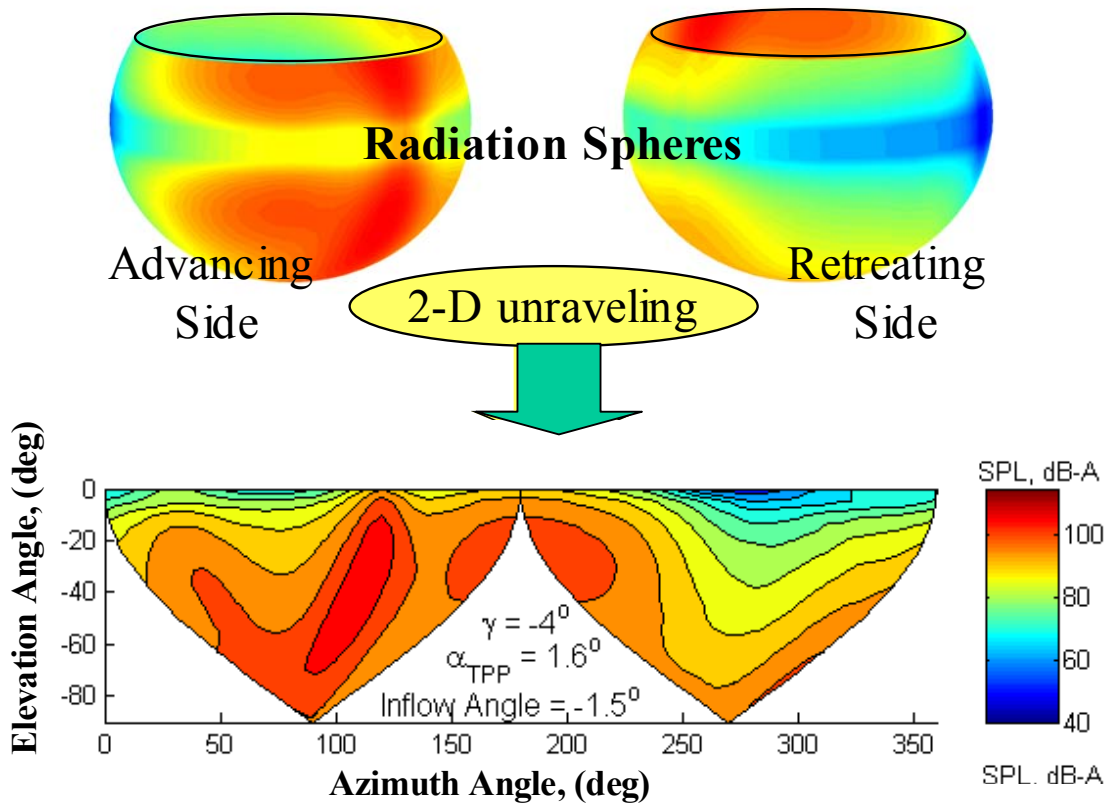


Figure 2.7 A 2-D representation of BVI radiation characteristics

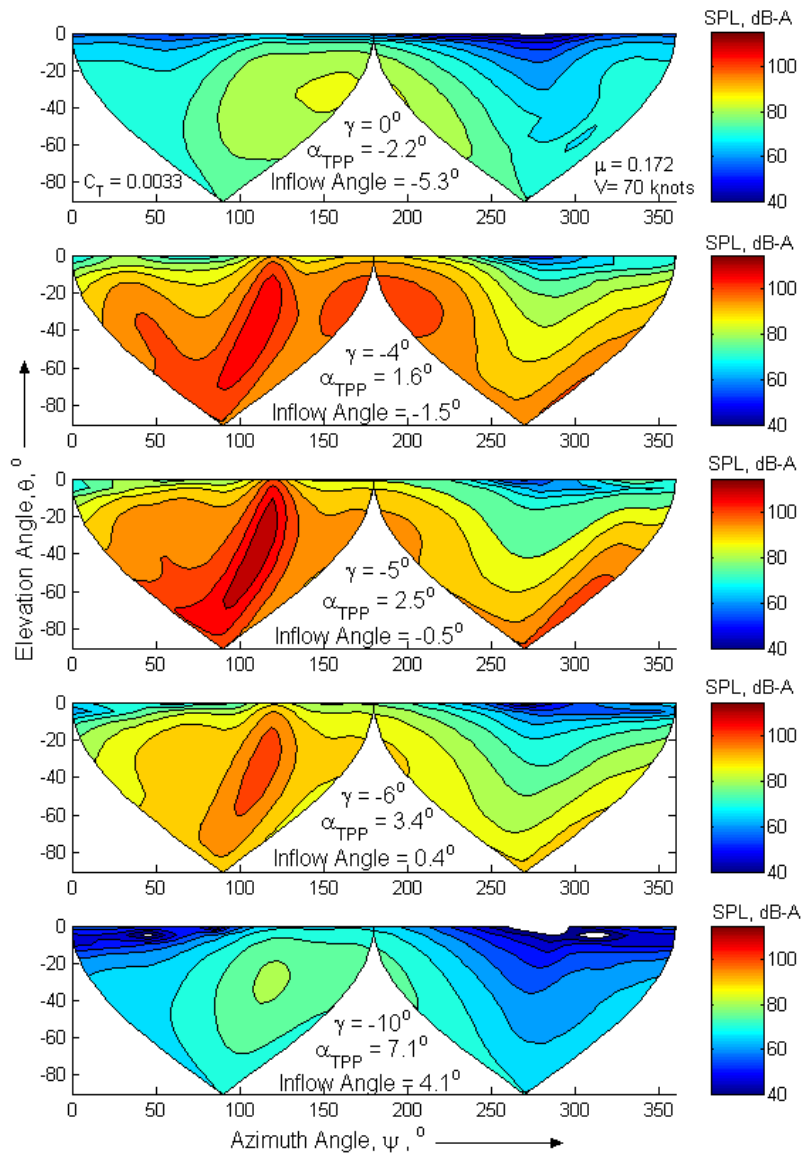


Figure 2.8 Computed trends of sound pressure levels radiated on a 3R sphere around the Bell206-B helicopter for varying inflow angles.  $\mu = 0.172$ .

Figure 2.9 shows the trends of this average radiated BVI sound power as a function of the main rotor non-dimensional variables, advance ratio and the tip-path plane angle (Fig. 2.9a) or the inflow angle (Fig. 2.9b). It is seen that average radiated BVI noise peaks close to the zero inflow angle condition (or the zero inflow condition) over the entire advance ratio range. At low advance ratios, around 0.1 ( $V = 40$  knots), the BVI noise tends to peak at slight negative inflow angles. It is seen that the peak BVI noise occurs at the condition  $\chi'' = \tan^{-1}\left(\alpha_{\text{TPP}} - k_1 \frac{V_I}{V}\right) = 0$  or  $\lambda' = V \sin \alpha_{\text{TPP}} - k_1 V_I = 0$ .

For the current model, a value of  $k_1=0.7$  gives reasonable correlation (Fig 2.9c). This effective inflow angle or effective inflow, as stated previously, accounts for the effect of non-uniform inflow on the miss-distance of the dominant BVI, and could be a function of the advance ratio. For the analytically computed noise trends, the parameter  $k_1$  would depend on the details of the wake structure.

Flight trajectory management of helicopter BVI noise further requires relating helicopter flight conditions to the key main-rotor non-dimensional variables, thrust coefficient, hover tip Mach number, advance ratio and tip-path plane angle. These parameters are shown below:

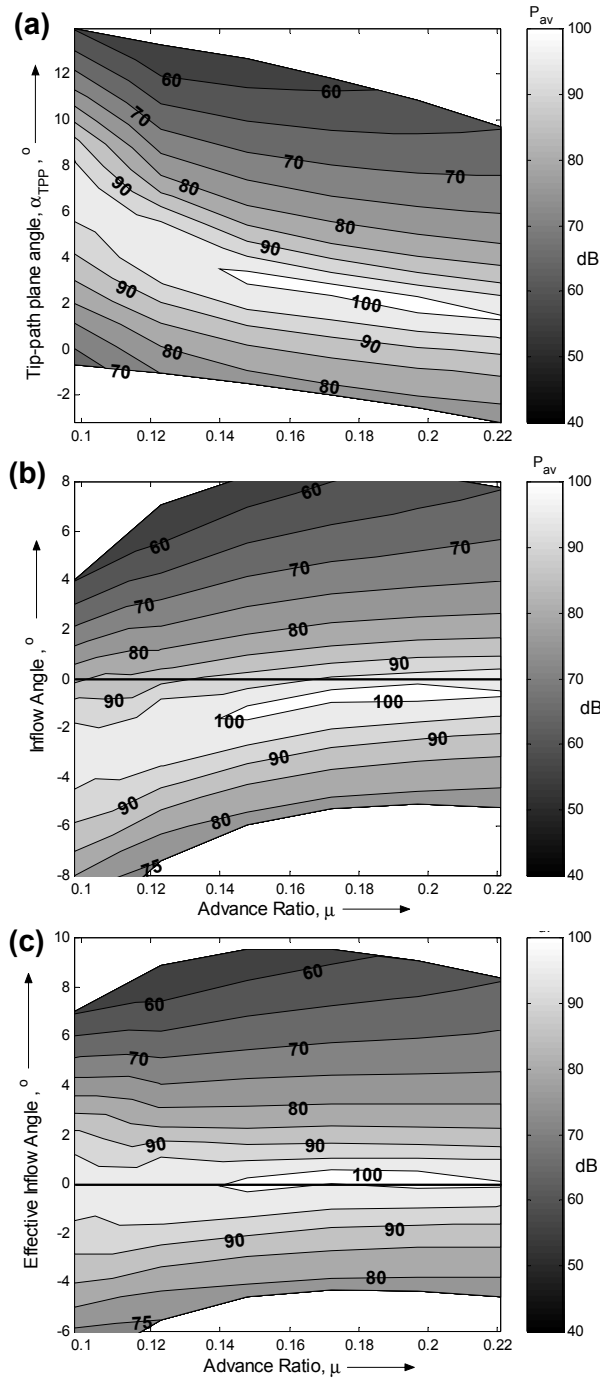


Figure 2.9 Average radiated noise level estimates for the Bell206-B as a function of the advance ratio and a) tip-path plane angle, b) inflow angle (wake skew angle -  $\pi/2$ ) and c) the effective inflow angle.

$$\begin{aligned}
C_T &= \frac{T}{\rho A (\Omega R)^2} \\
M_H &= \frac{\Omega R}{a_o} \\
\mu &\equiv \frac{V \cos \alpha_{TPP}}{\Omega R} \\
\alpha_{TPP} &\equiv f(V, \gamma, \dot{V}, \dot{\gamma}, \dots)
\end{aligned}
\tag{2.22}$$

Chapter 3 develops a general formulation for the tip-path plane angle and thrust, and then develops a methodology to study the tip-path plane angle variation as a function of flight conditions during slow longitudinal maneuvers. Other simplifying assumptions are made, in chapter 5, and a methodology to estimate all four non-dimensional parameters along longitudinal flight trajectories is developed. This procedure is then used to estimate the associated BVI noise radiation.

## Chapter 3

### Tip Path Plane Formulation and Methodology

The main objective of this chapter is to develop mathematical models to study tip-path plane performance and dynamic behavior during longitudinal maneuvers. The focus is on single main-rotor conventional helicopters, moderate flight velocities, 40 knots to 100 knots, nominal flight path angles, level flight to  $-10^\circ$ , and nominal accelerations parallel and perpendicular to the flight path as may be encountered during civilian descent operations.

First, several key coordinate systems of relevance to the analysis are described. Next, force balance equations of the helicopter are used to develop a general expression for the tip path plane angle. Low orders of flight dynamics modeling are coupled with static representations of helicopter trim. This model is used to study tip-path plane behavior during slow longitudinal maneuvers. Then, a higher order coupled helicopter flight dynamics model is described, and adapted to study longitudinal maneuvers and tip-path plane dynamic behavior. Finally, mathematical functional representations of idealized longitudinal trajectories are developed for use in the analysis.

### 3.1 Force Balances and Coordinate Systems

This section presents a treatment of the force balance equations of the helicopter to facilitate the development of insightful yet accurate expressions for tip-path plane performance.

In helicopter analysis, several coordinate systems are used to describe the motion and force balances of the helicopter system in flight [95], [96]. These coordinate systems are in general rotating accelerating systems. Any general non-inertial rotating right-handed coordinate system, with its origin at the center of gravity of the helicopter system, may also be used to express the force balance equations. In such a reference frame the force balance equations take the following form:

$$m \left( \frac{\partial \bar{V}}{\partial t} + \bar{\Omega}_{NI} \times \bar{V} \right)_{NI} = \bar{F}_{NI} \quad (3.1)$$

where the subscript “*NI*” refers to a general non-inertial rotating right handed coordinate system. The orientation of this generic coordinate system is specified by its Euler angles [97], [83],  $\phi_{NI}$ ,  $\theta_{NI}$  and  $\psi_{NI}$  relative to the gravity coordinate system (Fig. 1.1). The rotation rates,  $p_{NI}$ ,  $q_{NI}$  and  $r_{NI}$ , associated with this coordinate system, expressed along its own axes,  $x_{NI}$ ,  $y_{NI}$  and  $z_{NI}$ , with unit vectors  $\mathbf{i}_{NI}$ ,  $\mathbf{j}_{NI}$  and  $\mathbf{k}_{NI}$ , in terms of the Euler angles and their rates, are:

$$\begin{aligned}
 p_{NI} &= \dot{\phi}_{NI} - \dot{\psi} \sin \theta_{NI} \\
 q_{NI} &= \dot{\theta}_{NI} \cos \phi_{NI} + \dot{\psi}_{NI} \sin \phi_{NI} \cos \theta_{NI} \\
 r_{NI} &= \dot{\psi}_{NI} \cos \phi_{NI} \cos \theta_{NI} - \dot{\theta}_{NI} \sin \phi_{NI}
 \end{aligned}
 \tag{3.2}$$

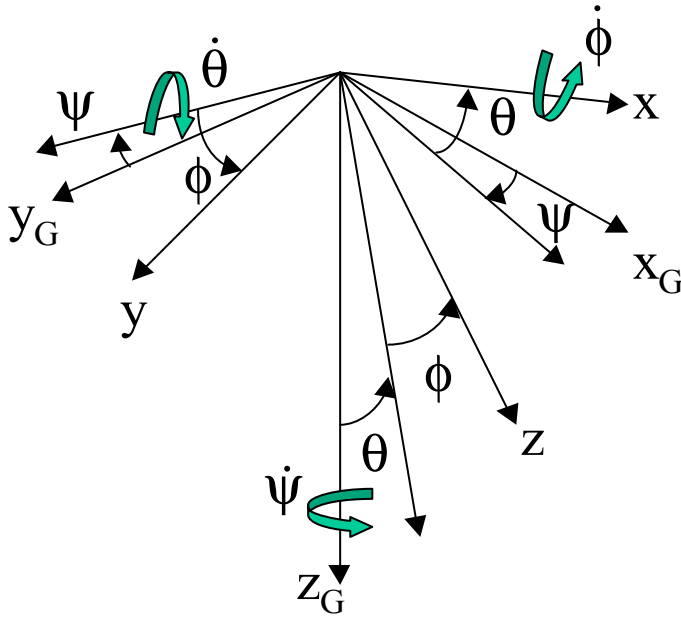


Figure 3.1 Euler angles and rotation rates of a general right-handed coordinate system (subscripts “NI” have been dropped).

In such a frame, the X, Y and Z force balance equations take the following form:

$$\begin{aligned}
 m(\dot{u}_{NI} + q_{NI}w_{NI} - r_{NI}v_{NI}) &= X_{NI} \\
 m(\dot{v}_{NI} + r_{NI}u_{NI} - p_{NI}w_{NI}) &= Y_{NI} \\
 m(\dot{w}_{NI} + p_{NI}v_{NI} - q_{NI}u_{NI}) &= Z_{NI}
 \end{aligned}
 \tag{3.3}$$

Three specific coordinate systems are generally used to describe the overall motion of the helicopter. These coordinate systems are:

1. the gravity coordinate system, “G”
2. the body-fixed coordinate system, “B”, and
3. the “wind” coordinate system, “W”.

The origins of all these coordinate systems are placed at the center of gravity of the helicopter fuselage. While the gravity coordinate system is a non-rotating, accelerating system, the “wind” and body coordinate systems are in general rotating accelerating systems, as is the tip-path plane coordinate system, described later.

The gravity coordinate system is used for reference. The “z” axis of this system points “down” in the direction of gravity. The choice of “x” and “y” axes is arbitrary and is selected based on convenience in the context of each specific application.

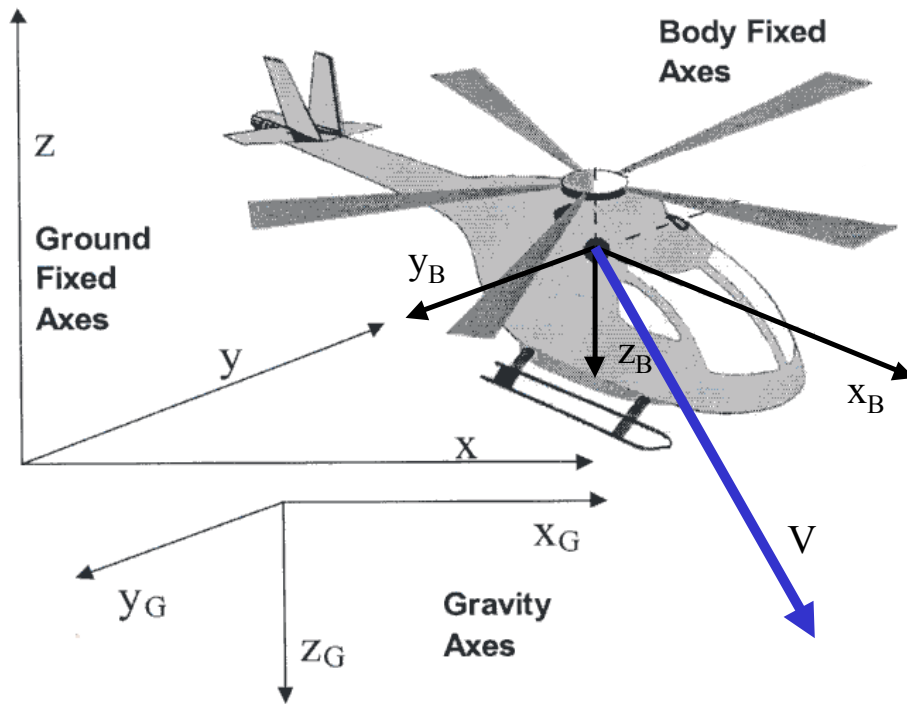


Figure 3.2 Ground fixed (inertial), gravity and body-fixed coordinate systems.

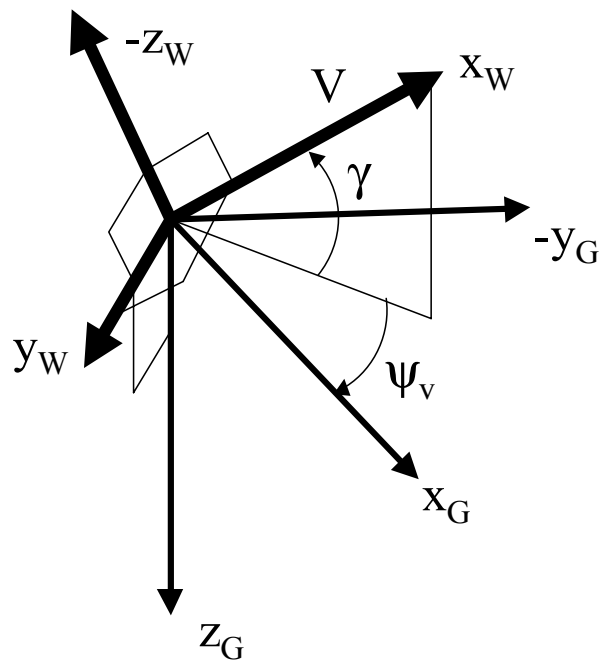


Figure 3.3 "Wind" coordinate system referenced to gravity coordinates.

The body-fixed coordinate system is defined in the usual way [95] with “x” pointing “forward”, y pointing “right” or starboard and “z” pointing “down” (Fig 3.2). The Euler angles for this system are  $\phi$ ,  $\theta$  and  $\psi$ , and the rotation rates are  $p$ ,  $q$  and  $r$  along the body “x”, “y” and “z” directions. The components of flight velocity along the “x”, “y”, and “z” directions are  $u$ ,  $v$  and  $w$  respectively. The above equations, expressed in body fixed coordinates, are typically used for flight dynamics analyses.

The “wind” coordinate system [97] is defined with the “x” axis pointing along the velocity vector. The “z” and “y” axes of the “wind” coordinate system are arbitrary, and may be referenced to body coordinates in some flight dynamics analyses [96]. In the current formulation, the “y” and “z” wind axes are referenced to the gravity coordinates as below (Fig. 3.3):

$$\begin{aligned}\hat{j}_W &= \hat{k}_G \times \hat{i}_W \\ \hat{k}_W &= \hat{i}_W \times \hat{j}_W = \hat{i}_W \times (\hat{k}_G \times \hat{i}_W)\end{aligned}\quad (3.4)$$

In figure 3.2,  $\gamma$  and  $\psi_r$  are the Euler pitch and yaw angles associated with the wind axis system respectively. The roll angle is zero.  $\gamma$  is commonly referred to as the flight path angle. It is assumed at this stage that the medium is stationary and there is no actual wind. The consideration of helicopter flight under steady wind conditions is addressed briefly in section 3.2, and in chapter 5. Currently, it is assumed that the velocities of the helicopter center of gravity relative to the medium and to the ground

are identical. The qualification of the term “wind”, by placing it within double-quotes, should be treated as a reminder of this assumption.

It is customary, in flight dynamics analyses, to express the force balance equations along body-fixed axes instead of the “wind” or “velocity” axis system [97], [83]. This choice is based on the convenience of representing the moment balance equations with fixed product of inertia terms [97]. But this benefit in the moment balance equations comes at the expense of additional force terms in the force balance equations (“left hand side” of equation 3.3). This problem can be effectively tackled by using two different reference frames in the analysis: expressing the force balance equations in the wind axis system described above and the moment balance in the body fixed coordinate system and then defining coordinate transformations between these frames of reference. Another consideration in selecting reference frames is that the “wind” axis system becomes ill-defined in and close to hover. The consideration of only moderate flight velocities in the present research avoids this issue altogether. For a more detailed discussion of the derivation of the tip-path plane performance equations that follow, refer to Appendix B.

The force balance equations, expressed in this “wind” coordinate system, take the following form:

$$m\dot{V} = X_w$$

$$mV\dot{\psi}_V \cos \gamma = Y_w$$

$$-mV\dot{\gamma} = Z_W \quad (3.5)$$

This choice of the “wind” coordinate system expresses the inertial acceleration terms in familiar forms that can be readily interpreted physically. The “x” acceleration represents the acceleration along the flight path, the “z” acceleration represents the acceleration perpendicular to flight path in the longitudinal plane and the “y” acceleration represents the horizontal centrifugal acceleration. The coupled Euler acceleration terms (“left hand side” of equation 3.3), present in the body-fixed formulation, do not appear in this “wind” axis formulation.

The treatment of the main rotor forces warrants special attention. The forces acting on the main rotor are most commonly computed in the shaft axis system and then transformed to the body-fixed coordinates. In the present formulation, the main rotor forces are resolved in the tip-path plane coordinates. The tip-path plane is defined by the fixed-frame Fourier Coefficients,  $\beta_{1C}$  and  $\beta_{1S}$ , obtained by transforming rotating frame rotor tip displacements through a Fourier Coordinate Transformation (FCT) [85], [95], [98].

$$\beta_{1C} = \frac{2}{N_b} \sum_{i=1}^{N_b} \tan^{-1} \left( \frac{w_{tip,i}}{R} \right) \cos \psi_i$$

$$\beta_{1S} = \frac{2}{N_b} \sum_{i=1}^{N_b} \tan^{-1} \left( \frac{w_{tip,i}}{R} \right) \sin \psi_i \quad (3.6)$$

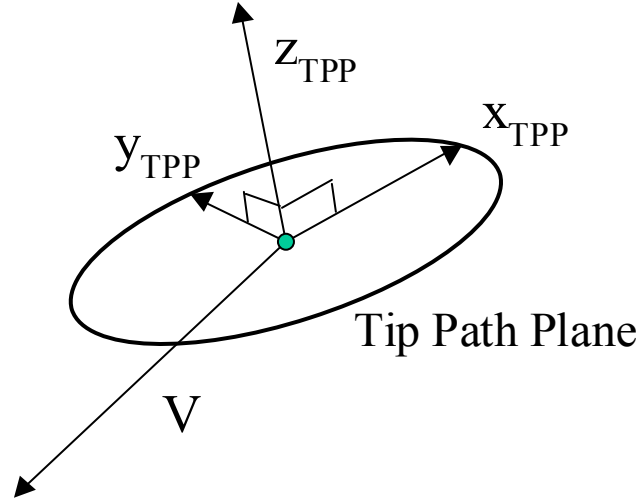


Figure 3.4 The tip-path plane coordinate system and the flight velocity vector.

The “z” axis of the tip path plane coordinate system is defined normal to this tip-path plane, and points “up”. The “x” and “y” directions are arbitrary and again, in some flight dynamics formulations [95], they are referenced to the shaft axes or the body-fixed system. In the present formulation the “x” and “y” coordinates are referenced to the wind coordinates as below (Fig. 3.4):

$$\begin{aligned}\hat{j}_{TPP} &= \hat{i}_W \times \hat{k}_{TPP} \\ \hat{i}_{TPP} &= \hat{j}_{TPP} \times \hat{k}_{TPP} = (\hat{i}_W \times \hat{k}_{TPP}) \times \hat{k}_{TPP}\end{aligned}\quad (3.7)$$

The main rotor forces expressed along the “z”, “x” and “y” axes of this tip-path plane coordinate system are referred to as the thrust ( $T$ ), the rotor  $H$  force in the tip-path plane ( $H_{TPP}$ ) and the rotor  $Y$  force in the tip path plane ( $Y_{TPP}$ ).

The  $X$ ,  $Y$  and  $Z$  force balance equations in the “wind” coordinate system can now be expressed as:

$$\begin{aligned}
 m\dot{V} &= -T \sin \alpha_{TPP} - D_{EFF} - W \sin \gamma \\
 mV\dot{\psi}_V \cos \gamma &= T \cos \alpha_{TPP} \sin \phi_{TPP} + Y_{EFF} \\
 -mV\dot{\gamma} &= -T \cos \alpha_{TPP} \cos \phi_{TPP} - L_{EFF} + W \cos \gamma
 \end{aligned} \tag{3.8}$$

where,

$$\begin{aligned}
 D_{EFF} &= D_F + H \cos \alpha_{TPP} + D_{HS} + D_{TR} + D_{VT} + D_I \\
 L_{EFF} &= L_{HS} + L_F - H_{TPP} \sin \alpha_{TPP} \cos \phi_{TPP} - Y_{TPP} \sin \phi_{TPP} + L_{TR} + L_{VT} + L_I \\
 Y_{EFF} &= Y_{TR} + Y_{VT} + Y_F - H_{TPP} \sin \alpha_{TPP} \sin \phi_{TPP} + Y_{TPP} \cos \phi_{TPP} + Y_{HS} + Y_I
 \end{aligned}$$

In the above equations,  $\phi_{TPP}$  (Fig. 3.5) refers to the angle between the normal to the tip path plane and the  $z$  axis of the “wind” coordinate system, positive “for starboard down”, and the subscript “ $I$ ” refers to forces due to any interference effects.

### 3.2 Equations Governing Tip Path Plane Performance

The current research focuses only on longitudinal flight conditions. The  $X$  and  $Z$  force balance equations can be used to obtain an expression for the tip-path plane angle:

$$\sin \alpha_{TPP} = \frac{-\frac{D_{EFF}}{W} - \sin \gamma - \frac{\dot{V}}{g}}{T/W} \quad (3.9)$$

and

$$\frac{T}{W} = \frac{\left( \cos \gamma + V \frac{\dot{\gamma}}{g} - \frac{L_{EFF}}{W} \right)}{\cos \alpha_{TPP} \cos \phi_{TPP}} \quad (3.10)$$

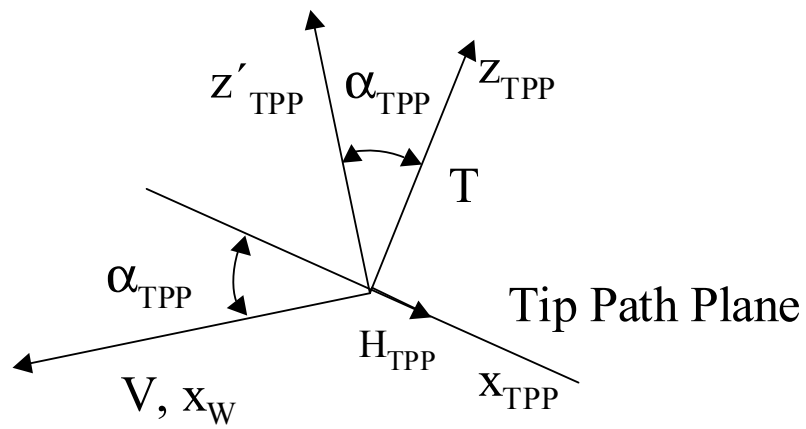
or,

$$\frac{T}{W} = \frac{\sqrt{\left( \cos \gamma + V \frac{\dot{\gamma}}{g} - \frac{L_{EFF}}{W} \right)^2 + \left( V \frac{\dot{\psi}}{g} \cos \gamma + \frac{Y_{EFF}}{W} \right)^2}}{\cos \alpha_{TPP}}$$

This expression for the main rotor tip-path plane angle follows from the definitions adopted in the current research, and if appropriately interpreted, is valid for all levels of modeling, from the simplest most basic physical model to the most sophisticated analysis.

As stated in chapter 2, the inflow distribution at any velocity is primarily governed by the main rotor thrust and tip-path plane angle. The disk loading primarily governs the mean induced velocity over the rotor disk. The induced velocity is also a function of the tip-path plane angle especially at low flight velocities. The miss distances associated with any BVI are primarily set by the inflow distribution over the rotor disk. The effect of increasing main rotor thrust or making the tip-path plane more negative is to increase the inflow down through the rotor disk. And conversely, lowering the disk loading or making the tip-path plane angle more positive makes the

inflow up through the rotor disk increase. At any flight velocity, the above expressions of main rotor tip-path plane angle and thrust, define, at least to first order, the inflow distribution over the rotor disk.



### Planar Views

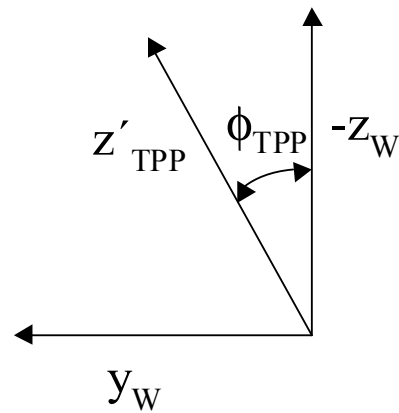


Figure 3.5 Lateral tilt of the tip-path plane :  $\phi_{TPP}$ .

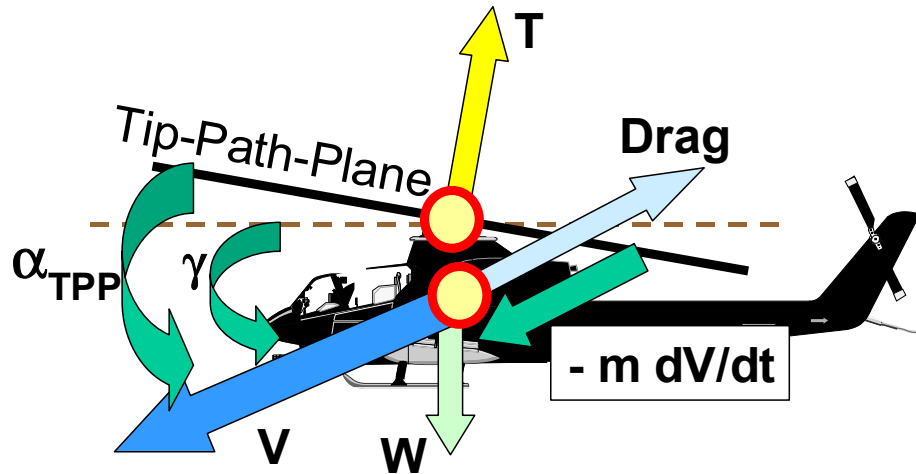


Figure 3.6 Longitudinal Force balance of a helicopter, shown for a descending decelerating condition.

In arriving at the above expression for the tip-path plane angle, several key assumptions, some implicit, were made:

- A conventional single main rotor helicopter is considered.
- Aircraft weight is considered fixed along the trajectory.
- The formulation is based on definitions of reference frames and other terms made earlier in this section.
- The main rotor RPM is assumed to remain fixed during any flight operation. The tip-path plane dynamics associated with changes in main rotor RPM are essentially ignored in the present analysis. This is valid for steady state and slow maneuvering flight conditions associated with small pilot control input changes, and for helicopters equipped with governors to hold the main rotor RPM approximately constant.

- In referring to the flight velocity and velocity of relative wind (as in the “wind” coordinate system) interchangeably, it is tacitly assumed that the medium is stationary. If the velocity of the medium was constant relative to the inertial or “earth-fixed” reference frame, all the above arguments and equations would still be valid. In this case, the “wind” axis system would be referenced to the relative wind, the flight path angle would refer to the aerodynamic flight path angle, and  $\psi_V$  would refer to the yaw angle associated with the velocity of the helicopter relative to the medium. If the wind velocity is not constant, care must be taken in interpreting the above equations. The problem with dealing with winds is that while the “left hand side” of the force balance equations consists of inertial flight velocities and acceleration, the “right hand side” deals with aerodynamic forces, which are function of the helicopter velocity relative to the medium, and with the tip-path plane angle, which is defined with respect to the relative wind. Therefore the above equation for tip-path plane angle should be used only in the context of a “steady wind”.
- While no physical interpretation of the tip-path plane and the associated reference frame is claimed yet, apart from its definition based on Fourier Coordinate transformation of blade tip displacements, one certainly is implied, based on experience and basic understanding of the helicopter system [74], [83], [84], [98], [99]. While not essential to the arguments above, this physical understanding of the significance of a physical tip-path plane puts the present analysis in a useful context, some of which is explored and delved into later in the text.

This equation for the tip-path plane angle is now interpreted through various levels of modeling to unravel some of its many implications, and to study tip-path plane performance and behavior during trim and longitudinal maneuvers.

Flight dynamics analyses of the helicopter in maneuvering flight involve solving a system of coupled differential equations [95], [100]. These equations include the equations of motion of the helicopter, the equations representing the dynamics of the main and tail rotors and supporting equations. This system of equations can be represented by:

$$F(\dot{y}, y, \dot{u}, u, t) = 0 \quad (3.11)$$

where  $y$  refers to the state vector and  $u$  refers to the control vector. The system  $F$  may consist of algebraic equations as well. The control vector  $u$  consists of the collective, lateral cyclic and longitudinal cyclic pitch inputs at the main rotor and the pedal controls at the tail rotor. A maneuver is typically defined as a transition from one trim flight state to another. A trim state for the helicopter system is defined as a periodic

solution for the state vector  $y$  over one rotor revolution such that  $\int_0^T \dot{y}_i dt = 0$ , which

essentially implies that the average state of the helicopter remains constant. A trim state is typically characterized by an average value of flight velocity  $V$ , flight path angle  $\gamma$  and yaw rate  $\dot{\psi}$ .

Several levels of flight dynamics maneuver and trim modeling are studied in this research to assess the behavior of the tip-path plane during slow longitudinal maneuvers. A lower level trim model of the helicopter in longitudinal flight is first briefly discussed in relation to tip-path plane performance. This model essentially relies on the solution of a coupled set of algebraic equations that represent the average state of the helicopter over one rotor revolution. Over each rotor revolution, during trim flight, the helicopter system actually experiences unsteady oscillatory loads and dynamical motion. At this lower level of trim modeling, the effect of vibratory loads and unsteady aerodynamics on the average trim state of the helicopter is ignored. Some details of this simple trim model are presented in Appendix A.

Starting from this static algebraic trim analysis, the dynamical degrees of freedom of the system are selectively “released” or introduced in the appropriate equations and the order of the system is successively increased, starting from a first order system representation of longitudinal dynamics. This process of successively “releasing” the static constraints on the “outermost loops” of flight dynamics and control, specifying or holding some flight variables or degrees of freedom while determining others through the process of iterative balance of static algebraic equations, is quite typical in flight dynamics analyses. What is unique in the present research is the use of a wind axis system for the force balance equations and body-fixed coordinates for the pitching moment balance equation, which allows a direct evaluation of tip-path plane performance characteristics during longitudinal maneuvers, and the use of “effective controls” that relate directly to tip-path plane performance. At each level of modeling

and system order, helicopter aerodynamic and dynamics modeling issues are discussed in terms of their relevance to tip-path plane performance estimation. The order of the system of differential equations is discussed in relation to the number of variables, and the selection of effective system controls. This selection of controls usually classifies the solution methodology as either an “inverse simulation” or “direct time integration” [95, 96, 100]. This is discussed in more detail in further sections of this chapter.

### **3.3 Levels of Tip Path Plane Modeling During Longitudinal Maneuvers**

Low order systems representing the longitudinal dynamics of the helicopter are now introduced to gain physical insights into the performance and behavior of the tip-path plane during longitudinal dynamic maneuvers. The analysis begins with a first order system. The model is progressively built up to fourth order. Common to all these lower order models are the following assumptions:

- Lateral forces and moments are intrinsically balanced, and not therefore considered in the analysis; lateral dynamics are considered to be uncoupled from longitudinal dynamics [83]. The lateral tilt of the tip-path plane is ignored. The effects of the tail rotor and the vertical tail are ignored.
- Longitudinal force balances are conducted in the wind axis system while the pitching moment balance equation is expressed in the body axis system.

- Small angle assumptions are used for the tip-path plane angle and flight path angle.

Finally a higher order coupled flight dynamics and control simulation model [95], with all six degrees of motion of the helicopter, is described and adapted for use in the present research. At each level of modeling, the assumptions are carefully reviewed and evaluated.

Two customary ways of studying dynamic maneuvers are employed: inverse simulation and direct time integration. In an inverse simulation approach, the longitudinal flight trajectory is known. The equations of motion of the helicopter are used to obtain the values of controls and performance parameters along the flight trajectory. When a sequence of controls is considered to be the input (time integration approach), the governing differential equations are solved to obtain the flight trajectory and the associated pitch dynamics of the helicopter.

### **3.2.1 First-Order Longitudinal Performance, Dynamics and Control Model**

The X-force balance equation essentially sets the tip path plane angle during slowly accelerating or decelerating flight. The following additional assumptions are made in this level of modeling:

- Flight path angle is held fixed.

- The main rotor thrust usually remains close to the aircraft weight during nominal longitudinal straight-line flight at moderate airspeeds, and is taken to be equal to weight ( $T = W$ ). It is assumed that the lift of the fuselage, tail surfaces and tail rotor are small compared to aircraft weight.
- The tip-path plane angle and flight path angles are assumed to be “small” angles ( $<10^\circ$ ), such that  $\sin \theta \approx \theta$  and  $\cos \theta \approx 1$ .
- The pitching moment is assumed to be balanced along the flight trajectory. The static pitching moment balance equation may be used to determine helicopter pitch attitude along the maneuver. Helicopter pitch dynamics is not considered.
- Main rotor flap dynamics are not considered. At each instance, steady-state harmonic balance is used to estimate main rotor flapping.

These simplifying assumptions result in the following governing first-order ordinary differential equation:

$$\frac{dV}{dt} = -g \left\{ \frac{D_{EFF}}{W} - \gamma \right\} - g\alpha_{TPP} \quad (3.12)$$

In the above equation,  $D_{EFF}$  refers to the effective drag of the helicopter, in the direction of flight velocity. The effective drag force is first approximated by the fuselage drag at zero angle of attack [49]:

$$\frac{D_{EFF}}{W} \approx \frac{D_{F,0}}{W} \approx \frac{1}{2} \rho V^2 \frac{f_x}{W} \quad (3.13)$$

The equivalent flat plate area accounts for the nominal effects of the vertical tail and horizontal stabilizer as well. The effect of fuselage angle of attack on changes in fuselage drag is considered to be small for nominal flight at moderate airspeeds.

The H-force in the tip path plane is usually small compared to fuselage drag at low to moderate airspeeds [99], [98], [49]. A simple estimate of the rotor H-force in the tip-path plane, based on main rotor airfoil characteristics and the effective angle of attack encountered during a given flight condition, is also included at this level of modeling:

$$D_{EFF} \approx D_{F,0}(V) + H_{TPP}(V, \alpha_{TPP}) \quad (3.14)$$

The governing differential equation therefore can be written as:

$$\frac{dV}{dt} = f(V, \alpha_{TPP}) - g\alpha_{TPP} \quad (3.15)$$

This first order differential equation has two variables:  $V$  and  $\alpha_{TPP}$ . This equation can be solved by assuming one of these variables to be the effective control along the maneuver. The two solution methods are:

- *Time Integration:* The tip-path plane angle is assumed to be the “effective control” along the trajectory. The governing equation reduces to a first order ODE in flight velocity  $V$ . This first order system, when linearized, is well-damped with

a single negative root ( $-\partial D/\partial V$ ). The state vector and control vector for this system are given by:

$$\begin{aligned} y &= \{V\} \\ u &= \{\alpha_{TPP}\} \end{aligned} \quad (3.16)$$

- *Inverse Simulation:* The acceleration profile is specified along the trajectory. The governing equation reduces to an algebraic expression for the tip path plane angle. The acceleration profile is integrated along the trajectory to obtain the flight velocity as a function of time:

$$V = \int \dot{V} dt$$

In level flight trim conditions, these simplifying assumptions result in the following expression for the tip-path plane angle [49]:

$$\alpha_{TPP}^{SS,level} \approx -\frac{D_{EFF}}{W} \Bigg|_{\substack{\text{Level Flight} \\ \text{Trim}}} \quad (3.17)$$

In trim flight [49], at a flight path angle,  $\gamma$ , the tip-path plane angle becomes:

$$\alpha_{TPP}^{SS} \approx -\frac{D_{EFF}}{W} - \gamma \quad (3.18)$$

It is also assumed that the effective drag of the helicopter is not a strong function of flight path angle [98]. Therefore, to first order:

$$\frac{\partial}{\partial \gamma} \left( \frac{D_{EFF}}{W} \right) \approx 0 \quad \text{and,}$$

$$\alpha_{TPP}^{SS} \approx - \frac{D_{EFF}}{W} \Big|_{\substack{\text{Level Flight} \\ \text{Trim}}} - \gamma \left( 1 + \frac{\partial}{\partial \gamma} \left( \frac{D_{EFF}}{W} \right) \right) \approx - \frac{D_{EFF}}{W} \Big|_{\substack{\text{Level Flight} \\ \text{Trim}}} - \gamma \quad (3.19)$$

For slowly accelerating flight at a constant flight path angle at moderate flight velocities, the tip path plane angle becomes:

$$\alpha_{TPP} \approx - \frac{D_{EFF}}{W} - \gamma - \frac{\dot{V}}{g} \quad (3.20)$$

It is obvious from this expression that if acceleration in g's is "small" (less than 0.1), there is a direct equivalence between acceleration in g's and climb angle in radians. Therefore, in this quasi-static sense, a 0.1 g acceleration parallel to the flight path is equivalent to 0.1 radians (5.7 degrees) of climb angle. This equivalence alludes to an effective flight path angle, such that

$$\gamma_{EFF} = \gamma + \dot{V}/g \quad (3.21)$$

and, 
$$\alpha_{TPP} \approx -\frac{D_{EFF}}{W} - \gamma_{EFF}.$$

And, from equation 3.19: 
$$\alpha_{TPP} \approx -\frac{D_{EFF}}{W} \Big|_{\substack{\text{Level Flight} \\ \text{Trim}}} - \gamma_{EFF}.$$

The tip-path plane angle is therefore a function, to first order, only of the drag to weight ratio in level flight trim and the effective flight path angle. This means that the tip-path plane operating conditions during slowly decelerating flight at a fixed flight path angle would be nearly identical to an equivalent steady state flight condition at the same flight velocity and effective flight path angle. In fact, the operating state of the entire helicopter in the medium reference frame would be nearly identical.

However, the tip-path plane pitch attitude relative to the horizon during these two equivalent flight conditions would not be the same:

$$\theta_{TPP} = \alpha_{TPP} + \gamma \approx -D_{EFF}/W - \dot{V}/g \quad (3.22)$$

Therefore, the orientation of the tip-path plane relative to the horizon would be more nose-up (positive) during the deceleration maneuver compared to the equivalent steady state flight condition. The pitch rate associated with the tip-path plane is given by:

$$q_{TPP} \approx -\frac{\partial}{\partial V} \left( \frac{D_{EFF}}{W} \right) \dot{V} - \frac{\ddot{V}}{g} = -\frac{\partial \alpha_{TPP}^{SS,level}}{\partial V} \dot{V} - \frac{\ddot{V}}{g} \quad (3.23)$$

The fuselage pitch attitude of a helicopter in trim is known to be a function of flight velocity but fairly insensitive to small changes in flight path angles (<10°). This is because both helicopter drag and longitudinal flapping angle are not strong functions of the flight path angle. Therefore, the helicopter pitch attitude during a deceleration maneuver would be more nose-up compared to the trim value at the same flight velocity:

$$\theta = \alpha_{TPP} + \gamma + \theta_s - \beta_{1C} \approx \theta^{SS} - \dot{V}/g \quad (3.24)$$

In equation 3.24 it is assumed that the change in pitch attitude due to a small change in effective flight path angle is negligible. By introducing a static pitching moment balance equation, the steady-state flapping equations and a static Z-Force balance equation, an estimate may be made of the helicopter pitch attitude and the main rotor longitudinal flapping relative to the shaft. The effect of fuselage angle of attack can now be introduced in the fuselage drag, lift and pitching moments as well as on the horizontal stabilizer lift and drag. The governing equations now become:

$$\frac{dV}{dt} = g f_1(V, \alpha_{TPP}, \theta) - g \alpha_{TPP} f_2(V, \theta) = f(V, \alpha_{TPP}, \theta) \quad (3.25)$$

$$F(V, \theta, \alpha_{TPP}, \dots) = 0$$

where,  $F$  is a partial set of coupled static trim equations. The effects of these inclusions on the estimation of tip-path plane performance are usually negligible in nominal longitudinal flight.

The equation for uniform inflow is repeated here to emphasize its dependence on the thrust and tip-path plane angle:

$$\lambda = -\frac{T/A}{2\rho\sqrt{V^2 + \lambda^2}} + V\alpha_{\text{TPP}} \quad (3.26)$$

The uniform inflow gives an indication of the wake operating state relative to the rotor disk. High positive or negative uniform inflow conditions imply a wake structure that is primarily below or above the rotor disk in the first and fourth quadrants, where important BVIs are known to occur. These conditions would be associated with relatively large miss-distances and low BVI noise radiation. The quasi-static tip-path plane angle and thrust therefore determine a quasi-static inflow level which governs miss distances and therefore the BVI noise radiation. If the thrust is assumed a constant, the inflow becomes a function of the tip-path plane angle and flight velocity or the flight path angle, flight velocity and vehicle acceleration.

Once the quasi-static thrust coefficient and tip-path plane angle are determined by this method, the BVI noise over the radiation sphere is determined from steady state flight and can be mapped to the acoustic far field. This static equivalence (treating

acceleration as a known control parameter) has been used to develop strategies to avoid strong BVI noise radiation. The implicit assumption is that the dynamics of how the pilot controls the aircraft do not affect the radiated BVI noise to first order. This treatment of the deceleration along the flight path also assumes that the maneuver is slow enough that the associated pitch rates, accelerations and rates of change in main rotor inflow have a negligible effect on the aerodynamic forces of the helicopter, especially the main rotor. In terms of the acoustic equivalence, it is further assumed that unsteady wake distortion effects associated with these rates of change of pitch, pitch rate, inflow and flight velocity are negligible.

### 3.2.2 Second-Order Longitudinal Performance, Dynamics and Control Model

Both velocity and flight path angle are allowed to vary along the trajectory. The effect of accelerations both parallel and perpendicular to the flight path is introduced in to the force balance equations. The equations for tip-path plane angle and the thrust to weight ratio now become:

$$\alpha_{TPP} \approx \frac{-D/W - \gamma - \dot{V}/g}{T/W}$$

$$T/W \approx 1 + V\dot{\gamma}/g \quad (3.27)$$

By treating the acceleration parallel and perpendicular to the flight path as independent static parameters in the force balance equations, the main rotor

operational parameters can be estimated for such slow maneuvers. These equations can also be expressed as a second order system of differential equations:

$$\begin{aligned}\frac{dV}{dt} &= -\frac{D_{EFF}(V, \alpha_{TPP}, T, \theta)}{W} - g\alpha_{TPP} \frac{T}{W} - g\gamma \\ \frac{d\gamma}{dt} &= \frac{g}{V} \left( \frac{T}{W} - 1 + \frac{L_{EFF}(V, \theta)}{W} \right) \\ F(V, \theta, \alpha_{TPP}, T, \dots) &= 0\end{aligned}\tag{3.28}$$

This second order system of coupled ordinary differential equations contains four variables:  $V(t)$ ,  $\gamma(t)$ ,  $T(t)$  and  $\alpha_{TPP}(t)$ . To solve these equations starting from a given trim state ( $\dot{V} = 0, \dot{\gamma} = 0$ ), two of these four variables need to be specified as the effective “controls” along the maneuver. This can again be done in two ways:

- *Inverse Simulation*: Given a specified maneuvering longitudinal flight trajectory ( $\dot{V}(t), \dot{\gamma}(t)$ ), the main rotor tip path plane operating state can be estimated as a function of time using these force balances alone. The rates of change of velocity and flight path angle along the trajectory are treated as the “effective controls” along the longitudinal maneuver. The initial condition is a prescribed trim state. From that initial condition, it is assumed that the two longitudinal controls can be varied in time, subject to reasonable physical constraints and bounds, to achieve different maneuvering flight conditions. The values of these “controls” specify the acceleration parallel and perpendicular to the flight path as a function of time. These can further be integrated to obtain the time histories of flight velocity and flight path angle.

- *Time integration:* The tip-path plane angle and main rotor thrust are assumed to be the controls during the maneuver. If these main rotor parameters are specified as controls along the trajectory, the acceleration parallel and perpendicular to the flight path can be evaluated, and integrated to obtain the flight trajectory. The state vector,  $y$ , and the control vector  $u$  are given by:

$$y = \begin{Bmatrix} V \\ \gamma \end{Bmatrix}, u = \begin{Bmatrix} \alpha_{TPP} \\ T \end{Bmatrix} \quad (3.29)$$

### ***First Order System with Two controls***

Alternately, the rotor thrust can be eliminated as a variable by substituting for  $T/W$  into the first equation to obtain the following governing equation:

$$\dot{V} = g(f_1(V, \alpha_{TPP}, \dot{\gamma}) - \gamma) - g \left( 1 + V \frac{\dot{\gamma}}{g} \right) \alpha_{TPP} \quad (3.30)$$

In this case, the tip path plane angle  $\alpha_{TPP}(t)$  and flight path angle  $\gamma(t)$  can be considered to be the controls of the problem, and the acceleration time history can be computed along the trajectory. The state vector,  $y$ , and the control vector  $u$  are given by:

$$y = \{V\}, u = \begin{Bmatrix} \alpha_{TPP} \\ \gamma \end{Bmatrix} \quad (3.31)$$

This first order system with two controls reduces to equation 3.12 if the flight path angle is held fixed.

### 3.2.3 Third and Fourth Order Longitudinal Flight Dynamics Analysis

The pitching dynamics associated with longitudinal maneuvers is introduced next. A fourth order system results.

$$\begin{aligned}
 \frac{dV}{dt} &= -\frac{D(V, \alpha_{TPP}, T)}{W} - g\alpha_{TPP} \frac{T}{W} - g\gamma \\
 \frac{d\gamma}{dt} &= \frac{g}{V} \left( \frac{T}{W} - 1 \right) \\
 \frac{dq}{dt} &= \frac{M(V, \alpha_{TPP}, T, \theta, q, \gamma)}{I_y} \\
 \frac{d\theta}{dt} &= q
 \end{aligned} \tag{3.32}$$

This system of four equations has six unknowns. Again, if thrust and tip-path plane angle are treated as the effective controls of the maneuver, the differential equations can be solved for  $V$ ,  $\gamma$ ,  $q$  and  $\theta$ . The state vector, “ $y$ ”, and the control vector “ $u$ ” are given by:

$$y = \begin{Bmatrix} V \\ \gamma \\ \theta \\ q \end{Bmatrix}, u = \begin{Bmatrix} \alpha_{TPP} \\ T \end{Bmatrix} \quad (3.33)$$

Inverse simulation renders the force balance equations into algebraic expressions for the tip path plane angle and main rotor thrust. The pitching moment dynamics equations are integrated independently, as for the direct integration approach. It is noted again, that in the current treatment of these equations, the force balance equations and the moment balance equations are expressed in two different coordinate systems.

As was done previously, the order of this system can be reduced by one by eliminating thrust, as assuming flight path angle to be an additional control.

$$\begin{aligned} \frac{dV}{dt} &= -\frac{D(V, \alpha_{TPP}, \dot{\gamma})}{W} - g\alpha_{TPP} \left( 1 + V \frac{\dot{\gamma}}{g} \right) - g\gamma \\ \frac{dq}{dt} &= \frac{M(V, \alpha_{TPP}, \dot{\gamma}, \theta, q, \gamma)}{I_y} \\ \frac{d\theta}{dt} &= q \end{aligned} \quad (3.34)$$

A constant flight path angle maneuver would be a special case of this system. In this level of modeling, the force balance equations are uncoupled from the pitching

moment equation and are essentially unaffected by these new equations.  $V$  and  $\gamma$  can therefore be obtained independently, and then pitch dynamics can be computed.

The helicopter drag and lift are weak functions of pitch attitude. This weak coupling of the force balance equations with the pitching moment equations is now introduced:

$$\begin{aligned}
 \frac{dV}{dt} &= -\frac{D(V, \alpha_{TPP}, T, \theta, q)}{W} - g\alpha_{TPP} \frac{T}{W} - g\gamma \\
 \frac{d\gamma}{dt} &= \frac{g}{V} \left( \frac{T}{W} - 1 + \frac{L(V, \theta, \gamma, q)}{W} \right) \\
 \frac{dq}{dt} &= \frac{M(V, \alpha_{TPP}, T, \theta, q, \gamma)}{I_y} \\
 \frac{d\theta}{dt} &= q
 \end{aligned} \tag{3.35}$$

The “roots” associated with the linearization of this system would not be typical because the equations are defined in different coordinate systems, with the transformations between these systems added to the list of supporting equations. Inverse simulation again renders the force balance equations into algebraic equations. The pitching moment dynamics equations are now coupled with algebraic equations, and can be solved iteratively. If direct time integration is conducted, based on tip-path plane angle and thrust as controls, the four coupled first order ODE’s can be solved.

Helicopter main rotors are actually controlled through collective and cyclic pitch inputs. Algebraic equations can be used to relate the “effective controls” – thrust and

tip-path plane angle to the actual pitch control inputs – collective and cyclic pitch angles [84]:

$$\begin{aligned}\theta_o &= f(T, \alpha_{TPP}, \beta_{1c} + \theta_{1s}, V, q) \\ \theta_{1s} &= -\beta_{1c} + f(\theta_o, \alpha_{TPP}, V, q)\end{aligned}\quad (3.36)$$

and based on geometric compatibility:

$$\alpha_{TPP} = \theta - \gamma - \beta_{1c} + \theta_S \quad (3.37)$$

To first order the collective controls main rotor thrust and the cyclic controls tip-path plane angle and thrust. By substituting for these controls and eliminating the tip-path plane angle and thrust from the differential equations, the X-Force balance equation becomes strongly coupled with helicopter pitch attitude. Also the thrust, at any flight velocity, now becomes a function of the controls, collective and cyclic, as well as the inflow distribution over the rotor disk. The collective and cyclic pitch control main rotor thrust and tip-path plane angle which set the level of main rotor inflow at any flight velocity.

An inverse simulation scheme, depicted in Fig. 3.7, is adopted for the estimation of flight performance during slow maneuvers. A velocity and flight path angle profile is assumed and the control inputs required are computed along with the associated tip-path plane angle, thrust coefficient, main rotor inflow and the longitudinal flapping.

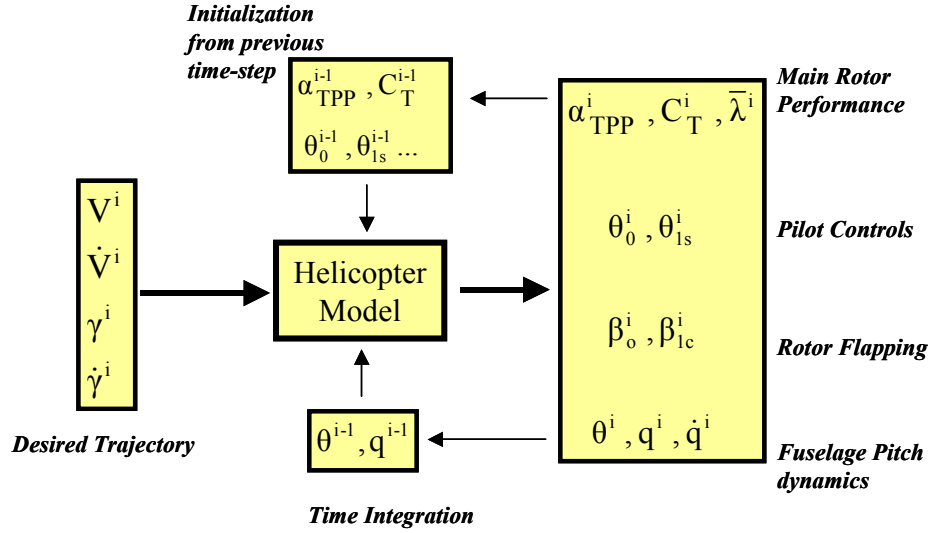


Figure 3.7 Schematic showing the inverse simulation scheme for slowly maneuvering flight.

The pitch attitude and pitch rate are computed using successive time integration of the moment balance equation. A time step size of one-half rotor revolution is adopted. Iterations are performed at each time step “i” till the value of each performance parameter converges to within a specified tolerance.

$$\dot{q}^i = \frac{M}{I_y}$$

$$q^i = q^{i-1} + \frac{\Delta t}{2} (\dot{q}^i + \dot{q}^{i-1})$$

$$\theta^i = \theta^{i-1} + \frac{\Delta t}{2} (q^i + q^{i-1}) \quad (3.38)$$

The perturbations from trim conditions are assumed to be “slow” and “small” enough to assume a quasi-static assumption in the main rotor response. Over each half of a rotor revolution these performance parameters are assumed to approach a quasi-static value in response to external perturbations, control inputs and/or changes in vehicle rotation or translation rates.

Slowly maneuvering flight is studied in a two-step process. First the pitch rates and moments are assumed to be zero and only the effect of the acceleration parallel and perpendicular to the flight path are considered (Second-order analysis). This restriction is then relaxed and the effect of pitch rates and moments are brought in (Fourth order analysis). Flight maneuvers are considered “slow” or “quasi-static”, for the purpose of the current study, if the results of these two analyses, with and without pitch dynamics, are nearly identical.

The pitch rate associated with the tip path plane is given by:

$$q_{TPP} = q - \dot{\beta}_{1C} \quad (3.39)$$

In the current analysis a frozen approximation is made for the inflow, which is modeled using a prescribed Beddoe’s wake [82]. At each time-step, a steady-state inflow distribution based on the instantaneous rotor operational parameters is assumed. While the quasi-steady gyroscopic and aerodynamic effect of a pitch rate is modeled on the main rotor tip-path plane aeromechanics, the effect of these rates,

along with the rates of change of the advance ratio and inflow, on the unsteady behavior of the wake structure and the unsteady aerodynamic loads of the main rotor are ignored. This assumption is expected to be reasonable for slow maneuvers.

The next higher order model would include the effect of main rotor flap and inflow dynamics. The main rotor flap and inflow equations would now incorporate dynamic effects. The maneuvers considered in this research are thought to be slow enough not to excite these dynamic modes of the helicopter system. This is investigated by considering results from a much higher order flight dynamics analysis adapted for use in this research. This is introduced in the next section.

### **3.4 Higher Order Trim and Flight Dynamics Modeling**

A higher order coupled flight dynamics model of the helicopter [95], used for the estimation of main rotor tip-path plane dynamics and rotor thrust, is described in this section. The formulation has essentially remained unchanged compared to previous work [95]. The existing features in this formulation are discussed in this section. Adaptations and modifications made are briefly discussed in the latter part of this section and in Chapter 5.

The main features of this analysis, as it applies to the present research, are listed below:

- The medium is assumed to be stationary in an earth-fixed coordinate system.

- The helicopter subsystems considered in the analysis are the main rotor, the tail rotor and the fuselage which includes the effects of the horizontal stabilizer and the vertical tail.
- The fuselage airframe is a rigid body with constant mass. The x-z body plane is a plane of symmetry.
- The six-degree of freedom coupled equations of motion of the helicopter are solved. The equations of motion are actually evaluated for the fuselage airframe. Forces and moments from the main and tail rotors are transferred to the fuselage center of gravity and resolved along the body-fixed axes. The body accelerations and moments are then evaluated along these body axis directions.
- The state vector,  $y$ , and the control vector  $u$  are given by:

$$y = \{u, v, w, p, q, r, \phi, \theta, \psi, \lambda_o, \lambda_c, \lambda_s, \lambda_t, \dot{\beta}_i^j, \beta_i^j\} \quad (3.40)$$

$$u = \{\delta_o, \delta_{lat}, \delta_{lon}, \delta_{ped}\}$$

The state vector consists of the fuselage velocity ( $u, v, w$ ) and rotation rate ( $p, q, r$ ) components along body-fixed coordinates, as well as fuselage Euler angles ( $\phi, \theta, \psi$ ), the main rotor dynamic inflow components ( $\lambda_o, \lambda_c, \lambda_s$ ) uniform, cosine and sine components respectively, uniform tail rotor inflow ( $\lambda_t$ ) and blade modes. The structural modes associated with each blade in the rotating frame are transformed using a modal coordinate transform to reduce the number of degrees of freedom of the system. Each mode for each individual blade is represented by one generalized displacement and one generalized velocity value.  $\dot{\beta}_i^j$  and  $\beta_i^j$  represent the generalized velocity and displacement respectively associated with the  $j^{th}$  mode of the

$i^{th}$  blade. The order of the system for  $N_b$  blades and  $m$  retained blade modes is  $13+2*N_b*m$ . For a typical value of 4 blades and 3 modes, this results in a system of order 37. The control vector  $[\delta_o, \delta_{lat}, \delta_{lon}, \delta_{ped}]$  specifies the collective, lateral, longitudinal and pedal control inputs, respectively, in inches. These are transformed to blade pitch inputs using a transformation matrix.

- The main and tail rotor blades are assumed to rotate at a constant angular speed. Engine and engine control system dynamics are neglected.
- Main rotor aerodynamics uses quasi-steady aerodynamics based on look-up tables derived from wind tunnel tests. The lift, drag and moment coefficients are tabulated as a function of angle of attack, for Mach numbers ranging from 0.3 to 1.0. 2-D strip theory is used along the blade to estimate blade loads. Aerodynamic forces and moments on the blade sections are based on the airflow velocity at the elastic axis of the blade. Tip losses due to 3-D effects are approximated by considering the outboard 3% of the blade to be ineffective aerodynamically. Effect of dynamic stall is not modeled.
- All blades are assumed to have identical mass, stiffness and geometric properties. The main rotor dynamics analysis involves a finite element representation of individual blade structural modes (flap, lag and torsion). The main rotor blades are individually modeled in the rotating frame as flexible beams undergoing coupled flap, lag, torsion and axial motion. A modal coordinate transform is performed on the coupled, rotating blade mode shapes to reduce the number of degrees of freedom of the main rotor blades. The baseline analysis uses three modes (first flap, first lag and first torsion mode).

- The blade pitch control system dynamics are not modeled.
- The Pitt-Peters dynamic inflow model [67] with dynamic maneuver correction effects [68] is used to model main rotor inflow for the baseline case.
- The fuselage, horizontal stabilizer and vertical tail aerodynamics are modeled using look-up tables as a function of angle of attack and side slip angle. The aerodynamic data is derived from wind tunnel tests without the main rotor. Side-wash and downwash interference velocities from the main rotor and empennage are also obtained from look-up tables.
- The tail rotor is modeled using rigid blades, uniform inflow and quasi steady aerodynamics.
- This flight dynamics model simulates maneuvering flight through either an inverse simulation or direct time integration. In the inverse simulation procedure, the controls along the flight trajectory are specified as the control vector. Control values are specified every two rotor revolutions and a linear variation with time is assumed between these values. The objective function for this optimization procedure is constructed to reflect differences between the desired and actual trajectories:

$$F = \sum_{j=1}^{\substack{\text{No. of} \\ \text{State} \\ \text{Variables}}} k_j \left( y_j^i - y_{j,des}^i \right)^2 \quad (3.41)$$

This flexible optimization “driver” of the main flight dynamics simulation code can be modified depending on the specific application.

New reference frames are defined to better study the performance and dynamics of the main rotor tip-path plane: these are the “wind” coordinate system and the tip-path plane coordinate system. These new reference frames were described in section 3.1. The force balance equations are recast in the wind axis system with the main rotor forces expressed in the tip-path plane coordinate system. The moment balance equations are left in the body-fixed coordinate system. This transformation is only used to post-process the data for use in the present study. Coordinate transformations are used to express forces in the body fixed frame to the wind coordinate system:

$$\begin{Bmatrix} \hat{i}_W \\ \hat{j}_W \\ \hat{k}_W \end{Bmatrix} = \begin{bmatrix} T_{WB}^{1,1} & T_{WB}^{1,2} & T_{WB}^{1,3} \\ T_{WB}^{2,1} & T_{WB}^{2,2} & T_{WB}^{2,3} \\ T_{WB}^{3,1} & T_{WB}^{3,2} & T_{WB}^{3,3} \end{bmatrix} \begin{Bmatrix} \hat{i}_B \\ \hat{j}_B \\ \hat{k}_B \end{Bmatrix} \quad (3.42)$$

where,

$$T_{WB}^{1,1} = \cos \alpha_F \cos \beta_F$$

$$T_{WB}^{1,2} = \cos \alpha_F \sin \beta_F$$

$$T_{WB}^{1,3} = \sin \alpha_F$$

$$T_{WB}^{2,1} = \sin \phi \cos \theta \sin \alpha_F - \cos \phi \cos \theta \cos \alpha_F \sin \beta_F$$

$$T_{WB}^{2,2} = \cos \phi \cos \theta \cos \alpha_F \cos \beta_F - \sin \theta \sin \alpha_F$$

$$T_{WB}^{2,3} = -\sin \theta \cos \alpha_F \sin \beta_F - \sin \phi \cos \theta \cos \alpha_F \cos \beta_F$$

$$\begin{aligned} T_{WB}^{3,1} &= -\sin \theta \cos^2 \alpha_F \sin^2 \beta_F - \sin \phi \cos \theta \cos^2 \alpha_F \cos \beta_F \sin \beta_F \\ &\quad - \cos \phi \cos \theta \cos \alpha_F \sin \alpha_F \cos \beta_F - \sin \theta \sin^2 \alpha_F \end{aligned}$$

$$T_{WB}^{3,2} = \sin \theta \cos^2 \alpha_F \cos \beta_F \sin \beta_F + \sin \phi \cos \theta \cos^2 \alpha_F \cos^2 \beta_F \\ + \sin \phi \cos \theta \sin^2 \alpha_F - \cos \phi \cos \theta \cos \alpha_F \sin \alpha_F \sin \beta_F$$

$$T_{WB}^{3,3} = \cos \phi \cos \theta \cos^2 \alpha_F \cos^2 \beta_F - \sin \theta \sin \alpha_F \cos \alpha_F \cos \beta_F \\ - \sin \phi \cos \theta \cos \alpha_F \sin \alpha_F \sin \beta_F + \cos \phi \cos \theta \cos^2 \alpha_F \sin^2 \beta_F$$

where  $\alpha_F$  and  $\beta_F$  refer to the angle of attack and the sideslip angle of the fuselage respectively. The transformation for the main rotor forces from body fixed coordinates to the tip-path plane coordinates is given by:

$$\begin{Bmatrix} \hat{i}_{TPP} \\ \hat{j}_{TPP} \\ \hat{k}_{TPP} \end{Bmatrix} = \begin{bmatrix} T_{TPP,B}^{1,1} & T_{TPP,B}^{1,2} & T_{TPP,B}^{1,3} \\ T_{TPP,B}^{2,1} & T_{TPP,B}^{2,2} & T_{TPP,B}^{2,3} \\ T_{TPP,B}^{3,1} & T_{TPP,B}^{3,2} & T_{TPP,B}^{3,3} \end{bmatrix} \begin{Bmatrix} \hat{i}_B \\ \hat{j}_B \\ \hat{k}_B \end{Bmatrix} \quad (3.43)$$

where,

$$T_{TPP,B}^{1,1} = \begin{pmatrix} \cos \alpha_F \cos \beta_F \cos \beta_{1C} \sin \beta_{1S} \\ -\cos \alpha_F \sin \beta_F (-\sin \beta_{1C} \cos \theta_S - \cos \beta_{1C} \cos \beta_{1S} \sin \theta_S) \\ (-\sin \beta_{1C} \cos \theta_S - \cos \beta_{1C} \cos \beta_{1S} \sin \theta_S) \\ -(\cos \alpha_F \sin \beta_F (-\sin \beta_{1C} \sin \theta_S + \cos \beta_{1C} \cos \beta_{1S} \cos \theta_S) - \sin \alpha_F \cos \beta_{1C} \sin \beta_{1S}) \\ (-\sin \beta_{1C} \sin \theta_S + \cos \beta_{1C} \cos \beta_{1S} \cos \theta_S) \end{pmatrix}$$

$$T_{TPP,B}^{1,1} = (\cos \alpha_F \sin \beta_F (-\sin \beta_{1C} \sin \theta_S + \cos \beta_{1C} \cos \beta_{1S} \cos \theta_S) - \sin \alpha \cos \beta_{1C} \sin \beta_{1S}) \\ (\cos \beta_{1C} \sin \beta_{1S}) \\ - \begin{pmatrix} -\cos \alpha_F \cos \beta_F (-\sin \beta_{1C} \sin \theta_S + \cos \beta_{1C} \cos \beta_{1S} \cos \theta_S) \\ + \sin \alpha_F (-\sin \beta_{1C} \cos \theta_S - \cos \beta_{1C} \cos \beta_{1S} \sin \theta_S) \end{pmatrix} \\ (-\sin \beta_{1C} \cos \theta_S - \cos \beta_{1C} \cos \beta_{1S} \sin \theta_S)$$

$$T_{TPP,B}^{2,1} = \cos \alpha_F \sin \beta_F (-\sin \beta_{1C} \sin \theta_S + \cos \beta_{1C} \cos \beta_{1S} \cos \theta_S) - \sin \alpha_F \cos \beta_{1C} \sin \beta_{1S}$$

$$T_{TPP,B}^{2,2} = -\cos \alpha_F \cos \beta_F (-\sin \beta_{1C} \sin \theta_S + \cos \beta_{1C} \cos \beta_{1S} \cos \theta_S) \\ + \sin \alpha_F (-\sin \beta_{1C} \cos \theta_S - \cos \beta_{1C} \cos \beta_{1S} \sin \theta_S)$$

$$T_{TPP,B}^{2,3} = \cos \alpha_F \cos \beta_F \cos \beta_{1C} \sin \beta_{1S} \\ - \cos \alpha_F \sin \beta_F (-\sin \beta_{1C} \cos \theta_S - \cos \beta_{1C} \cos \beta_{1S} \sin \theta_S)$$

$$T_{TPP,B}^{3,1} = -\sin \beta_{1C} \cos \theta_S - \cos \beta_{1C} \cos \beta_{1S} \sin \theta_S$$

$$T_{TPP,B}^{3,2} = \cos \beta_{1C} \sin \beta_{1S}$$

$$T_{TPP,B}^{3,3} = -\sin \beta_{1C} \sin \theta_S + \cos \beta_{1C} \cos \beta_{1S} \cos \theta_S$$

where,  $\theta_S$  refers to the in-built shaft tilt, positive for tilt aft. The rotation rates associated with the tip-path plane, relative to the stationary medium can be expressed as:

$$p_{TPP} = \cos \beta_{1C} (-p \cos \theta_S + r \sin \theta_S) + \sin \beta_{1C} \sin \beta_{1S} (q - \dot{\beta}_{1C}) \\ + \sin \beta_{1C} \cos \beta_{1S} (-p \sin \theta_S - r \cos \theta_S + \dot{\beta}_{1S}) \\ q_{TPP} = \cos \beta_{1S} (q - \dot{\beta}_{1C}) + \sin \beta_{1S} (-p \sin \theta_S - r \cos \theta_S + \dot{\beta}_{1S}) \\ r_{TPP} = -\sin \beta_{1C} (-p \cos \theta_S + r \sin \theta_S) + \cos \beta_{1C} \sin \beta_{1S} (q - \dot{\beta}_{1C}) \\ + \cos \beta_{1C} \cos \beta_{1S} (-p \sin \theta_S - r \cos \theta_S + \dot{\beta}_{1S}) \\ (3.44)$$

Using these coordinate transformations the force balance equations and its various components were cast into a form suitable for the tip-path plane performance analysis that is the focus of the present research. Implementation-specific modifications of the existing code are addressed in the next chapter.

### 3.5 Sample Longitudinal Maneuvers: Mathematical Functional Representations

In this section, idealized mathematical functional representations of sample longitudinal maneuvers are developed. Both flight path angle transitions and velocity transitions from one steady-state value to another are considered. “Sigmoidal” functions [101] are selected to represent the variation of flight path angle and flight velocity during these longitudinal maneuvers.

Flight path angle transitions at a fixed flight velocity are considered first. Such a transition is characterized by the initial flight path angle, total change in flight path angle and the maximum rate of change of the flight path angle.

$$\gamma = \gamma_o + \Delta\gamma \left[ \frac{1}{1 + e^{-ct}} \right]$$
$$\dot{\gamma}_{\max} = \frac{c}{4} \Delta\gamma \quad (3.45)$$

The maximum acceleration perpendicular to the flight path is given by  $V \frac{\dot{\gamma}_{\max}}{g}$ .

For a decelerating straight-line trajectory a double-sigmoidal function is selected to allow greater flexibility and control in specifying the maneuver:

$$\dot{V} = \dot{V}_{\max} \left[ \frac{1}{1+e^{-c(t+t_o)}} - \frac{1}{1+e^{-c(t-t_o)}} \right] \frac{1+\cosh(ct_o)}{\sinh(ct_o)}$$

$$V = V_o + \frac{\dot{V}_{\max}}{c} \ln \left[ \frac{1+e^{c(t+t_o)}}{1+e^{c(t-t_o)}} \right] \frac{1+\cosh(ct_o)}{\sinh(ct_o)} \quad (3.46)$$

where,  $\Delta V = V(+\infty) - V(-\infty) = 2t_o \dot{V}_{\max} \frac{1+\cosh(ct_o)}{\sinh(ct_o)}$

and  $|\ddot{V}_{\max}| = |\ddot{V}(\pm t_o)| = \frac{c}{4} |\dot{V}_{\max}| \frac{1+\cosh(ct_o)}{\sinh(ct_o)} \tanh^2(ct_o)$ .

For a given maximum deceleration value  $|\dot{V}_{\max}|$  and a fixed velocity budget (total change in velocity  $\Delta V$ ), different deceleration profiles can be obtained by varying the value of the parameter  $c$ , which is proportional to the maximum rate of change of deceleration. If it is assumed that  $\tanh(ct_o)$  is approximately equal to 1.0 then the following simplification results:

$$\dot{V} = \dot{V}_{\max} \left[ \frac{1}{1+e^{-c(t'-t_o)}} - \frac{1}{1+e^{-c(t'+t_o)}} \right]$$

$$V = V_o + \frac{\dot{V}_{\max}}{c} \ln \left[ \frac{1+e^{c(t'+t_o)}}{1+e^{c(t'-t_o)}} \right] \quad (3.47)$$

where,  $\Delta V = 2t_o \dot{V}_{\max}$ ,

$$|\ddot{V}_{\max}| = \frac{c}{4} |\dot{V}_{\max}|$$

and  $\tanh(ct_0) \approx 1.0$  or  $ct_0 > 3.0$ .

The maximum deceleration value is reached at  $t' = 0$  sec. The deceleration profile is symmetric about time  $t' = 0$ . The maximum rate of change of deceleration occurs at  $t' = \pm t_0$ . These smooth controlled variations in flight profile are considered to be acceptable representations of longitudinal maneuvers for the purpose of the present study.

Three different sample deceleration cases are constructed using these functions. The velocity is varied from 80 knots to 40 knots. The values of the associated equation parameters are summarized in Table 3.1. The comparisons of the associated velocity, acceleration and rate of change of acceleration profiles are shown in Figures 3.8, 3.9 and 3.10. The first case is a “slow deceleration” over 50 seconds. The maximum deceleration value is 0.075g, the maximum rate of change of deceleration is 0.094g. The product of the parameters  $c$  and  $t_0$  is 7.0. The second case is a “quick stop”, which occurs over less than 20 seconds, with a maximum deceleration of 0.25g and a rate of change of deceleration of 0.06 g per sec. The third case is an “extreme” deceleration maneuver. The same velocity change now occurs over 10 seconds. The maximum deceleration is 0.4 g and the rate of change of deceleration is 0.2 g per sec. These profiles are implemented using the higher order flight dynamics model and used to study and evaluate longitudinal flight maneuvers and the associated main rotor performance parameters in the next chapter.

Case No.	$ \dot{V} _{\max}$ , (g)	$ \ddot{V} _{\max}$ , (g per sec)	Maneuver Time (sec)	C, (sec <sup>-1</sup> )	t <sub>0</sub> , (sec)
1	0.075	0.0094	50	0.5	14.0
2	0.25	0.0624	20	1	4.2
3	0.4	0.2	10	2	2.6

Table 3.1 Characteristic parameters associated with three sample deceleration cases.

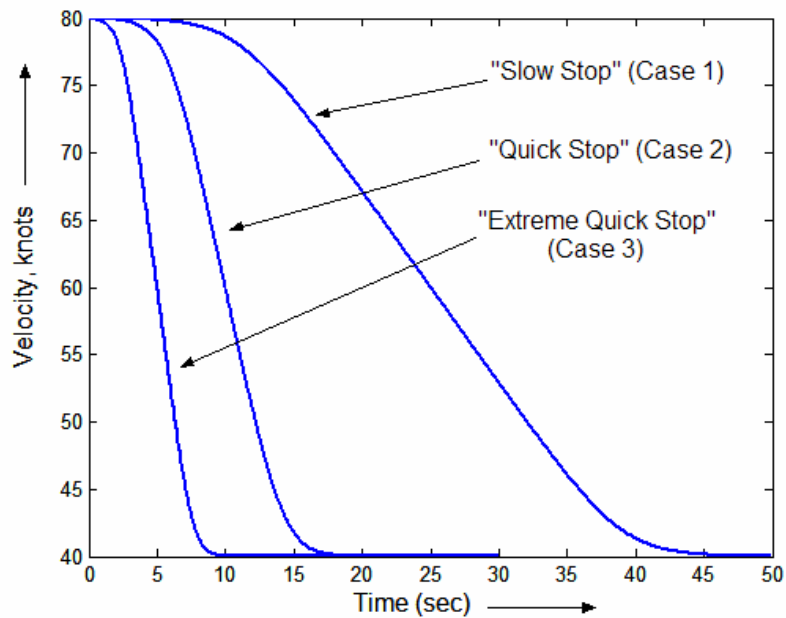


Figure 3.8 Velocity profile along three sample deceleration cases.

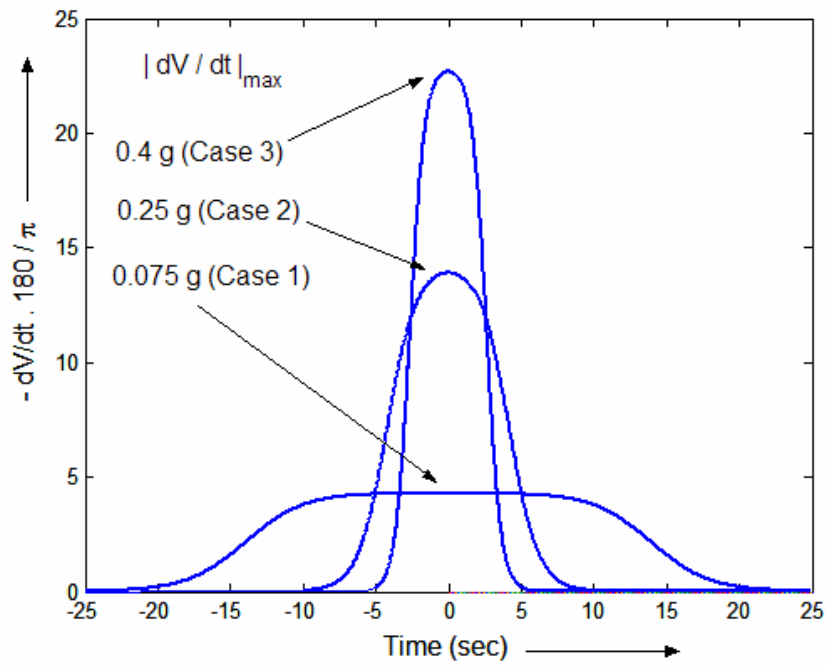


Figure 3.9 Acceleration profile along three sample deceleration cases.

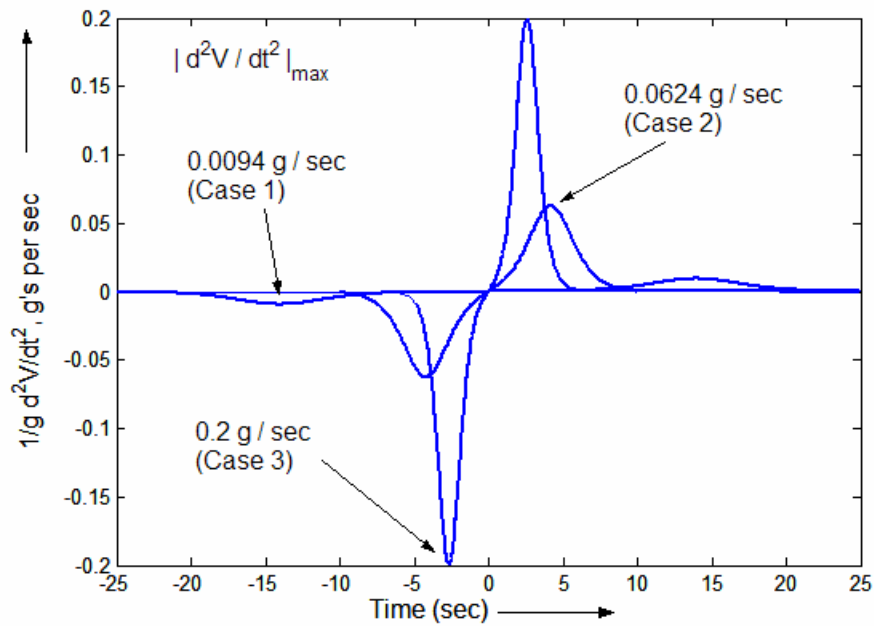


Figure 3.10 Rate of change of acceleration profile along three sample deceleration cases.

## Chapter 4

### Tip Path Plane Performance and Dynamics: Results

The flight dynamics models developed in the previous chapter are used to study tip-path plane behavior during slow longitudinal maneuvers. A slow deceleration maneuver is implemented using the higher order flight dynamics model. The implementation issues are discussed. The results are analyzed in the context of tip-path plane behavior and performance and its implications to the associated main rotor BVI noise radiation. The equivalence between descent and deceleration, its validity and bounds are explored and investigated. Lower order models are used to develop several different slow longitudinal maneuvers. The tip-path plane performance parameter variations along the trajectories are discussed. These parameters include the tip-path plane angle, thrust and main rotor inflow. Control requirements along these trajectories are also discussed.

This research focuses on slow maneuvers during nominal descent conditions as might be encountered during civilian operations. A slow maneuver, for the purpose of this research is defined as an acceleration of less than  $0.1g$  along the flight path and  $1\pm 0.05g$  perpendicular to the flight path. Flight velocities in the range 40 knots to 100

knots are considered. Flight velocities in the range from 40 knots to 60 knots are referred to as “low”, velocities between 60 knots to 80 knots are considered “moderate” and above 80 knots velocities are referred to as “high”. Flight path angles of less than  $\pm 10^\circ$  are considered “small”. These parameters set a longitudinal flight operational envelope of interest to the present research.

It is re-emphasized that the tip-path plane angle, along with main rotor thrust and main rotor advance velocity, set the inflow distribution over the rotor disk. The inflow governs miss-distances along any BVI, which has a significant effect on BVI noise levels. Near-zero uniform or effective inflow conditions are known to be associated with high BVI noise radiation. The study of tip-path plane behavior in this chapter should be viewed in this context.

## **4.1 Higher order Model Results**

The higher order flight dynamics model [95] is used in this section to study slow longitudinal maneuvers. The objectives of this higher order flight dynamics model study are summarized below:

1. To establish the “equivalence” between descent and deceleration and to investigate its limits:
  - a. To investigate the validity of a static interpretation of the tip-path plane equation (“Performance equivalence”).

- b. To investigate the effect of longitudinal maneuvers on inflow through the rotor disk and tip-path plane pitch rate, using a dynamic inflow model (“Local Aerodynamic Equivalence”).
2. To investigate the validity of ignoring thrust changes during maneuvers, on its effect on tip-path plane angle.
3. To compare fuselage pitch and main-rotor flap dynamics with tip-path plane behavior.
4. To “validate” lower order models of flight dynamics and performance in their ability to estimate the tip-path plane angle during slow longitudinal maneuvers.

The higher order model can simulate either the UH-60 or the BO-105. The UH-60 was selected for the current implementation. Relevant vehicle design and operational parameters are summarized in Table 4.1.

#### **4.1.1 Trim Results**

##### **4.1.1.1 Effect of Flight Velocity**

Figure 4.1 shows the component wise drag to weight components for the UH-60 helicopter, based on the higher order modeling, and the tip-path plane angle at a flight velocity of 40 knots, over a one rotor revolution period. The controls were held fixed and the flight dynamics equations were integrated over a period of 1 second. It is observed that the tip-path plane angle is  $-2.2^\circ$ , and is equal to the vehicle drag to

thrust. Assuming thrust to be equal to weight incurs an error of less than  $0.1^\circ$  in tip-path plane angle estimation. The main contributors to the effective drag of the helicopter are the fuselage,  $-1.5^\circ$  (which includes the effect of the horizontal stabilizer) and the main rotor H force in the tip-path plane,  $-0.7^\circ$ . The tail rotor contribution to the effective helicopter drag, and therefore to the tip-path plane angle, is negligible (less than  $-0.05^\circ$ ).

<i>Parameter</i>	<i>Symbol</i>	<i>Value (Range)</i>	<i>Units</i>
Gross Weight	$GW$	14262	Lb
Gross Weight Coefficient	$C_w$	0.00505	-
Main rotor RPM	$RPM$	258	RPM
	$\Omega$	27	rad/sec
Main rotor tip-speed	$\Omega R$	724	feet/sec
Main rotor revolution Time period	$T$	0.23	Sec
Main rotor Radius	$R$	26.83	Feet
Number of Blades	$N_b$	4	-
Equivalent flat plate area	$f_x$	37	feet <sup>2</sup>

Table 4.1 Relevant design and operational parameters for the UH-60 model.

Figure 4.2 shows the main rotor (“fixed-frame”) flapping angles as a function of time over a one rotor revolution period at a flight velocity of 40 knots. The coning angle,

longitudinal and lateral flapping angles are seen to be held nearly fixed during trim. The longitudinal flapping shows variations of less than  $0.005^\circ$ . The differential coning angle is seen to be of the order of  $0.1^\circ$ . This sets one bound for the tip-path plane accuracy considerations. From a practical standpoint, changes of less than  $0.5^\circ$ , perhaps even a degree, would not make an appreciable difference on BVI noise radiation for a helicopter in atmospheric flight. It is also noted that the higher harmonic vibratory component of vehicle acceleration is of the same order as the differential coning in degrees. In degrees, the peak to peak value of the 4 per rev acceleration “g” levels is about  $0.15^\circ$ . The variations in tip-path plane angle during the same trim condition are less than  $0.005^\circ$ .

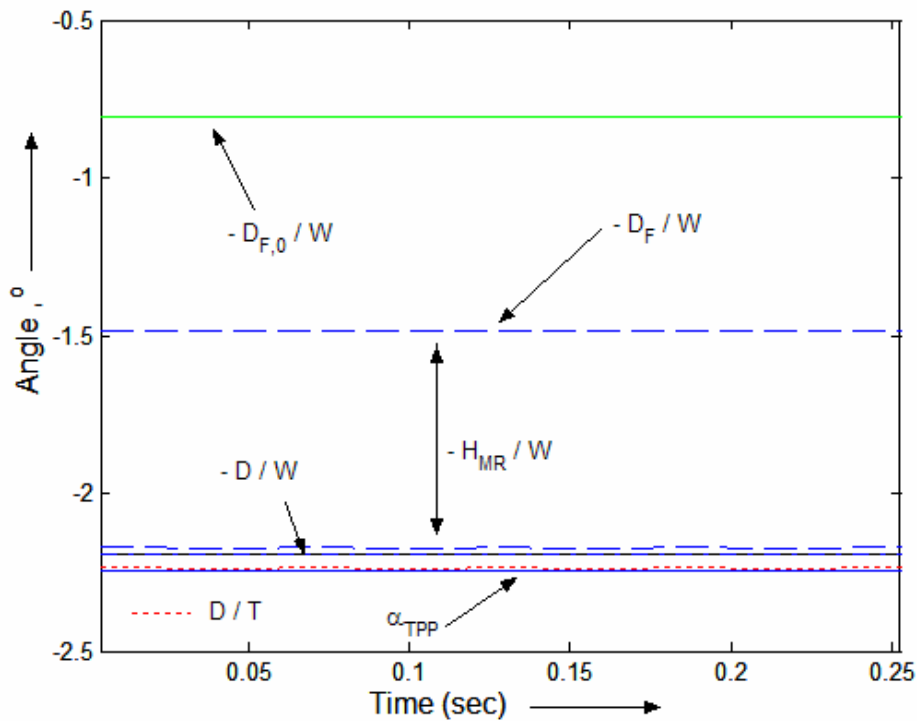


Figure 4.1 Component wise drag to weight terms and the tip-path plane angle at a flight velocity of 40 knots.

Figure 4.3 shows the same tip-path plane angle results (as shown in Fig. 4.1) as a function of flight velocity from 40 knots to 100 knots. Tip path plane angle is seen to be equal to the effective drag by thrust of the helicopter. Assuming thrust to be equal to weight is a reasonable approximation, incurring an error of less than  $0.1^\circ$ .

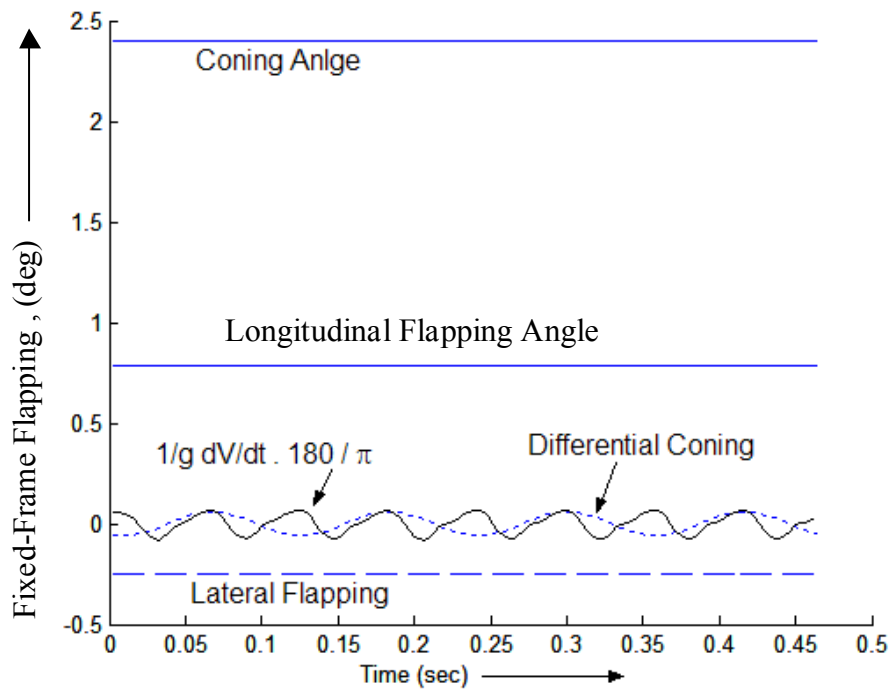


Figure 4.2 Fixed frame flapping angles and vehicle acceleration as a function of time at a trim condition of 40 knots.

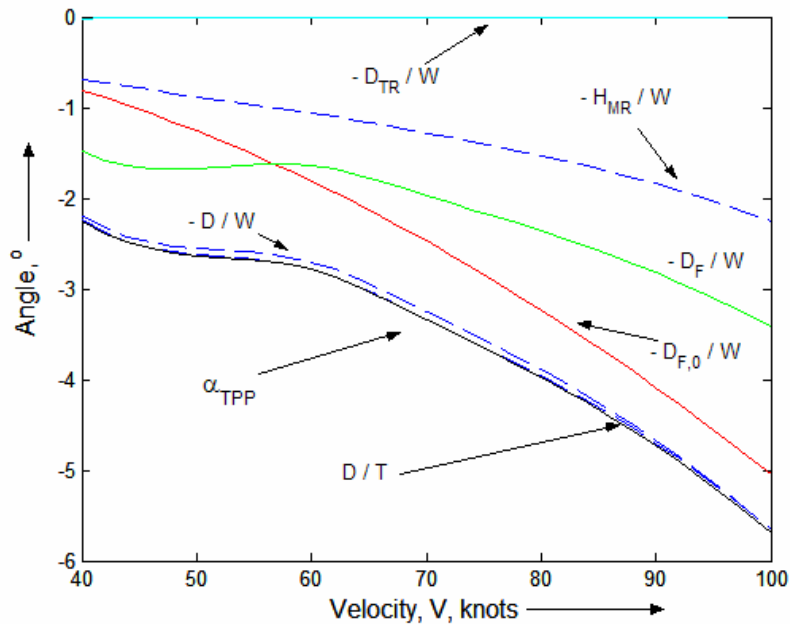


Figure 4.3 Component wise drag to weight terms and the tip-path plane angle as a function of flight velocity.

The main contributors to the effective drag of the helicopter are fuselage, main rotor and horizontal stabilizer. The contribution from the main rotor H force in the tip-path plane is less than  $1^\circ$  at 40 knots and is about  $2^\circ$  at 100 knots. The tail rotor contribution to effective helicopter drag is negligible at all flight velocities. An estimate of the drag to weight ratio based on the equivalent flat plate area of the helicopter fuselage ( $D_{F,0}/W$ ), is seen to approximate the tip-path plane angle (based on the higher order model) to within  $1^\circ$  in the moderate to high velocity range. A “hump” is observed in the tip-path plane angle results at low velocities (around 40 knots) using the higher order model. This is attributed to the interference from the main rotor downwash on the horizontal stabilizer at these low flight velocities.

#### 4.1.1.2 Effect of Flight Path Angle

Figure 4.4 shows the effect of flight path angle on the tip-path plane angle, and fixed frame flapping angles at a flight velocity of 70 knots. The flight path angle is varied from  $0^\circ$  to  $-16^\circ$ . The tip-path plane angle varies nearly linearly with descent angle, up to  $-16^\circ$ . In comparison, the variation in the fixed-frame flapping angles is small – less than  $0.5^\circ$  over a flight path angle change of  $16^\circ$ .

Figure 4.5a shows the helicopter pitch attitude and longitudinal flapping angle as a function of flight path angle ( $0^\circ$  to  $-16^\circ$ ) at a flight velocity of 50 knots. This plot also shows the error in assuming a constant tip-path plane pitch attitude as a function of flight path angle, or that  $\partial\alpha_{TPP}/\partial\gamma = -1$ . While the fuselage pitch angle increases by about  $1.85^\circ$  and the longitudinal flapping angle increases by about  $1.35^\circ$  over a flight path angle change of  $-12^\circ$ , the effect of these changes on the pitch attitude associated with the tip-path plane, or the drag to weight of the helicopter, is less than  $0.5^\circ$ . Therefore, by tabulating the tip-path plane angle values for level flight trim, the effect of changes in flight path angle can be obtained by this simple static relation:

$$\alpha_{TPP}^{SS} \approx \alpha_{TPP}^{SS} \Big|_{\gamma=0} - \gamma \quad \text{or} \quad \theta_{TPP}^{SS} \approx \theta_{TPP}^{SS} \Big|_{\gamma=0} \quad (4.1)$$

The error in tip-path plane estimation using this assumption is seen to be less than  $0.5^\circ$  over a flight path angle change of  $-12^\circ$ .

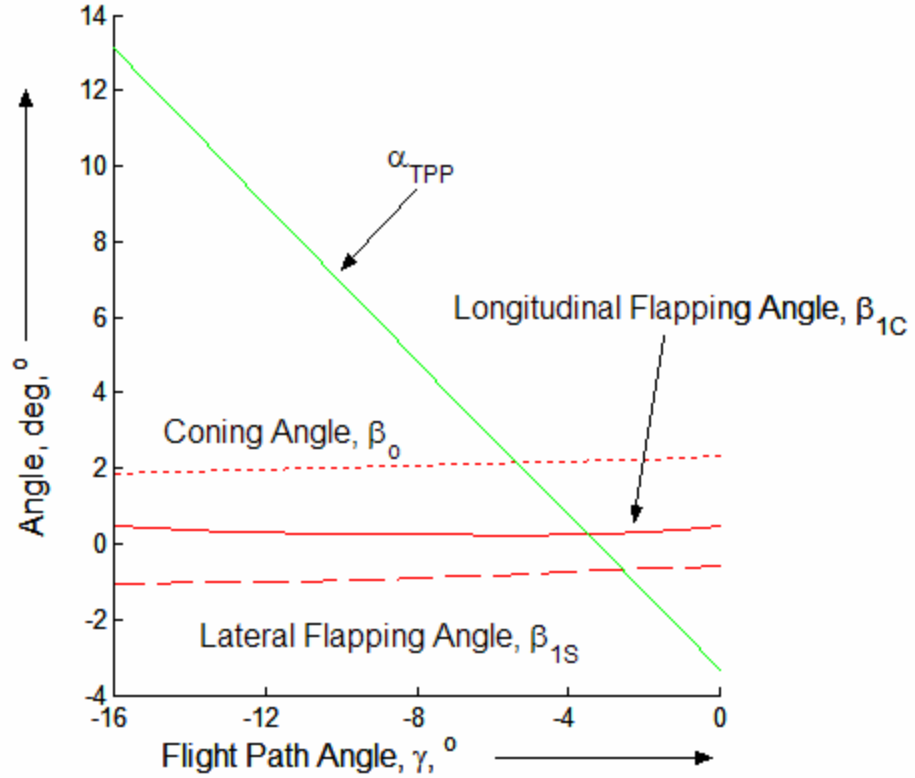


Figure 4.4 Effect of flight path angle on Tip-path plane angle and fixed-frame flapping angles at a flight velocity of 70 knots.

Figure 4.5b shows the same trends for a flight velocity of 70 knots. At this flight velocity, the variation in the fuselage pitch attitude and the longitudinal flapping angle is less than  $0.5^\circ$  over a descent angle change of  $16^\circ$ . The error associated with equation 4.1 is now seen to be less than  $0.45^\circ$  over the same flight path angle range.

Figure 4.6 shows the effect of changing the flight path angle on the control input requirements at flight velocities of 70 knots and 50 knots. At 70 knots the only significant change is observed in the collective control, while the longitudinal, lateral and pedal controls are seen to be insensitive to changes in flight path angle, changing by less than 0.2 inches over a flight path angle change of  $-16^\circ$ . The collective control input required for trim reduces, almost linearly, with descent angle, at a rate of  $-0.16$  inch per degree of flight path angle. This is because the thrust remains approximately the same during descent as compared to level flight, while the inflow “up” through the rotor disk increases. Therefore for the same average angle of attack, the main rotor blades would require a lower collective pitch input. At 50 knots the collective control sensitivity to changes in flight path angle reduces while that of longitudinal cyclic increases slightly.

The observations made in this section have a direct bearing on the effect of deceleration on various flight and control parameters, as will be shown in subsequent sections.

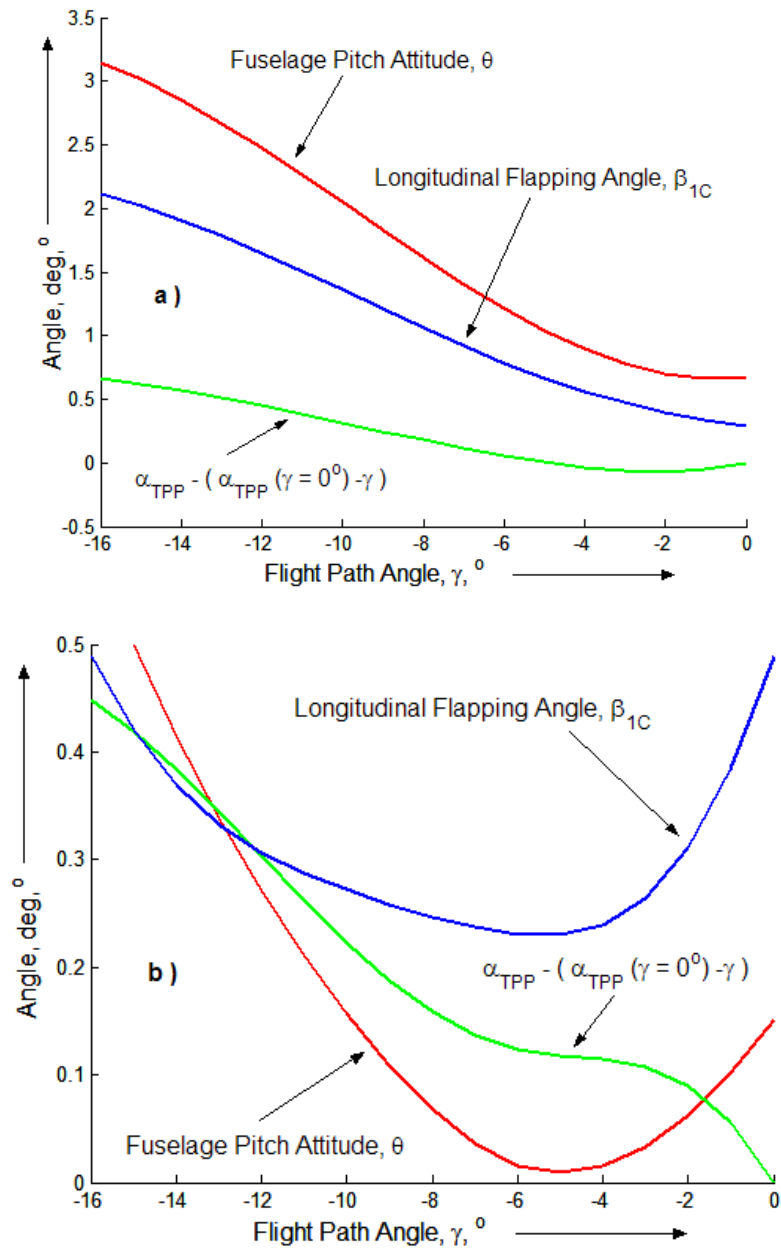


Figure 4.5 Effect of flight path angle on tip-path plane angle, longitudinal flapping angle and fuselage pitch attitude, at a flight velocity of a) 50 knots and b) 70 knots.

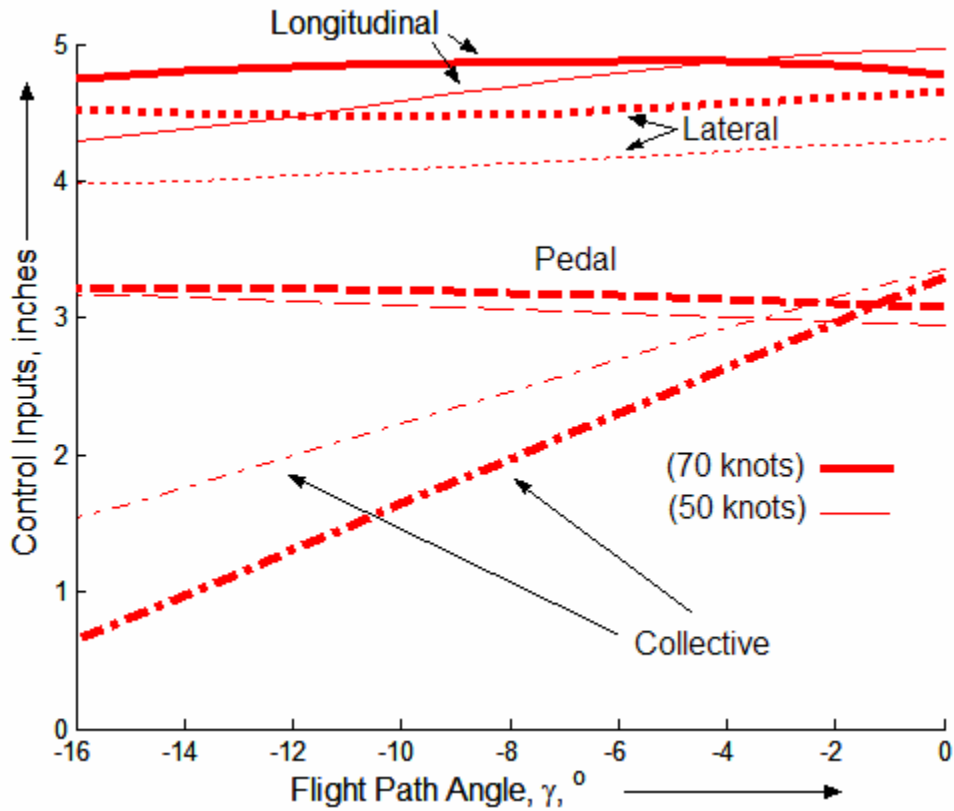


Figure 4.6 Control input requirements as a function of flight path angle, at a flight velocity of 50 knots and 70 knots.

#### 4.1.2 Higher Order Model – Maneuver Implementation

Several changes had to be incorporated in the existing higher order flight dynamics model to implement slow longitudinal maneuvers.

The model used a variable time-step third-order accurate Adams Bashforth time integration scheme. To reduce simulation time while maintaining accuracy, a numerical study was conducted. A fixed time step size was used with the RK-4

method, an explicit fourth-order accurate method. A second-order accurate implicit time marching method was also implemented. For this method the residuals were iterated till convergence to a specified tolerance at each time step. This method was finally used for the simulations. A numerical study was conducted to assess the effect of a fixed time step size on accuracy. Comparisons were made with the variable time step results. The time step for the time integration was finally taken to be 5° of main rotor azimuth (0.00323 sec). The benefit of changing the numerical integration scheme from a variable to a fixed-time step was a dramatic reduction in total simulation time, which reduced from 30 hours to about 4 hours, for a 60 second simulation.

In the baseline configuration of the flight dynamics simulation, for the UH-60 helicopter, the horizontal stabilizer is a function of flight velocity for trim flight. But during the time integration, it was assumed fixed even as the flight velocity varied. This resulted in different pitch attitudes compared to the regular UH-60 trim for the later stages of the simulation. This feature was modified so that at each time step the flight computer readjusts the horizontal stabilizer to the appropriate trim setting. Therefore, in the current model, it is assumed that the flight computer automatically repositions the horizontal stabilizer during a maneuver to represent the “rigged” trim value at each flight velocity.

The objective function for the trajectory-matching optimization procedure was modified to implement the slow deceleration maneuver and the following objective function was developed:

$$F = \sum_{i=1}^{\text{No. of Time Steps}} k_V (V^i - V_{des}^i)^2 + \sum_{i=1}^{\text{No. of Time Steps}} k_v (v^i)^2 + \sum_{i=1}^{\text{No. of Time Steps}} k_\gamma (\gamma^i - \gamma_{des}^i)^2 + \sum_{i=1}^{\text{No. of Time Steps}} k_\psi (\psi^i)^2 \quad (4.2)$$

The trajectory-matching inverse-simulation procedure was originally designed for short maneuvers, 6 seconds or less. For 60 second slow deceleration maneuvers, this procedure became impractical in terms of run time.

A new methodology is developed to implement the maneuver, applicable to slow maneuvers over longer durations. A control-sequence “predictor-corrector” scheme is implemented to achieve the desired longitudinal trajectories. The control sequence is first predicted based on the equivalent trim states. A trim sweep is conducted to obtain pilot controls and helicopter operating parameters as a function of flight velocity and flight path angle. The flight velocity is varied from 30 knots to 100 knots while the flight path angle is varied from level flight to a 20° descent. Based on the quasi-static equivalence between descent and deceleration ( $\gamma_{EFF} = \gamma + \frac{\dot{V}}{g}$ ), the effective controls corresponding to each flight state along the maneuver are obtained using a two-dimensional interpolation within the stored trim database. This sequence of controls is used as an initial prediction of pilot controls. This equivalence in the

controls was suggested by the lower order model study of slow decelerating flight. It was observed that the entire state of the helicopter relative to the medium, as well as the control vector, was nearly identical during equivalent descent and decelerating flight conditions. A “control correction” scheme is then used to modify these estimated control values to obtain the actual controls required to stabilize and guide the resulting maneuver trajectory solution. This control corrector has the following form:

$$U_l^{i+1} = U_{l,o}^{i+1} + G_{l,m} \Delta y_m^{i,n} + S_{l,m} \dot{y}_m^i \quad (4.3)$$

where,

$$\Delta y^{i,n} = y^i - y_{des}^{i+n}.$$

The coefficients “G” and “S”, required for the guidance and stability of the solution, in general vary along the trajectory. The specific form of the control corrections used in the implementation is shown below:

$$\begin{aligned} \Delta \delta_{lat} &= G_\phi \cdot (\phi - \phi_{des, QS}) + S_p \cdot (p) + G_v \cdot (v) + S_{\dot{v}} \cdot (\dot{v}) \\ \Delta \delta_{lon} &= G_\theta \cdot (\theta - \theta_{des, QS}) + S_q \cdot (q) + G_u \cdot (u - V_{des}) + S_{\dot{u}} \cdot (\dot{u}) \\ \Delta \delta_{col} &= G_\gamma \cdot (\gamma - \gamma_{des}) \frac{V}{g} \\ \Delta \delta_{ped} &= G_\psi \cdot (\psi - \psi_{des, QS}) + S_r \cdot (r) \end{aligned} \quad (4.4)$$

The above equations represent the corrections applied to the control at any time step. The coefficients of all rate terms are designated by “S” (Stability factors), and the coefficients of all state variable correction terms are designated by “G” (Guidance factors). The desired values of the flight path angle and flight velocity were prescribed. The desired values of the Euler angles are based on quasi-static trim estimates. The form initially assumed was:

$$\begin{aligned}\phi_{des,QS} &= \phi(\gamma = 0, V_{des})|_{trim} \\ \theta_{des,QS} &= \theta(\gamma = 0, V_{des})|_{trim} - \frac{\dot{V}}{g}|_{des} \\ \psi_{des,QS} &= 0\end{aligned}\tag{4.5}$$

The optimization-based inverse simulation coupled with a systematic trial-and-error approach was initially used to find these coefficients for a particular maneuver trajectory. The optimization was conducted over the “control correction” factors, which were initially held fixed along the trajectory. The design vector in this optimization approach consists of the coefficients “G” and “S” along the trajectory. This control sequence prediction-correction strategy is used to simulate longitudinal flight trajectories. A systematic trial-and-error approach was finally used to estimate these control correction coefficients, assumed constant along the entire trajectory. This, coupled with the optimization procedure was deemed to be a more practical way of finding the desired gains rather than using the optimization procedure alone. This

is mainly because of difficulties in developing a robust objective function that resulted in meaningful or useful optimized results, and long simulation times. The “control gains” or correction factors used for the results shown in the following sections for the higher order model, therefore, do not guarantee any degree of optimality of the solutions. The final values of the control correction factors used for all maneuvers, and held fixed over the entire time of the maneuver, are shown in table 4.2.

The trim study values in Table 4.2 refer to nominal values required to stabilize a trim condition over a 60 second simulation. Stick fixed time integrations result in an unstable divergence, because the helicopter system is intrinsically unstable. The same control correction scheme (Equation 4.4) was used to stabilize the trim solution. These “control gains” or “control correction” factors were required for control and stability of the solution. Using marginal correction factors the trim state could be held fixed for a long simulation time, at least 60 seconds. The correction factors required for holding trim conditions for 60 seconds were in general smaller than those required for the maneuver (Table 4.2).

Control Correction Coefficient	Value used in Maneuver study	Value used in Trim study	Dimensions/ Units
$G_\theta$	-12.00	-5.00	Inch
$S_q$	-1.50	-1.50	Inch-sec
$G_\phi$	-20.00	-5.00	Inch
$G_p$	-2.00	-1.50	Inch-sec
$G_\psi$	-20.00	-5.00	Inch
$S_r$	-2.00	-1.50	Inch-sec
$G_u$	0.50	0.05	inch-sec/ft
$S_{\dot{u}}$	0.01	0.01	Inch-sec <sup>2</sup> /ft
$G_\gamma$	-7.50	-0.10	inch/sec
$G_v$	-0.05	-0.02	inch-sec/ft
$S_{\dot{v}}$	0.00	0.00	Inch-sec <sup>2</sup> /ft

Table 4.2 Control correction factor values used for the trim and maneuver study, along with the associated units.

#### 4.1.3 Level Flight Deceleration Maneuvers

Results of the higher order flight dynamic simulation are now presented for sample deceleration maneuvers. This maneuver involves a controlled reduction in flight

velocity at a fixed flight path angle from one trim state to another. A baseline case is defined and described mathematically in the next section. This maneuver will also be referred to as a “slow stop” maneuver. Comparisons are made between higher order modeling of flight dynamics and main rotor performance, and quasi-static estimates obtained using the longitudinal force balance equations. Results for another level flight deceleration maneuver, a “quick stop” maneuver are also presented to test the limits of quasi-static assumptions. These maneuvers were also introduced in section 3.5.

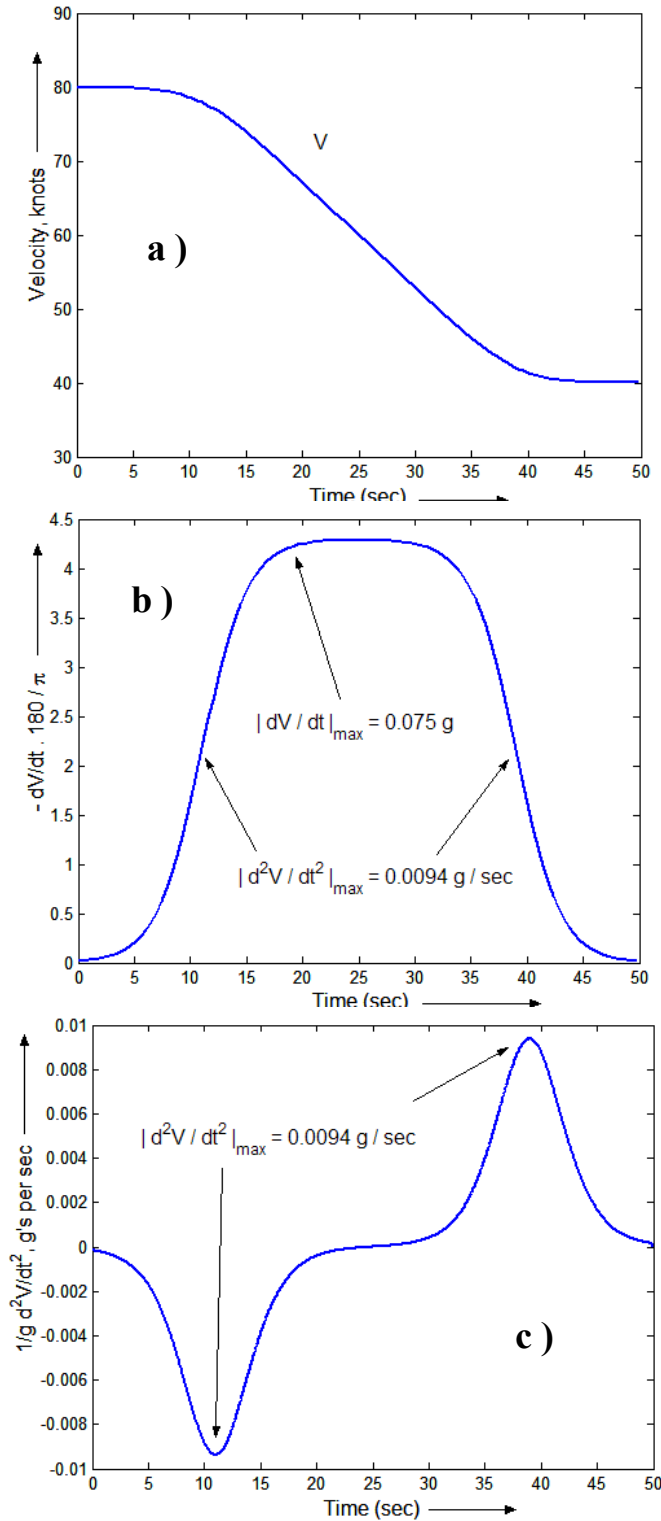


Figure 4.7 Baseline slow deceleration or “Slow Stop” maneuver showing: a) velocity profile, b) acceleration profile and c) rate of change of acceleration profile.

#### 4.1.3.1 Baseline Deceleration Maneuver Description

The variation of velocity, acceleration and the rate of change of acceleration along the baseline maneuver are shown in Figures 4.7a, b and c respectively. Starting from level flight trim at 80 knots, the flight velocity is reduced to 40 knots in 50 seconds. The maximum deceleration value is 0.075g. The maximum rate of change of deceleration is 0.0094 g per sec. The mathematical representation used for the flight velocity variation along the trajectory is (Section 3.5):

$$\dot{V} = \dot{V}_{\max} \left[ \frac{1}{1 + e^{-c(t'-t_0)}} - \frac{1}{1 + e^{-c(t'+t_0)}} \right]$$

$$V = V_0 + \frac{\dot{V}_{\max}}{c} \ln \left[ \frac{1 + e^{c(t'+t_0)}}{1 + e^{c(t'-t_0)}} \right] \quad (4.6)$$

where ,

$$V_0 = 80 \text{ knots}, \Delta V = -40 \text{ knots}, \dot{V}_{\max} = -0.075g, \ddot{V}_{\max} = 0.0094 \text{ g per sec},$$

$$t_0 = 14 \text{ sec}, t' = t - 25 \text{ sec}, c = 0.5, ct_0 = 7.0 \text{ and } \tanh(ct_0) = 1.0.$$

The deceleration profile is symmetric about the midpoint at time  $t = 25$  sec. The profile is divided into three distinct stages, an initial and final trim state, a constant deceleration state and an intermediate transient state where the helicopter transitions from trim to constant deceleration or vice versa.

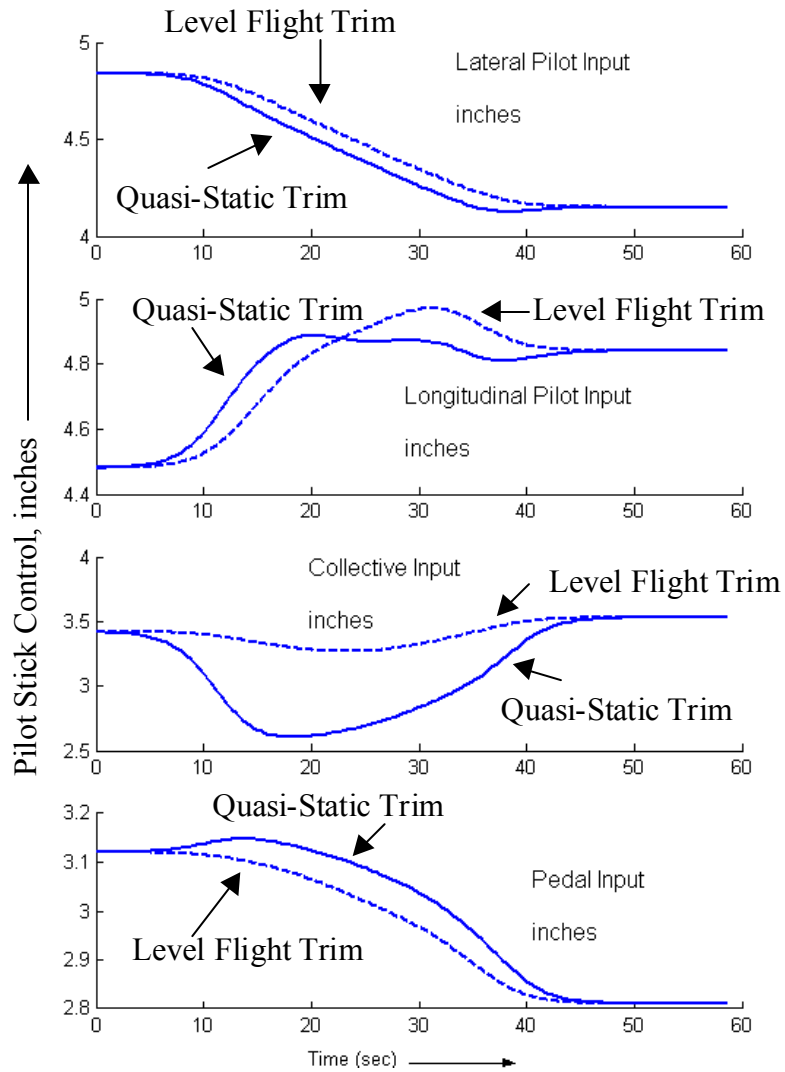


Figure 4.8 Variation of effective trim and quasi-static control inputs along the baseline slow stop maneuver.

#### 4.1.3.2 Deceleration Maneuver Results: Higher Order Model

Figure 4.8 shows the estimated quasi-static trim control values for all the four pilot controls as a function of time along the slow deceleration maneuver. Plotted alongside are the corresponding level flight trim values. The lateral and pedal controls

are close to level flight trim values. This relative insensitivity to flight path angle was observed in Fig. 4.6. The longitudinal control input is also fairly close to the level flight values. The collective shows the maximum differences from level flight. This is because at approximately the same thrust setting, the increase in inflow through the rotor disk is compensated by reducing the collective pitch. At an effective descent of  $4.3^\circ$ , the collective requirement changes by less than 1". These trends were also discussed in relation to Fig. 4.6.

Figures 4.9 through 4.15 show the actual results of implementing the higher order modeling. The control correction values used are those presented in table 4.2. Figure 4.9 shows the velocity profile as a function of time. The desired profile is nearly coincident to the one obtained. Therefore, applying the control correction factors to a prediction of the required control sequence based on quasi-static trim values is seen to be a successful approach in slow-maneuver trajectory matching. Fig. 4.10 shows the actual control requirements along this maneuver (solid lines). These four control sequences, one each for the collective, longitudinal and lateral cyclic and pedal controls are compared with the quasi-static values (dashed lines) based on the equivalent descent condition. The controls required for the actual maneuver are seen to be very close to the quasi-static values. The implication of this result is that for a slow decelerating maneuver the pilot essentially executes a series of near quasi-static control input changes to achieve a controlled deceleration profile. The final values of all the controls excluding the collective are somewhat different at the end of the

maneuver compared with the quasi-static trim values. This is because of a slightly different non-unique lateral trim condition.

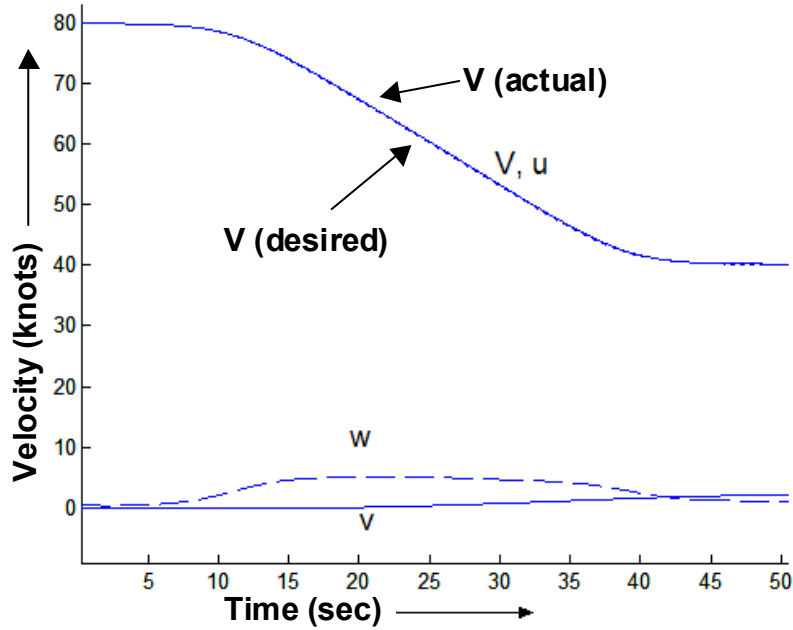


Figure 4.9 Velocity profile along the baseline slow deceleration maneuver.

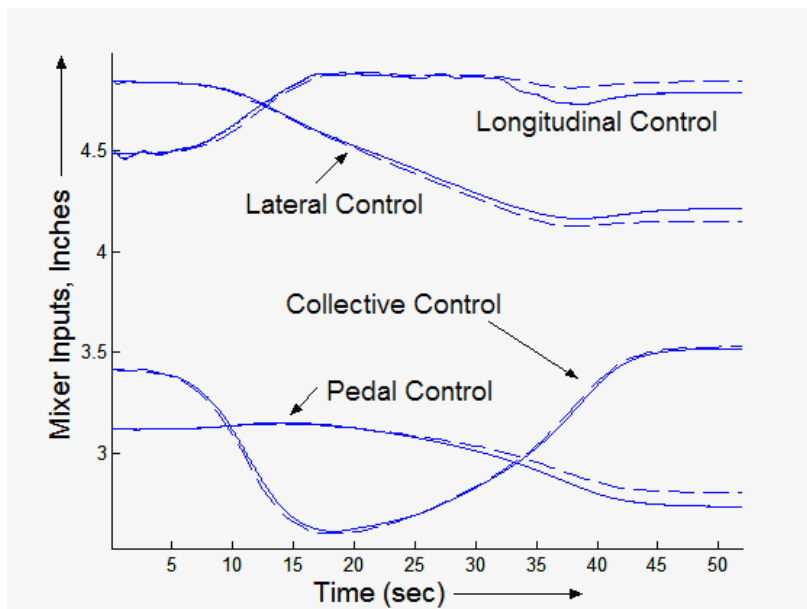


Figure 4.10 Variation of Control input requirements along the baseline slow stop maneuver.

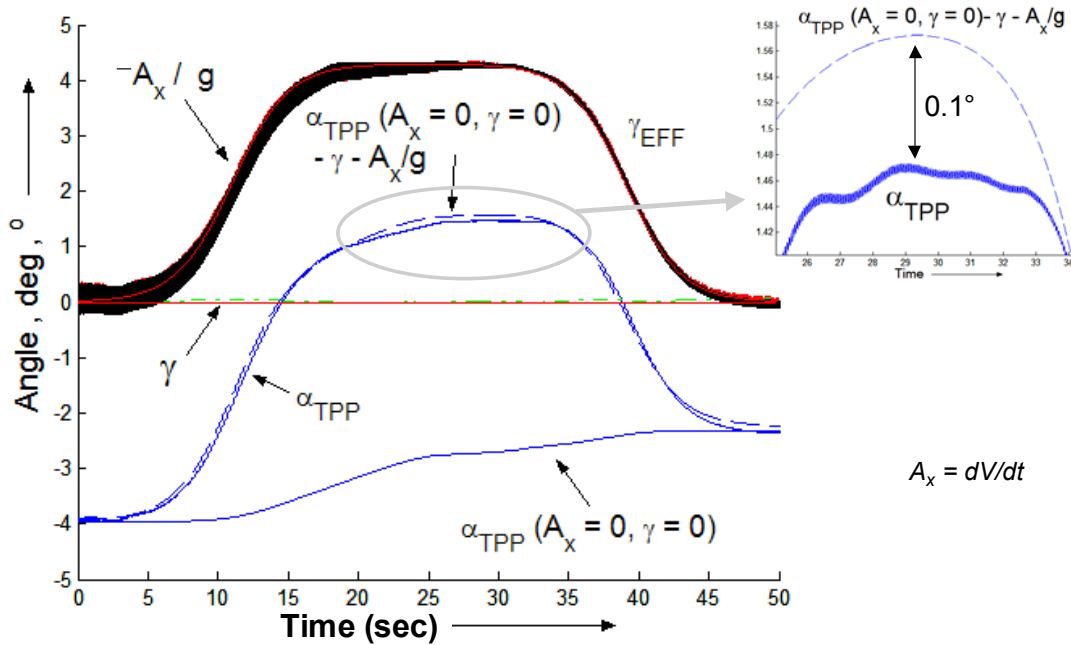


Figure 4.11 Variation of tip-path plane angle, deceleration in g's and flight path angle along the baseline slow stop maneuver.

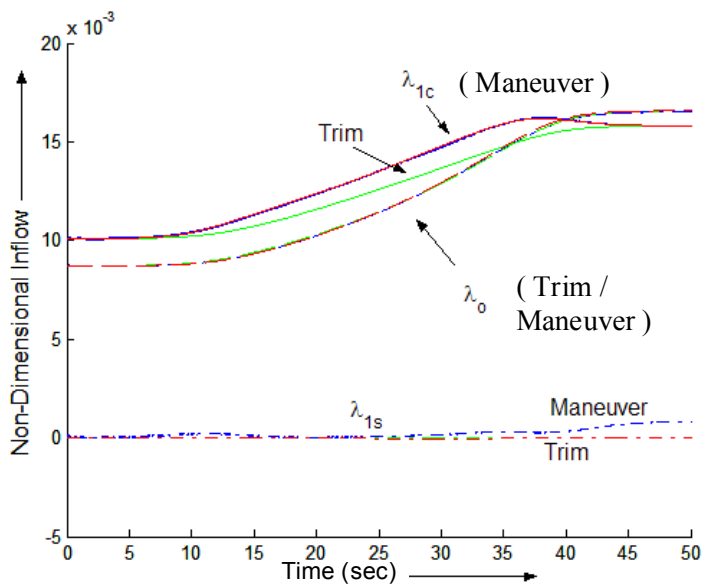


Figure 4.12 Variation of non-dimensional dynamic inflow (induced velocity) coefficients along the slow deceleration maneuver.

Figure 4.11 shows the acceleration profile as a function of time. Also shown are the desired acceleration profile, the tip-path plane angle and flight path angle variation, the level flight trim values for the tip-path plane angle and the tip-path plane angle expected from the quasi-static equation. The deceleration profile is observed to exhibit a vibratory component, as was seen under trim flight conditions (Fig. 4.2). The average deceleration profile is seen to follow the prescribed trajectory well. The higher harmonic vibratory component of vehicle acceleration is a function of flight speed, and in general reduces as the flight velocity changes from 80 knots to 40 knots. The flight path angle is held fairly close to zero ( $< 0.2^\circ$ ) along the trajectory. The main rotor tip-path plane angle is also plotted along the trajectory. The variation is smooth with no significant higher frequency oscillations. The vibratory component of the acceleration profile does not affect tip-path plane dynamics, a fact that was observed under trim conditions as well (the differential coning, however, was observed to be of the same order). The tip-path plane angle is seen to vary in a quasi-static manner along the trajectory. Assuming thrust to be equal to weight along the trajectory, in estimating the tip-path plane angle is seen to be a good approximation. Therefore, for this maneuver, the static approximation to the tip-path plane angle is seen to be a good approximation, to within  $0.1^\circ$ , or:

$$\alpha_{TPP} \approx \alpha_{TPP}^{SS} \Big|_{\gamma=0} - \gamma - \left( \frac{\dot{V}}{g} \right)_{avg} \quad (4.7)$$

where, the subscript “avg” implies an average over one rotor revolution.

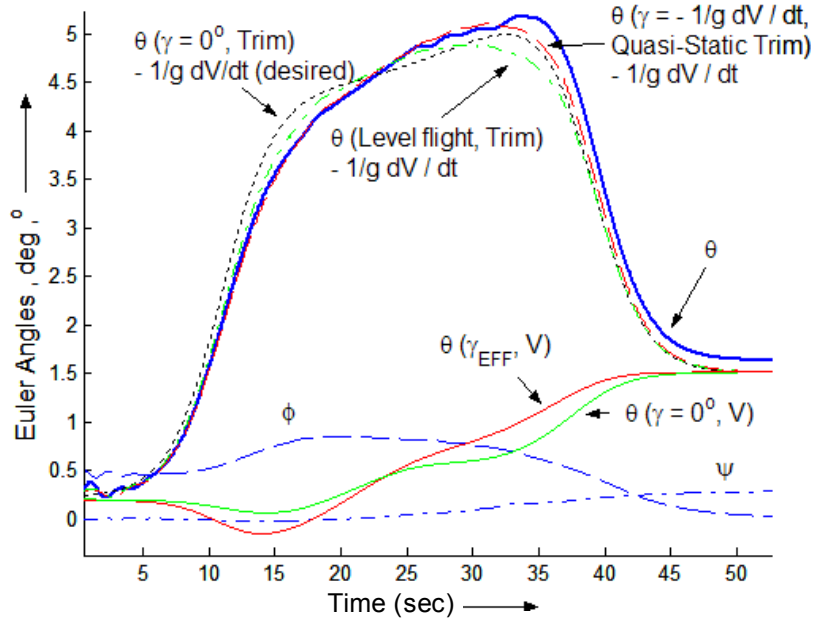


Figure 4.13 Variation of Euler angles along the baseline slow stop maneuver.

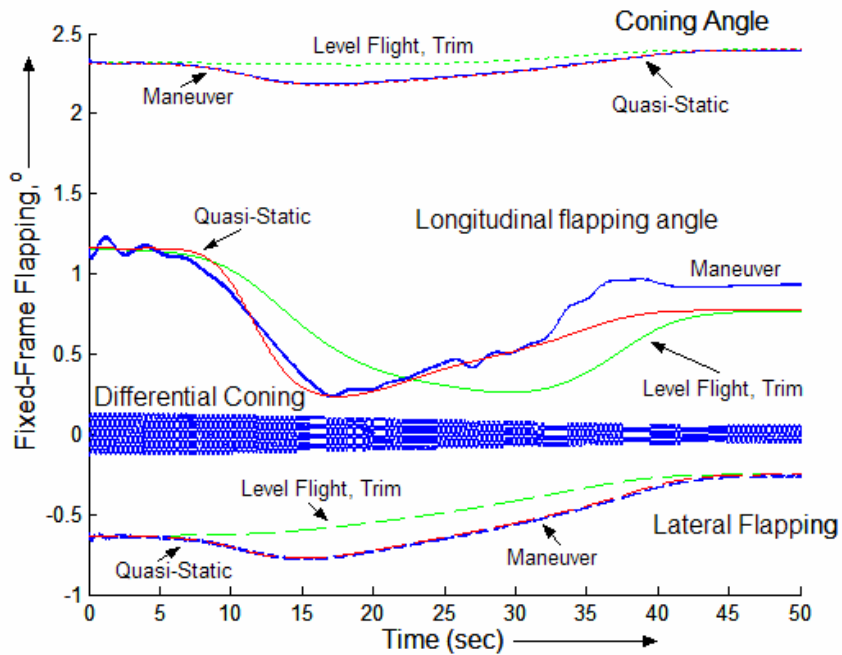


Figure 4.14 Variation of main rotor flapping angles relative to the hub plane along the baseline slow stop maneuver.

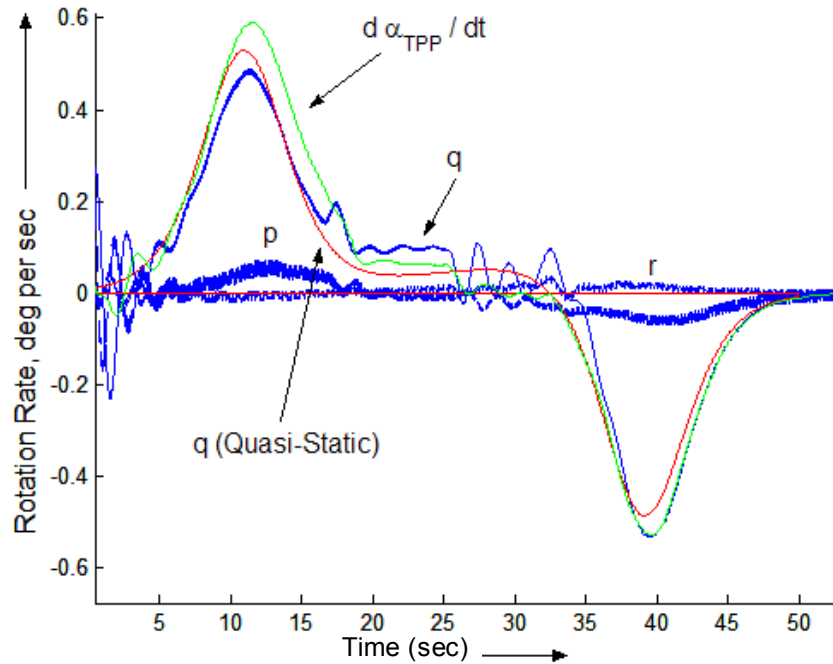


Figure 4.15 Variation of body and tip-path plane rotation rates along the baseline slow stop maneuver.

Also the pitch attitude of the tip-path plane relative to the horizon,  $\alpha_{TPP} + \gamma$ , is

approximately equal to  $\alpha_{TPP}^{SS} \Big|_{\gamma=0} - \left( \frac{\dot{V}}{g} \right)_{avg}$ , and therefore unaffected by the flight path

angle, to first order.

Figure 4.12 shows the dynamic inflow components – uniform, cosine and sine, as a function of time along the maneuver. The corresponding trim and quasi-static values are also plotted. The variations of these induced velocity coefficients are seen to be near quasi-static. The lateral inflow coefficient is different at the end trim state, from the expected value, because of the non-unique lateral trim state.

Fig. 4.13 shows the helicopter pitch attitude along the trajectory, along with the roll and yaw angles. The pitch attitude is seen to be a good indicator of deceleration at any flight velocity. Its variation is close to the quasi-static values. A fairly reasonable approximation to the helicopter pitch attitude along the maneuver is:

$$\theta = \theta^{SS} \Big|_{\gamma=\gamma_{EFF}} - \left( \frac{\dot{V}}{g} \right)_{avg} \approx \theta^{SS} \Big|_{\gamma=0} - \left( \frac{\dot{V}}{g} \right)_{avg} \quad (4.8)$$

The roll and yaw angle at the end of the maneuver are different from regular trim values ( $\psi = 0^\circ$ ). The pitch attitude is also offset by  $0.2^\circ$  at the end trim state. Some oscillations in the pitch attitude profile are observed. These pitch dynamics, however, do not affect the tip-path plane angle. Fig. 4.14 shows the main rotor flapping response along the trajectory. Again the variation of the flap parameters is near quasi-static. The longitudinal flapping is observed to exhibit complementary oscillations to those exhibited by the helicopter pitch. With the tip-path plane angle primarily governed by the X-force equation, moment equilibriums determine helicopter pitch dynamics relative to the horizon and the rotor flap dynamics relative to the shaft or fuselage. This explains the complementary oscillations observed in the helicopter pitch and longitudinal flap variations, and is essentially a demonstration of the equivalence of flapping and feathering (or pitching). The longitudinal flapping angle is also seen to be offset by about  $0.2^\circ$  compared to the baseline trim state at 40 knots.

Fig. 4.15 shows the pitch rates associated with the fuselage compared to the quasi-static values estimated based on the lower order flight dynamics analysis (equation 3.23). Over the constant deceleration region, the pitch rates are low ( $q = 0.1^\circ$  per sec, or  $q/\Omega = 0.000065$ ). The maximum pitch rates during the transient phase are seen to be set by the rate of change of deceleration (Fig. 3.10), and are of the order of  $0.5^\circ$  per sec or  $q/\Omega = 0.00034$ . The tip-path plane rotation rate relative to the medium is also seen to be of the same order as the fuselage pitch rate. These small rotation rates have little effect on the main rotor performance parameters, tip-path plane angle, thrust and inflow, that set the level of BVI noise.

Based on comparisons made between the higher order model results and the quasi-static model for this longitudinal flight maneuver, the following observations can be made:

1. The tip path plane angle during the slow deceleration maneuver follows the quasi-static equivalence between descent and deceleration based on the X-force equation.
2. The tip-path plane remains well defined, its variation along the maneuver remains fairly smooth and does not exhibit higher order dynamics.
3. The equivalence between the helicopter operating state during a steady-state descent and an equivalent level flight decelerating condition applies to not only the tip path plane angle, but to the entire operating state of the helicopter relative to the medium, including the flight controls.

4. Since the equivalence applies to the helicopter operating state relative to the freestream velocity, pitch angles or orientations relative to the horizon are offset by the difference in the flight path angles associated with the two equivalent states.
5. An initial estimate of the control requirements along the maneuver may be made based on the quasi-static trim requirements.
6. The variation of the inflow along the maneuver is near quasi-static. The effect of the small pitch rates during the constant deceleration portion of the maneuver is negligible.

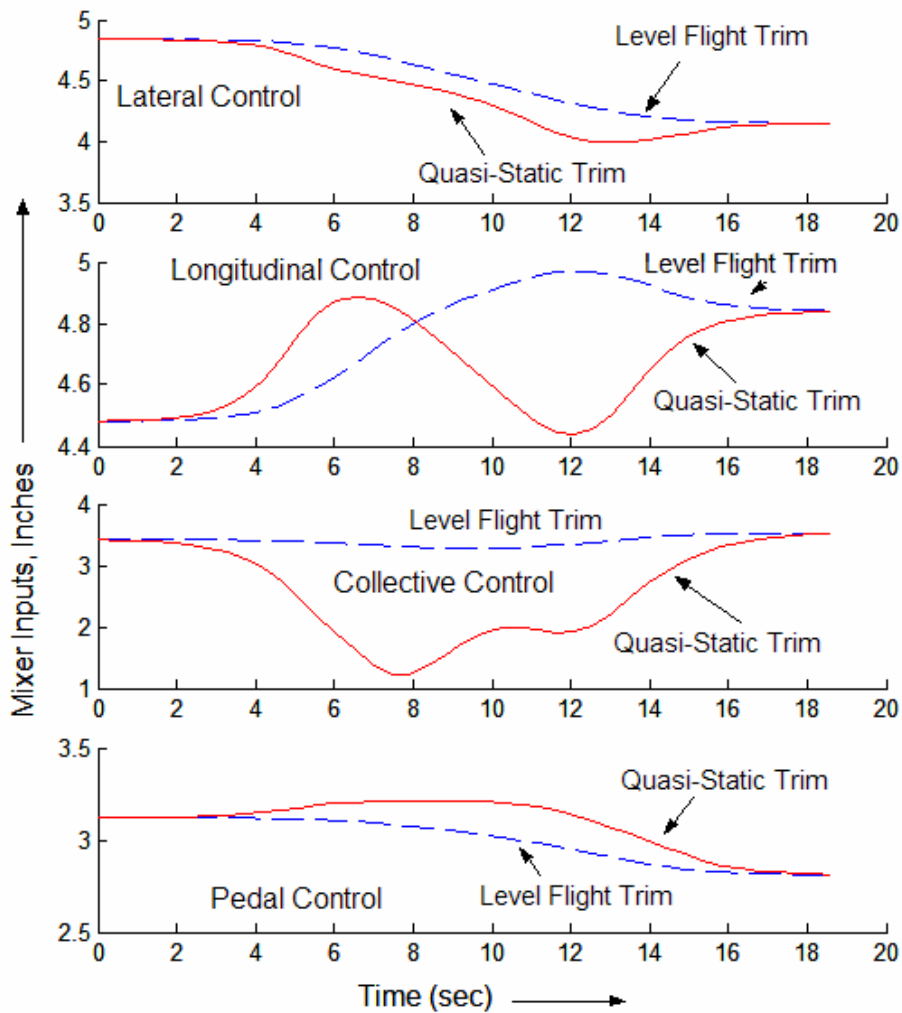


Figure 4.16 Variation of effective trim and quasi-static control inputs along the “quick stop” maneuver.

A “quick stop” maneuver is investigated next. The maneuver was described in section 3.5, Figures 3.8, 3.9 and 3.10. The maximum deceleration along this maneuver is 0.25g, which would be considered a “quick stop”. The maximum rate of change of deceleration is 0.06 g per sec. This maneuver was again implemented using the same

methodology as was done for the “slow stop” maneuver. Figure 4.16 shows a comparison of the associated level flight trim and quasi-static trim control requirements. The departures of the quasi-static control input values from level flight trim values are now seen to be more significant than in Fig. 4.8, though they are qualitatively very similar. The change in collective input is now as much as 2 inches along the maneuver. Again, lateral controls are seen to be less sensitive than the longitudinal controls to changes in flight path angle, as is expected during longitudinal maneuvers. Fig. 4.17 shows the velocity variation obtained along the maneuver, using the same control correction factors as in the “slow stop” maneuver. A “time lag” is observed in the velocity profile compared to the desired trajectory. This mainly comes about because in the “control-corrector” scheme, a small angle assumption was made for  $\theta$  and  $u_{des}$  is taken equal to  $V$ . The preferred form of the control correction scheme would be:

$$\phi_{des, QS} = \phi(\gamma = \gamma_{EFF, des}, V_{des})$$

$$\theta_{des, QS} = \theta(\gamma = \gamma_{EFF, des}, V_{des}) - \frac{\dot{V}}{g} \Big|_{des} \quad \text{and} \quad u_{des} = V_{des} \cos \theta_{des, QS}.$$

$$\psi_{des, QS} = 0$$

Figure 4.18 shows the actual control requirements along the trajectory. The lateral and pedal controls are very close to quasi-static. The collective and longitudinal controls show some differences, an effect of the higher pitch rates experienced in this maneuver (Fig. 4.19). The longitudinal controls are most different from the quasi-

static control requirements during the transient phase of the maneuver, an effect of pitch rate, while the collective shows some differences in the middle of the trajectory as well. The pitch rates experienced in this “quick stop” maneuver are of the order of  $1^\circ$  per sec ( $q/\Omega = 0.00065$ ) in the middle of the maneuver. Maximum pitch rates are observed to be of the order of  $5^\circ$  per sec ( $q/\Omega = 0.0032$ ). The rotation rate associated with the tip-path plane relative to the medium is of the same order as the fuselage pitch rate. What is remarkable is that though the details of the variation of the pitch rate is a function of the actual pilot control gains, the maximum level and trends associated with the pitch rates are reasonably well captured by the static model (equation 3.23).

$$q \approx \frac{\partial}{\partial V} \left( \theta^{SS} \Big|_{\gamma=0} \right) \dot{V} - \left( \frac{\ddot{V}}{g} \right)_{avg / des}$$

The time lag, observed in the velocity profile, compared to the desired or expected quasi-static values, is observed in the pitch rate profile as well, and also in all other performance parameters studied.

Figure 4.20 shows the average deceleration profile, and the tip-path plane angle variation along the trajectory. As observed in previous plots, these lag from the desired profile. The tip-path plane does exhibit “trim-like” characteristics. If the actual averaged acceleration profile is used to estimate the tip-path plane angle during the deceleration maneuver using the quasi-static equation, an error of about  $0.5^\circ$

(Figure 4.21) is now observed. This is because of pitch rates encountered during the maneuver, and changes in the thrust to weight ratio along the trajectory. Four different quasi-static approximations to the tip-path plane angle are shown in Fig. 4.21.

$$\alpha_{TPP} \approx \alpha_{TPP}^{SS} \Big|_{\gamma=0} - \left( \frac{\dot{V}}{g} \right)_{avg} \quad (1)$$

$$\alpha_{TPP} \approx \alpha_{TPP}^{SS} \Big|_{\gamma=\gamma_{EFF}} - \left( \frac{\dot{V}}{g} \right)_{avg} \quad (2)$$

$$\alpha_{TPP} \approx \alpha_{TPP}^{SS} \Big|_{\gamma=0} - \gamma - \left( \frac{\dot{V}}{g} \right)_{avg} \quad (3)$$

$$\alpha_{TPP} \approx \alpha_{TPP}^{SS} \Big|_{\gamma=\gamma_{EFF}} - \gamma - \left( \frac{\dot{V}}{g} \right)_{avg} \quad (4)$$

While all expressions are seen to be almost equally effective in estimating the tip-path plane angle during the maneuver, the best approximation (4) is obtained if the actual flight path angle is considered in the calculations, and the trim value of the tip-path plane angle is taken at the correct effective flight path angle. However, even the simplest of these approximations (1) incurs an error of only about  $0.6^\circ$ , and is a reasonable estimate of the tip-path plane angle. This corroborates the trend observed in Fig. 4.5, where a flight path angle of  $14^\circ$  was observed to change the vehicle drag to thrust by less than  $0.4^\circ$ .

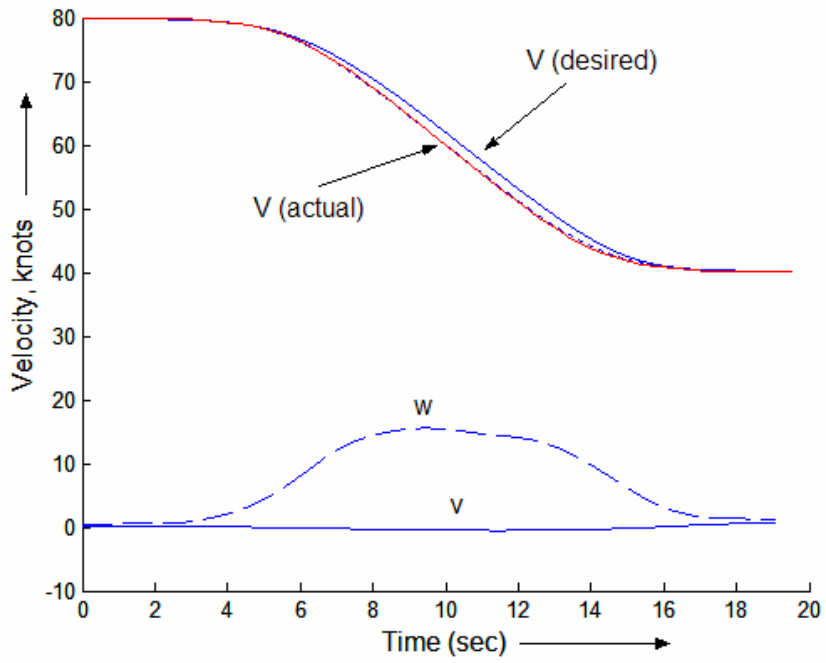


Figure 4.17 Velocity profile along the “quick stop” maneuver.

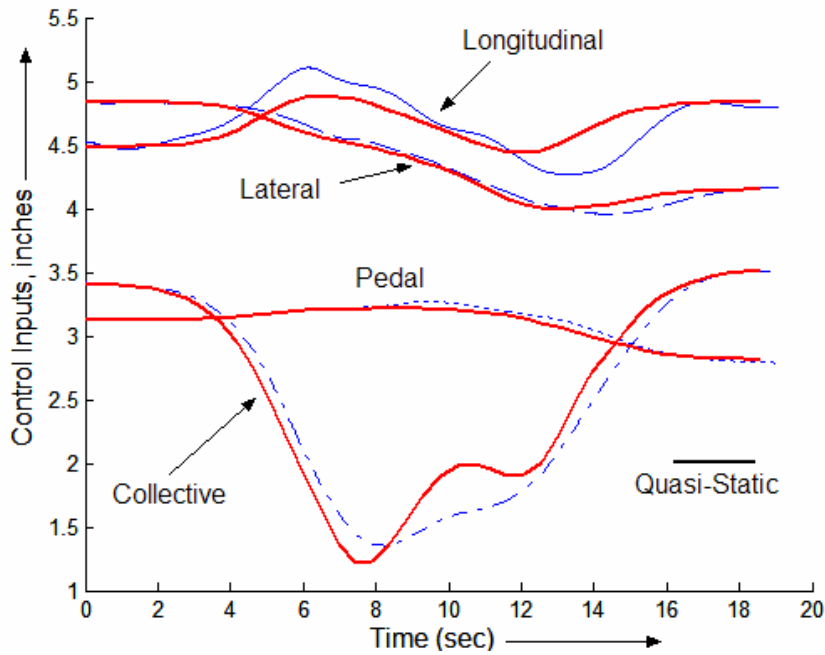


Figure 4.18 Variation of Control input requirements along the “quick stop” maneuver.

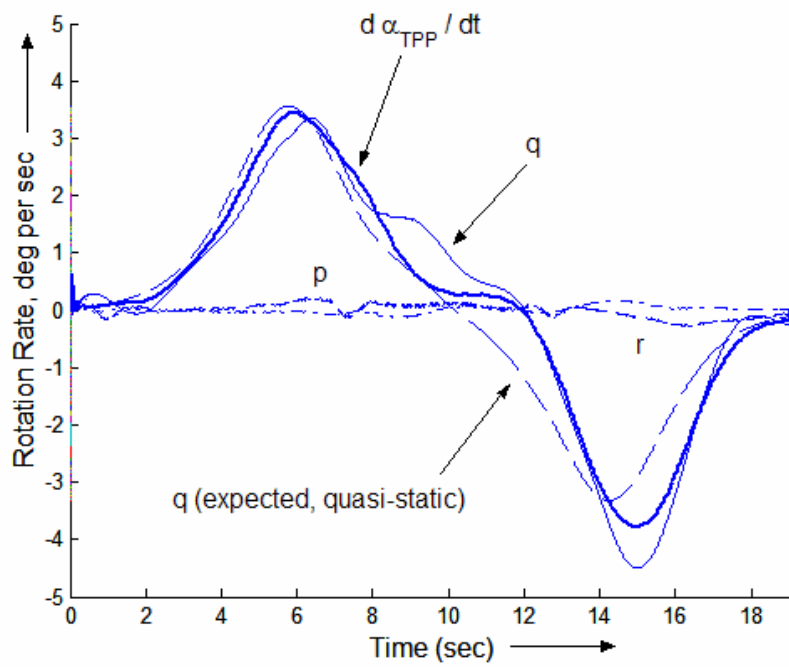


Figure 4.19 Variation of body and tip-path plane rotation rates along the “quick stop” maneuver.

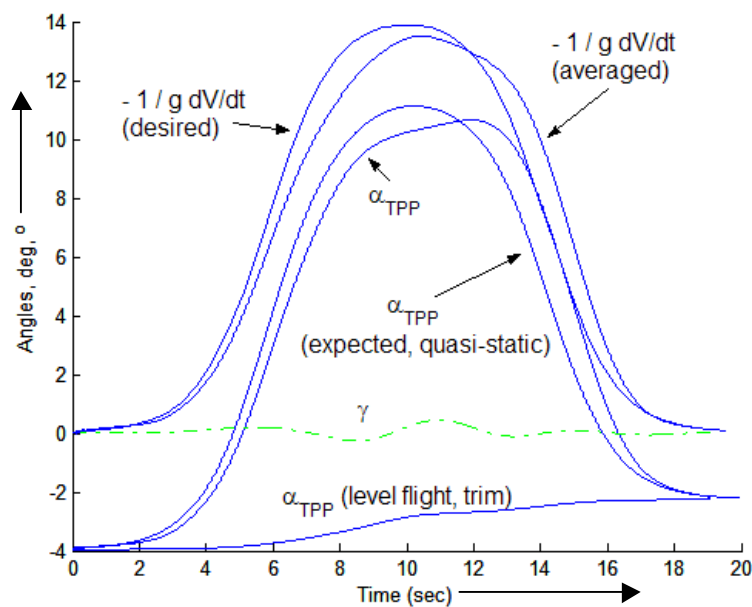


Figure 4.20 Variation of tip-path plane angle, deceleration in g's and flight path angle along the “quick stop” maneuver.

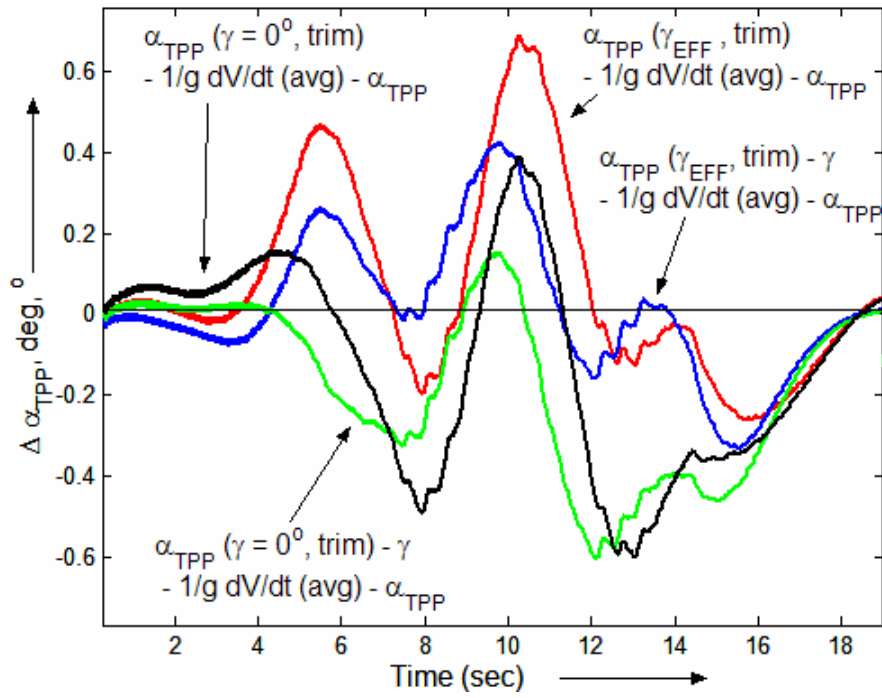


Figure 4.21: Errors in tip path plane estimation based on the quasi-static assumption, for the “quick stop” maneuver results.

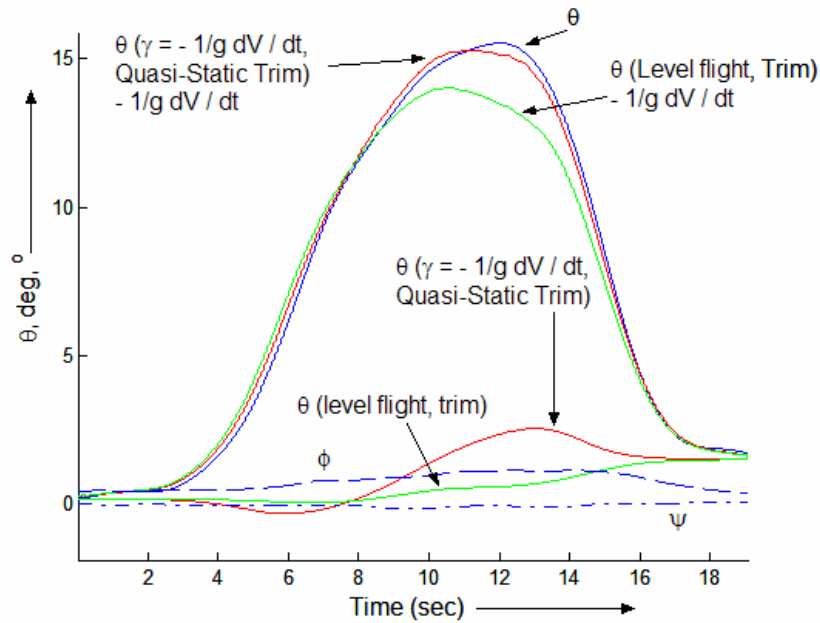


Figure 4.22 Variation of Euler angles along the “quick stop” maneuver, along with the corresponding level flight trim and quasi-static values of fuselage pitch attitude.

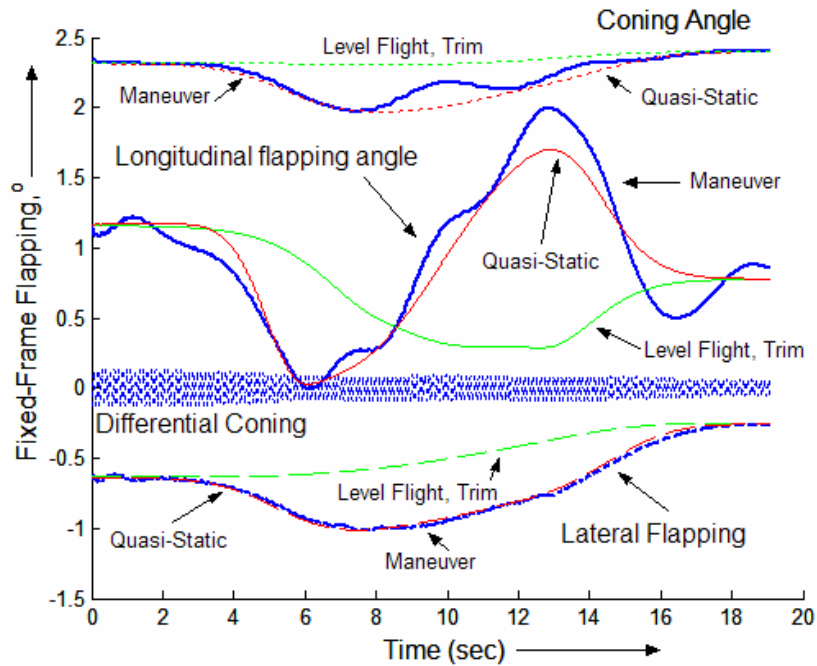


Figure 4.23 Variation of main rotor flapping angles along the “quick stop” maneuver. Corresponding level flight trim and quasi-static values are also shown.

Figure 4.22 shows the variation in Euler angles along the trajectory. The yaw and roll angles are seen to remain small. The control of lateral dynamics using near quasi-static pedal and lateral stick controls is successful even for this “quick stop maneuver”. The effect of changes in flight path angle on the pitch attitude is now noticeable: about  $2^\circ$  when the flight path angle changes by about  $15^\circ$ . Therefore, while the tip-path plane angle estimates can be based on level flight trim values alone, fuselage angle of attack must be based on the quasi-static trim values at the effective flight path angle, for  $\gamma_{EFF} > 10^\circ$ :

$$\theta_{TPP} \approx \theta_{TPP}^{SS} \Big|_{\gamma=0} - \left( \frac{\dot{V}}{g} \right)_{avg}$$

$$\theta_F \approx \theta_F^{SS} \Big|_{\gamma=\gamma_{EFF}} - \left( \frac{\dot{V}}{g} \right)_{avg}$$

Figure 4.23 shows the variation of fixed-frame rotor flapping characteristics compared with corresponding trim and quasi-static values. The difference between the trim and quasi-static values, essentially an effect of flight path angle on longitudinal flapping angles, is quite noticeable for the longitudinal flapping (almost 1.5°). The difference between quasi-static and maneuver value is the effect of the additional rotation rates during the maneuver. This can be clearly evidenced in the longitudinal flapping characteristics.

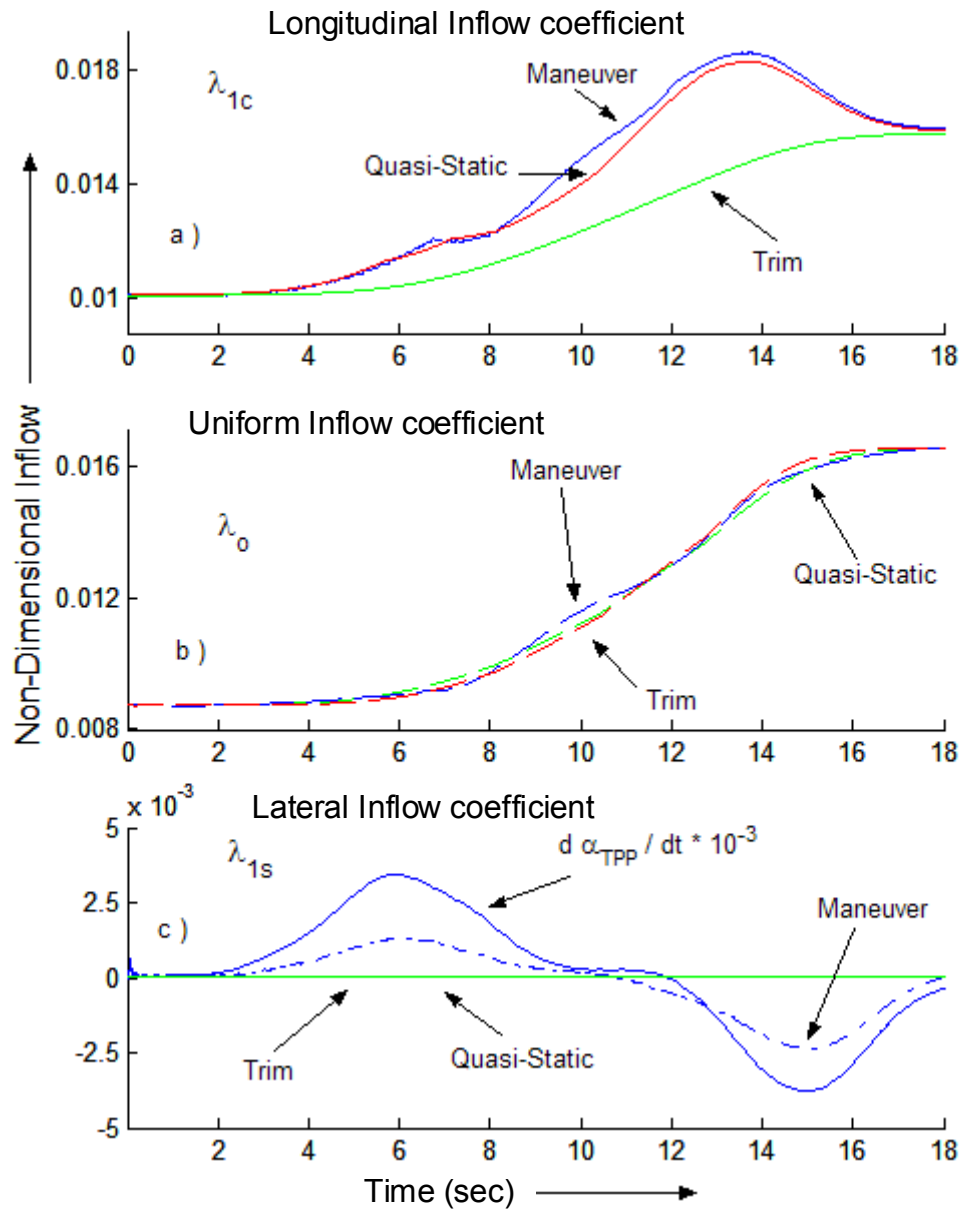


Figure 4.24 Variation of non-dimensional dynamic inflow (induced velocity) coefficients along the “quick stop” maneuver. The corresponding level flight trim and quasi-static values are also shown.

Figure 4.24 shows the variation of dynamic induced velocity components along the maneuver. The effect of pitch rate is now perceptible on these induced velocity

coefficients, during the transient maneuver stage. The lateral induced velocity coefficient shows a marked effect that is proportional to the tip-path plane pitch rates observed (Fig 4.19). Blade-vortex interaction miss-distances are sensitive to changes in lateral inflow distributions, and this is considered to be a limiting consideration in the application of the quasi-static acoustic equivalence.

### **4.3 Longitudinal Maneuver Results : Lower Order Modeling**

Various longitudinal maneuvers are now studied and developed using the lower order models described in Chapter 3. Longitudinal maneuvers are defined as transitions from one longitudinal trim state to another within the same longitudinal plane. Such maneuvers can be described by the associated  $V(t)$  and  $\gamma(t)$  profiles along the maneuver. Three different longitudinal maneuvers are studied:

1. “Slow” deceleration maneuver,
2. Flight path angle transition maneuver, and
3. Constant effective flight path angle maneuver.

These three maneuvers are briefly described next. The slow deceleration maneuver, studied in the previous section, is a straight-line controlled deceleration from a trim state at one flight velocity to another. The flight path angle is held fixed along the trajectory. Velocity and acceleration profiles are prescribed using the mathematical functions developed in section 3.5. The flight path angle transition maneuver consists of a transition from a steady-state trim state at one flight path angle to another at the

same flight velocity. Flight velocity remains approximately constant along such a trajectory. A flight velocity variation function is assumed based on the functions presented in section 3.5. Finally a constant effective flight path angle maneuver is presented. This maneuver effectively combines both changes in flight path angles and vehicle deceleration along the trajectory such that the effective flight path angle remains fixed. These maneuvers are used to study tip path plane performance during slowly maneuvering longitudinal flight.

#### **4.3.1 Slow Deceleration Maneuver Results: Lower Order Modeling**

Sample deceleration maneuvers are now implemented for the Bell206-B model, using the second and fourth order models developed in the previous chapter. The results from the inverse simulation are presented in this section.

Figure 4.25 shows the variation of flight parameters during a decelerating trajectory (Fig. 4.25a) with a maximum deceleration of 0.075g at a flight path angle of  $-5^\circ$ , a “slow deceleration” maneuver. Flight velocity was varied from 90 knots down to 40 knots (Fig. 4.25b). Control requirements and performance parameter variations during the maneuver both with and without pitch dynamics are compared to the corresponding trim values. Quasi-static performance calculations, both with and without pitch dynamics, give nearly identical results. “Trim” values (dash lines in Fig. 4.25) refer to the variation of flight variables at corresponding steady flight

conditions at the same flight path angle and flight velocity as the maneuvering flight condition.

To achieve this maneuver, the pilot starts by reducing collective (Fig. 4.25c) to account for the increase in inflow. The thrust coefficient reduces slightly as flight velocity reduces under trim conditions. During the transient maneuver the thrust coefficient reduces slightly (about 2%). The collective requirements during the constant deceleration maneuver itself change very little (about  $0.5^\circ$  in 10 seconds). Finally the collective is increased back to the trim value. Longitudinal cyclic requirement (Fig. 4.25d), a near linear increase, is very similar to trim values at the corresponding flight velocities along the trajectory.

The effect of deceleration is to make the tip-path plane angle more positive (Fig 4.25f), which increases inflow up through the rotor disk (Fig 4.25i). The helicopter pitch follows this variation in the tip-path plane and the helicopter pitches nose up during this maneuver (Fig 4.25g). Compared to this helicopter pitch variation during the maneuver, the pitch values at the equivalent steady state flight conditions (shown as the dash line in Fig. 4.25g) are much lower (less nose-up). As the velocity decreases, the tip-path plane angle and the pitch attitude continue to become more positive. However, inflow up through the rotor disk decreases as flight velocity reduces (Fig 4.25i), because the induced velocity increases. Finally, when the level of deceleration reduces down to zero, the trim condition at the lower velocity is achieved, and both the tip-path plane and the helicopter pitch reduce to trim values.

The pitch rates encountered during this maneuver are shown in Fig. 4.25h and seen to be relatively small. The pitch rate associated with the tip-path plane angle is seen to be of the same order. The maximum pitch rates are experienced during the transient stage of the maneuver) ( $|q/\Omega| < 4 \times 10^{-4}$ ), when the level of deceleration is either increasing or decreasing. During the steady deceleration phase the pitch rates are an order of magnitude lower ( $|q/\Omega| < 5 \times 10^{-5}$ ).

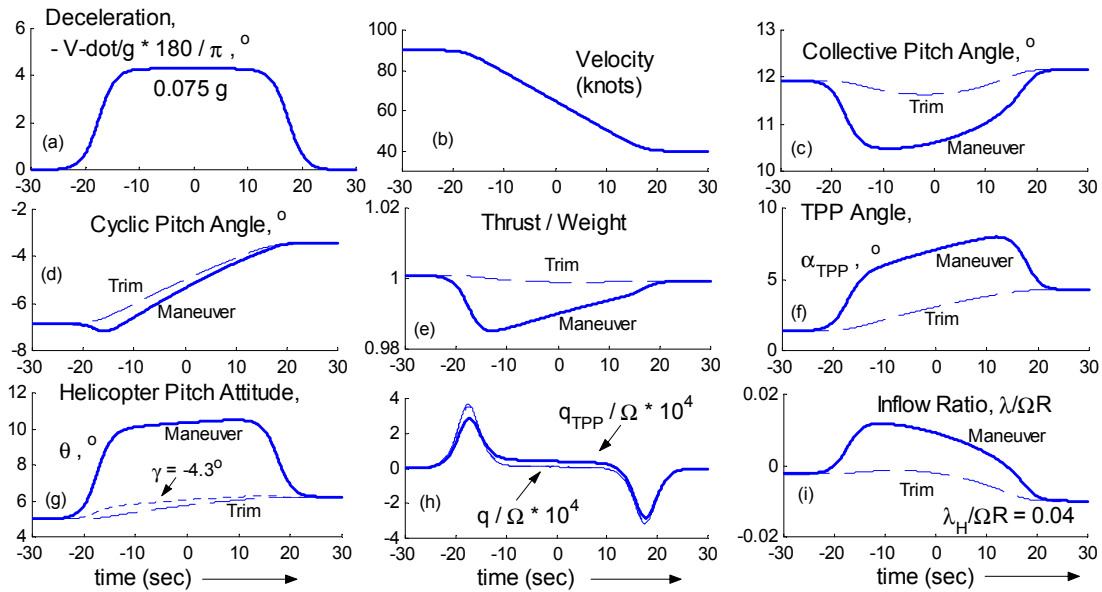


Figure 4.25 The “Slow Deceleration” Maneuver: Variation of performance and control parameters.

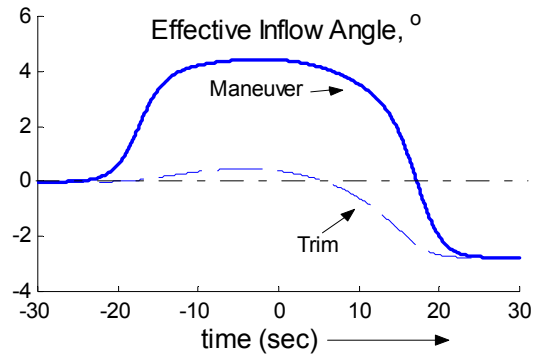


Figure 4.26 The “Slow Deceleration” Maneuver: variation of effective inflow angle.

Figure 4.26 shows the variation of the effective inflow angle during the maneuver. A zero value at the beginning of the maneuver indicates that the main-rotor is operating close to the maximum BVI condition at a velocity of 90 knots and a flight path angle of  $-5^\circ$ . As the helicopter decelerates, the effective inflow angle increases to about  $4^\circ$ , which results in a significant reduction in radiated BVI noise. As the flight velocity and the level of deceleration reduce towards the end of the maneuver, the effective inflow angle crosses  $0^\circ$ , the maximum BVI condition at that velocity. Finally as the helicopter approaches the steady flight condition at 40 knots, the effective inflow angle becomes negative and the BVI noise reduces again. A  $-5^\circ$  approach at 40 knots ( $\mu = 0.098$ ) does not correspond to maximum BVI noise radiation.

Figure 4.27 shows results for an idealized  $0.5g$  “extreme quick stop” maneuver. A velocity reduction of 50 knots is achieved in a little over 10 seconds. A theoretically estimated change in tip-path plane angle and helicopter pitch attitude of more than

25° is observed. This maneuver would be considered quite extreme, and would be associated with higher order dynamics, none of which, of course, are captured by this lower order model. The inverse simulation procedure using the lower order model serves to provide an idealized solution, that approximates the higher order solution well for slow maneuvers, but provides unachievable idealized solutions for extreme maneuvers. The pitch rates associated with the fuselage and tip-path plane are seen to be of the order of 40° per sec. These maximum pitch rates estimated by the lower order models can be used as a criterion for establishing quasi-static limits for different maneuvers.

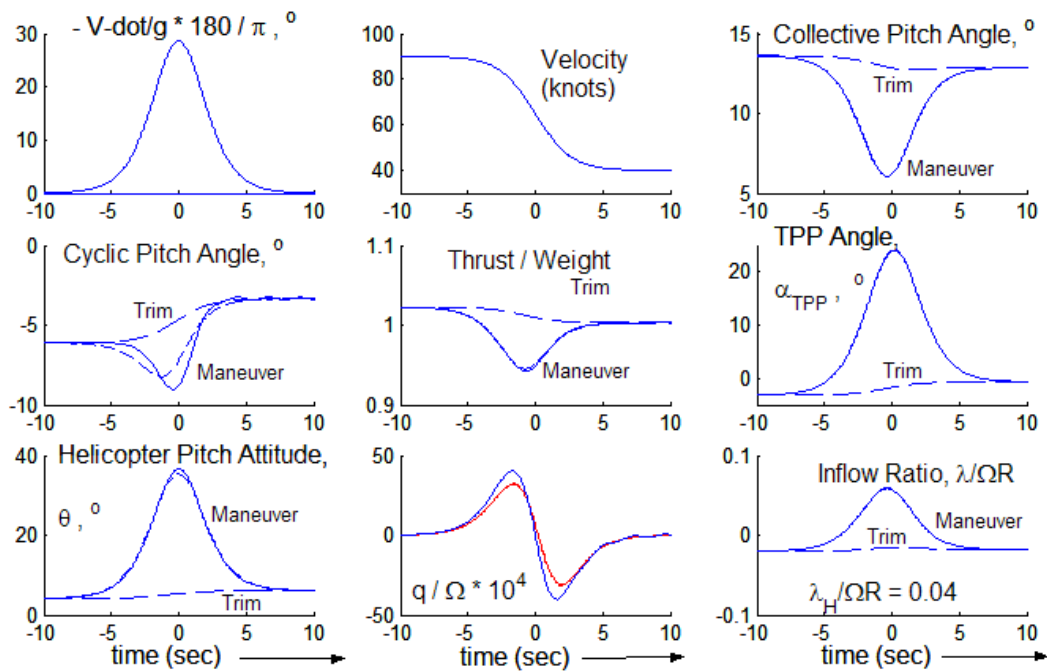


Figure 4.27 The “Quick Stop” Maneuver: Variation of performance and control parameters.

### 4.3.2 Flight Path Angle Transition Maneuver Results: Lower Order Modeling

The flight path angle is varied from one trim value to another at the same flight velocity (Fig. 4.28). A “sigmoidal” variation in the flight path angle is prescribed (Fig. 4.28a and Equation 3.45, Section 3.5) while holding the flight velocity fixed at 70 knots. Figure 4.28 shows the effect of this maneuver on flight parameters for a maximum acceleration of 0.05g perpendicular to flight path (Fig. 4.28b).

The collective pitch is the primary control for this maneuver. It is reduced to account for the increase in inflow (Fig. 4.28c). The collective requirements during the maneuver are lower than the corresponding trim values to account for the reduction in thrust (Fig. 4.28e). The cyclic pitch changes by about  $0.5^\circ$  during the entire maneuver, and the variation is nearly identical to the corresponding trim values (Fig. 4.28d). The variation of thrust (Fig. 4.28e) follows the variation of the acceleration perpendicular to flight path. The tip-path plane increases in a quasi-static manner as the flight path angle becomes more negative (Fig. 4.28f). The pitch rate associated with the fuselage and the tip-path plane are seen to be small ( $|q / \Omega| < 10^{-4}$ ).

During this maneuver, the inflow through the rotor disk increases progressively (Fig 4.28i) with very small changes in pitch rate or advance ratio. This means that for such slow flight path angle transitions, the inflow through the rotor disk is set by the instantaneous flight path angle. While the initial and final trim states are associated with relatively low BVI noise, peak BVI noise radiation would occur at an

intermediate flight path angle (between  $-4^\circ$  and  $-5^\circ$ ). This is further illustrated by the variation of the effective inflow angle (Fig. 4.29). A close to zero value near time  $t = 0$  ( $\gamma = -4^\circ$ ), indicates the maximum average radiated BVI noise condition.

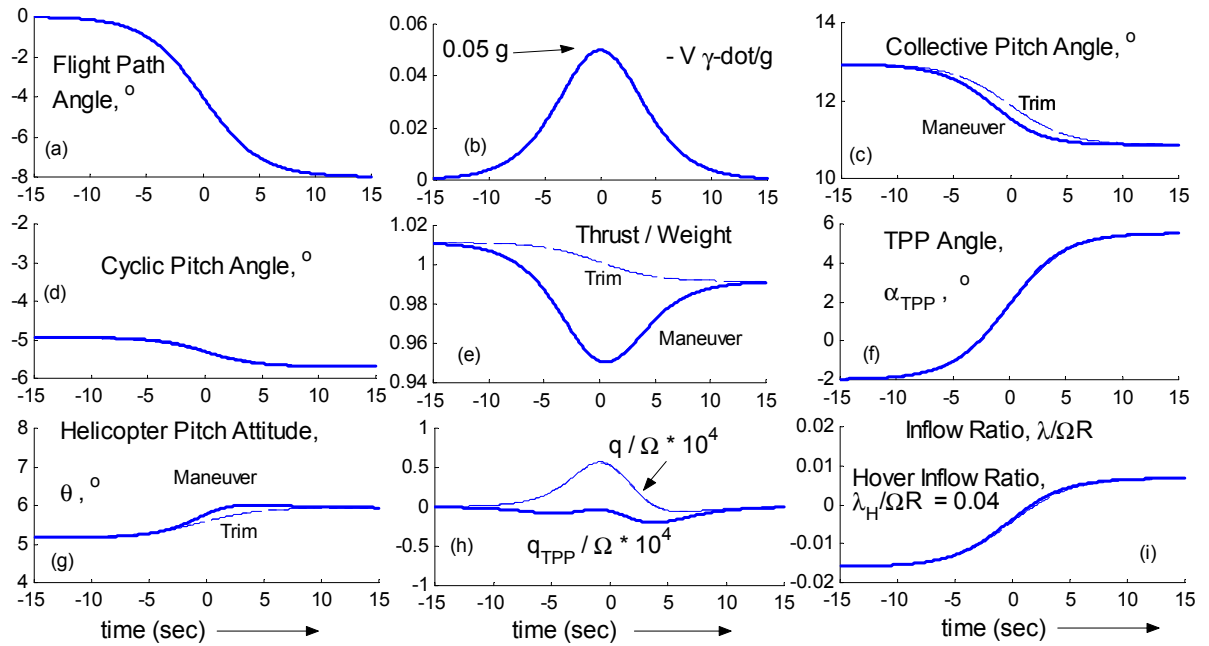


Figure 4.28 Performance parameter variations during the flight path angle transition maneuver at 70 knots.

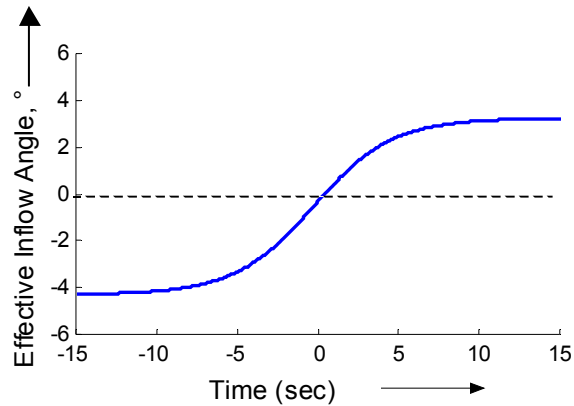


Figure 4.29 The “Flight-Path Angle Transition” Maneuver: variation of effective inflow angle.

#### 4.2.3 Constant “ $\gamma$ -effective” maneuver results: Lower level modeling

A constant effective flight path angle ( $\gamma + \dot{V}/g$ ) maneuver is designed in this section (Fig. 4.30) as a possible candidate trajectory for flight test validation. In this maneuver the sum of the descent angle in radians and the deceleration in g’s is held fixed. The pilot begins the maneuver from a trim condition at a given flight path angle. From that trim state the pilot may maneuver the helicopter into any slowly decelerating condition such that the effective flight path angle ( $\gamma + \dot{V}/g$ ) is constant – in other words the helicopter controls are used to trade changes in flight path angle for changes in the helicopter deceleration. Further, it is assumed that the rate of change of flight path angle and deceleration are very small. This ensures that the pitch rates and the changes in thrust coefficient remain small during the maneuver.

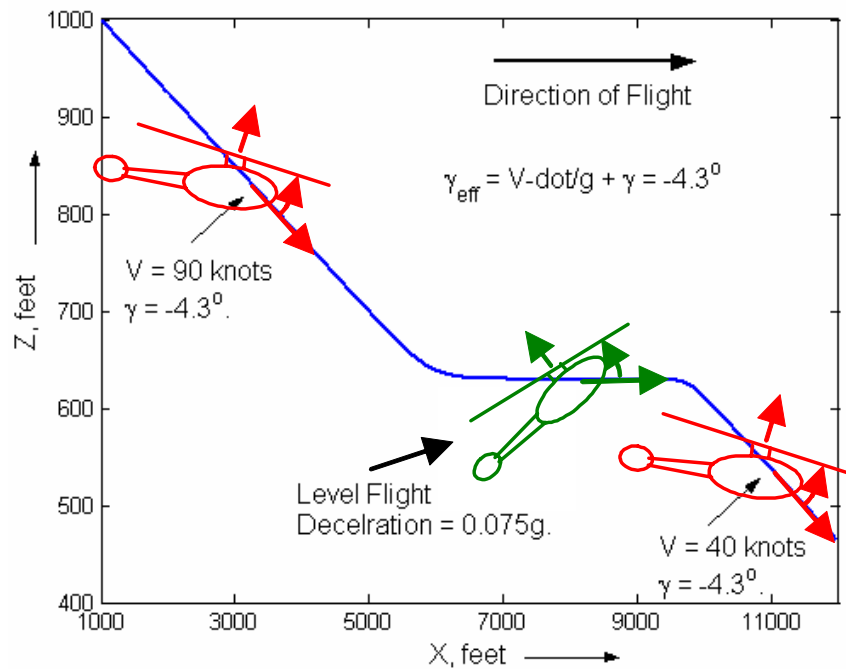


Figure 4.30 The “ $\gamma$ -effective” maneuver.

Such a sample flight trajectory, with an effective flight path angle of  $-4.3^\circ$ , is shown in Fig. 4.31. The trajectory begins with steady descent at a  $-4.3^\circ$  glide slope at 90 knots (Fig 4.31a). The pilot then flattens the flight path to level flight at very low load factors (Fig. 4.31b) while reducing flight velocity. Collective input changes very little (Fig 4.31c). The cyclic pitch input is the primary control (Fig. 4.31d). The helicopter continues to decelerate at a constant rate of  $0.075g$  for about 20 seconds. Finally the level of deceleration is reduced in conjunction with a corresponding increase in descent angle, till a descent angle of  $-4.3^\circ$  at a constant flight velocity are achieved. The effective inflow angle remains close to zero during the first half of the maneuver

(Fig. 4.32), but becomes progressively more negative as the flight velocity reduces below 60 knots.

By starting at a chosen descent angle, the level of deceleration for the maneuver at level flight is intrinsically chosen. The entire maneuver is then performed with very small changes in collective. Relative to the tip-path plane the noise radiation characteristics of the helicopter during this maneuver would correspond to a change in velocity at a fixed flight path angle.

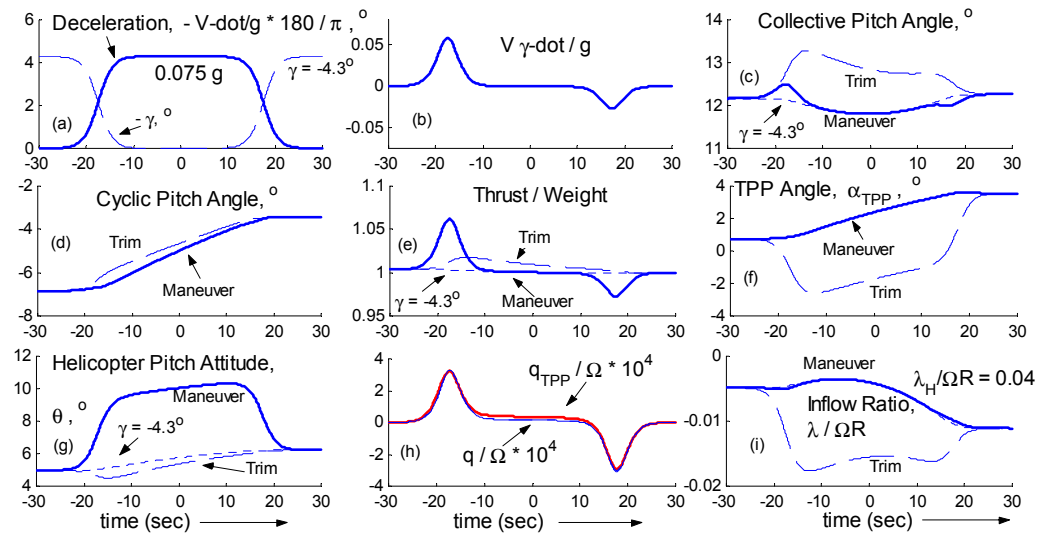


Figure 4.31 The “ $\gamma$ -effective” maneuver – variation of performance parameters.

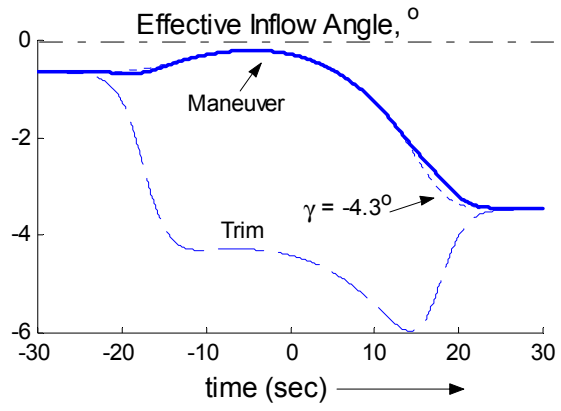


Figure 4.32 The “ $\gamma$ -effective” Maneuver: variation of effective inflow angle.

## **Chapter 5**

### **Flight Trajectory Management of Helicopter BVI Noise**

This chapter deals with the control of BVI noise radiation through flight trajectory management and vehicle design changes. The effects of changes in flight velocity, flight path angle, deceleration along the flight path, vehicle design changes and longitudinal winds are assessed on ground noise radiation. A new methodology for flight trajectory control of BVI noise, which incorporates the important quasi-static effect of slow longitudinal maneuvers on BVI noise radiation is developed and implemented. Piloting techniques and flight trajectories that reduce BVI ground noise radiation are investigated. The effect of piloting choices under steady wind conditions are evaluated in terms of its effect on BVI noise radiation and ground noise exposure.

#### **5.1 The Quasi-Static Acoustic Mapping (Q-SAM) Technique**

A new method that capitalizes on the advantages of quasi-static performance modeling of rotor performance states and the storage-based acoustic mapping approach is proposed. This method, conceptually depicted in Fig. 5.1, is called the “Quasi-Static Acoustic Mapping” technique [56, 72]. This method is implemented

and used to assess the ground noise exposure associated with longitudinal trajectories in section 5.2. Section 5.3 assesses the important effect of steady headwind and tailwind on noise radiation and ground noise exposure using the Q-SAM method.

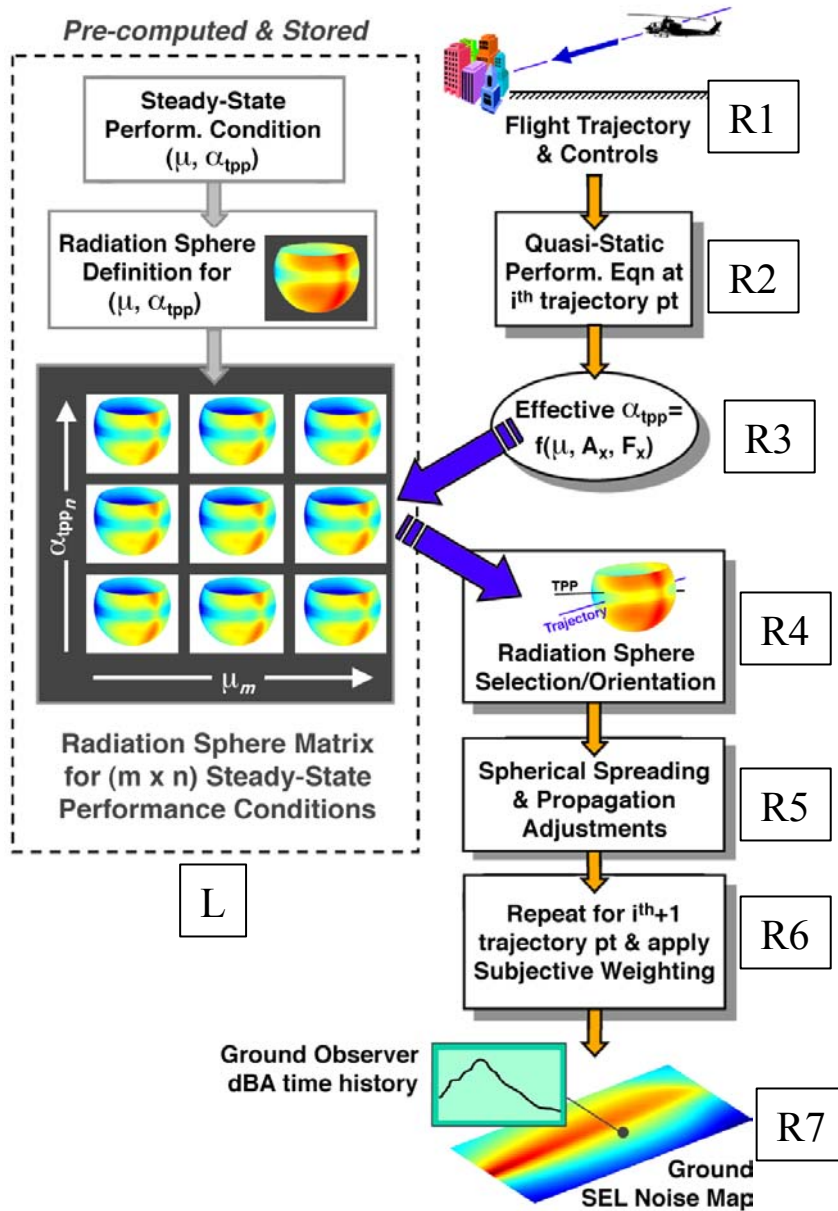


Figure 5.1 Schematic of the Quasi-Static Acoustic Mapping Technique.

The Q-SAM method is based on the concept that the noise, produced when a rotorcraft undergoes small changes from steady-state equilibrium flight, can be represented by the noise that is produced by a rotorcraft operating at an equivalent, but different, steady-state operating condition. This acoustical equivalence is defined in terms of the key non-dimensional variables of the individual noise source being modeled. The power of the Q-SAM method depends upon the existence of an equivalence relationship between steady-state and maneuvering flight. The Quasi-Static Acoustic Mapping (Q-SAM) method combines the best features of both a steady-state acoustics database storage based approach and first-principles based approaches in an attempt to estimate the noise radiation during slowly maneuvering flight.

Conceptually, the Q-SAM method interpolates a measured or predicted set of acoustic data taken in trimmed level steady-state flight to equivalent quasi-static conditions (the non-dimensional flight variables governing acoustic radiation), and then maps the resulting acoustics at these equivalent conditions to positions on the ground. The method is most accurate for small accelerations, which are typical for helicopter landing/approach trajectories.

This method relies on a database of stored steady-state BVI noise radiation characteristics (left hand side of Fig. 5.1). This steady-state acoustic data can be obtained either through experimental measurements or through analytical modeling, or a combined “data fusion” approach. The development of this acoustic database is

conducted “offline”. This acoustic database is stored as a function of the non-dimensional parameters that govern the particular noise source of interest. In the case of BVI noise, which is the subject of the present study, the governing non-dimensional parameters are Thrust Coefficient  $C_T$ , Hover Tip Mach Number  $M_H$ , advance ratio  $\mu$  and the tip-path plane angle  $\alpha_{TPP}$  [14].

The actual process of estimating the acoustic radiation associated with any flight trajectory comprises of three steps:

1. Determination of vehicle trim state along the trajectory,
2. Radiation sphere selection, and
3. Ground noise estimation.

These steps are briefly described next. The longitudinal flight parameters, flight velocity, flight path angle, vehicle acceleration and equivalent flat plate area along a trajectory are used to determine the main rotor performance parameters that govern BVI noise radiation: Thrust Coefficient  $C_T$ , Hover Tip Mach Number  $M_H$ , advance ratio  $\mu$  and the tip-path plane angle  $\alpha_{TPP}$ . If  $C_T$  and  $M_H$  are assumed constant (typical assumptions for a specific helicopter during landing approach), BVI noise can be expressed as a function of two variables – advance ratio,  $\mu$  and tip-path plane angle,  $\alpha_{TPP}$ . These main rotor performance parameters, that under the current set of assumptions, completely determine BVI noise radiation, are used to pick out a sphere from the database that best represents the associated acoustic radiation. After this sphere selection process, it is correctly positioned and oriented along the trajectory and atmospheric and acoustic propagation tools are used to map these noise levels on the ground (Fig. 5.2). This process is repeated along the trajectory to obtain a Sound

Pressure Level (SPL) time history on the ground. These noise levels are processed to obtain various noise metrics that are then used to assess the acoustic radiation characteristics of the associated trajectory. Some implementation details of the model developed for this research are discussed in Appendix C.

The ground noise mapping procedure essentially consists of two distinct parts – source noise estimation (the left hand side of Fig. 5.1, and “R1” through “R4”) and the propagation of noise to the ground (essentially the right hand side of Fig. 5.1, “R5” through “R7”). The Q-SAM technique emphasizes the importance of source noise estimation, its underlying physics and selection of appropriate noise radiation characteristics from the database based on the governing parameters of the noise source (or sources) under consideration (boxes “L” and “R1” through “R4” in Fig. 5.1). In this regard there are two major features associated with the proposed Q-SAM technique that distinguish it from existing acoustic mapping techniques in use today:

1. The noise radiation is expressed and stored as a function of the governing non-dimensional variables rather than the flight conditions.
2. The quasi-static effect of vehicle acceleration / deceleration on the tip-path plane angle is explicitly accounted for.

Similarly to the “acoustic mapping” method, an important advantage of using the Q-SAM method with experimentally acquired acoustic data is that it implicitly captures the detailed aerodynamics of BVI that are normally quite difficult to predict from direct calculations.

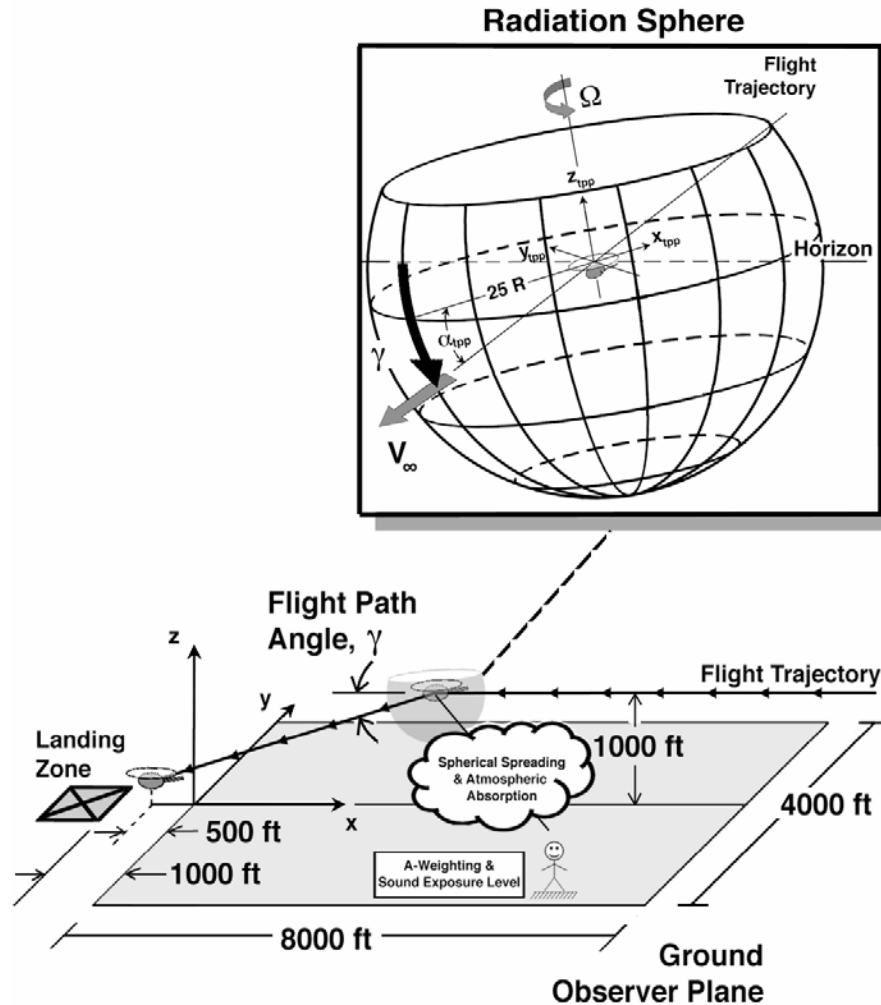


Figure 5.2 An illustration of the storage based acoustic mapping approach to the evaluation of ground noise metrics associated with flight trajectories.

### 5.1.1 Major Assumptions

Several simplifying assumptions are made in the current implementation of the Q-SAM technique. The goal of the current research is a basic physical understanding of BVI noise radiation, and the associated ground noise exposure trends. The effect of

only main rotor BVI noise is considered in the present study. BVI noise is assumed to be a function of the four non-dimensional variables shown below:

$$C_T \equiv \frac{W}{\rho_o A (\Omega_o R)^2} \equiv \text{Constant}$$

$$M_H \equiv \frac{\Omega_o R}{a_o} \equiv \text{Constant}$$

$$\mu \equiv \frac{V}{\Omega_o R}$$

$$\alpha_{TPP} \equiv -\frac{D_{EFF}}{W} - \gamma - \frac{\dot{V}}{g} \approx -\frac{1}{2} \rho V^2 \frac{f_x}{W} - \gamma - \frac{\dot{V}}{g} = f\left(V, \gamma, \frac{\dot{V}}{g}, f_x\right)$$

(5.1)

The above expressions highlight several other underlying simplifying assumptions. The main rotor thrust is assumed equal to weight throughout the present study. The density of air is assumed constant and equal to the standard sea level value. Main rotor RPM is assumed fixed. A nominal value of the sonic velocity is assumed throughout this study, based on standard sea level conditions. The thrust coefficient and hover tip Mach number, therefore, are assumed to be constant along a trajectory for a particular helicopter in the current implementation, and helicopter BVI noise is assumed to be a function of only two non-dimensionalized variables: advance ratio and the quasi-steady tip-path plane angle, which explicitly includes the effects of deceleration parallel to the flight path. It should be noted that in actual “steady-state” flight, the main rotor thrust does change slightly with changes in flight velocity, flight

path angle and fuel weight. Also changes in atmospheric conditions, like temperature and density, would alter both Hover Tip Mach number and Thrust Coefficient. Changes in rotor RPM due to atmospheric gusts or changes in pilot inputs are also ignored. Changes in thrust coefficient are usually small enough not to significantly impact the BVI noise radiation process, but the effect of changes in temperature on hover tip Mach number could potentially be a significant effect.

The effect of vehicle acceleration parallel to the flight path on the tip-path plane angle is assumed to be quasi-static. The higher order effects of tip-path plane rotation rates on wake distortion and the associated change in BVI noise radiation are ignored. It is implicitly assumed that the flight operations considered are within the bounds of the quasi-static assumption. “Small” decelerations ( $< 0.1g$ ) are assumed. The rate of change of deceleration is also assumed to be small ( $< 0.01$  g per sec).

Drag by weight of the helicopter is approximated by the equivalent flat plate area. Additional drag due to deployable X-Force devices [49] is accounted for by a simple increase in the equivalent flat plate area of the fuselage.

Atmospheric effects like changes in temperature, gusts, wind shear, on BVI noise radiation is ignored. Standard steady sea level conditions are assumed. The effect of spherical spreading and atmospheric absorption is accounted for. The effect of atmospheric absorption is accounted for based on the ANSI standard (Appendix C

[102]). A nominal humidity of 40% is assumed. The effect of ground attenuation and other surface effects are ignored.

This idealized model is a natural complement to higher level storage based noise mapping approaches like RNM [60, 61]. Without the smearing effect of higher order atmospheric and ground effects on ground noise, a fundamental cause and effect relationship between noise radiation and ground noise exposure can be obtained using the Q-SAM technique in its current implementation. This lends considerable physical insight into the ground noise exposure trends associated with helicopter descent operations.

### **5.1.2 Steady State BVI noise: Storage and Representation**

The development of the acoustic database is of course critical to this acoustic mapping procedure. Again, if Hover Tip Mach Number  $M_H$  and Thrust Coefficient  $C_T$  are assumed constant (typical assumptions for a specific helicopter during landing approach), steady-state BVI noise can be expressed as a function of two variables – advance ratio,  $\mu$  and tip-path plane angle,  $\alpha_{TPP}$ . For each combination of  $\alpha_{TPP}$  and  $\mu$  an acoustic radiation hemisphere is obtained. This hemisphere is either computed or measured (from flight or wind-tunnel testing) and stored in the database. These hemispheres of stored BVI noise form the radiation sphere matrix from which the acoustic radiation at any point in space can be computed for the helicopter in steady-state flight.

In the present research, the radiation spheres are developed using the analytical modeling introduced in chapter 2. The acoustic radiation spheres represent a spherical map of the acoustic energy radiated by the helicopter over one rotor revolution. In the current work, radiation spheres or the mapping surfaces are assumed to be fixed to the medium. No transformations of the acoustic data (in terms of additional Doppler amplification effects) are required while mapping the noise to the ground under no-wind conditions because the ground observers are stationary with respect to the medium. For hub-fixed radiation spheres moving with the helicopter, the situation is similar to measurements made in a wind-tunnel, and the acoustic information has to be appropriately transformed before it can be propagated to the ground. A no wind condition is assumed at this initial stage.

A model of the full-scale AH-1 helicopter is used for this study, and is used throughout this chapter. Some relevant rotor geometry and operational parameters for this study of the AH-1 helicopter are summarized in Table 5.1.

AH-1 Helicopter Parameters		
Number of Blades	N	2
Blade Radius	R	22 ft
Blade Chord	c	2.2 ft
Angular Rotation	$\Omega$	324.35 RPM
Hover-Tip Mach Number	$M_{HT}$	0.664
Thrust Coefficient	$C_T$	0.0054
Equiv. Flat Plate Area	f	14 ft <sup>2</sup>
Helicopter Weight	W	10,600 lb

Descent Parameters		
Advance Ratio (Velocity)	$\mu$ (V)	0.120 (53 knots) – 0.210 (93 knots)
Flight Path Angle	$\gamma$	-2° to -9°
X-Force Equiv. Flat Plate Area	$f_x$	14 ft <sup>2</sup>
Deceleration	$A_x$	0.05g, 0.10g

Table 5.1 AH-1 helicopter geometry and flight parameters.

The mapping surface is chosen to be a radiation sphere centered on the acoustic event in inertial space and located 25 rotor radii from its effective source point (Fig. 5.3). The spherical shape allows the radiation sphere to capture the complete directivity of the noise and also facilitates the projection of that directivity to positions on the ground plane. The large distance from the effective source point insures that this radiation sphere only captures far-field acoustic radiation. Once the far-field acoustic radiation is captured (or predicted) on the radiation sphere, it can be related to larger or smaller radiation spheres by using far-field scaling laws that also account for the effects of atmospheric corrections.

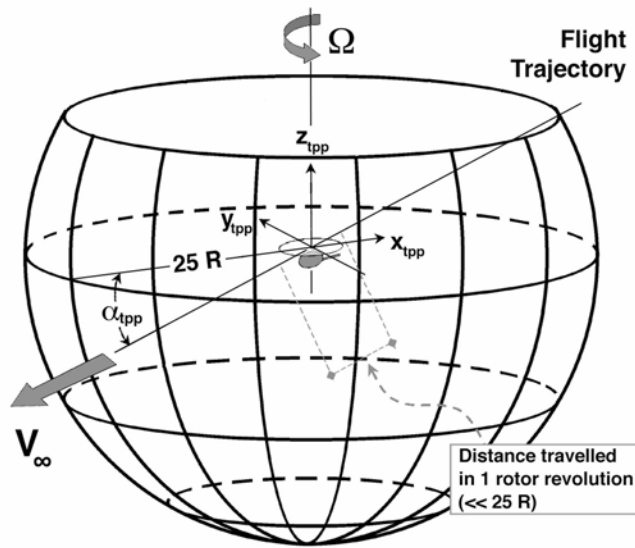


Figure 5.3 Radiation sphere used in the Q-SAM method

Although it is acknowledged that unsteady 3-D aerodynamics can be quite important for accurately predicting impulsive BVI events, the airloads are evaluated by using only quasi-steady, 2-D aerodynamics (strip theory). This simplified modeling was found to provide generally good agreement in the BVI noise trends for the AH-1 helicopter [73]. It is expected that the same modeling would be good enough to discern the changes in BVI noise due to changes in the rotor's operating states. Because a quasi-steady aerodynamics model, along with a prescribed rotor wake geometry, is used to approximate the unsteady blade air-loads induced by the BVI events, the predicted noise levels shown in this dissertation must be viewed on a relative basis, and not in absolute terms.

The BVI radiation sphere acoustic calculations made, with the helicopter in steady-state trimmed flight, contain the noise information needed for the Q-SAM method. For a given tip-path-plane angle and advance ratio, noise radiation time histories are generated for a period of one rotor revolution for each point on the radiation sphere. Power spectra of these signals are computed and stored in the form of one-third octave band levels, for later reference, as a function of each azimuth and elevation position. This process is repeated until the radiation spheres are developed and stored for all combinations of tip-path-plane angle and advance ratio that the helicopter could possibly encounter during a landing approach.

The 2-D surface representation of the radiation spheres is shown in Fig. 5.4 using a transformation that preserves area of surface elements formed by the latitudes and longitudes, but not orthogonality of latitude-longitude intersections. Note that  $\psi =$  constant contours on the surface of the sphere are referred to as longitudes and  $\theta =$  constant contours are referred to as latitudes.

Some of the predicted BVI acoustics on the radiation spheres are illustrated in Figure 5.5a for the AH-1 helicopter at a constant approach speed of 73 knots ( $\mu = 0.165$ ). The four cases illustrate the noise radiated by the AH-1 helicopter in trim level flight, and at  $-3^\circ$ ,  $-6^\circ$  and  $-9^\circ$  flight path angles. For the four different tip-path-plane angles shown, sound pressure level (SPL) contours indicate that the most intense BVI noise occurs when the rotor tip-path-plane angle is between  $+1.63^\circ$  to  $+5.63^\circ$ . In this range of  $\alpha_{\text{TPP}}$ , the rotor is tilted back such that it is constantly operating in its own wake;

hence resulting in small miss-distance interactions and stronger BVI noise radiation. At lower and higher values of  $\alpha_{TPP}$ , the wake is displaced further away from the rotor disk. This effectively increases the blade-to-wake miss-distance and reduces the radiated BVI noise. For the series of contours shown in Figure 5.4a, the change in the directivity patterns between  $\alpha_{TPP}$  of  $+1.63^\circ$  and  $+4.63^\circ$  is attributed to a smaller miss distance at an oblique and a parallel BVI, respectively. The oblique BVI has a decelerating supersonic trace Mach number that tends to amplify noise directly ahead of the rotor, whereas the parallel BVI, with its trace Mach number profile approaching infinity, tends to amplify sound more towards the  $135^\circ$  azimuth on the advancing side. For these reasons, the peak BVI noise is observed to shift from  $180^\circ$  azimuth, directly ahead of the rotor, at lower tip-path-plane angles, to the advancing side of the rotor as the tip-path-plane angle is increased.

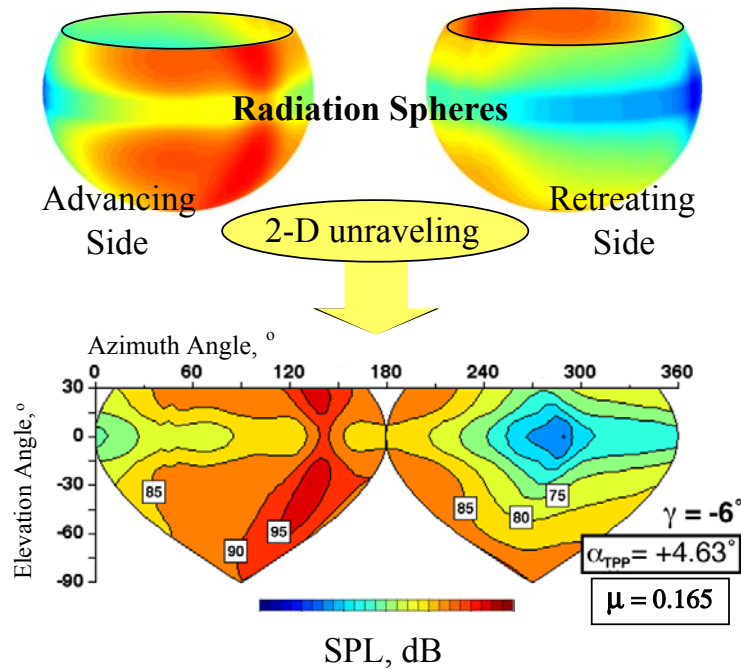


Figure 5.4 A 2-D representation of BVI radiation characteristics.

Similar noise contours are shown in Figure 5.5b for an advance ratio sweep with the tip-path-plane angle fixed at  $+2^\circ$ . At these settings, the oblique BVI with decelerating, supersonic trace Mach numbers, dominates; with most of its noise radiated directly ahead of the rotor. For the advance ratio case of 0.210, this in-phase noise radiation mechanism increases the BVI noise.

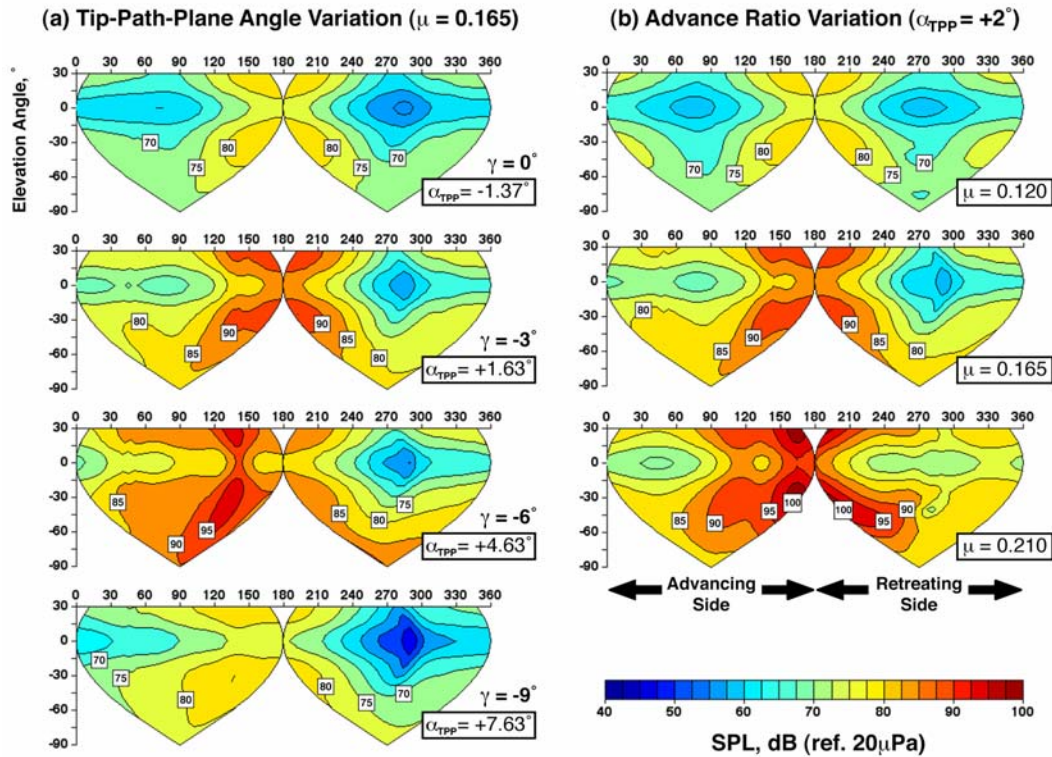


Figure 5.5 Variations of sound pressure levels on radiation spheres with: (a) tip-path-plane angle, (b) advance ratio.

The average acoustic power,  $P_{av}$  that is radiated by the rotor is defined in Equation 5.2:

$$P_{av} = 10 \log_{10} \left[ \sum_j \left( 10^{\frac{SPL_j}{10}} \cdot \frac{\Delta A_j}{A_s} \right) \right] \quad (5.2)$$

and is presented in Figure 5.6a as a function of  $\mu$  and  $\alpha_{TPP}$  for the AH-1 helicopter. This noise metric provides a measure of the spatial average acoustic energy per unit time radiated by the helicopter at any given steady or quasi-static performance state of the rotor. As shown in Figure 5.6a, the rotor tip-path-plane angle,  $\alpha_{TPP}$ , strongly influences the radiated BVI power at all airspeeds. The largest value of sound power occurs at the highest advance ratio, near  $\alpha_{TPP} = +2.5^\circ$ . As the advance ratio decreases, Figure 5.7a indicates a general decrease in the maximum sound power. At any given advance ratio, sound power has a maximum level and falls off with changes in tip-path-plane angle from that maximum level.

If acceleration parallel to the flight path is assumed to be zero, then the choice of flight path angle or rate of sink uniquely determines the steady performance-state of the helicopter. Therefore, the overall radiated power may be re-plotted versus advance ratio as shown in Figures 5.6b and 5.6c with sink rate and flight path angle on the ordinates of their respective plots. These representations are more familiar to pilots who normally use cockpit instruments to guide them as they attempt to fly noise abatement trajectories. Rate of sink,  $R/S$ , is normally displayed in the helicopter cabin as a separate dial-gauge but can also be part of an integrated display. Flight path angle, either with respect to the ground or with respect to relative velocity of the

helicopter and the air, is normally presented in an integrated display. In either presentation of the data, very similar noise patterns to figure 5.6a are noticed when advance ratio and rate of sink (Figure 5.6b), and advance ratio and flight path angle (Figure 5.6c), are used as independent variables. Figure 5.6b clearly shows that in steady-state flight, the maximum level of radiated sound power occurs at a sink rate of about 700 ft/min for all advance ratios. Thus, simply maintaining a higher or lower rate of sink than 700 ft/min for the AH-1 helicopter at airspeeds can minimize sound power radiation. Notice that the contour plot in this figure is limited by the  $-12^\circ$  descent angle line at low advance ratios. Angles steeper than  $-12^\circ$  are more difficult to fly as they have unacceptably high rates of sink at lower airspeeds and approach auto-rotation conditions.

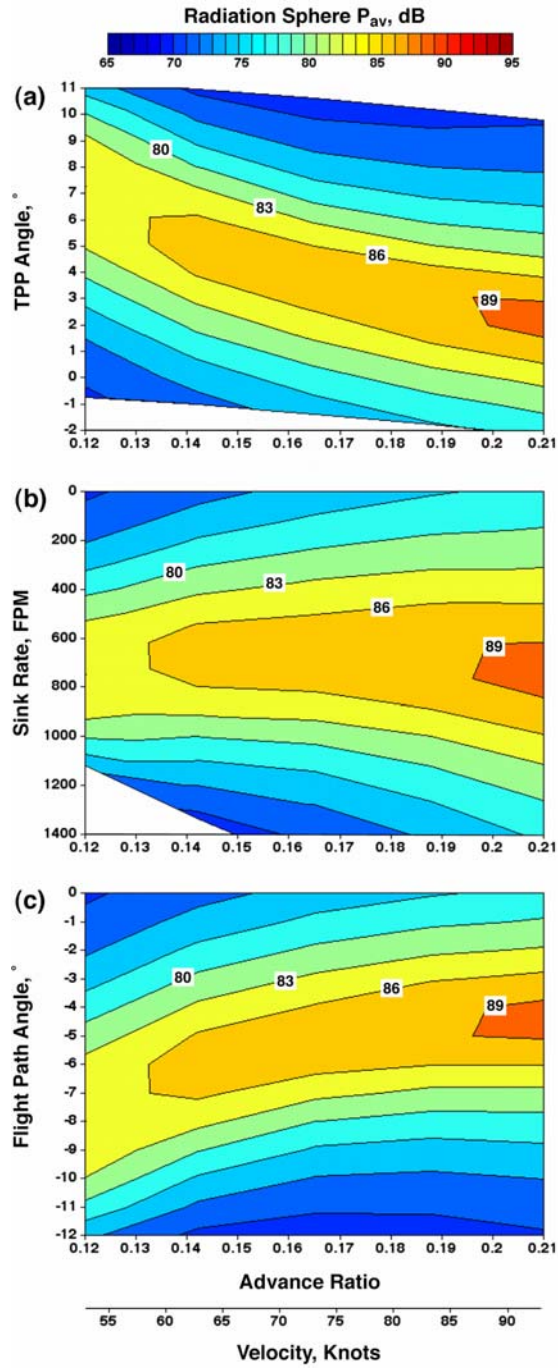


Figure 5.6 Average radiated sound power as a function of: a)  $\mu$  and  $\alpha_{TPP}$ ; b)  $\mu$  and  $R/S$ ; c)  $\mu$  and  $\gamma$

If flight path angle and advance ratio are used as the independent variables, a slightly different picture emerges as shown in Figure 5.6c. Maximum BVI noise occurs near a descent angle of  $5.5^\circ$  at high advance ratio, increasing to a descent angle of about  $7.5^\circ$  at the lowest advance ratio.

### 5.1.3 Reduction of BVI Noise Radiation

The performance analysis presented in chapters 3 and 4, related vehicle design and flight parameters to the tip-path plane angle. The tip-path plane angle was shown to be a function of the vehicle drag to weight, flight path angle and deceleration/acceleration parallel to the flight path (Equation 3.15).

$$\alpha_{TPP} \approx -\frac{D_{EFF}}{W} - \gamma - \frac{\dot{V}}{g}$$

The effective inflow angle, defined in chapter 2, can be approximated as:

$$\chi'' \approx -k \frac{v_I}{V} + \alpha_{TPP} \approx -k \frac{T}{2\rho AV \sqrt{V^2 + \lambda^2}} - \left( \frac{D_{EFF}}{W} + \gamma + \frac{\dot{V}}{g} \right) \quad (5.3)$$

In the above expression small angle assumptions have been made. If a high speed assumption is also made ( $\mu > 0.1$ ) [85], and the vehicle drag by weight is estimated

using the equivalent flat plate area, an approximate but insightful expression for the effective inflow angle results:

$$\alpha'' \approx -k \frac{T}{2\rho AV^2} - \frac{1}{2} \rho V^2 \frac{f_x}{W} - \gamma_{EFF} \quad (5.4)$$

Using a nominal value of 0.6 for the induced inflow factor  $k$ , the effective inflow angle contours for the AH-1 helicopter are plotted as a function of advance ratio and effective flight path angle in Fig 5.7. The zero effective inflow angle line is seen to correlate to the maximum average radiated BVI noise contours in Fig. 5.6.

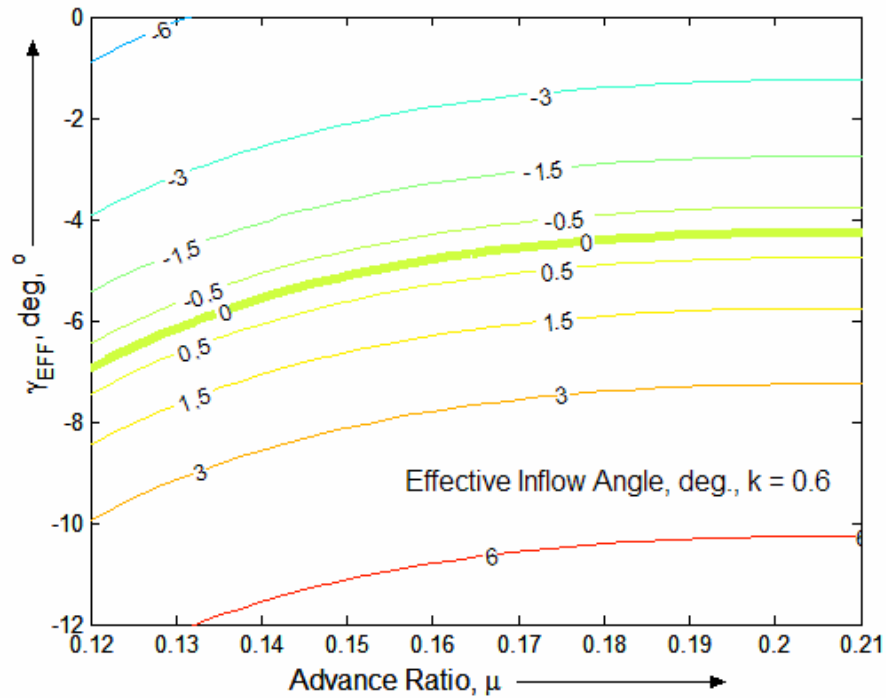


Figure 5.7 Effective Inflow Angle as a function of advance ratio and effective flight path angle for the AH-1 helicopter.

Based on these observations, several strategies that minimize radiated sound power are suggested. Negative inflow angles reduce BVI noise when the helicopter is descending at low speeds. This mode of operation keeps the rotor wake beneath the rotor disk, which increases the blade-to-wake miss-distance and reduces noise. At higher speed descents, the radiated sound power is reduced by using either a large positive inflow angle to maintain the wake above the rotor plane, or by using a negative inflow angle to keep the wake below the rotor plane. The tip-path plane angle can be reduced or made more negative by increasing the effective drag, by making the flight path angle more positive (shallow descents or climbs) and through vehicle acceleration. Conversely, a reduction in vehicle drag, steeper descent angles and vehicle decelerations result in more positive tip-path plane angles. Some of these noise reduction strategies are explored, in subsequent sections, in more detail by looking at their effects on ground noise.

#### **5.1.4 Landing Trajectories: Description and Assumptions**

The longitudinal trajectories investigated in this chapter consist of single and/or multiple approach flight segments, at some prescribed flight path angle, with either constant speed or small deceleration (up to 0.1g). The range of descent flight parameters considered in this dissertation is summarized in Table 5.1.

A rectangular ground observer plane is assumed to lie 1000 feet away from the landing point of the helicopter directly below the flight path (Fig. 5.8). The observer

plane extends to 2000 ft on either side of the trajectory (in the y-direction) and is 8000 ft in length (along the x-direction). For the calculations in this chapter, ground observers are spaced at 55 ft (2.5 R) intervals in both the x and y direction.

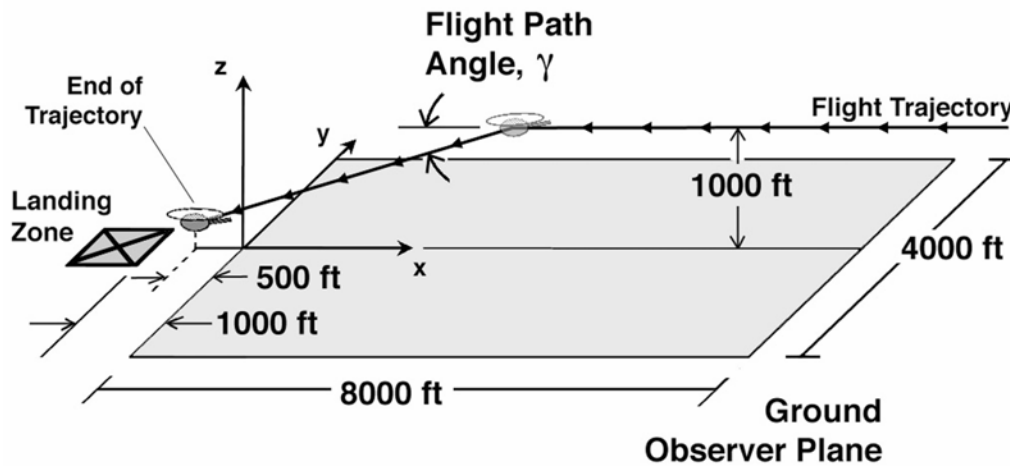


Figure 5.8 Helicopter trajectory and ground observer plane.

As shown in Figure 5.8, the helicopter is assumed to be approaching along the centerline ( $y = 0$ ) from the positive x-direction. For all the approach flights considered, it is also assumed that the helicopter is in level flight ( $\gamma = 0^\circ$ ) at an altitude of 1000 ft above ground level, prior to descent. Because the current prediction methods do not simulate the final stages of approach (e.g. flare and hover), noise calculations are terminated when the helicopter is 500 ft past the y-axis. This stipulation also allows a more complete evaluation of the observer time histories (and the SEL) for observers closest to the termination point of flight. In all cases, both source and observer times are referenced to the zero time which occurs when the helicopter flies directly over the point  $x = 0, y = 0$ .

Ground noise radiation and exposure metrics associated with different trajectories are obtained by propagating the acoustic data from the noise radiation spheres to the ground. The SEL (Sound Exposure Level) is used as a metric to express the effect of time exposure to noise annoyance at each ground observer location. The SEL noise metric is calculated from the observer time history using a continuous time integration formulation [8].

$$SEL = 10 \log_{10} \left( \sum_{i=1}^n \left\{ 10^{\frac{SPL-A_i}{10}} \frac{\Delta t_i}{(1 \text{sec.})} \right\} \right) \quad (5.5)$$

where, SPL-A represents the A-weighted Sound Pressure Level, the subscript “i” refers to the time step along the trajectory,  $\Delta t_i$  refers to the  $i^{th}$  time interval (taken to be one rotor revolution in the current implementation, shown normalized by a reference time interval of 1 second). A contour plot of SEL over the ground observer plane determines the relative “noisiness” of the associated trajectory, and is a simple way to account for the effect of exposure due to the duration of sound.

## 5.2 Flight Trajectory Management without Wind Effects

The design of low noise trajectories requires an understanding of the effect of various trajectory and design parameters (advance ratio, flight path angle, vehicle acceleration, vehicle design changes) on noise metric profiles on the ground. A

parametric study is conducted to gain insights into some of these complex relationships and to exercise the acoustic mapping method over the theoretically computed data set of noise radiation spheres. The results are expressed as SEL distributions over the observer plane and as dB-A time histories both at specified observer locations and over the entire observer plane. Because a quasi-steady compact-chord 2-D strip aerodynamic model, along with a prescribed rotor wake geometry, is used to generate the acoustic data used in this thesis, the predicted noise levels shown here must be viewed as trends in relative BVI noise levels, and not in absolute terms. Absolute levels can be obtained through the use of experimental acoustic data, which implicitly contains the complicated unsteadiness associated with blade-vortex interactions. Quasi-Steady aerodynamics is observed to capture the trends associated with BVI noise directivity reasonably well, but the absolute levels computed are usually larger, especially for BVI associated with small miss-distances, than those actually observed. This must be borne in mind while examining the results throughout this work.

### **5.2.1 Effects of Flight Path Angle & Flight Velocity**

The effect of flight path angle on BVI noise on the ground is shown in Figures 5.9 for the AH-1 helicopter at an approach speed of 73 knots ( $\mu = 0.165$ ). SEL contours on the ground observer plane are plotted for various descent angles (negative flight path angles) ranging from  $\gamma = -2^\circ$  to  $-8^\circ$ . Time histories at three specified observers are also plotted for comparison; Observer A is located at  $x = 2200$  ft,  $y = -1100$ ft (on the

retreating side), Observer B at  $x = 2200\text{ft}$ ,  $y = 0$  ft directly below the flight path, and Observer C at  $x = 2200$  ft,  $y = 1100$  ft (on the advancing side).

For all these trajectories and at all the performance states encountered at a given advance ratio or flight speed, the radiation spheres are oriented nearly identically with respect to the horizon. This is because in trimmed flight,  $(\gamma + \alpha_{\text{TPP}})$  is primarily a function of the helicopter drag, which remains fairly constant for a given advance ratio. Differences in ground noise patterns for these different descent angles reflect changes in directivity and noise levels on the radiation spheres, as well as the effect of trajectory variations (distance and directivity effects), A-weighting and atmospheric sound absorption. In general, higher SEL values are observed near  $x = 0$ ,  $y = 0$  directly below the flight path owing to closer proximity to the trajectory.

The concept of effective rotor inflow (Equation 5.3) explains some of the predicted noise trends shown in Figures 5.9. In general, strong positive and negative inflow “pushes” the rotor wake further away from the rotor disk which reduces the likelihood of close blade-vortex interactions that radiate strong BVI noise (Fig. 5.10). When the inflow angle is near zero, the rotor wake remains mostly in the rotor tip-path-plane which increases the likelihood of severe BVI noise radiation.

For all the descent cases shown in Figure 5.9, the radiated noise from the level flight ( $\gamma = 0^\circ$ ,  $\alpha_{\text{TPP}} = -1.37^\circ$ ) segment is found to be quite small. This is because in level flight, both the  $\alpha_{\text{TPP}}$  term and the rotor induced velocity to flight velocity ratio

combine to form a strong negative inflow (downwash) that displaces the wake below the rotor and reduce BVI. Some indications of this effect are also shown in Figure 5.5a for the radiation sphere acoustics predicted at this trim state.

When the helicopter is in descent, the negative flight path angle (descent angle) tends to make the tip-path-plane angle more positive. The positive  $\alpha_{TPP}$  term in Equation (5.3) may become strong enough to negate the effects of the negative rotor induced velocity to flight velocity ratio. At very shallow descent angles ( $\gamma = -2^\circ$ ,  $\alpha_{TPP} = +0.63^\circ$ ) the inflow angle remains negative which helps to keep the wake underneath the rotor. As the helicopter descends at a steeper angle ( $\gamma = -4^\circ$ ,  $\alpha_{TPP} = +2.63^\circ$ ), the tip-path-plane angle tips further back and the wake moves close to the plane of the rotor. The rotor inflow approaches zero as the  $\alpha_{TPP}$  contribution becomes more positive. Consequently, the highest ground noise is predicted for this descent approach (Fig. 5.9b). For even steeper descents ( $\gamma = -6^\circ$  and  $-8^\circ$ ),  $\alpha_{TPP}$  becomes large enough (positive) to override the effect of a negative induced velocity to flight velocity ratio. The effective rotor inflow angle becomes positive which “pushes” the wake above the rotor to increase the BVI miss distances and reduces noise (Fig. 5.9c, 5.9d).

It is also noticed that the SEL contours becomes asymmetric (with respect to the plane of the flight path) with steeper descents. This change in ground noise pattern signifies a different BVI directivity as a result of the greater (more positive) tip-path-plane tilt that minimizes the miss- distance associated with the “older” BVI formed

further aft of the rotor. The transition to asymmetry is observed to occur after conditions corresponding to peak BVI noise radiation ( $\gamma$  steeper than  $-4^\circ$ ).

The predicted observer time histories for all these different descent conditions exhibit similar increasing and decreasing noise trends. This variation in the noise received by a ground observer is not only due to the proximity of the helicopter but also the directivity of the radiated BVI noise at the particular performance state. In general, the same trends observed in the SEL contour plots are also observed for the time histories shown in Figures 5.9. However, the observer time histories show much greater detail and therefore enable a better understanding of the BVI noise radiation at different flight trajectory settings. It can be observed that at shallow approaches, the time histories have sharper peaks compared to the time histories predicted for steeper descents. This variation is likely to be due to the increased distance between the observer and the helicopter at steeper descents. The discontinuity in time history (Fig. 5.9d) at  $t_{\text{obs}} = -46.5$  sec represents a “switch” from level flight to descent.

The effect of advance ratio on *SEL* for a constant flight path angle ( $\gamma = -6^\circ$ ) is shown in Figures 5.11 through 5.15. The advance ratio is varied from 0.10 to 0.24 in steps of 0.01. Several interesting trends associated with BVI noise radiation are observed. At an advance ratio 0.1, the noise levels on the ground are relatively low and are distributed symmetrically about the plan of the flight path. As advance ratio increases, the peak of BVI noise radiation increases. This is mainly because at an advance ratio of 0.1 the high induced velocities ensure that the wake operates below the rotor disk

(in the first and fourth quadrants of the disk). This keeps the miss- distances relatively high. Increasing the advance ratio has the effect of lowering the induced downwash through the rotor disk. This “pushes” the wake into the rotor disk and the noise starts to increase.

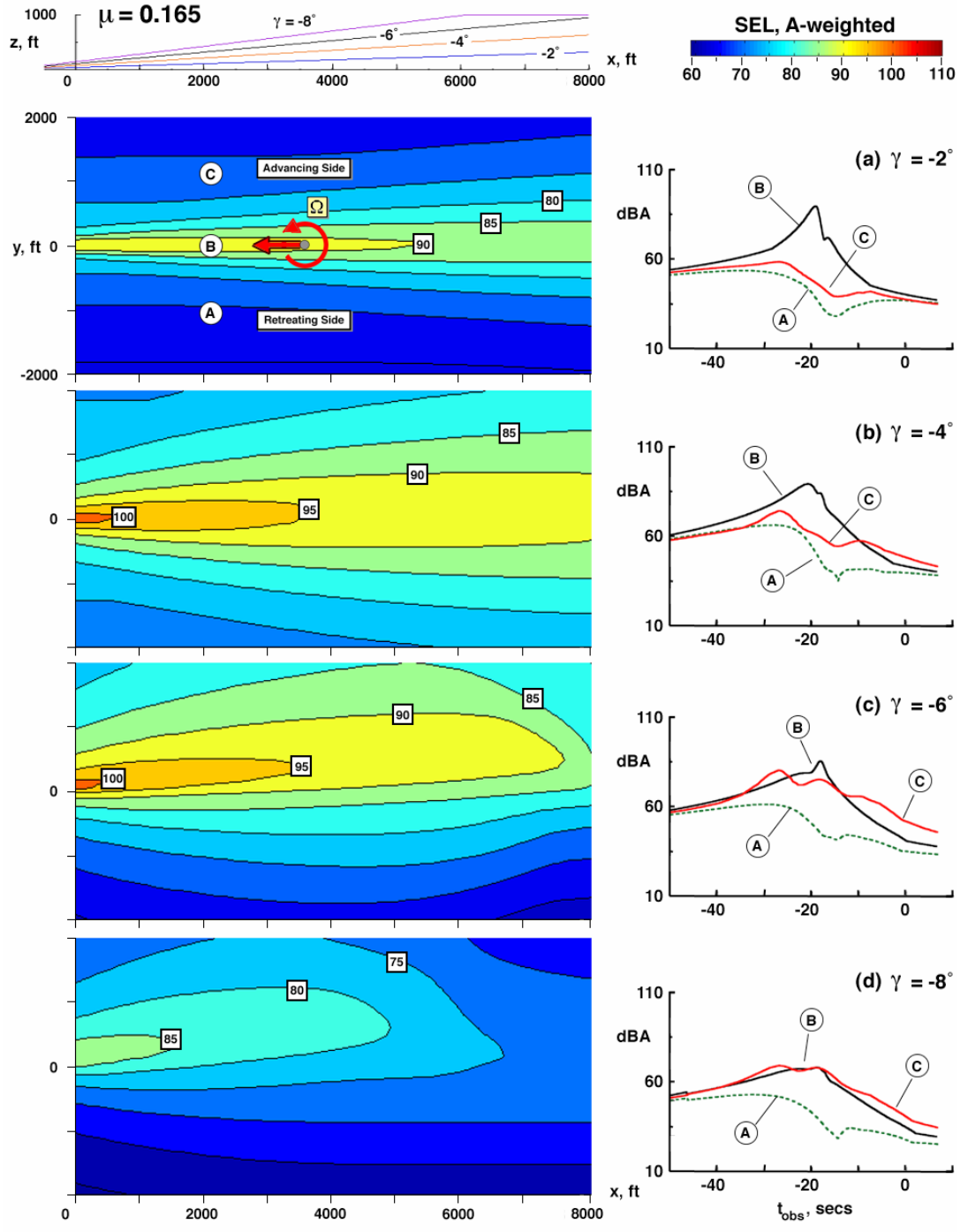


Figure 5.9 Predicted SEL ground noise contours and acoustic time histories for  $\mu = 0.165$  at different flight path angles: (a)  $\gamma = -2^\circ$ , (b)  $\gamma = -4^\circ$ , (c)  $\gamma = -6^\circ$ , (d)  $\gamma = -8^\circ$ .

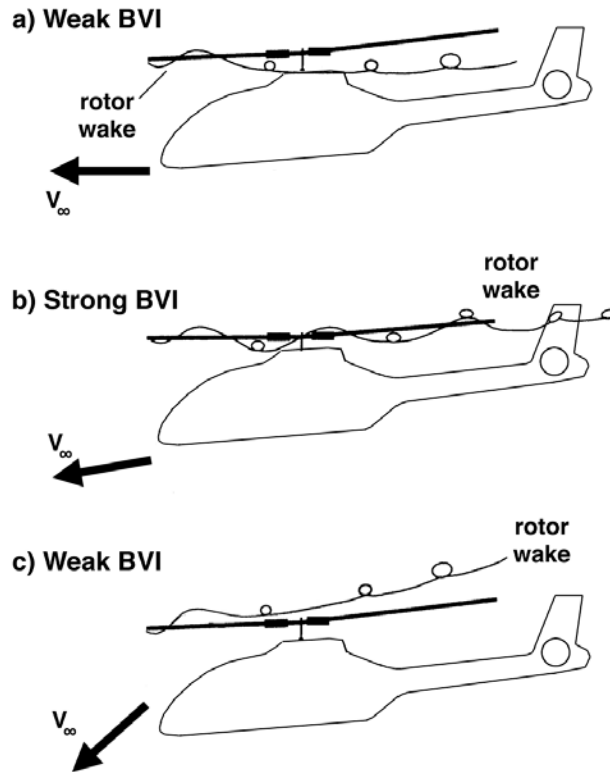


Figure 5.10 The effect of descent angle on miss-distances and the location of the wake relative to the rotor disk.

Peak BVI noise radiation on the ground plane is observed close to the landing point, center of the left edge of the ground plane. As advance ratio increases, the peak levels on the ground start to increase. At the same time the noise footprint becomes more asymmetric. The noise is now directed more toward the advancing side of the rotor (top-half of plane). BVI noise radiation on the ground peaks at an advance ratio of 0.14 at this flight path angle ( $-6^\circ$ ), after which it starts to reduce again. The area on the ground with SEL values over a 100 dB becomes a maximum at an advance ratio

of 0.14 and then starts to decrease again. Beyond an advance ratio of 0.21 however, the peak BVI noise level is seen to increase again.

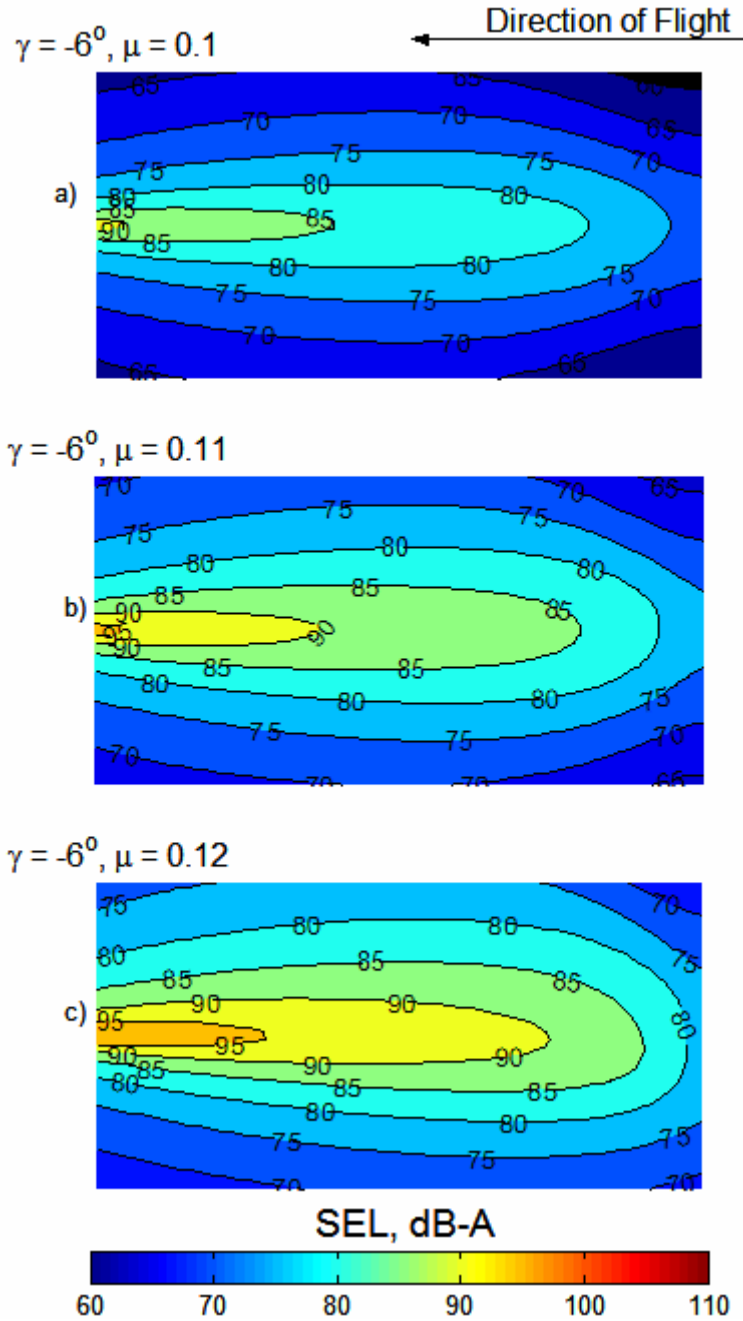


Figure 5.11 Predicted SEL ground noise contours for  $\gamma = -6^\circ$  at different advance ratios: (a)  $\mu = 0.10$ , (b)  $\mu = 0.11$ , (c)  $\mu = 0.12$ .

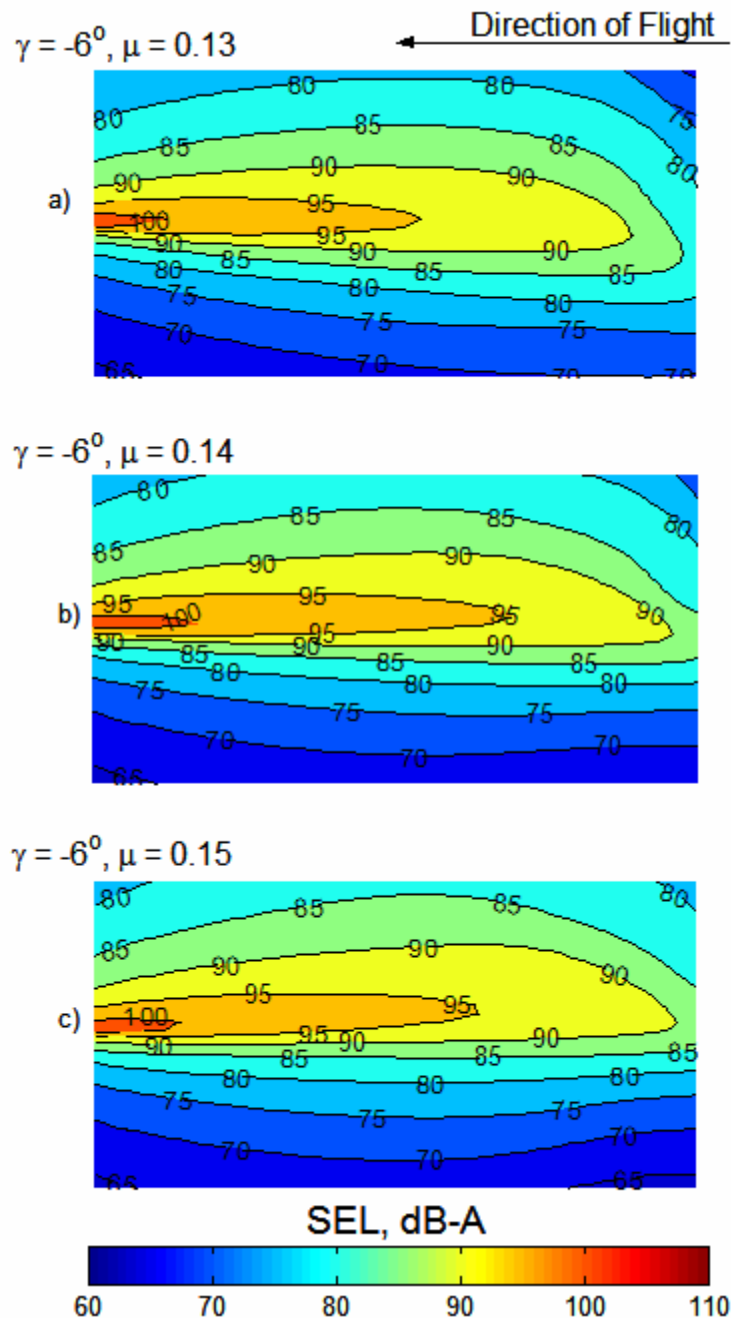


Figure 5.12 Predicted SEL ground noise contours for  $\gamma = -6^\circ$  at different advance ratios: (a)  $\mu = 0.13$ , (b)  $\mu = 0.14$ , (c)  $\mu = 0.15$ .

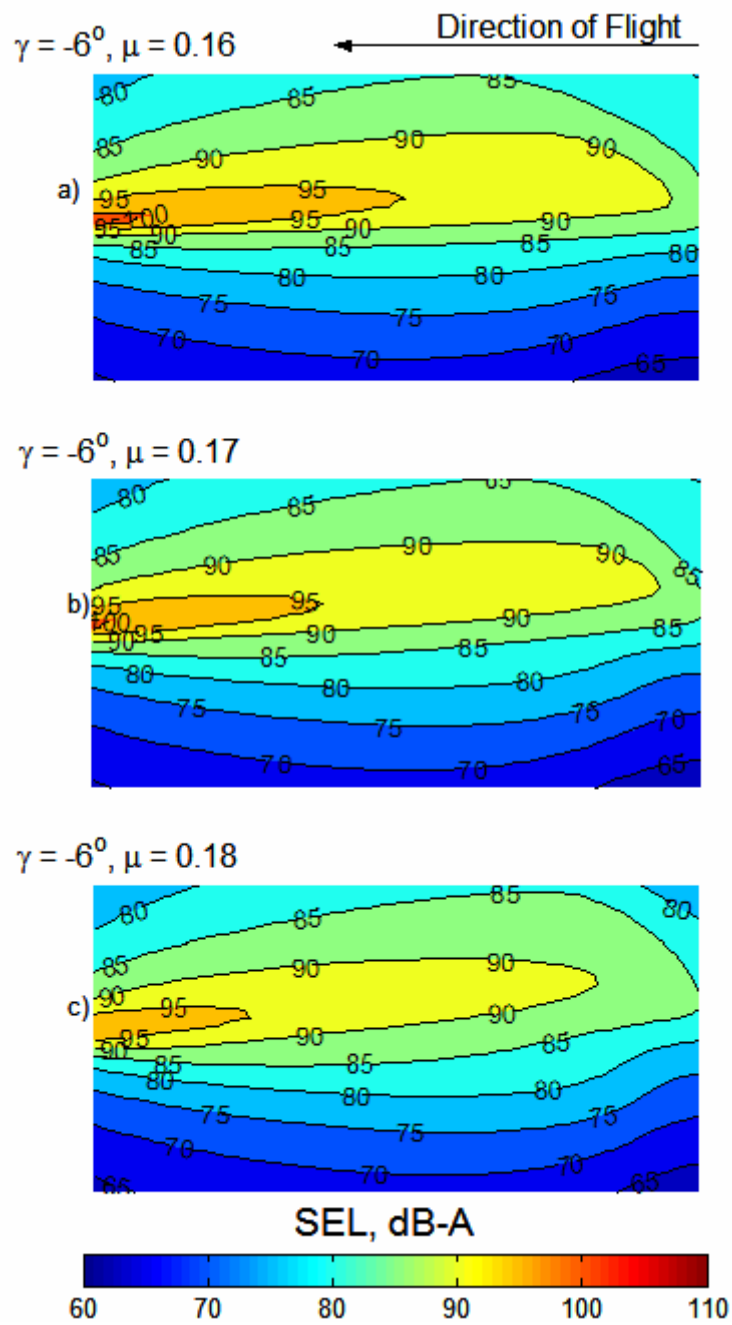


Figure 5.13 Predicted SEL ground noise contours for  $\gamma = -6^\circ$  at different advance ratios: (a)  $\mu = 0.16$ , (b)  $\mu = 0.17$ , (c)  $\mu = 0.18$ .

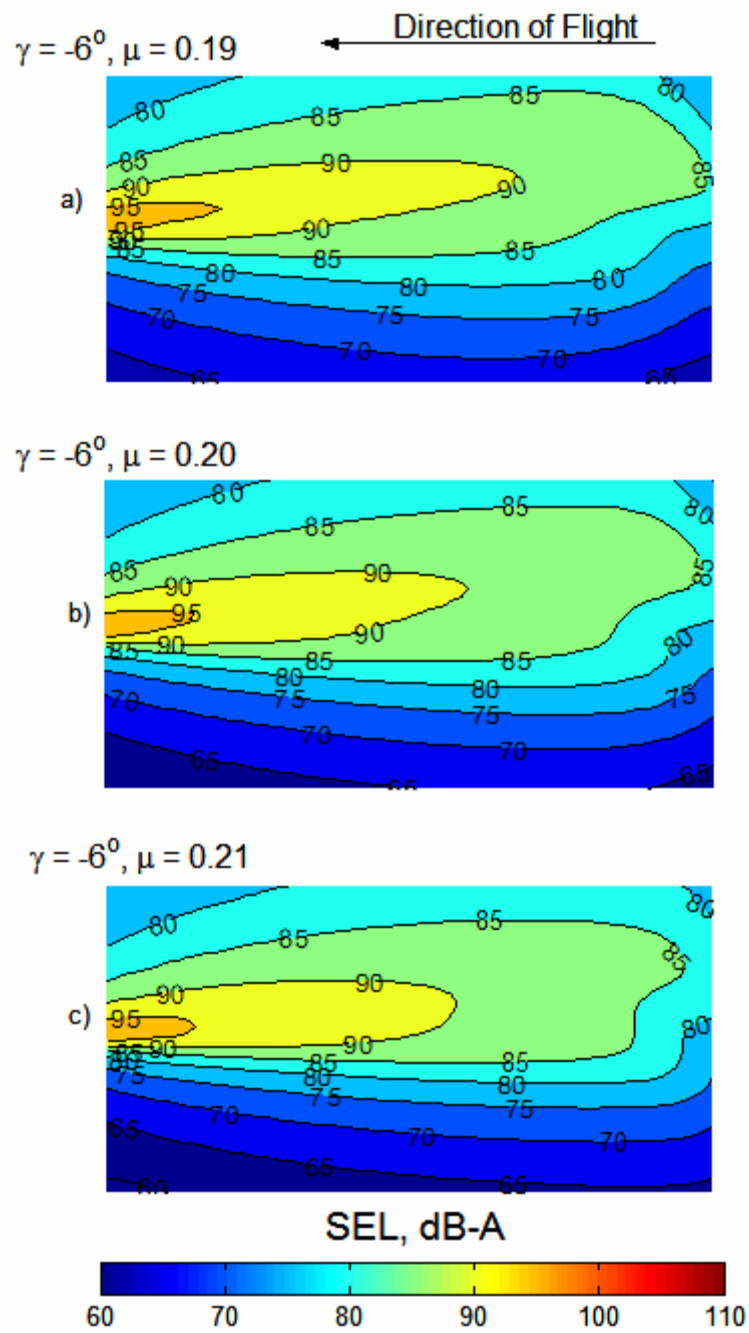


Figure 5.14 Predicted SEL ground noise contours for  $\gamma = -6^\circ$  at different advance ratios: (a)  $\mu = 0.19$ , (b)  $\mu = 0.20$ , (c)  $\mu = 0.21$ .

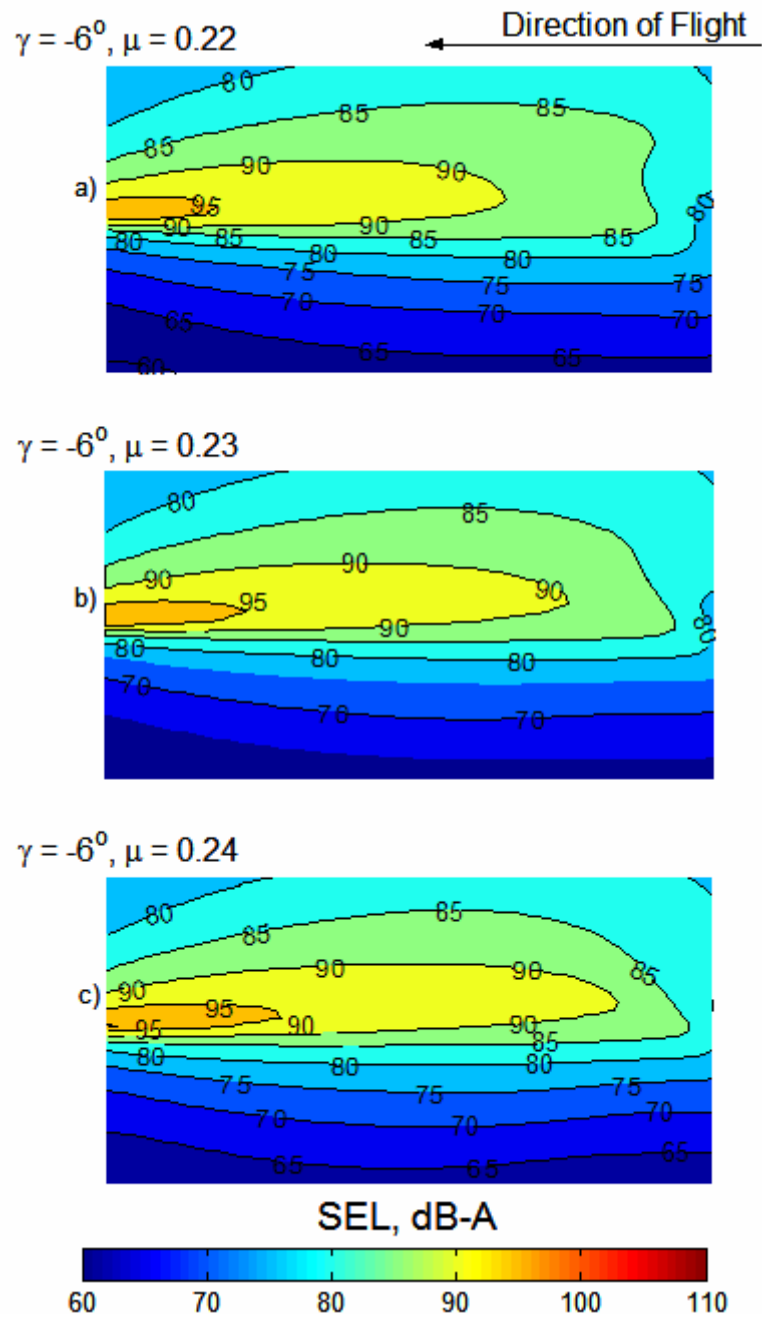


Figure 5.15 Predicted SEL ground noise contours for  $\gamma = -6^\circ$  at different advance ratios: (a)  $\mu = 0.22$ , (b)  $\mu = 0.23$ , (c)  $\mu = 0.24$ .

It is instructive to derive metrics from the SEL distribution over the observer plane, which can then be used to easily quantify the “noisiness” of each trajectory, thus simplifying comparison, though possibly at the cost of loss of detailed information. One such metric is obtained by area-averaging SEL values over the bounded ground plane, on an energy basis. This proposed noise metric represents an average value for exposure to A-weighted acoustic energies over the plane. This is referred to as  $SEL_{av}$  and expressed in dBA.

$$SEL_{av} = 10 \log \left( \sum \frac{10^{\frac{SEL_i}{10}} \Delta A_i}{A} \right) \quad (5.6)$$

While this very simple integrated annoyance metric does not account for annoyance sensitivity due to land use and many other factors, it does represent the total relative annoyance measured on the ground for selected combinations of flight path and control parameters. As such, it can be used to qualitatively judge the “goodness” of one flight path over another. This new metric, introduced in reference [72], was devised to give an indication of the integrated effect of the spatial distribution of noise exposure on the ground.

$SEL_{av}$  contours are shown as a function of constant advance ratio and constant rate of sink in Figure 5.16a.  $SEL_{av}$  values are large in a region that almost spans the entire advance ratio range at an almost constant rate of sink of about 700 ft/min. The  $SEL_{av}$  values show a modest increase with advance ratio at these maximum levels.

Minimum  $SEL_{av}$  values occur at low rates of sink, especially at low advance ratios, where larger rotor induced velocities push the wake system far beneath the rotor's tip-path-plane. At high rates of sink, where the wake is forced above the tip-path-plane of the rotor,  $SEL_{av}$  values are quite low, especially at high advance ratios. These contours are re-plotted in Figure 5.16b as a function of advance ratio and flight path angle.

It is apparent from the previous discussion that many factors contribute to the trends shown in Figure 5.16 for the AH-1 helicopter. Therefore it is quite remarkable that the trends of the  $SEL_{av}$  curves match the trends of average sound power ( $P_{av}$ ) radiated by the helicopter (Figure 5.6) so well. Both sets of contours show that maximum noise or annoyance regions can be avoided by flying at higher or lower rates of sink than the maximum level condition at about 700 ft/min. However, there is one notable difference between the two figures. The  $SEL_{av}$  values in Figure 5.16 decrease more rapidly from their peak level with increases or decreases in rates of sink than the  $P_{av}$  values decrease from their peak level shown in Figure 5.6. This difference is larger when rates of sink are greater than 700 ft/min, probably because the flight path of the helicopter is higher over the measurement locations, causing the radiated noise to travel further from the point of emission before contacting the ground plane. Spherical spreading and atmospheric absorption over these greater distances weaken the  $SEL_{av}$  values. The  $SEL_{av}$  curves of Figure 5.16 also indicate that minimum average ground annoyance can be achieved by slow, shallow approaches or moderate speed, steep approaches. The  $P_{av}$  curves of Fig. 5.6 give similar results; minimum

radiated acoustic power over a spherical surface surrounding the AH-1 helicopter can be achieved by flying slow, shallow approaches or moderate speed, steep approaches. The comparative evaluation of Figures 5.16 and 5.6 also suggest that flying the helicopter along constant velocity, constant flight path angle trajectories to minimize average radiated sound power may also minimize the average annoyance on the ground for the AH-1 helicopter.

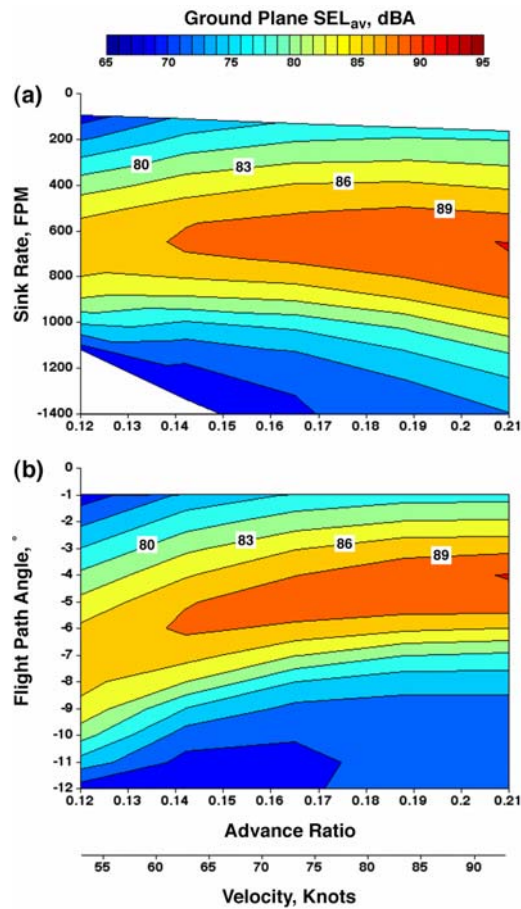


Figure 5.16 Predicted  $SEL_{av}$  ground noise contours as a function of: a)  $\mu$  and  $R/S$ ;  
 b)  $\mu$  and  $\gamma$ .

### 5.2.2 Effect of Vehicle Deceleration

Next, a moderate to steep approach which uses deceleration parallel to the flight path of the helicopter is studied. Figure 5.17 shows the *SEL* contours corresponding to the AH-1 helicopter executing a 0.05g decelerating approach at a flight path angle of  $-6^\circ$ . For this approach, the helicopter begins its descent from level flight at a 1000 ft altitude to the  $-6$  degree approach path at  $x \approx 8500$  ft, up-range of the landing point. The flight speed during the initial descent phase is 93 knots. At  $x \approx 5200$  ft,  $z = 650$  ft, the aircraft begins a deceleration of 0.05g (or about 0.95 knots per second) reaching a flight speed of 53 knots at  $x = 0$ ,  $z = 105$  ft, and maintains that speed till the aircraft is about 500 ft from the heliport. The *SEL* levels, in regions on the ground below the deceleration segment of the trajectory, are considerably reduced compared to constant speed trajectories with a flight path angle of  $-6^\circ$  at any flight speed from 50 to 90 knots. A deceleration of 0.05g corresponds to an effective increase of about  $2.9^\circ$  in tip-path-plane angle. This change in the effective tip-path-plane angle significantly alters BVI noise radiation levels.

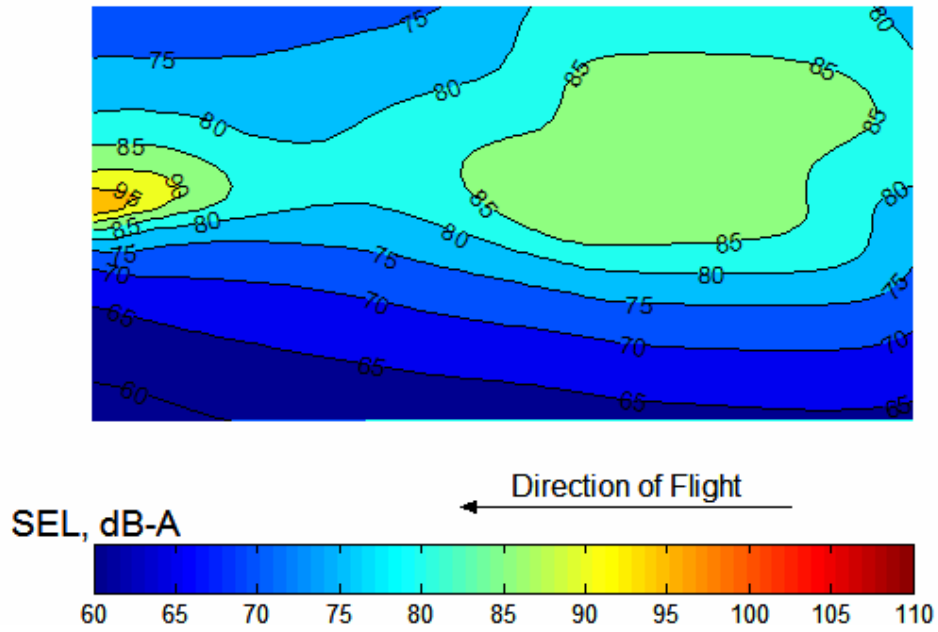


Figure 5.17 SEL contours for a deceleration approach (0.05g) at a flight path angle of  $-6^\circ$ .

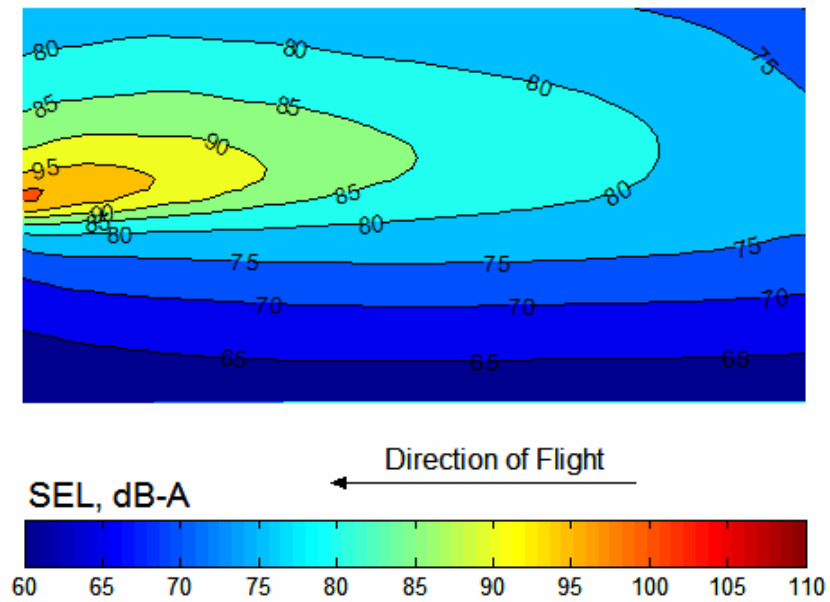


Figure 5.18 SEL contours for a deceleration approach (0.025g) at a flight path angle of  $-6^\circ$ .

The highest *SEL* regions in Figure 5.17 occur near the terminal portion of the trajectory where the helicopter is decelerating close to the ground and the distances between the ground observer locations and the effective BVI source positions are quite small. The performance state corresponding to a deceleration of 0.05g at  $-6^\circ$  is approximately equivalent to a steady state condition at the same speed but with an effective flight path angle of about  $-9^\circ$ . At this effective flight path angle, noise levels increase as advance ratio decreases, further contributing to the high *SEL* values close to  $x = 0$  ft,  $y = 0$  ft. Figure 5.18 shows the effect of a 0.025g deceleration. It can now be seen that noise level reductions are obtained over a larger portion of the ground plane compared to constant speed approaches at the same flight path angle. The terminal area is associated with higher noise levels compared to the 0.05g case because the tip-path plane angle now corresponds to high BVI noise radiation at 40 knots.

### **5.2.3 Effect of Vehicle Drag Changes**

An X-Force device (Ref. [49]) is a deployable drag device that results in an increase in the flat plate area of the helicopter. By changing the vehicle drag to weight ratio and hence the tip-path plane angle, BVI noise radiation at any flight velocity can be altered. This aerodynamic drag device is obviously most effective at higher flight velocity. The effect of doubling the fuselage drag for the AH-1 helicopter at a

constant velocity of 93 knots ( $\mu = 0.210$ ) and a  $3^\circ$  descent angle is shown in Figure 5.19b. The effect of doubling the drag is compared to the baseline case (5.19a), without the increase in drag, or X-force. At this shallow flight path angle, increasing the drag of the helicopter through aerodynamic X-Force control makes the tip-path-plane angle more negative causing a greater component of the airspeed to flow down through the rotor disk. The net effect is to increase the miss distances between the shed vortices and the passing rotor blades, which reduces BVI noise radiation. Substantial reductions in *SEL* levels are noted over the entire ground plane.

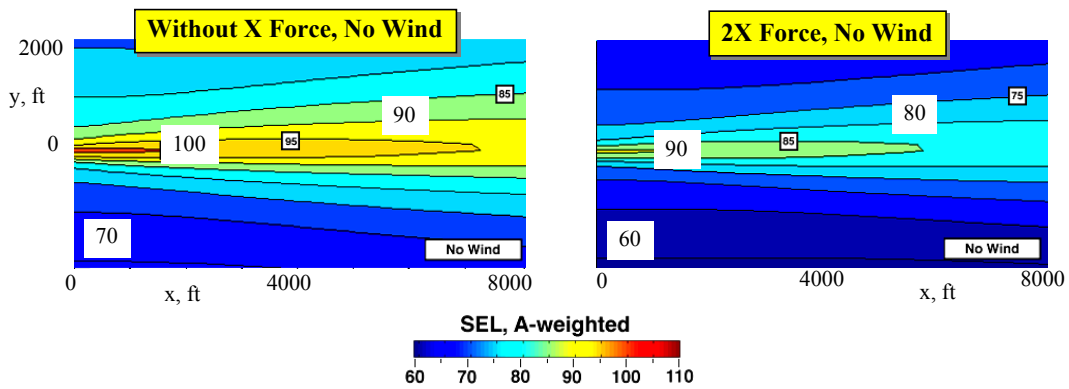


Figure 5.19 Effect of X-force on SEL contours on the ground plane: a) without X-force and b) with X-force.

#### 5.2.4 Sample Noise Abatement Profiles

Previous sections have demonstrated how flight velocity, flight path angle, vehicle acceleration, and vehicle drag changes can be used to reduce BVI noise radiation. Some sample multi-segment approaches are considered in this section.

Figure 5.20 shows a two-segmented approach at 73 knots. A moderately steep descent of  $-6^\circ$  is followed by a shallow approach at  $-2^\circ$ . The noise levels on the ground are seen to be lower compared to the  $-6^\circ$  descent case at the same flight velocity. The highest noise levels are associated with the  $-6^\circ$  descent segment when the helicopter is fairly close to the ground. By applying deceleration along this critical flight segment, substantial SEL reduction is achieved (Fig. 5.21). For this trajectory the initial velocity is 93 knots and the final velocity is 53 knots. Appendix D introduces a methodology for the development of approach trajectories that minimize the average BVI noise exposure on the ground.

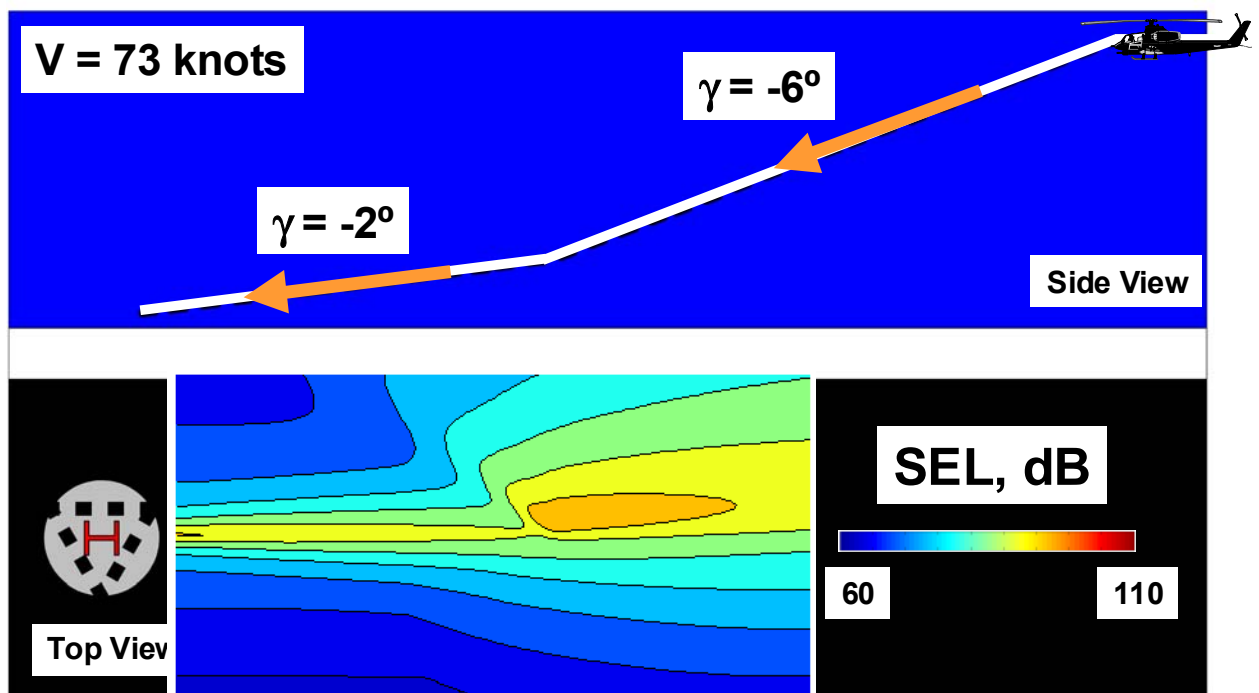


Figure 5.20 A 2-segmented approach at 70 knots.

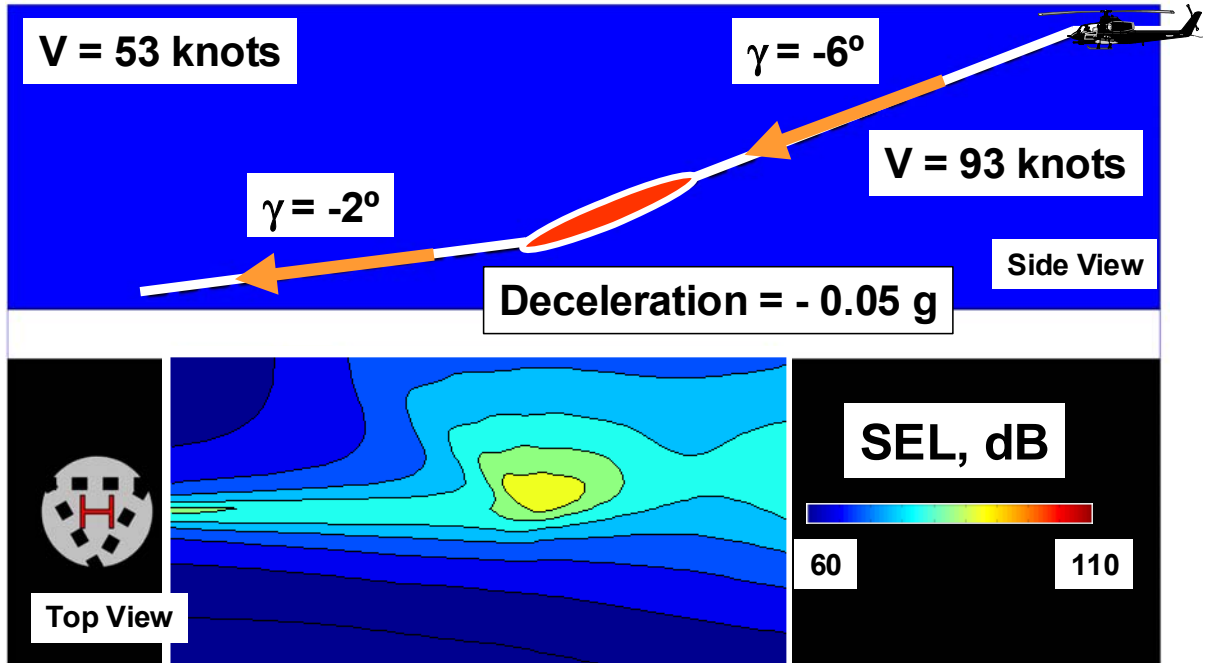


Figure 5.21 A decelerating 2-segmented approach.

### 5.2.5 Piloting Implications

It is tempting to judge the “goodness” of approach to landing trajectories based solely on the annoyance contours and/or average annoyance ( $SEL_{av}$ ) on the ground. Unfortunately, noise or annoyance is only one of the many factors that must be considered when rotorcraft are in the landing stages of flight. Only a few of these factors are discussed in what follows.

Paramount to all other considerations, safety of flight must be maintained. Flight safety encompasses many related areas including; maintaining the structural integrity of the helicopter, flying the helicopter so that it comfortably stays within its

performance envelope, insuring that the pilot has good handling qualities and adequate displays, judging the difficulty of the landing situation etc.

Flying at low airspeeds is to be avoided for most rotorcraft. Getting close to the ground with high sink rates at low airspeeds can be dangerous. The high sink rates must be arrested prior to touchdown by applying power, reducing the forward speed (kinetic energy) of the helicopter through deceleration, and/or bleeding the kinetic energy of the rotor system. Under normal conditions, the landing trajectories considered in this dissertation are thought to be have adequate performance envelope margins. However, landing downwind (with a tailwind) is not recommended in most situations, because this performance state is close to the settling with power and/or vortex ring states.

If the helicopter were to loose all or partial engine power at critical points along the landing trajectory, the flight performance becomes critical, especially for downwind landings. It is therefore imperative that an adequate safety margin be maintained so the pilot can establish autorotation in these critical situations. This suggests that a rate of sink boundary that is a function of forward airspeed and vehicle height should be developed for each helicopter and imposed as a constraint on aircraft operations to guarantee flight safety.

Flying slowly and trying to control airspeed or ground speed and altitude is also difficult without some stability augmentation. For a helicopter flying at low airspeeds

such that it is operating on the “backside of the power required curve”, it is difficult for the pilot to control altitude by trading airspeed. As a result, overshoot errors can occur during demanding regulator control tasks – such as maintaining position and airspeed along a specified trajectory defined with respect to the ground. Pilot workload also increases, making landing at low airspeeds a more difficult task in situations where the pilot must pay close attention to his physical surroundings. Although not predicted in this study, noise levels would be likely to increase as the pilot tries to adjust his controls to maintain the specified airspeed and altitude of his chosen noise abatement profile. Automating the landing procedure using DGPS for spatial guidance and on-board computers to control the landing has been shown to help reduce excursions and the resulting additional noise.

Cabin visibility can also be a challenge at high pitch attitudes because it can block the pilot’s view of the landing site. Deceleration causes the helicopter tip-path-plane to incline rearward with respect to the relative velocity vector, countering the trend of drag to tilt the rotor forward. The fuselage attitude is normally “rigged” to minimize rotor flapping with respect to the shaft under most flight conditions, which causes deceleration to effectively pitch the helicopter relative to the horizon. Both low noise techniques encounter this problem because both eventually require deceleration to bring the helicopter to rest with respect to the ground.

## 5.3 Flight Trajectory Management with Steady Headwinds and Tailwinds

The effect of steady “headwinds” and “tailwinds” on helicopter ground-noise exposure levels is analytically investigated using the Quasi-Static Acoustic Mapping (Q-SAM) method in this section. Two distinct approach procedures are formulated and their impact on ground noise exposure assessed. The pros and cons of these landing procedures are discussed in the context of reducing noise exposure, safety, and piloting procedures.

### 5.3.1 Modeling Methodology

Winds add a new dimension of concerns in terms of both piloting issues and noise abatement. Aircraft performance, aerodynamics and acoustics are a function of the motion of the helicopter in the medium, while approach trajectories to a designated landing point are specified with respect to the ground (or space).

A sketch of the important relationships between the air-mass and ground coordinate systems is shown in Figure 5.22. The air-mass coordinate system,  $R_{AM}$  (axes:  $x',y',z'$ ), moves at constant velocity,  $V_w$  (shown for a headwind), with respect to the ground coordinate system,  $R_F$  (axes:  $x,y,z$ ). The axes  $x',y',z'$  of  $R_{AM}$  are defined parallel to

$x,y,z$  respectively at any time. Trajectories are prescribed as location-velocity or location-time coordinates relative to the ground reference system. Flight velocities and flight path angles in the ground and air-mass frames are related through the equations below. Essentially the rate of sink remains invariant across both frames in the presence of horizontal winds. Therefore,

$$V_a \sin \gamma_a = V_g \sin \gamma_g \quad (5.7)$$

$$V_a \cos \gamma_a = V_w + V_g \cos \gamma_g$$

BVI acoustic radiation in the medium at any given time is a function of the motion of the aircraft with respect to the medium, i.e. in the coordinate system  $R_{AM}$ . Therefore, it is important to begin an analysis for the effects of wind in the air-mass system and then relate these results to the ground based system. Over each rotor revolution along the trajectory, the main rotor is assumed to “deposit” its acoustic radiation characteristics in the medium in the form of its radiation sphere. Under “wind-on” conditions, the flight parameters,  $\mu$  and  $\gamma$ , are evaluated with respect to the moving medium (i.e. in frame  $R_{AM}$ ) to reflect the vehicle airspeed and aerodynamic flight path angle. These wind-modified  $\mu_a$  and  $\gamma_a$  are used to calculate an effective tip-path-plane angle,  $\alpha_{TPP}^{EFF}$ , which is then used to select a noise radiation sphere corresponding to the quasi-static conditions with wind. For observers on the ground, the center of this radiation sphere (the mid-revolution hub position) moves with the velocity of the medium  $V_w$ . And equivalently in the frame  $R_{AM}$ , the radiation sphere center is stationary, while the observer moves with velocity,  $-V_w$ . For far-field

observers, stationary in the ground fixed frame  $R_F$ , the radiation sphere can be thought of as an acoustic “bubble” whose radius grows as the speed of sound, and whose center moves with velocity  $V_w$ . The point on the sphere at which this acoustic “bubble” meets a far field observer ground location, determines the sound pressure level in the medium at that observer location. Atmospheric absorption and spherical spreading are applied at the “bubble expansion” stage. The measured sound pressure levels at the ground locations are Doppler shifted to account for the motion of the medium with respect to the observer in the effective direction of acoustic propagation. These values are then A-weighted and summed over frequency to indicate the level of annoyance at each position. To be physically consistent it is important to apply atmospheric absorption before, and A-weighting after, the frequencies have been Doppler corrected.

### **5.3.2 Major Assumptions**

The major assumptions in the current analysis are summarized below:

1. The effects on only steady longitudinal winds are considered. Headwinds and tailwinds of less than 30 knots are considered. The effect of crosswinds, gusts, atmospheric turbulence, vertical winds and wind shear are ignored. The effect of wind and temperature gradients are also ignored.

2. A constant wind velocity is assumed throughout a particular trajectory. Effects of changes in wind velocity or direction are not accounted for.
3. The effect of the relative motion of steady wind relative to the stationary observer is accounted for by an appropriate Doppler shift.
4. All the general assumptions made for the current implementation of the Q-SAM method in 5.1.1 are retained.

### **5.3.3 Piloting Strategies**

Two distinct piloting strategies or choices that maintain the flight path (with respect to the ground) of a suggested/specified trajectory and either hold airspeed or rate of sink constant are identified. During nominal descent conditions, the helicopter pilot would most likely choose his approach direction to be into the wind, maintain a constant speed with respect to the air-mass, and adjust his rate of sink to maintain a constant visual flight path angle and thus set up a safe, easily flyable trajectory. Compared to the no wind situation (Figure 5.23a), this approach procedure with headwinds is sketched below (Approach Procedure 1 - Figure 5.23b). For a pilot flying into a headwind holding a constant velocity with respect to the air-mass, rates of sink would have to be decreased to hold a constant flight path angle with respect to the ground. The associated changes in aerodynamic flight path angle and tip-path-plane angle and other factors associated with propagation in the presence of wind will

affect the sound and annoyance levels on the ground. Upon nearing the landing zone, the pilot would simultaneously reduce the helicopter's rate of sink and forward speed to reach zero touchdown velocity with respect to the ground at the landing point.

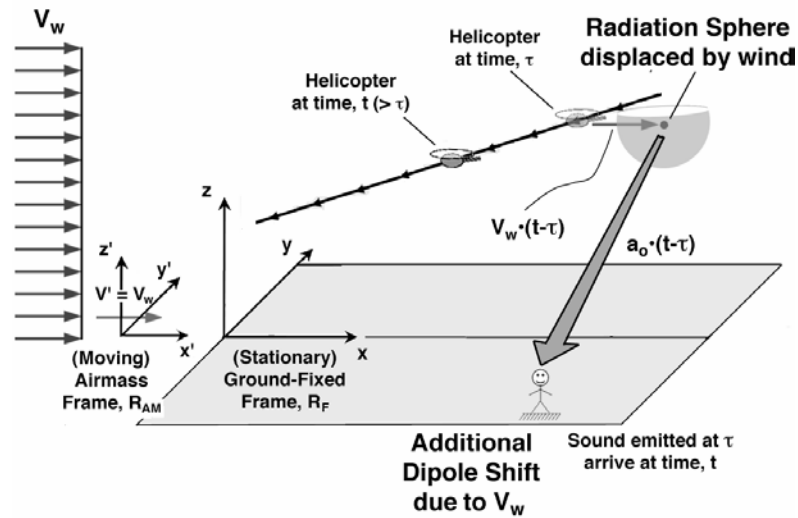


Figure 5.22 Geometrical relationships between air mass and ground fixed frames with wind.

More recently, precision decelerating approaches using DGPS for guidance have been developed for helicopters [53-55]. In this case, the pilot would fly to fixed spatial positions and predetermined fixed spatial velocities (Approach Procedure 2 - Figure 5.23c). Wind is accounted for by adjusting the airspeed to whatever is needed to achieve the specified inertial velocities, under wind conditions, while holding rate of sink the same. For example, to maintain ground speed with a headwind while flying a ground referenced trajectory, the airspeed of the helicopter with respect to the air-mass must be increased. This change in airspeed with respect to the ground

will also affect the sound and annoyance levels on the ground, but somewhat differently than the first approach procedure. These strategies and their impact on ground noise are assessed in subsequent sections.

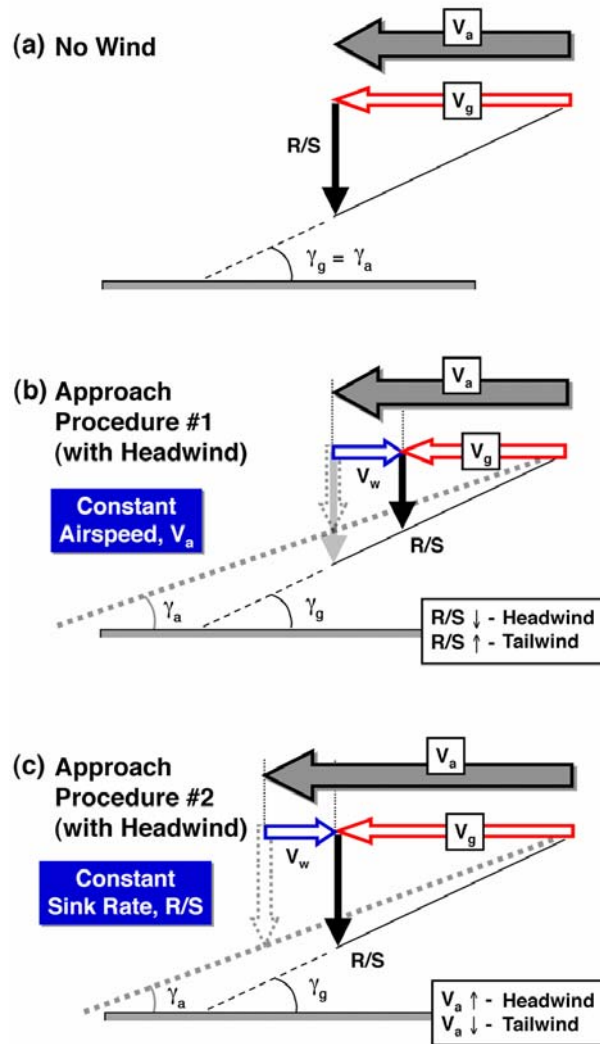


Figure 5.23 Flight parameter adjustments to maintain fixed ground flight path with headwinds

### 5.3.3.1 Approach Procedure 1 (Piloting Strategy 1) : Holding airspeed and flight path in the ground reference frame

In approach procedure 1 (Fig. 5.23b) it is assumed that, in the presence of wind, the pilot holds the specified airspeed and the prescribed flight path angle relative to the ground the same as in the no-wind situation. In the formulations below the subscript “NW” represents the no-wind conditions, or the prescribed invariants in an approach. The subscript “a” refers to physical quantities measured in the air-mass reference frame, while the subscript “g” refers to those measured in the ground reference frame. Therefore, for approach 1:

$$\begin{aligned} V_{NW} &= V_a \\ \gamma_{NW} &= \gamma_g \end{aligned} \quad (5.8)$$

The above relations are substituted in equations 5.7, and the aerodynamic flight path angle  $\gamma_a$  is expressed in terms of the airspeed and the inertial glideslope, the two invariants in this approach procedure (Equations 5.8).

$$\begin{aligned} \frac{V_g}{V_{NW}} &= \sqrt{1 - \left(\frac{V_w}{V_{NW}}\right)^2} \sin^2 \gamma_{NW} - \cos \gamma_{NW} \frac{V_w}{V_{NW}} \\ \sin \gamma_a &= \frac{V_g \sin \gamma_{NW}}{V_{NW}} \end{aligned} \quad (5.9)$$

The aerodynamic flight path angle and airspeed are then used to estimate the effective tip-path-plane angle. The orientation of the tip-path-plane relative to the horizon is  $\gamma_a + \alpha_{\text{TPP}}$ , which remains unchanged compared to the no-wind condition. Using small angle assumptions the above equations can be approximated to:

$$V_g = V_{NW} - V_w \quad (5.10)$$

$$\gamma_a = \gamma_{NW} \left( 1 - \frac{V_w}{V_{NW}} \right)$$

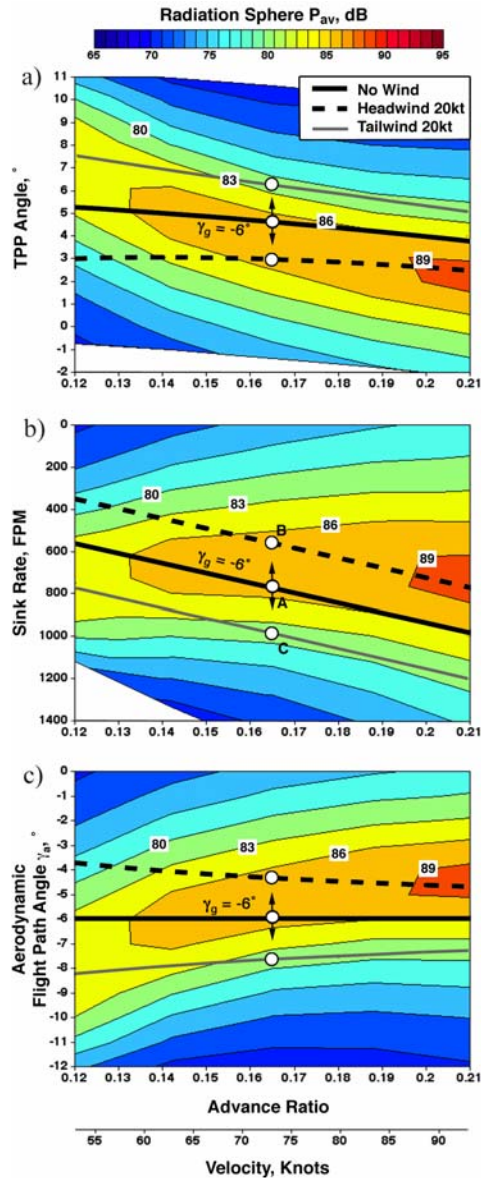


Figure 5.0.24 Variation of tip-path-plane angle, sink rate and aerodynamic flight path angle for Piloting Strategy 1 in the presence of a 20 knot head/tailwind compared to the no-wind values at an inertial descent angle of  $-6^\circ$ .

Therefore, in the presence of a headwind, the ground speed reduces while the aerodynamic descent angle becomes more shallow. The rate of sink and tip-path plane angle can also be expressed in terms of the no-wind conditions as shown below.

$$R / S_a = R / S_{NW} \left( 1 - \frac{V_w}{V_{NW}} \right) \quad (5.11)$$

$$\alpha_{TPP} = \alpha_{TPP,NW} + \gamma_{NW} \frac{V_w}{V_{NW}}$$

The rate of sink and tip-path-plane angle reduce in a headwind and increase in the presence of a tailwind, during descent. The effect of this piloting strategy on the effective inflow through the rotor disk is shown below:

$$\Delta \lambda' = \left( 1 - \frac{k}{V_{NW}} \frac{\partial \lambda}{\partial \alpha_{TPP}} \right) \gamma_{NW} V_w \approx \gamma_{NW} V_w \quad (\text{High Velocity Approximation})$$

(5.12)

where,  $k = 1$  for average or uniform inflow, but typically less than 1 for BVI noise radiation considerations ([49] and section 2.3 and 5.1.3). Therefore, for descent flight, the change in inflow through the rotor disk is proportional to the descent angle as well as the wind velocity. Inflow decreases during a headwind, under descent conditions, and increases in a tailwind.

For this approach therefore the pilot holds airspeed but changes rate of sink, reducing it during a headwind, so as to maintain a specified glide slope relative to the ground reference system. Consequently, the time required to descend increases in a headwind and it decreases in a tailwind.

These parametric relationships and the associated effect on average radiated sound power are expressed graphically in Fig. 5.24 for a  $\pm 20$  knot wind. The central bold black line in Figures 5.24a, b and c represent the tip-path-plane angle, sink rate and aerodynamic flight path angle respectively for a descent at  $-6^\circ$  at different advance ratios or airspeeds under no-wind conditions. The dashed and gray lines reflect the effect of a 20 knot headwind and tailwind respectively, on these parameters, using this approach procedure. The operational tip-path-plane angle of the rotor at any specified airspeed is seen to decrease in a headwind, and it increases in a tailwind (Fig. 5.24a). This corresponds to a shallower aerodynamic descent angle in a headwind as compared to the no wind situation (Fig. 5.24c). The rate of sink also reduces in a headwind, and increases in a tailwind (Fig. 5.24b). These changes in tip-path-plane angle and aerodynamic flight path angle are directly proportional to the ratio of wind speed to helicopter airspeed (Equations 5.7 and 5.8), and also to the inertial flight path angle, while the changes in rate of sink is equal to the wind velocity times the inertial flight path angle. The rate of sink, therefore, changes more dramatically under high wind velocity and steep descent approach situations. It is noted that the change in rate of sink at all airspeeds for a given inertial glideslope is the same for a given wind velocity (Fig. 5.24b). Superimposing these parameter

variation plots on the corresponding  $P_{av}$  contour plots gives us an estimate of the changes in average radiated power, in different flight conditions, in the presence of a  $\pm 20$  knot wind. The  $P_{av}$  values under wind conditions can be obtained by traversing “vertically” along contours of constant airspeed. For an advance ratio of 0.165, during a relatively steep  $-6^\circ$  approach, which corresponds to point A in Fig. 5.24b, small headwinds would tend to increase the average radiated sound power (shift towards point B), and tailwinds would cause it to reduce (shift towards C). For high enough headwinds the  $P_{av}$  levels could be expected to start reducing again, based on the typical variation of  $P_{av}$  with effective aerodynamic flight path angle at any airspeed. The wake operates close to but above the rotor disk at this steep descent condition. In a headwind the wake moves closer relative to the rotor disk, reducing miss-distances and increasing BVI noise. If the headwind is strong enough the wake may move over to the other side below the rotor disk and the noise levels may begin to reduce again. Under shallower descent conditions, say  $-3^\circ$ , the wake operates below the rotor disk under no-wind conditions. Here a headwind alleviates noise levels by pushing the wake further below relative to the rotor. However, tailwinds move the wake closer to the rotor disk, and the reduction in miss-distances results in an increase in BVI noise levels. The effect of this piloting choice in the presence of a headwind, in terms of changes in effective flight path angle or tip-path-plane angle at a given airspeed, is therefore similar to that of an acceleration parallel to flight path. The effect of a tailwind on the other hand is similar to that of a deceleration, making the tip-path-plane more positive.

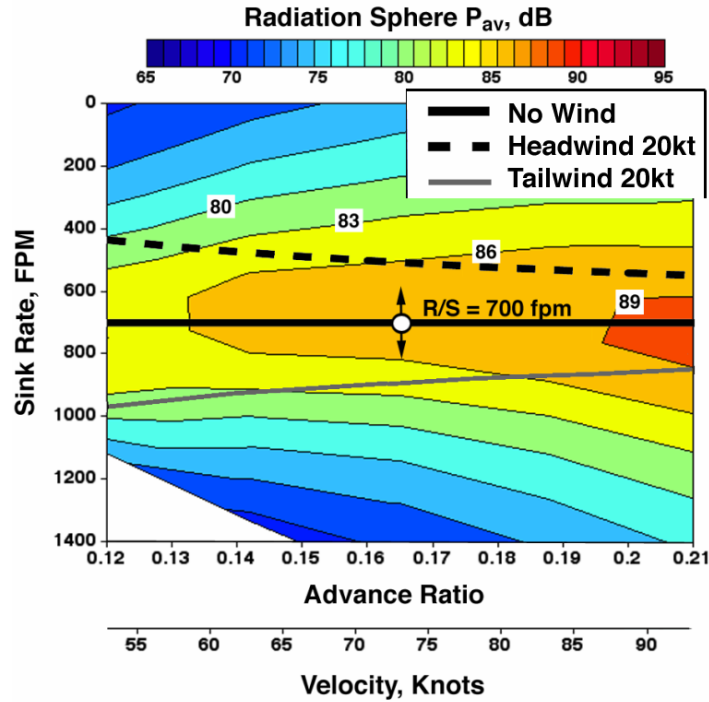


Figure 5.25 Variation of sink rate and for Piloting Strategy1 in the presence of a 20 knot head/tailwind compared to the no-wind values at a sink rate of 700 fpm.

Figure 5.25 shows the variations in rates of sink under 20 knot head/tailwind conditions but for a descent rate of 700 fpm, at various airspeeds. This rate of descent corresponds to the maximum radiated sound power at all airspeeds. In these flight conditions therefore the wake is very close to the rotor disk and the miss-distances are small. Both headwinds and tailwinds cause a reduction in noise levels by “pushing” the rotor wake below or above the rotor disk respectively.

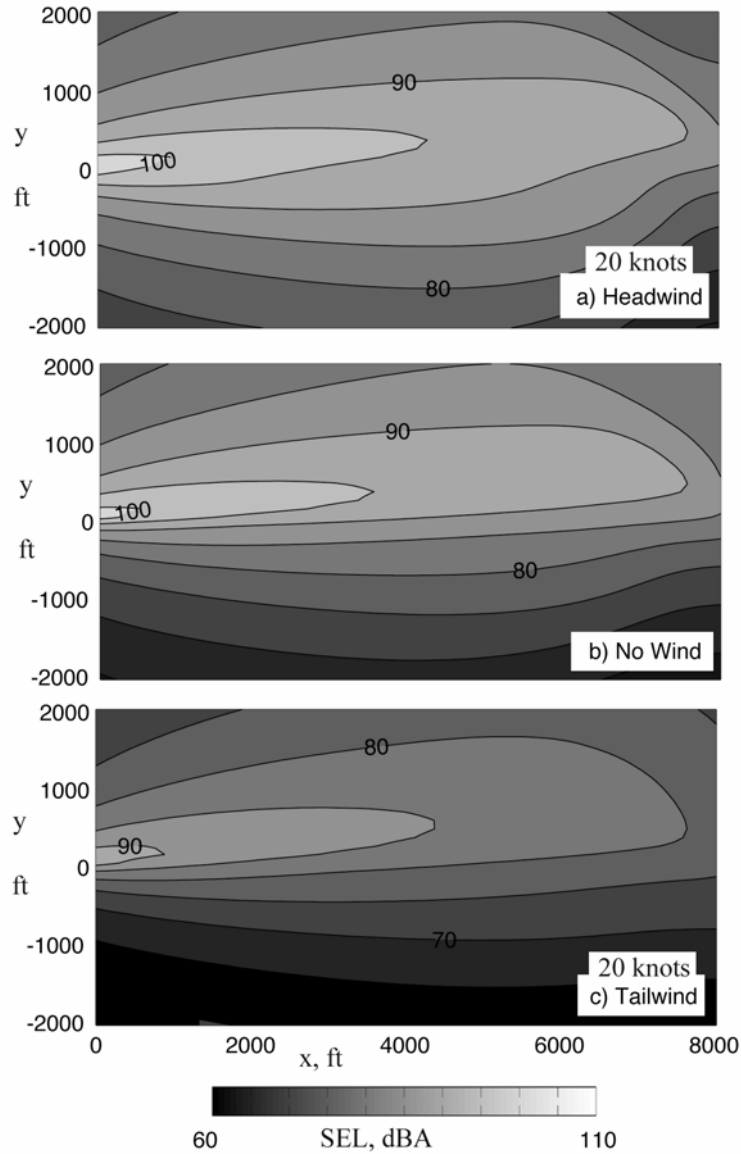


Figure 5.26 Effect of Piloting Strategy1 on ground noise exposure (SEL) contours at  $\mu = 0.165$  and  $\gamma_g = -6^\circ$ : a) 20 knot headwind, b) no wind and c) 20 knot tailwind.

The effect of  $\pm 20$  knot winds on the *SEL* contours on the ground is investigated in Fig. 5.26 for a typical approach at an airspeed of 73 knots (corresponding to an advance ratio of 0.165) and a flight path angle of  $-6^\circ$  defined with respect to the

inertial reference frame. It is observed that with headwinds, the peak *SEL* values on the ground increase slightly, and with tailwinds the levels are reduced. This corroborates the previous expectation based on the variation of  $P_{av}$  with aerodynamic flight path angle and airspeed (Fig. 5.24). A 20 knot headwind changes the aerodynamic flight path angle from  $-6^\circ$  to  $-4.3^\circ$ . For this advance ratio, the  $P_{av}$  values are seen to peak at an effective flight path angle of about  $-5^\circ$ , and slightly higher at a  $-4.3^\circ$  descent angle than at  $-6^\circ$ . A 20 knot tailwind steepens the aerodynamic flight path from  $-7^\circ$  to  $-7.6^\circ$ , which corresponds to a significant reduction in noise radiation.

At a descent angle of  $-3^\circ$ , a 20 knot head wind results in a change in flight path angle by  $-0.8^\circ$  (from Equation 5.10). For this shallow descent condition, headwinds cause the peak ground noise levels to decrease and tailwinds cause the levels to increase (Figure 5.27), as expected from radiation sphere trends (Figures 5.24 and 5.25).

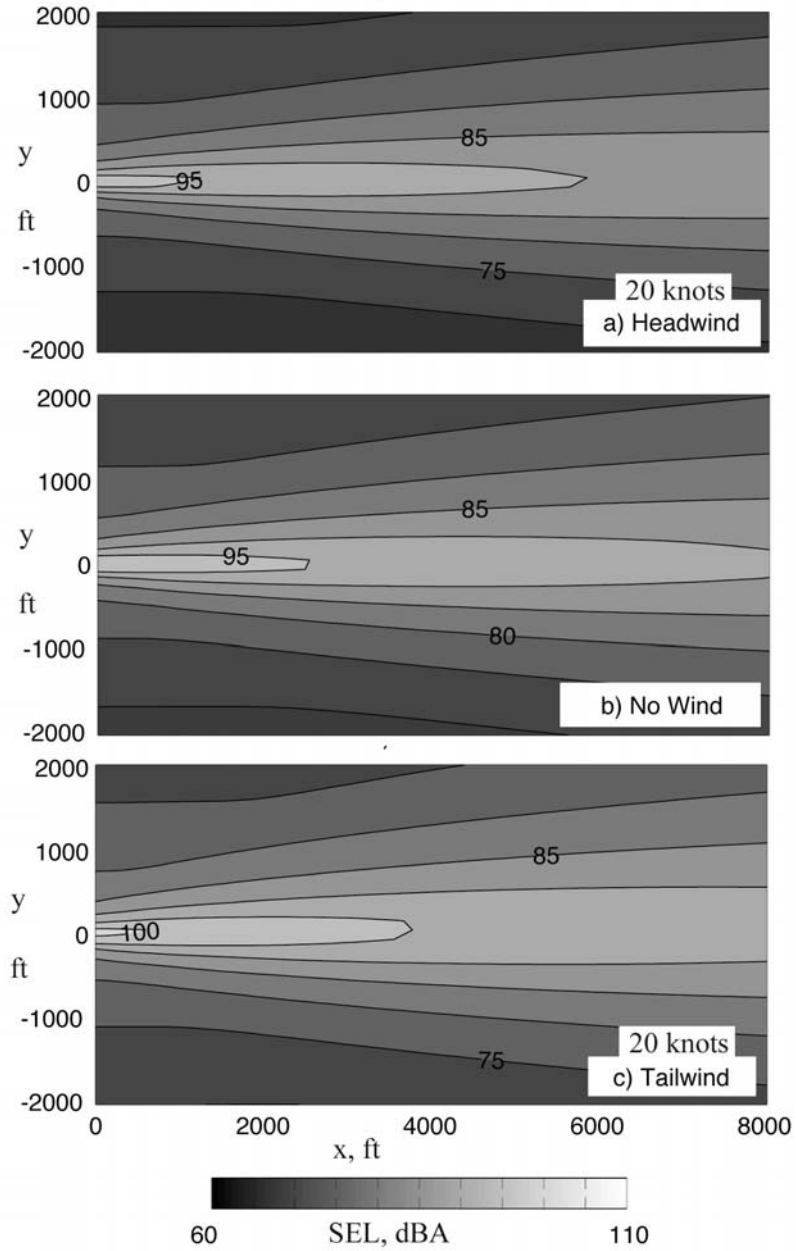


Figure 5.27 Effect of Piloting Strategy 1 on ground noise exposure (SEL) contours at  $\mu = 0.165$  and  $\gamma_g = -3^\circ$ : a) 20 knot headwind, b) no wind and c) 20 knot tailwind.

Figure 5.28 shows the variation of  $SEL_{av}$  values as the windspeed changes from  $-30$  knots to  $+30$  knots at two different inertial flight path angles. For the  $-6^\circ$  glideslope,

headwinds tend to first slightly increase the  $SEL_{av}$  values; at higher headwind velocities the  $SEL_{av}$  values begin to reduce again. As headwind values increase from 0 to 10 knots, the  $P_{av}$  values increase steadily, peaking at conditions corresponding to 10 knots, which corresponds to an effective/aerodynamic flight path angle of  $-5.1^\circ$ . In the presence of stronger headwinds, the  $P_{av}$  values begin to reduce again. Under tailwind conditions, the tip-path-plane angle becomes more positive and the  $SEL_{av}$  values reduce. For the shallower flight path angle, tailwinds result in higher peak  $SEL_{av}$  levels while headwinds are accompanied by a reduction in noise levels. These results correlate well with trends in  $P_{av}$  values discussed previously.

Figure 5.29 shows the contour plots of  $SEL_{av}$  expressed as a function of airspeed and either rate of sink, the aerodynamic flight path angle or the inertial flight path angle. The first column shows  $SEL_{av}$  levels as a function of inertial flight path angles and advance ratio or airspeed. Under headwind conditions, the aerodynamic flight path angle becomes less negative, and so the peak noise levels are pushed to steeper values of  $\gamma_g$ . The effect is more pronounced at lower airspeeds and steeper flight paths, because these flight conditions are associated with the maximum change in aerodynamic flight path angle. The opposite is observed in the presence of tailwinds, with peak noise conditions being achieved at shallower descent angles.

The second column, 2a through c, of Fig. 5.29 shows  $SEL_{av}$  levels as a function of aerodynamic flight path angles and advance ratio or airspeed. Differences between  $SEL_{av}$  levels on corresponding points in the three plots (same airspeed and

aerodynamic flight path angle) are observed to be rather small, and arise due to geometry, propagation and doppler effects. The last column, plots 3a through c, of Fig. 5.29 shows  $SEL_{av}$  levels as a function of sink rate and advance ratio or airspeed. Again, airspeed and sink rate uniquely define tip-path-plane angle, and hence the steady-state radiation characteristics; the small differences in levels between the three plots are a result of propagation effects, both temporal and spatial, associated with wind. These effects include doppler, displacement of acoustic sources by wind, and timing effects associated with the fact that the helicopter's speed along the flight path changes depending on the wind condition.

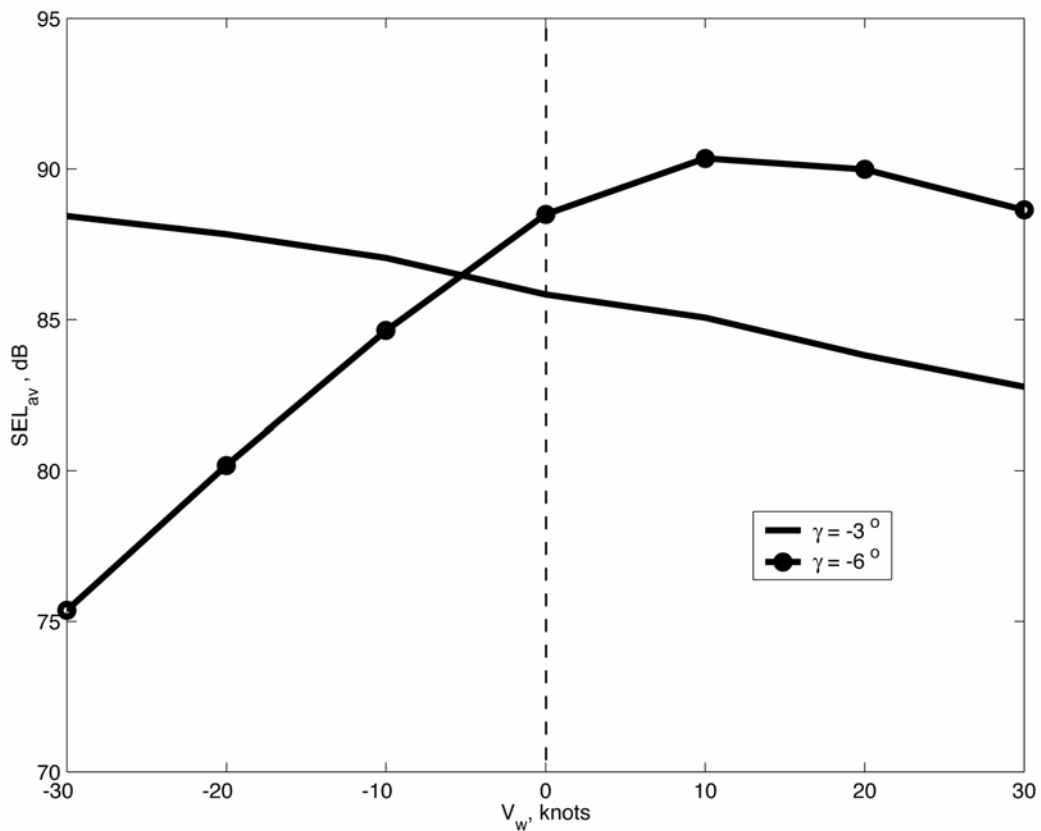


Figure 5.28 Effect of Piloting Strategy 1 on  $SEL_{av}$  for constant speed descent at  $\mu = 0.165$ ,  $\gamma_g = -3^\circ$  and  $-6^\circ$  at different wind speeds.

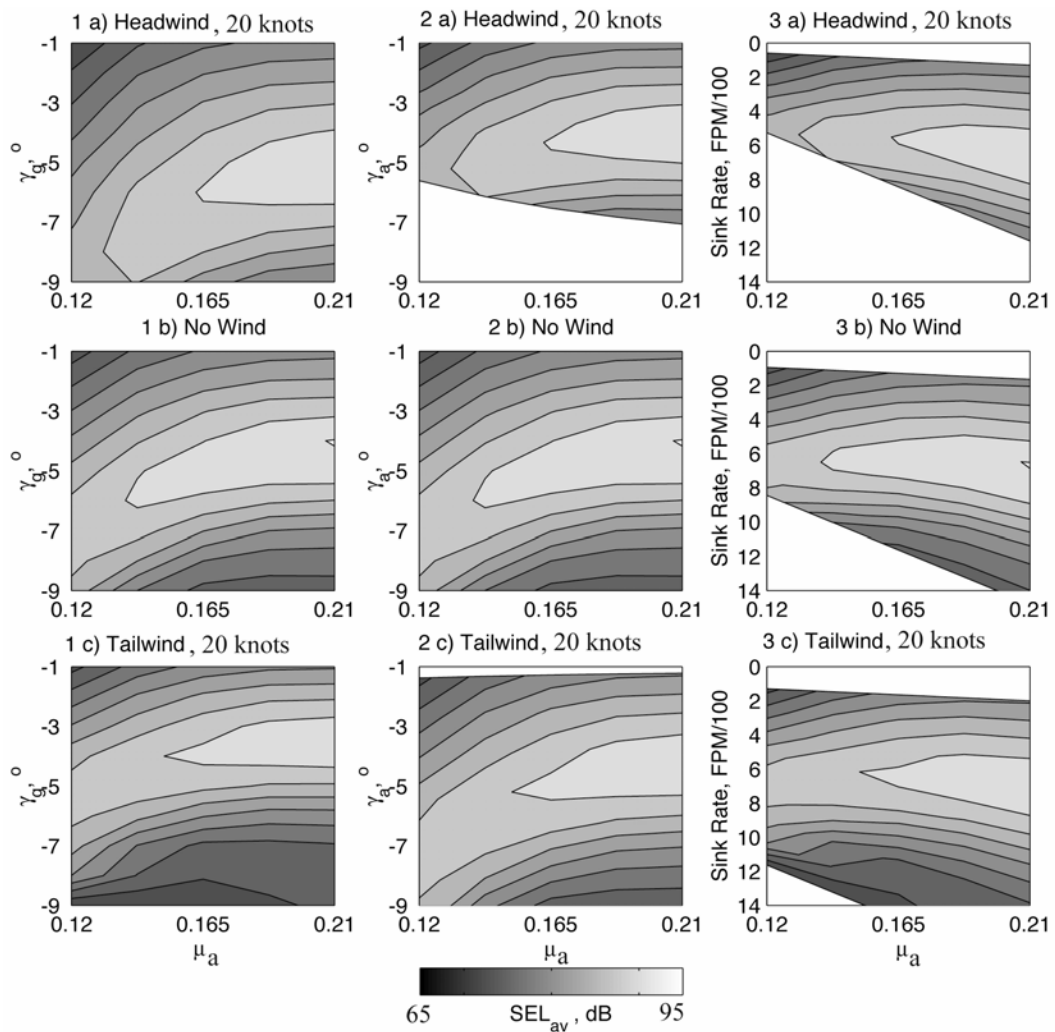


Figure 5.29 Effect of Piloting Strategy1 on SEL<sub>av</sub> as a function of 1)  $\gamma_g$  ; 2)  $\gamma_a$  and 3) Sink Rate in FPM under a) 20 knot headwind, b) no wind and c) 20 knot tailwind conditions.

### 5.3.3.2 Approach Procedure 2 (Piloting Strategy 2): Holding Rate of Sink and Flight Path in the ground reference frame

In the second approach it is assumed that the trajectory is fixed in space and that ground velocities at each spatial position are also specified:

$$V_{NW} = V_g \quad (5.13)$$

$$\gamma_{NW} = \gamma_g$$

This requires that the pilot or the guidance computer adjust the velocity of the helicopter with respect to the air-mass, to maintain a constant flight speed with respect to the ground at a prescribed glideslope. The aerodynamic flight path and the airspeed can be computed as follows:

$$\tan \gamma_a = \frac{\sin \gamma_{NW}}{\frac{V_w}{V_{NW}} + \cos \gamma_{NW}} \quad (5.14)$$

$$\frac{V_a}{V_{NW}} = \sqrt{1 + \left( \frac{V_w}{V_{NW}} \right)^2 + 2 \frac{V_w}{V_{NW}} \cos \gamma_{NW}}$$

Using small angle assumptions these relations can be approximated as

$$\gamma_a = \frac{\gamma_{NW}}{\frac{V_w}{V_{NW}} + 1} \quad (5.15)$$

$$\frac{V_a}{V_{NW}} = 1 + \left( \frac{V_w}{V_{NW}} \right)$$

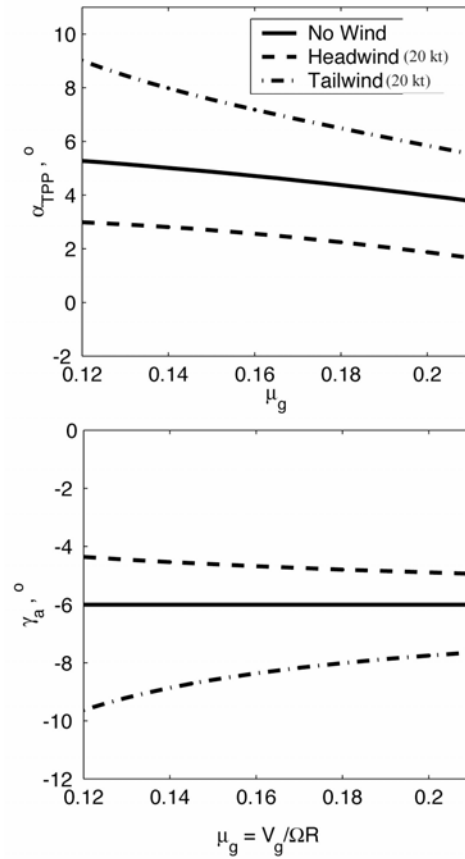


Figure 5.30 Variation of tip-path-plane angle and aerodynamic flight path angle as a function of non-dimensionalized ground speed in the presence of a 20 knot head/tailwind compared to the no-wind values during a  $-6^\circ$  descent for Piloting Strategy 2.

In this approach, the pilot, in the presence of wind, maintains the specified flight speed and flight path with respect to the ground, and holds rate of sink, the same as in the no-wind situation. This causes the helicopter to operate at higher airspeeds in a headwind and makes the aerodynamic descent angle more shallow, resulting in a tip path plane angle that is more negative in a headwind than in the absence of wind. Figure 5.30 shows the variation of tip-path-plane angle and aerodynamic flight path angle as a function of non-dimensionalized ground speed. A 20 knot headwind results in a higher airspeed, a lower tip-path-plane angle and a shallower aerodynamic flight path angle. 20 knot tailwinds have the opposite effect. Unlike in approach procedure 1, parameter changes are not directly proportional to wind velocity, changes in tip-path-plane and aerodynamic flight path angle are observed to be greater for a tailwind than for a headwind. In Fig. 5.30, the baseline case, corresponding to the central solid black line represents a  $-6^\circ$  descent in the absence of wind. Figure 5.31 shows the effect of Piloting Strategy 2 on tip-path-plane angle and the aerodynamic flight path angle, in the presence of a 20 knot head and tailwind. Changes in these parameters are observed to be greater under tailwind conditions at low flight speeds.

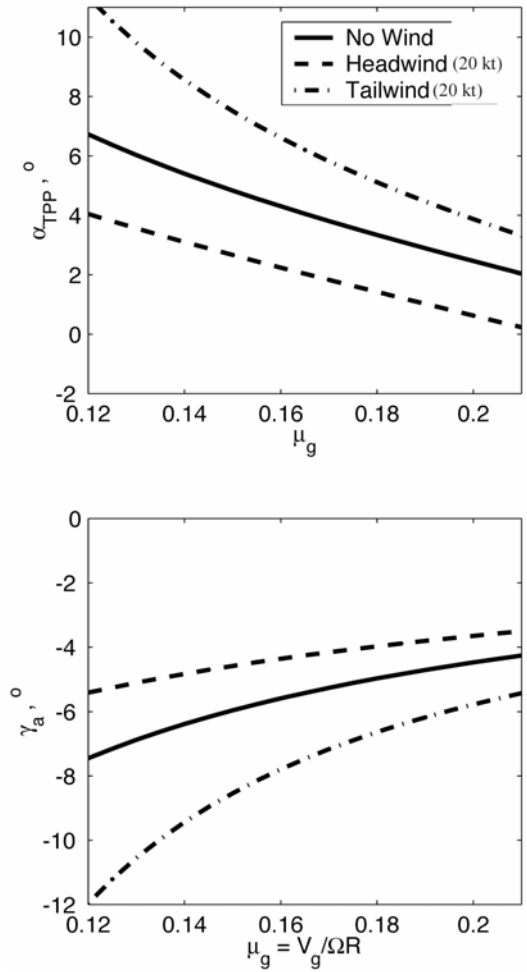


Figure 5.31 Variation of tip-path-plane angle and aerodynamic flight path angle as a function of non-dimensionalized ground speed in the presence of a 20 knot head/tailwind compared to the no-wind values at a sink rate of 700 fpm for Piloting Strategy2.

The effect of wind velocity ( $V_w = 0, \pm 10, \pm 20, \pm 30$  knot) on the  $SEL_{av}$  on the ground is shown in Figure 5.32 for a typical approach with a flight speed of 73 knots and a flight path angle of  $-6^\circ$  and  $-3^\circ$ , defined with respect to the ground. It is observed that with headwinds at a  $-6^\circ$  inertial glideslope, the  $SEL$  values on the ground

increase, and with tailwinds the levels are reduced. The curve is quite non-linear and emphasizes the complex tradeoffs that are involved in calculating the effect of wind on ground annoyance levels. The basic trend can be partially explained by considering the variation of  $P_{av}$  with aerodynamic flight path angle and airspeed (Figure 5.33), as in the previous section. The three white dots in the center of each plot in this figure represent the  $P_{av}$  values on the radiation sphere for this approach under no wind conditions of a flight path angle of  $-3^\circ$ ,  $-6^\circ$  and  $-9^\circ$ . The  $P_{av}$  values under wind conditions can be obtained by traversing along contours of constant rate of sink, which are represented by the bold black lines in Figures 5.33. Since all flight path angles considered are shallower than  $-12^\circ$ , the airspeeds under wind conditions can be approximated to be  $V - V_w$ , where  $V$  is the flight speed with respect to the ground. For a 20 knot headwind, airspeed increases to about 93 knots and the  $P_{av}$  levels, obtained by traversing right along the constant rate of sink contours, are seen to be higher. A tailwind of 20 knots moves the airspeed left along the same curve to about 53 knots and the  $P_{av}$  level is observed to decrease for all the glideslope cases. The  $P_{av}$  values, corresponding to wind conditions, can therefore be obtained from Fig. 5.33 by moving along contours of constant rate of sink to the appropriate airspeed.

Figure 5.34 shows the contour plots of  $SEL_{av}$  expressed as a function of airspeed and inertial flight path angle. Under headwind conditions, the aerodynamic flight path angle becomes less negative and the airspeed increases, and so the  $SEL_{av}$  values increase. The opposite is observed in the presence of tailwinds, with  $SEL_{av}$  values reducing.

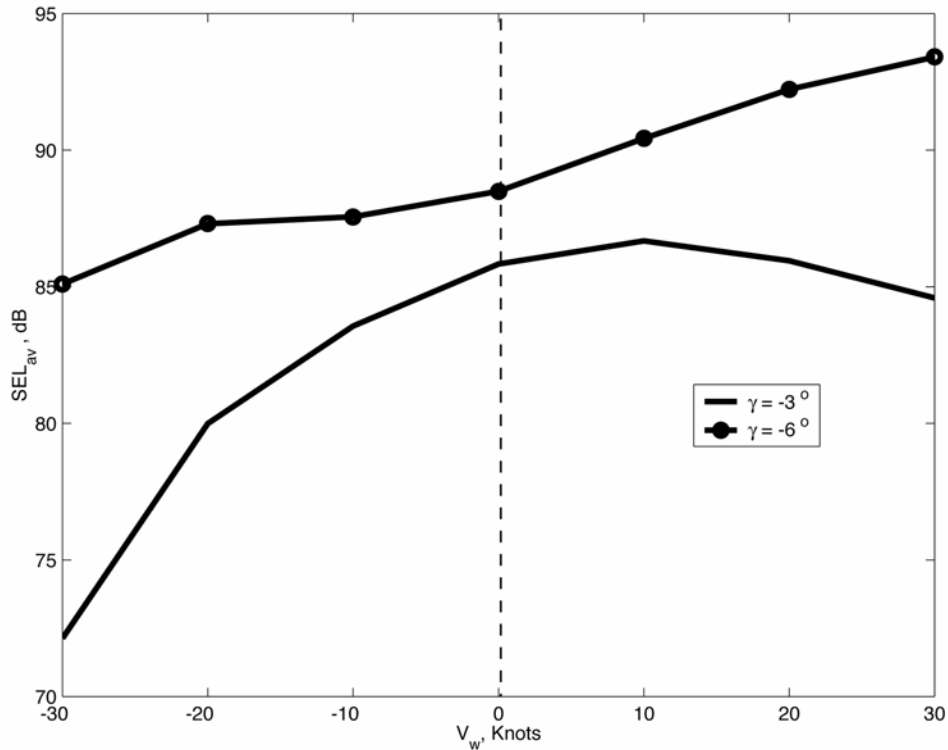


Figure 5.32 Effect of Piloting Strategy 2 on  $SEL_{av}$  for constant speed descent at  $\mu = 0.165$ ,  $\gamma_g = -3^\circ$  and  $-6^\circ$  at different wind speeds.

### 5.3.4 Noise Abatement Profiles and the Effect of Wind

In the previous section two distinct landing approaches were selected as candidate trajectories for lowering BVI noise: the use of steep approaches with a controlled deceleration along the flight path, and the deployment of an X-Force device at moderate airspeeds and shallow flight path angles. Both control techniques were predicted to be effective at substantially reducing noise annoyance levels on the ground in zero wind conditions. Their effectiveness in the presence of a steady headwind or tailwind, using Approach Procedure 2, is evaluated below.

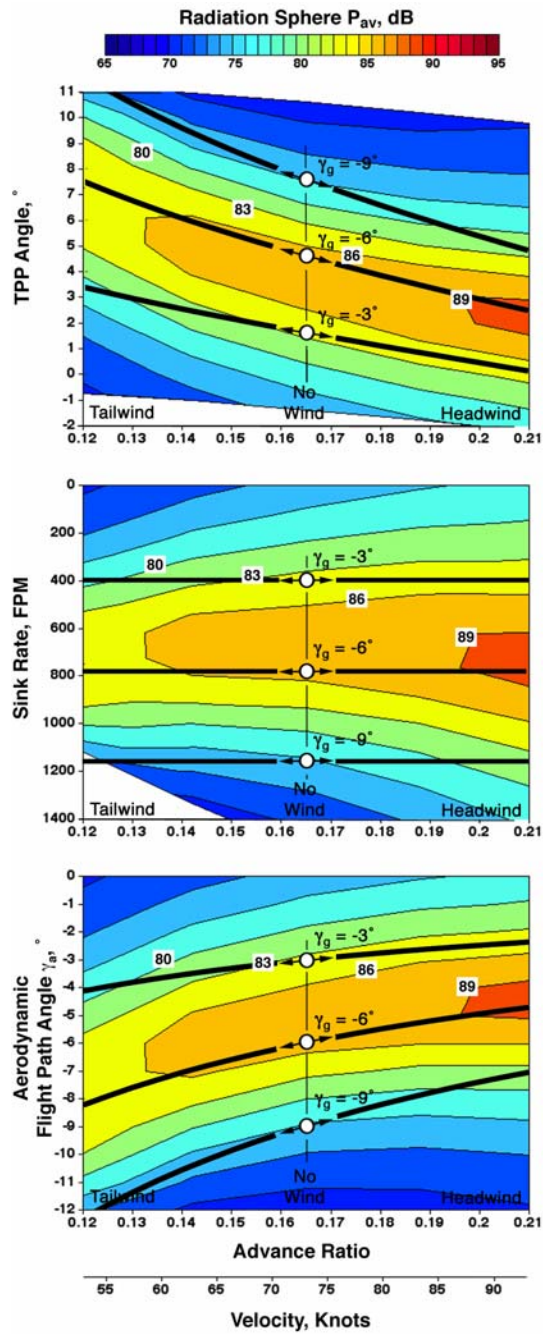


Figure 5.33 Changes in average radiated sound power in the presence of a 20 knot head/tailwind for approach procedure 2 at  $\gamma_g = -3, -6$  and  $-9$  and  $\mu_g = 0.165$ .

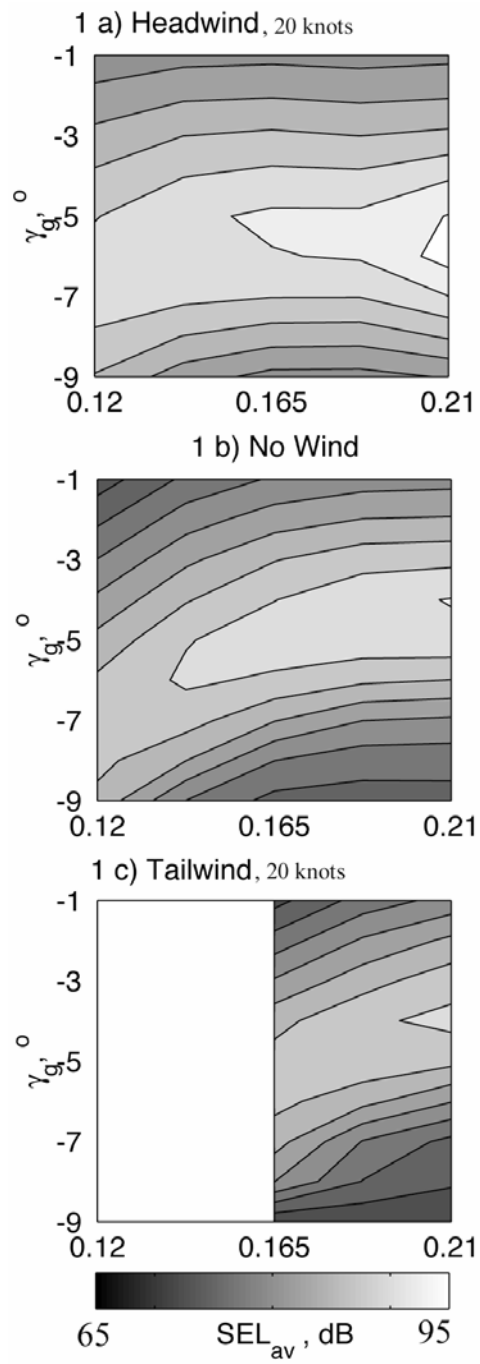


Figure 5.34 Effect of Piloting Strategy 2 on  $SEL_{av}$  as a function of  $\gamma_g$  under a) 20 knot headwind, a) no wind and a) 20 knot tailwind conditions.

The first noise abatement technique considered employs a moderate to steep approach and uses deceleration parallel to the flight path of the helicopter to help reduce ground annoyance noise levels. Figure 5.35b shows the *SEL* contours generated by the AH-1 helicopter executing a 0.05g decelerating approach at a flight path angle of  $-6^\circ$  (Fig. 5.17). The flight velocity is varied from 93 knots ( $\mu=0.21$ ) to 53 knots ( $\mu=0.12$ ). The deceleration is applied at the final stage of the trajectory, with the deceleration ending at location  $x = 0$ ,  $y = 0$ . The *SEL* levels, in regions on the ground below the deceleration segment of the trajectory, are considerably reduced compared to constant speed trajectories with a flight path angle of  $-6^\circ$  at any flight speed from 50 to 90 knots.

The highest *SEL* regions in Figure 5.35b occur near the terminal portion of the trajectory where the helicopter is decelerating close to the ground and the distances between the ground observer locations and the effective BVI source positions are quite small. The performance state corresponding to a deceleration of 0.05g at  $-6^\circ$  is approximately equivalent to a steady state condition at the same speed but with an effective flight path angle of about  $-9^\circ$ . At this effective flight path angle, noise levels increase as advance ratio decreases, further contributing to the high *SEL* values close to  $x = 0$  ft,  $y = 0$  ft.

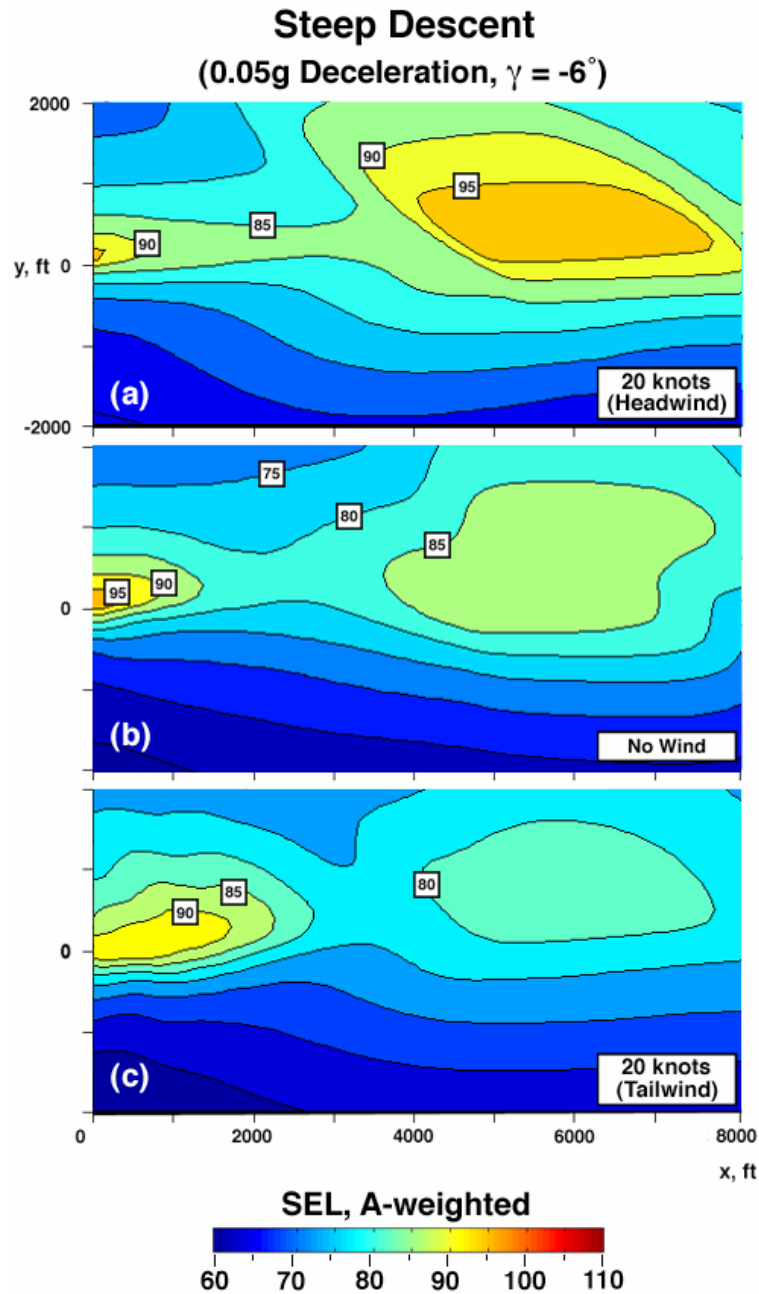


Figure 5.35 Effects of wind on steep decelerating descents: a) 20 knot headwind; b) no wind; c) 20 knot tailwind

The *SEL* contour levels for the decelerating trajectory described above, are also presented for a helicopter with 20 knot headwind and tailwind conditions (Figure

5.35a and 5.35c, respectively). With headwinds (Figure 5.35a), as the helicopter descends at a constant speed of 93 knots with respect to the ground ( $x > 5000$  ft), the pilot must increase airspeed to 113 knots to maintain his chosen trajectory in the ground based axis system, causing significant increases in *SEL* levels on the ground. The *SEL<sub>av</sub>* increases from 82.6 dB without wind to 88.9 dB with a 20 knot headwind. A majority of this increase is attributable to the constant speed portion of the trajectory.

With tailwinds (Figure 5.35c), the noise levels attributable to the constant speed segment, which now has an airspeed of 73 knots, are lessened. However, the *SEL* levels do increase near the terminal portion of the trajectory because of low effective advance ratios. The net effect is a *SEL<sub>av</sub>* reduction to 80.3 dB level. Consequently, Approach Procedure 2 with 0.05g deceleration is somewhat more effective under tailwind conditions, but fares poorly with headwinds.

The effect of winds on the noise abatement approach with fuselage drag changes (X-force control) at shallow flight path angles is examined next. Reduction of ground annoyance by the use of an X-Force device for the AH-1 helicopter at constant 93 knots ( $\mu = 0.210$ ) and 3° descent angle is shown in Figure 5.36b. For comparisons, the *SEL* contours for a descent under similar conditions, but without X-Force, is shown on the right side of Figure 5.36d. Substantial reductions in *SEL* levels are noted over the entire ground plane, as was shown in Fig. 5.19.

The effectiveness of using an X-Force device for noise abatement in the presence of wind is analyzed by studying the change in *SEL* contours under 20 knot headwind and tailwind conditions. Headwinds tend to reduce *SEL* levels for the case shown in Figure 5.36a with the AH-1 helicopter descending at 93 knots ( $\mu = 0.21$ ) and a descent angle of  $3^\circ$  (Figure 5.36). The reason being that, with a headwind of 20 knots, the airspeed of the aircraft with respect to the airmass increases to about 113 knots and the aerodynamic flight path angle becomes shallower; thus, enabling the tip-path-plane angle to become more negative. The drag of the aircraft also increases and the induced downwash is reduced as airspeed with respect to the airmass increases. The net effect of all these factors is to push the wake further below the rotor and substantially reduce the ground annoyance levels compared to the zero wind case.

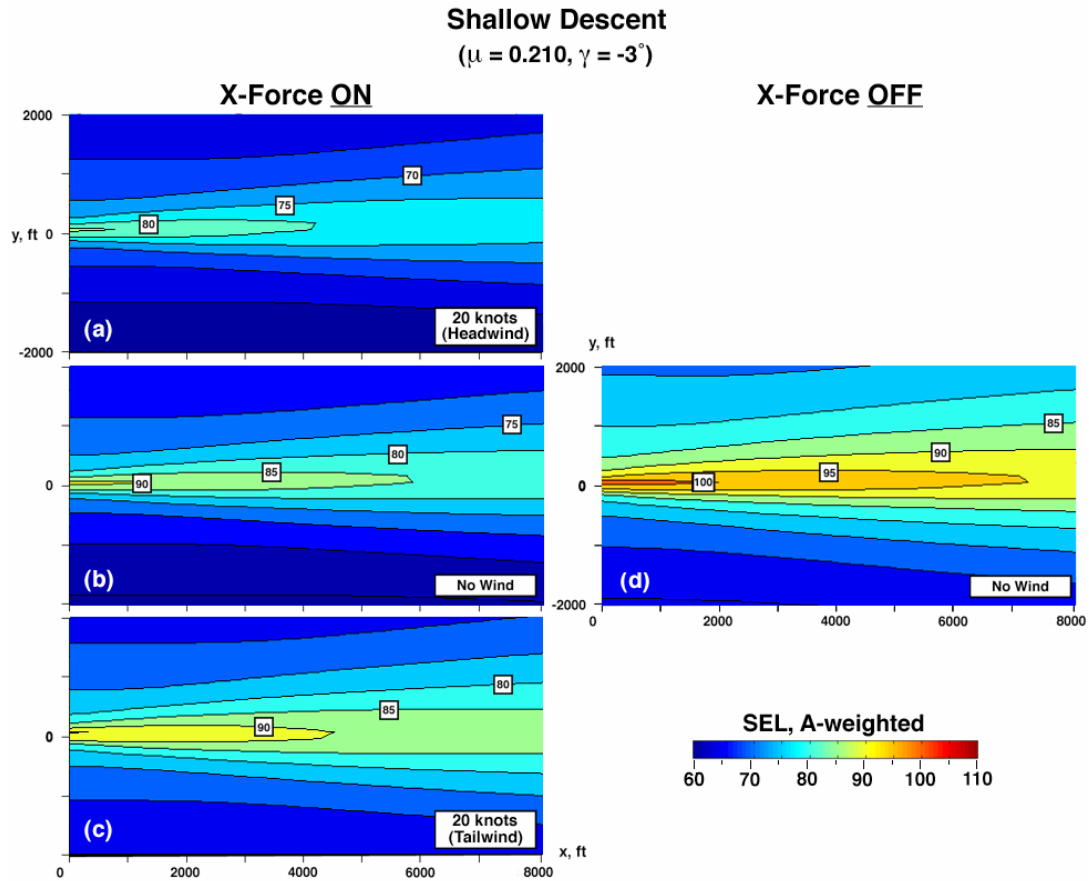


Figure 5.36 Effects of wind on shallow descents: with X-Force, a) 20 knot headwind; b) no wind; c) 20 knot tailwind; d) no X-Force, no wind

The trend is reversed for the tailwind situation as shown in Figure 5.36c. Under tailwind conditions, the airspeed with respect to the airmass reduces to about 73 knots. This causes the downwash to increase; but this is more than compensated by the reduction in the downward component of airspeed passing through the rotor disk. The net effect is to cause the shed vortices to operate closer to the rotor blades, resulting in an increase in BVI noise exposure on the ground. However, it should be noted that even under the unfavorable effect of tailwinds, the *SEL* levels are

significantly lower than if the X-Force devices are turned “off” for the same approach (Figure 5.36d). X-Force devices are thus deemed to be a reasonably good noise abatement strategy in the presence of headwinds and tailwinds of about 20 knots.

### **5.3.5 Noise Exposure and Piloting Implications**

As is apparent from the previous discussions on the two possible piloting approaches under head/tailwind conditions, the acoustic radiation in the medium seems to dominate ground noise trends. These radiation characteristics are different for each helicopter and can be described by a mapping of total BVI sound power as a function of velocity and descent angle. Consequently, the airspeed and the effective aerodynamic flight path angle determine ground exposure levels at a given inertial flight path angle.

Approach procedure 1, changes the aerodynamic flight path angle while maintaining airspeed; the orientation of the tip-path plane with respect to the horizon also remains unchanged compared to the no wind situation. The ground speed changes and so the helicopter takes a longer time along the descent path in a headwind. Under shallow descent conditions for the AH-1 helicopter, headwinds tend to reduce ground noise levels while small tailwinds increase ground noise. Under steeper descent conditions the effect is reversed, with headwinds increasing noise levels and tailwind lowering noise levels. Tailwinds tend to increase the air-mass rate of sink (decreasing the flight

path further), which may become a safety issue when flying relatively high rates of sink.

In Approach 2, airspeed, aerodynamic flight path angle and the orientation of the tip-path-plane relative to the horizon change. Using this approach for the AH-1 helicopter, headwinds tend to generally increase noise levels while tailwinds reduce noise levels. The possibility of coming close to high sink rate boundaries in the presence of a tailwind is greater than in approach 1 because the steepening of aerodynamic flight path angle is accompanied by a reduction in airspeed. The change in flight path angle associated with approach procedure 2 is always greater than that in approach procedure 1 – implying that using approach 2 in the presence of tailwinds must be done carefully so as to keep the helicopter within its operational limits.

The effect of approach procedures 1 and 2 on the average radiated BVI sound power are compared in Fig. 5.37, for a wind velocity of 10 knots, on a rate of sink versus flight velocity plot. The baseline flight condition is taken to be a flight velocity of 73 knots and a rate of sink of 700 feet per min. Approach 1 is accompanied with a reduction in the radiated noise for both headwinds and tailwinds. Approach 2 results in an increase in noise during a headwind and a decrease in noise during a tailwind. This operational plot can be used to estimate and compare the effect of these two piloting approaches under different headwind and tailwind conditions and for different baseline operational flight conditions.

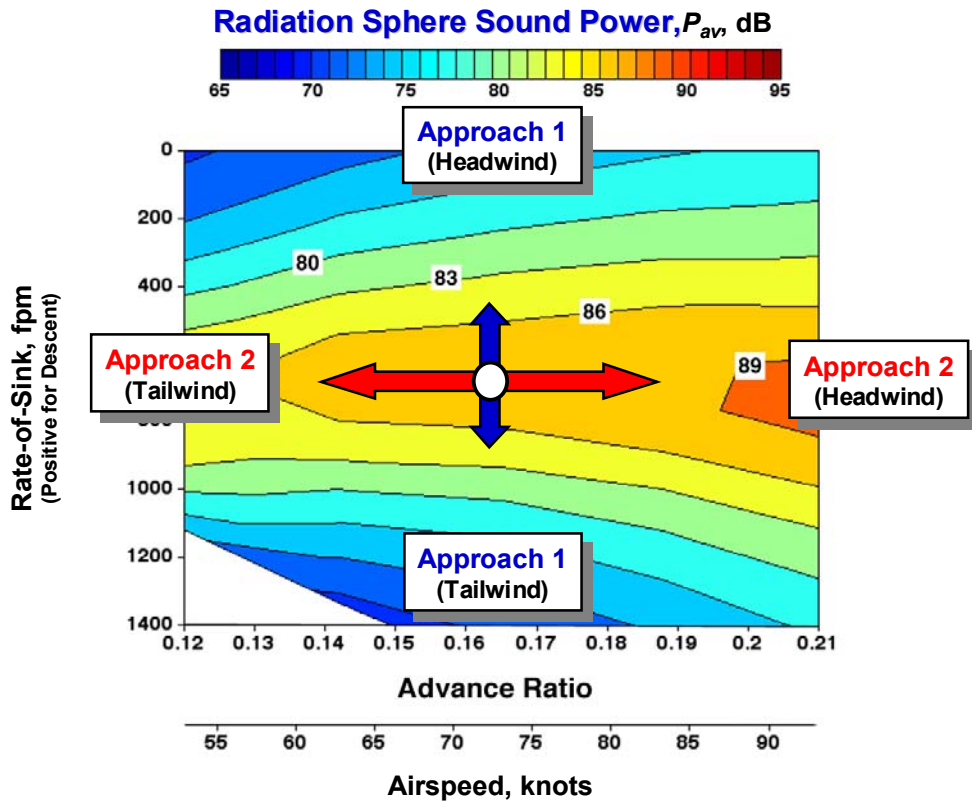


Figure 5.37 Effect of Approach Procedures 1 and 2 on the average radiated sound power.

## Chapter 6

### Summary and Conclusions

This research develops and investigates a Quasi-Static Acoustic Mapping (Q-SAM) approach to the flight trajectory management of helicopter Blade-Vortex Interaction (BVI) noise. The Q-SAM approach is based on the principle that the noise that is radiated by the helicopter during slowly maneuvering flight is similar to the noise radiated during equivalent but different steady state flight conditions.

The quasi-static equivalence between descent and deceleration, based on the X-force balance equation expressed in the “wind” axis system, is studied through various orders of flight dynamics modeling. A lower order flight dynamics model is developed to study tip-path plane performance behavior during slow longitudinal maneuvers. A higher order flight dynamics model is also adapted and used to simulate slow longitudinal maneuvers. The predicted tip-path plane performance parameters, tip-path plane angle, thrust and inflow through the rotor disk, are compared with the quasi-static X-force equation.

A storage-based acoustic mapping technique, extended to slowly maneuvering longitudinal flight based on the Q-SAM approach, is implemented to study helicopter main rotor Blade-Vortex Interaction (BVI) noise radiation and exposure associated

with helicopter descent operations. The Quasi-Static Acoustic Mapping (Q-SAM) method has been used to relate helicopter performance and trajectory parameters to control BVI in-flight noise radiation and ground noise and annoyance levels. The Q-SAM method can use measured or predicted acoustic data to map equivalent steady-state noise levels on a series of radiation spheres to positions on the ground plane using quasi-static estimates of helicopter performance. It explicitly includes helicopter velocity (advance ratio), flight path angle, acceleration parallel to the flight path, and vehicle drag as independent parameters enabling noise radiation to be directly tied and physically related to the quasi-static performance of the helicopter. Various approach trajectories are formulated and analytical estimates of the BVI noise radiation characteristics associated with a full-scale two-bladed rotor are mapped to the ground using this quasi-static mapping approach.

A methodology is developed to study the effect of steady headwinds and tailwinds on ground noise exposure and noise radiation associated with helicopter BVI noise. This methodology is implemented using the Q-SAM technique developed, and associated sound exposure metrics on a ground observer plane are estimated.

## **6.1 Major Conclusions**

The major conclusions are:

1. **The main rotor tip-path plane exhibits “trim-like” behavior during slow decelerating flight.** The main rotor performance parameters, tip-path plane angle, thrust and inflow, during slowly decelerating longitudinal flight are shown to be nearly identical to equivalent steady-state descent conditions. This equivalence is seen to extend to the entire flight state of the helicopter relative to the wind axis system.

2. **Pilot control requirements along slow deceleration maneuvers are close to the equivalent trim values.** The variation of control requirements during slow longitudinal maneuvers is shown to be near quasi-static. This equivalence in control states has been successfully used to predict flight control requirements during slow longitudinal maneuvers. Lateral dynamics are shown to be effectively controlled and suppressed during these longitudinal maneuvers.

3. **The helicopter pitch attitude is a good indicator of the level of deceleration at a given flight velocity, for slow decelerations ( $|dV/dt| < 0.1g$ ) along shallow flight path angles ( $|\gamma| < 10^\circ$ ).** In the moderate flight velocity range, in level flight, the helicopter pitch attitude remains fairly level under steady flight conditions. Changes in deceleration in g's along the flight path can be directly discerned as changes in helicopter pitch attitude in radians. This can serve as a useful piloting cue to implement controlled deceleration profiles.

4. **The limits of the quasi-static acoustic equivalence are set by rotation rates of the tip-path plane relative to the medium.** The tip-path plane pitch rates are of the same order as the fuselage pitch rates for the deceleration maneuvers studied. The rotation rate is shown to be a function of vehicle drag characteristics, flight velocity, vehicle deceleration and rate of change of deceleration. The pitch rate remains small ( $q < 0.2$  deg per sec or  $q/\Omega < 0.00013$  for a deceleration of 0.075g) during the constant deceleration stage. During the transient stage, the rate of change of deceleration sets the level of peak pitch rate ( $q < 0.5$  deg per sec or  $q/\Omega < 0.0003$  for a rate of change of deceleration of 0.0094 g per sec). These rotation rates result in modifying the induced velocity distribution over the rotor disk. The lateral coefficient of the linear dynamic induced velocity distribution is seen to be sensitive to longitudinal rotation rates.

5. **Quasi-Static performance modeling captures many of the important effects of slow decelerations on the tip-path plane angle, helicopter pitch attitude and pitch rate.** Inverse simulation based lower order flight dynamics modeling provides idealized solutions of the actual trajectories obtained using the higher order modeling. These solutions work well for slow maneuvers within the limits of the quasi-static equivalence. For more severe maneuvers they fail to capture the details of the effect of pilot controls on vehicle and main rotor dynamics. These lower order models can therefore be used as a guide in the design of validation experiments or practical flight operations.

6. **The shape of the average radiated BVI sound power ( $P_{av}$ ) as a function of advance ratio and rate of sink is similar to the shape of the average BVI noise ground exposure level contours ( $SEL_{av}$ ) for the AH-1 helicopter.** This suggests that flying to avoid high levels of BVI noise radiation also minimizes the average level of annoyance on the ground in areas near the approach corridor. Shallow and steep approaches, at low airspeeds tend to minimize the average level of annoyance on the ground. Such flight conditions are associated with high inflow through the rotor disk and consequently large BVI miss distances. Intermediate sink rates cause the shed vortices to remain in the plane of the rotor causing the radiation of high average BVI power levels.

7. **Steady head and tailwinds significantly alter the ground annoyance levels for two piloting approach procedures suggested and analyzed in this research.** These trajectories maintain the inertial flight path in the presence of wind and either hold airspeed or ground speed the same.

- I. Approach Procedure I maintains the inertial glideslope and the airspeed the same as in the no-wind situation. Changes in ground noise profiles for low to moderate windspeeds are dominated by the resulting changes in aerodynamic flight path angle. Changes in wind-related propagation factors do not contribute significantly to ground noise levels for the flight conditions studied here. Tailwinds could potentially degrade safety and performance, especially at high rates of sink and low speeds. For the AH-1 helicopter in shallow descents, Approach Procedure I results in reduced noise levels in the presence

of a headwind and increased  $SEL_{av}$  in the presence of a tailwind. In steeper descents, the opposite trend is probable. At conditions corresponding to peak  $P_{av}$  for the AH-1 helicopter at any airspeed, the effect of either headwinds or tailwinds is to reduce noise levels.

II. Approach Procedure II maintains the inertial glideslope and the ground speed the same as in the no-wind situation. Changes in ground noise profiles for low to moderate windspeeds are dominated by the effect of changes in aerodynamic flight path angle and airspeed. Changes in wind-related propagation factors do not contribute significantly to ground noise levels for the flight conditions studied here. Tailwinds could especially degrade safety and performance, because a reduction in airspeed is accompanied by a steepening of flight path angle. For the AH-1 helicopter at all rates of sink this approach results in a reduction in noise levels in a tailwind and increased  $SEL_{av}$  in the presence of a headwind. However at some shallow flight path angles the SEL levels can reduce slightly in a headwind. It is this approach that will likely be used for many DGPS approaches.

8. **Noise abatement trajectories have been successfully formulated through the use of flight trajectory control of flight velocity, flight path angle and vehicle deceleration.** Steep approaches with deceleration are shown to be an effective noise abatement strategy. The effect of deceleration is to make the tip-path plane angle more positive. Steep descent angles are also associated with positive tip-path plane angles. The combination of a steep descent angle and deceleration along the flight

path has the effect of “pushing” the wake above the rotor disk in its first and fourth quadrants. This increases miss-distances associated with the important BVIs, which results in low BVI noise radiation. A two-segment decelerating trajectory has been shown to be especially effective in reducing ground noise exposure associated with BVI noise radiation. The influence of headwinds and tailwinds on steep decelerating approach trajectories along a constant flight path angle and with velocity specified at fixed positions in space along the trajectory has been investigated. Headwinds effectively increase the  $SEL_{av}$  levels while tailwinds lower the  $SEL_{av}$  levels. Tailwinds also force steeper flight path angles to be flown because the airspeed must be reduced to maintain the fixed space trajectory. A combination of low helicopter airspeeds and steep flight path angles is likely to make the helicopter more difficult to control precisely and may force the helicopter closer to its operational performance limits.

**9. An attempt to develop approach trajectories that minimize BVI noise radiation on the ground results in operations close to the acceptable performance limits of the helicopter during civilian descent flight.** Minimum BVI noise radiation is associated with steep accelerating climbs and steep decelerating descent flight conditions. Both these extreme performance conditions are likely to be dominated by other noise sources, like engine noise or tail rotor noise.

## 6.2 Recommendations for Future Work

The following research efforts are recommended for future work in this area:

**Experimental validation of the “Quasi-Static Acoustic Equivalence” between descent and deceleration.** A novel experimental in-flight test validation technique is proposed to validate the equivalence between the noise radiated during decelerating flight and the equivalent descent flight conditions. By attaching a spray-boom (Fig. 6.1), instrumented with microphones and sensors, to the helicopter, the acoustic signature of a maneuvering helicopter can be captured. The boom assembly remains fixed relative to the helicopter, which is a significant improvement over ground based-measurement techniques. This new in-flight technique, is suitable for maneuvering and turning flight.



Figure 6.0.1 In-flight test set-up – Bell206-B with spray boom.

This unique experimental technique poses interesting technical challenges. The directivity and location of the microphones relative to the effective noise sources associated with the helicopter are limited to the boom locations. The boom results in a significant increase in the effective flat-plate area of the fuselage, more than doubling the baseline value of  $6.5 \text{ ft}^2$  to about  $14 \text{ ft}^2$ . This significantly degrades the forward flight performance of the resulting experimental Bell-206 helicopter. The maximum allowable flight velocity is 90 knots ( $\mu = 0.22$ ) with the boom on. This additional “X-force” device [49], causes the zero average inflow condition to occur at higher descent angles at higher flight velocities compared to the baseline case. The tip-path plane angle and pitch attitude of the helicopter are more negative (lower) compared to the baseline Bell-206 at the same flight velocity. Also higher pitch rates are now experienced during the same deceleration maneuver, compared with the baseline configuration. The boom microphones are fixed relative to the helicopter fuselage while the main rotor BVI noise directivity is to be studied relative to the tip-path plane. The directivity or orientation of the microphones relative to the tip-path plane will vary as the longitudinal flapping of the helicopter varies. But since the longitudinal flapping is not significantly affected the low levels of pitch rates experienced during the maneuver, the equivalent descent and deceleration conditions would be associated with the approximately the same longitudinal flapping.

Further investigation of the Quasi-static acoustic mapping approach in longitudinal flight is recommended. The effect of changes in thrust coefficient and hover tip Mach number, on the radiated BVI noise should be explored. Also, the use of measured acoustic data, rather than analytical estimates, would yield more specific results pertaining to specific helicopters in an approach to a landing.

**Investigation of the effect of turning flight on radiated BVI noise** and the application of the quasi-static acoustic mapping approach to such low-g lateral maneuvers is recommended. The final approach to a heliport usually includes turning flight. The effect of changes in thrust coefficient, inflow, wake distortion and tip-path plane orientation effects on BVI noise radiation is likely to have an effect on ground noise exposure. The experimental program is ideally suited to study the acoustic radiation characteristics associated with turning flight.

**Investigation of the effect of real atmospheric effects like crosswinds, gusts and turbulence is also suggested.** Preliminary flight testing has shown the practical importance of the consideration of atmospheric gusts on the acoustic radiation of the helicopter. The consideration of sidewinds on vehicle trim and BVI noise radiation and exposure should be studied. This study will be very useful to generalize the effects of steady winds explored in this thesis. The study of these wind effects on source noise radiation, and its application to flight trajectory management tools is suggested.

**Investigation of other sources of helicopter noise** is also suggested. Apart from BVI noise, other main rotor noise sources like thickness noise, and harmonic loading noise should also be incorporated when trying to find acoustically optimal trajectories. Tail rotor noise could become significant when main rotor BVI noise is minimized. Tail rotor noise has not received much attention from researchers, owing mainly to a preoccupation with main rotor noise sources. However, tail rotor noise is accepted as a significant source of helicopter noise radiation, especially when BVI noise and HSI do not occur.

## Appendix A

### Tip path plane Estimation in Trim

A longitudinal trim model is developed to estimate the main-rotor performance parameters as a function of flight velocity and flight path angle during steady state flight, and closely follows the formulation in References [103] and [83]. Some salient features of this model are listed below:

- The helicopter subsystems included in this model are the main rotor, fuselage and the horizontal stabilizer.
- The main rotor equations are based on rigid, first harmonic flapping. Blade element theory and quasi-steady linear aerodynamics are used to approximate main rotor loads. Effect of blade flexibility is considered only for coning dynamics; the higher harmonics of elastic flapping are ignored. Effect of reverse flow is ignored. The effect of lag dynamics and elastic pitch dynamics are ignored. A fixed tip-loss and root cut-out are assumed. Close-form solutions are derived and used wherever possible [83].
- A prescribed wake model (Beddoe's wake [82]) is used for main rotor inflow. Effect of the main rotor downwash on the fuselage and the horizontal stabilizer are included using a curve fit of available data when available. The baseline analysis does not include this effect.

- The fuselage is modeled as a rigid body. The aerodynamic characteristics as a function of angle of attack and sideslip angle are included, when available. The baseline analysis assumed a constant equivalent flat plate area, and zero lift and pitching moment.
- The horizontal stabilizer is modeled using linear aerodynamics.

<i>Parameter</i>	<i>Symbol</i>	<i>Value (Range)</i>
Gross Weight	$GW$	3200 lb (2400-3200)
Gross Weight Coefficient	$C_w$	0.0033
Main Rotor RPM	$RPM$ $\Omega$	394 RPM 41.3 rad/sec
Main Rotor tip-Speed	$\Omega R$	688 fps
Main Rotor revolution time period	$T$	0.15 sec
Main Rotor Radius	$R$	16.65 feet
No. of Blades	$N_b$	2
Effective flat-plate area	$f_o$	6.5 feet <sup>2</sup>

Table A.1 Bell206-B Operational Parameters.

The longitudinal force balance equations are expressed in the wind axis system. The pitching moments are resolved along the body y-axis, about the helicopter center of gravity. The basic forms of the equations are shown below:

*X-Force Balance (Wind axis system):*

$$\alpha_{TPP} = \frac{-D/W - \gamma}{T/W}$$

where,

$$D \approx D_F + H_{TPP} + D_{HS}$$

*Z-Force Balance (Wind axis system):*

$$T/W = 1 - L/W$$

where,

$$L \approx L_F + L_{HS}$$

*Pitching moment Balance (Body axis system):*

$$0 = \frac{M_{MR} + M_{HS} + M_F}{I_y}$$

where,

$$M_{MR} = f(T, \beta_{1C}, H_{TPP})$$

$$M_{HS} = L_{HS} x_{HS}$$

$$M_F = M_{F,0} + M_{F,1} \alpha_F$$

*Compatibility:*

$$\theta = \alpha_{TPP} + \gamma + \beta_{1c} - \theta_S$$

*Main Rotor Forces and controls:*

$$\theta_o = f(T, \alpha_{TPP}, \beta_{1c} + \theta_{1s}, V, q)$$

$$\theta_{1s} = -\beta_{1c} + f(\theta_o, \alpha_{TPP}, V, q)$$

$$H_{TPP} = f(\theta_o, \alpha_{TPP}, V, q)$$

*Fuselage Aerodynamics:*

$$D_F = D_{F,0} + D_{F,1}\alpha_F + D_{F,2}\alpha_F^2$$

$$L_F = L_{F,0} + L_{F,1}\alpha_F$$

$$M_F = M_{F,0} + M_{F,1}\alpha_F$$

*Horizontal Stabilizer Aerodynamics:*

$$L_{HS} = L_{HS,0} + L_{HS,1}\alpha_{HS}$$

$$D_{HS} = D_{HS,0} + D_{HS,2}\alpha_{HS}^2 + \frac{L_{HS}^2}{f(V)}$$

Fuselage and horizontal stabilizer forces and moments are also incorporated using quasi-steady aerodynamics. The effect of the main rotor downwash on the fuselage and the horizontal stabilizer has been ignored at high advance ratios. At lower

advance ratios the effect of this downwash would be significant and its modeling is approximate at this stage. In reality the downwash factor would be some non-linear function of the advance ratio and the wake skew angle. This factor should be determined either experimentally or using sophisticated analytical codes. While these factors have a significant effect in determining the helicopter pitch attitude, the longitudinal flapping and the longitudinal cyclic pitch, their effect on the estimates of the tip-path plane angle, average inflow, the thrust coefficient and the collective control input are small.

This set of coupled static algebraic trim equations representing the average trim state of the helicopter over one rotor revolution can be expressed as:

$$F(V, \gamma, T, \alpha_{TPP}, \theta, \dots) = 0$$

with the flight velocity and flight path angle typically specified to characterize the trim state.

The RPM of the main rotor is assumed constant over the entire flight regime, even during slowly maneuvering flight. In reality the RPM governor would take some finite time to act, which would result in some additional main rotor dynamic modes, which have been ignored in the present study.

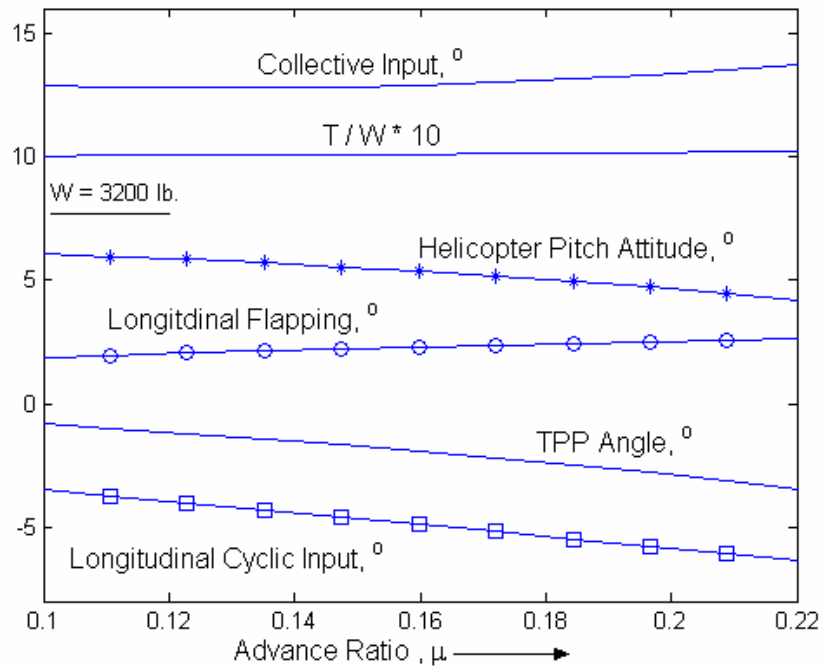


Figure A.1 Predicted performance parameters for the Bell-206B in trimmed steady-state forward flight: tip-path plane angle, thrust to weight ratio, collective pitch, longitudinal cyclic pitch, helicopter pitch attitude and longitudinal flapping.

The thrust coefficient, the main rotor tip-path plane angle, as well as the collective and longitudinal cyclic pitch inputs required to trim the model Bell 206 in level flight are shown in Fig. A.1 for a range of flight velocities ( $W = 3200$  lb). Also shown are the associated longitudinal flapping and helicopter pitch attitude. Comparisons are made with results obtained from the C-81 [103] code in Fig. A.2 ( $W = 2400$  lb). The thrust vector increases in magnitude slightly as advance ratio increases, and also tilts forward to balance the increase in fuselage drag. Also the tip-path plane becomes progressively more negative at higher flight velocities. This is primarily attributable to the increase in helicopter drag at higher flight velocities. The thrust coefficient and

the tip-path plane angle predictions compare very well with C-81 computations. These parameters are also the most significant in terms of main rotor BVI noise predictions. The predicted trends for the collective pitch match very closely.

When the H-force is resolved along the tip-path plane, its effect remains small, even up to an advance ratio of 0.2. It is to be noted that in the current analysis, the H-force in the tip-path plane is slightly under-predicted for advance ratios greater than 0.2.

The longitudinal cyclic input, pitch attitude and the longitudinal flapping predictions differ by about  $1^\circ$ . This alludes to differences in modeling the wake structure and rotor and body aerodynamics. The pitch attitude, the longitudinal cyclic pitch and flapping angle are sensitive to the modeling of rotor downwash on the fuselage and the horizontal stabilizer. The values shown assume that the induced velocity at the main rotor disk is felt entirely at both these aerodynamic bodies. An error of about  $1^\circ$  is attributable to this assumption over the entire range of flight path angle variation.

Some differences may also be attributable to the effect of lateral dynamics and control choices on longitudinal trim.

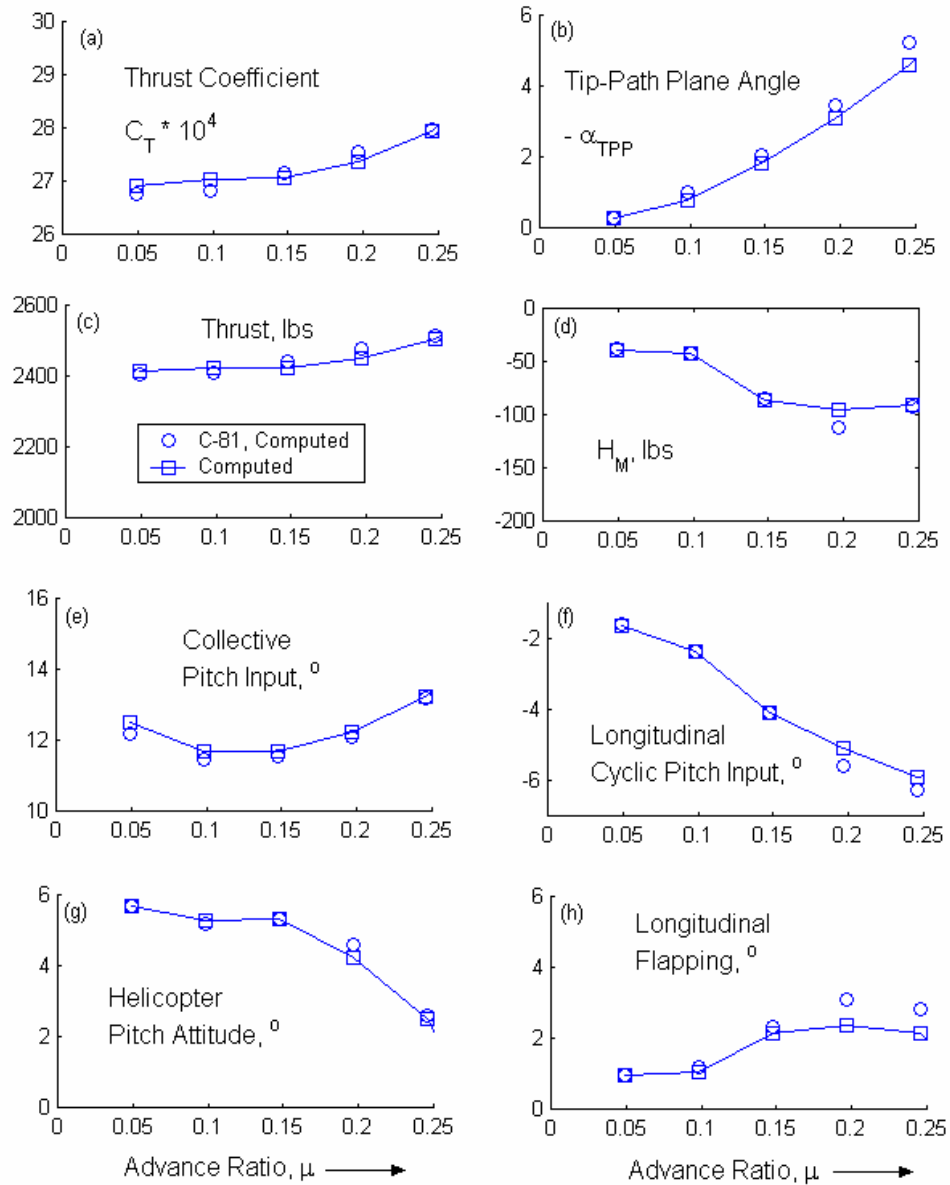


Figure A.2 Predicted performance parameters for the Bell-206B in trimmed steady-state forward flight: a) thrust coefficient, b) tip-path plane angle, c) thrust, d) main-rotor H force, e) collective pitch, f) longitudinal cyclic pitch, g) helicopter pitch attitude and h) longitudinal flapping.

## Appendix B

### Force Balances and Coordinate Systems

This appendix is an expanded treatment of some of the equations presented in section 3.1. Three coordinate systems are generally used to describe the overall motion of the helicopter. These are:

4. the gravity coordinate system,
5. the body fixed coordinate system, and
6. the “wind” coordinate system.

The origins of all these coordinate systems are placed at the center of gravity of the helicopter fuselage. The gravity coordinate system is used for reference. The z-axis of this system points “down” in the direction of gravity. The choice of x and y axes is arbitrary and is selected based on convenience in the context of each specific application. The basic force balance equations of the helicopter expressed in an inertial reference frame are:

$$m\dot{\vec{V}}_I = \vec{F}_I \quad (\text{B.1})$$

where the subscript “I” refers to the inertial reference frame, a non-accelerating, non-rotating coordinate system. While the gravity coordinate system is a non-rotating, accelerating system, the “wind” and body coordinate systems are in general rotating

accelerating systems, as is the tip-path plane coordinate system, described later. The force balance equations expressed along instantaneous gravity coordinates take the same form as the equation above,  $m\ddot{\bar{V}}_G = \bar{F}_G$ , where, the subscript “G” refers to the gravity coordinate system.

Any general non-inertial rotating right-handed coordinate system, with its origin at the center of gravity of the helicopter system, may also be used to express the above force balance equations. In such a reference frame the force balance equations take the following form:

$$m\left(\frac{\partial \bar{V}}{\partial t} + \bar{\Omega}_{NI} \times \bar{V}\right)_{NI} = \bar{F}_{NI} \quad (\text{B.2})$$

where the subscript “NI” refers to the general non-inertial rotating right-handed coordinate system. The orientation of this generic coordinate system is specified by its Euler angles,  $\phi_{NI}$ ,  $\theta_{NI}$  and  $\psi_{NI}$  relative to the gravity coordinate system (Fig. A.1). The rotation rates,  $p_{NI}$ ,  $q_{NI}$  and  $r_{NI}$ , associated with this coordinate system, expressed along its own axes,  $x_{NI}$ ,  $y_{NI}$  and  $z_{NI}$ , with unit vectors  $\mathbf{i}_{NI}$ ,  $\mathbf{j}_{NI}$  and  $\mathbf{k}_{NI}$ , in terms of the Euler angles and their rates, are:

$$\begin{aligned} p_{NI} &= \dot{\phi}_{NI} - \dot{\psi}_{NI} \sin \theta_{NI} \\ q_{NI} &= \dot{\theta}_{NI} \cos \phi_{NI} + \dot{\psi}_{NI} \sin \phi_{NI} \cos \theta_{NI} \\ r_{NI} &= \dot{\psi}_{NI} \cos \phi_{NI} \cos \theta_{NI} - \dot{\theta}_{NI} \sin \phi_{NI} \end{aligned} \quad (\text{B.3})$$

In such a frame, the X, Y and Z force balance equations take the following form:

$$\begin{aligned}m(\dot{u}_{NI} + q_{NI}w_{NI} - r_{NI}v_{NI}) &= X_{NI} \\m(\dot{v}_{NI} + r_{NI}u_{NI} - p_{NI}w_{NI}) &= Y_{NI} \\m(\dot{w}_{NI} + p_{NI}v_{NI} - q_{NI}u_{NI}) &= Z_{NI}\end{aligned}\tag{B.4}$$

The body-fixed coordinate system is defined in the usual way with  $x$  pointing “forward”,  $y$  pointing “right” or starboard and  $z$  pointing “down”. The Euler angles for this system are  $\phi$ ,  $\theta$  and  $\psi$ , and the rotation rates are  $p$ ,  $q$  and  $r$  along the body  $x$ ,  $y$  and  $z$  directions. The components of flight velocity along the  $x$ ,  $y$ , and  $z$  directions are  $u$ ,  $v$  and  $w$  respectively. The above equations, expressed in body fixed coordinates, are typically used for flight dynamics analyses.

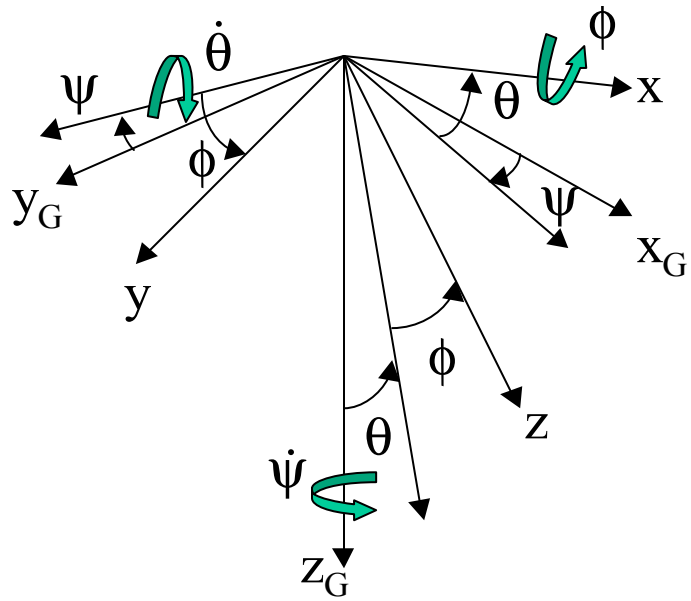


Figure B.1 Euler angles and rotation rates of a general right-handed coordinate system with respect to the inertial system.

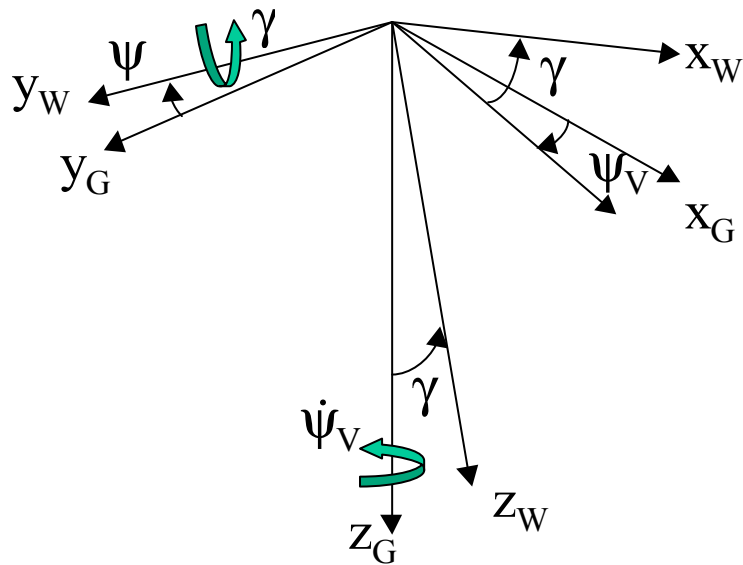


Figure B.2 Euler angles and rotation rates of the wind coordinate system with respect to the inertial system.

The “wind” coordinate system is defined with the x axis pointing along the velocity vector. The z and y axes of the “wind” coordinate system are arbitrary, and may be referenced to body coordinates in some flight dynamics analyses. In the current formulation, the y and z “wind” axes are referenced to the gravity coordinates as below:

$$\begin{aligned}\hat{j}_W &= \hat{k}_G \times \hat{i}_W \\ \hat{k}_W &= \hat{i}_W \times \hat{j}_W = \hat{i}_W \times (\hat{k}_G \times \hat{i}_W)\end{aligned}\quad (\text{B.5})$$

The flight velocity resolved along the “wind” axes, along with the associated Euler angles and rotation rates for the wind coordinate system, as shown in Fig. A.2, are:

$$\begin{aligned}u_W &= V; w_W = 0; v_W = 0 \\ \phi_W &= 0; \theta_W = \gamma; \psi_W = \psi_V \\ p_W &= -\dot{\psi}_V \sin \gamma \\ q_W &= \dot{\gamma} \\ r_W &= \dot{\psi}_V \cos \gamma\end{aligned}\quad (\text{B.6})$$

The force balance equations, expressed in this wind coordinate system, take the following form:

$$m\dot{V} = X_W$$

$$\begin{aligned}
mV\dot{\psi} \cos \gamma &= Y_W \\
-mV\dot{\gamma} &= Z_W
\end{aligned}
\tag{B.7}$$

The external forces,  $X$ ,  $Y$  and  $Z$ , are typically expressed in the body coordinates in flight dynamics simulations, and are now transformed to the wind coordinates using the transformation above.

$$\begin{aligned}
X_W &= \bar{F} \cdot \hat{i}_W \\
Y_W &= \bar{F} \cdot \hat{j}_W \\
Z_W &= \bar{F} \cdot \hat{k}_W
\end{aligned}
\tag{B.8}$$

where,  $\bar{F} = \bar{W} + \bar{F}_{MR} + \bar{F}_{TR} + \bar{F}_F + \bar{F}_{HS} + \bar{F}_{VT}$ . The  $x$ ,  $y$  and  $z$  components of the weight vector in the “wind” coordinate system are:

$$\begin{aligned}
\bar{W} \cdot \hat{i}_W &= -W \sin \gamma \\
\bar{W} \cdot \hat{j}_W &= 0 \\
\bar{W} \cdot \hat{k}_W &= W \cos \gamma
\end{aligned}
\tag{B.9}$$

The forces associated with the fuselage, tail rotor, horizontal stabilizer and vertical tail are transformed to obtain the effective force components along the three axis directions.

$$\begin{aligned}
\bar{F}_i \bullet \hat{i}_W &= -D_{i,W} \\
\bar{F}_i \bullet \hat{j}_W &= Y_{i,W} \\
\bar{F}_i \bullet \hat{k}_W &= -L_{i,W}
\end{aligned}
\tag{B.10}$$

where, the subscript “i” refers to each subsystem of the helicopter, excluding the main rotor: the tail rotor, horizontal stabilizer, vertical tail and the fuselage body.

## Appendix C

### Implementing the Q-SAM Method: Some Details

The Q-SAM method has been implemented as four distinct modules, each responsible for a specific task in Fig. C.1. These sub-tasks or modules are:

1. the *Aero-Acoustic module*,
2. the *Performance and Trajectory-Specification module*,
3. the *Sphere Selection module* and
4. the *Ground Noise module*.

The *Aero-Acoustic module* is responsible for developing the database of acoustic radiation spheres which forms the basis for ground noise prediction. This module is invoked off-line and makes an entire matrix of radiation spheres, required for use by the Q-SAM method, available to the program.

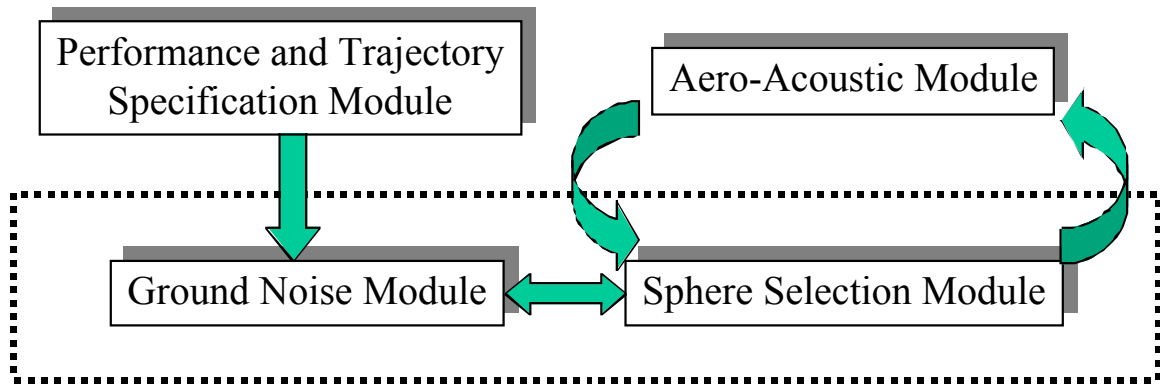


Figure C.1 The four modules used in the implementation of the Q-SAM method.

The *Performance and Trajectory-Specification module* is a model of the dynamics and performance of the rotorcraft. It computes the desired trajectory and the associated flight, control and trajectory parameters and stores the information in a file, thus, creating a database of trajectory files for use by the program.

The *Sphere Selection module* is responsible for obtaining an appropriate radiation sphere corresponding to each point along the trajectory. It essentially takes the flight and control parameter vector as input and uses this information to obtain a corresponding radiation sphere from the acoustic database.

Finally, the *Ground Noise module* computes various acoustic metrics on a specified observer plane taking into account the effects of sphere orientation and position relative to the observer plane, atmospheric absorption, Doppler shifts, spherical spreading, wind and A-weighting. Each module is described in greater detail in the rest of this section. The overlying code for the Q-SAM method, written in the C

language with some plotting subroutines implemented in Matlab, calls each module in turn to implement the entire ground noise mapping procedure.

### **Aero-Acoustic module**

The Q-SAM approach essentially decouples performance (dynamics and aerodynamics) calculations from the acoustic predictions. The quasi-static performance model is used to approximate the tip-path-plane and other relevant flight parameters to first order for “slowly” maneuvering flight. Acoustic radiation characteristics, however, are required for steady-state trimmed flight alone. This acoustic information is stored as spherical maps of noise radiation for each of several trim states as a function of the non-dimensional governing parameters. The Q-SAM approach can essentially work with many levels of aerodynamic and acoustic modeling – from very sophisticated analyses incorporating free-wake and three-dimensional, unsteady, compressible flow calculations, to simple prescribed wake, quasi-steady, incompressible methods. It is also possible to use measurements of acoustic data sets that surround the rotor, thus avoiding prediction of the noise altogether. The Aero-Acoustic module is responsible for developing, possibly multi-dimensional, matrices of radiation spheres, as a function of the governing non-dimensional parameters, for use by the Ground Noise prediction module. Currently, a simplified analytical model, that has been validated with some experimental data trends, is used (see Chapter 2). It is assumed that a separate matrix is made available

for each distinct source of rotorcraft noise. Currently only main rotor BVI noise is considered.

The acoustic radiation spheres represent a spherical map of the acoustic energy radiated by the helicopter over one rotor revolution. In the current work, radiation spheres or the mapping surfaces are assumed to be fixed to the medium. No transformations of the acoustic data (in terms of additional Doppler amplification effects) are required while mapping the noise to the ground under no-wind conditions because the ground observers are stationary with respect to the medium. For hub-fixed radiation spheres moving with the helicopter, the situation is similar to measurements made in a wind-tunnel, and the acoustic information has to be appropriately transformed before it can be propagated to the ground. A no wind condition is assumed at this initial stage.

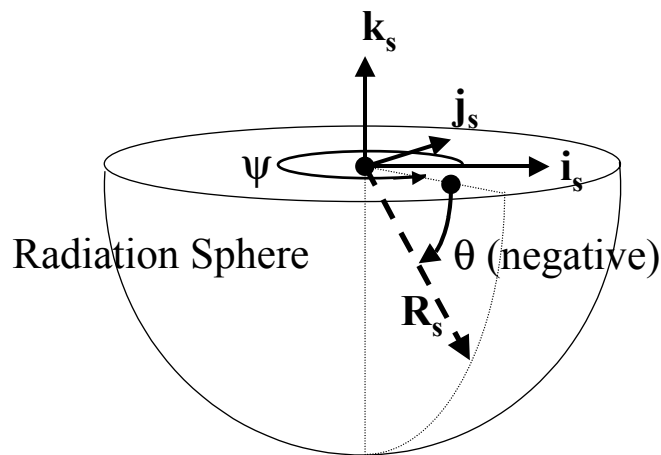


Figure C.2 Radiation sphere geometry.

The radiation spheres used are briefly described next. A point on the radiation sphere is described using spherical coordinates, by specifying the radius,  $R$ , the azimuth angle,  $\psi$ , and the elevation angle,  $\theta$ , as shown in Fig. C.2. For a specified choice of trim parameters  $(\mu, \alpha_{TPP})$ , the helicopter is assumed to perform one rotor revolution along a trajectory element, thus traversing a distance  $2\pi\mu R$  along the velocity vector. The center of the sphere is located at the mid-interval hub location, i.e. at the midpoint of this element (Fig. C.3). The median plane ( $\theta = 0^\circ$ ) is defined parallel to the tip-path plane. The elevation angle is taken to be negative below, and positive above this median plane. For instance, the flight velocity vector is oriented at an elevation angle of  $-\alpha_{TPP}$  relative to the median plane. All spheres used are defined with an elevation angle range of  $-90^\circ$  to  $30^\circ$ . The choice of  $0^\circ$  for the azimuth angle follows normal helicopter convention. It lies in the tip-path-plane (or median plane) and points opposite to the direction of the flight velocity of the helicopter. A positive azimuth angle corresponds to a counter-clockwise rotation in the median plane viewed from “above”. A cartesian coordinate system (with unit vectors  $\mathbf{i}_s, \mathbf{j}_s, \mathbf{k}_s$  along the  $x_s, y_s, z_s$  axis directions), with its origin at the center of the radiation sphere is also defined in addition to the spherical reference coordinates described above. The  $x_s$ - $y_s$  plane of this reference system lies in the median plane  $\theta = 0^\circ$ , with the  $x_s$ -axis pointing along  $\psi = 0^\circ$ ,  $y_s$ -axis pointing along  $\psi = 90^\circ$ , and the  $z_s$  axis pointing in the  $\theta = 90^\circ$  direction.

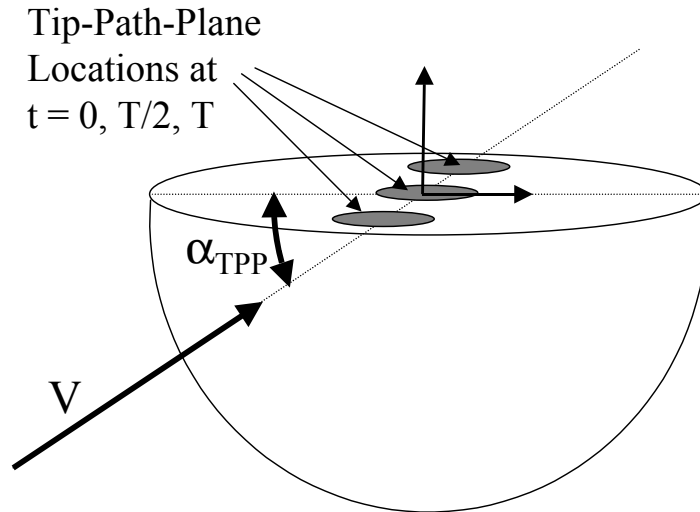


Figure C.3 Flight velocity vector and the tip-path-plane relative to the radiation sphere.

### Performance and Trajectory-Specification Module

A trajectory, in the present analysis, is divided into a sequence of contiguous trajectory elements as shown in Fig. C.4. An element corresponds to the distance traveled by the helicopter in one rotor revolution. An effective steady-state performance state  $(\mu, \alpha_{TPP})$ , representing an average over that rotor revolution, is assigned to each element at its control point. This point corresponds to the time and the position of the helicopter within each trajectory element when the rotor completes a half revolution. Thus, the trajectory is represented by a sequence of control points each of which is assigned a quasi-static performance state, along with an associated position and time.

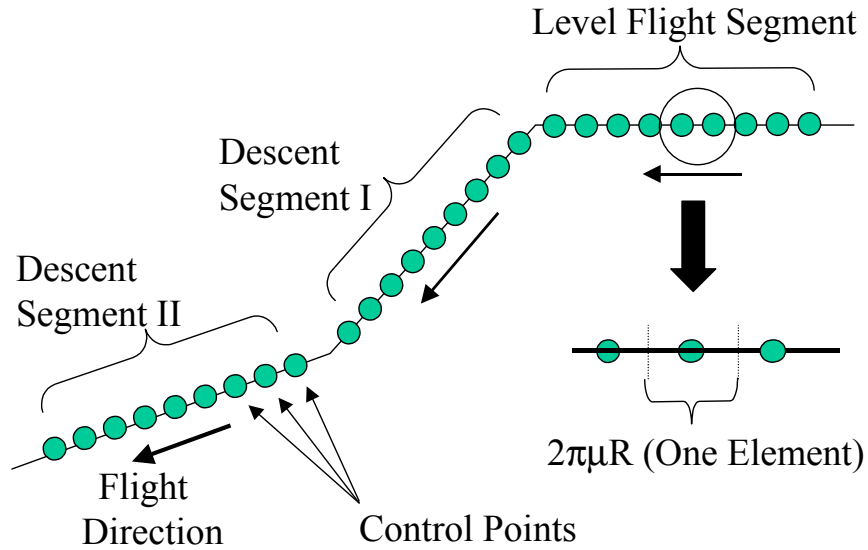


Figure C.4 Trajectory components: Segments, Elements and Control Points.

Each control point along the trajectory is specified by the control vector “ $X_{CP}$ ” =  $(t ; x, y, z, V; \gamma, f, dV/dt ; \mu, \alpha_{TPP}; M_{HT}, C_T)$ . Since at this stage only the main rotor acoustics is modeled, the trajectory is essentially a locus of hub locations along the flight path. Positions are specified with respect to a ground-based inertial reference axis system  $R_F$  with axes  $x, y, z$  and unit vectors  $\mathbf{i}, \mathbf{j}, \mathbf{k}$ .  $M_{HT}$  and  $C_T$  are usually held approximately constant for a given helicopter over the trajectory.

A sequence of contiguous control points or elements, with a constant value of  $[\gamma, f_x, dV/dt]$  is grouped together into a trajectory segment. Therefore, an aircraft trajectory is considered to be a sequence of one or more segments as shown in Fig. C.4. Cruise (Level flight at constant speed), for instance, is a single-segment trajectory which consists of flight at constant speed at a constant flight path angle ( $\gamma = 0^\circ$ ). Segments considered in the present work include:

1. flight at constant speed at a constant flight path angle, and
2. flight with a constant slow deceleration parallel to a constant flight path.

For the first case the performance state  $(\mu, \alpha_{TPP})$ , is constant along the segment and is the same for each control point, while in the second case the values of  $\mu$  and  $\alpha_{TPP}$  vary in a slow “quasi-static” manner along the segment.

The position of the aircraft is obtained by a direct integration of the velocity time history, which in turn is obtained from the specified acceleration time history profile along the trajectory. The Quasi-Static performance equation specifies the tip-path-plane angle at each time instant. Trajectories are constructed in reverse-time, which means that the specification commences at the final point on the trajectory, which is usually specified explicitly; the entire trajectory is then constructed by stepping back in time in one-rotor revolution decrements. The motivation for adopting this “backward-chaining” procedure is that for the approach trajectories considered in this study, the end state or final goal state ( $X_{CP}$ ) is usually “well-specified” or precisely defined, while the initial state, trim level flight at a given height, consists of a set of acceptable values for  $t$  and  $X_{HS}$ . This generalized implementation can handle multi-segment approach specifications, with constant flight path segments and either constant speed or a constant deceleration along that flight path. In general, as shown in Fig. C.5:

$$\left. \begin{aligned} \frac{dx}{dt} &= V \cos \gamma \cos \psi_v \\ \frac{dy}{dt} &= V \cos \gamma \sin \psi_v \\ \frac{dz}{dt} &= V \sin \gamma \end{aligned} \right\} \quad (\text{C.1})$$

where  $\psi_v$  is the flight velocity “azimuth”, shown in Fig. C.5. Note that  $\gamma$  and  $\psi_v$  are defined in the same way as  $\theta$  and  $\psi$ , for the radiation sphere, in Fig C.2, and that in general  $V$ ,  $\gamma$  and  $\psi_v$  could be specified as any nominally achievable sequence of values along the trajectory. In the current stage of implementation of the Q-SAM technique, all trajectories considered are assumed to be contained within the vertical  $x$ - $z$  plane, therefore  $\psi_v$  and  $y$  are 0 at all times along the trajectory.

The time derivative of the state vector therefore becomes:

$$\frac{dX_{HS}}{dt} = \begin{pmatrix} \frac{dx}{dt} \\ \frac{dy}{dt} \\ \frac{dz}{dt} \\ \frac{dV}{dt} \end{pmatrix} = \begin{pmatrix} V \cos \gamma \\ 0 \\ V \sin \gamma \\ \frac{dV}{dt} \end{pmatrix} \quad (\text{C.2})$$

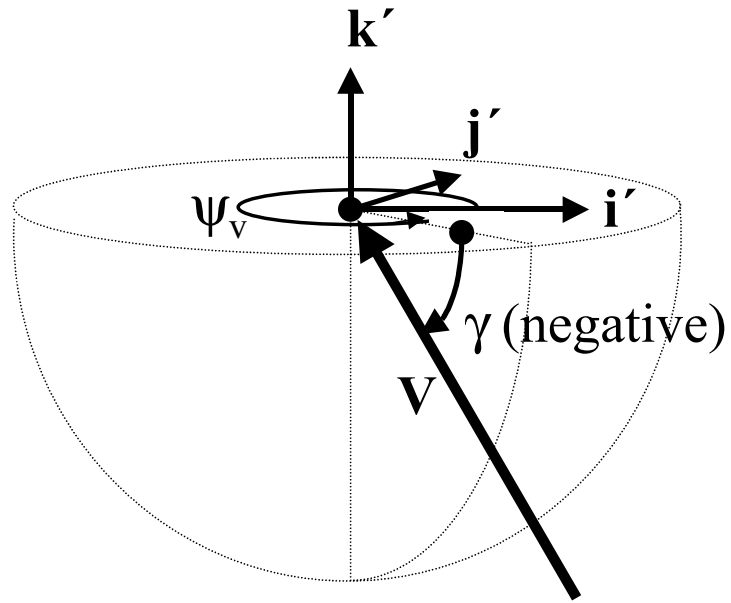


Figure C.5 Orientation of the flight velocity vector.

If “ $s$ ” is defined as a distance measure along the flight path (in the reverse direction), then state variables are updated using the following relations based on the value of the state vector at each time “ $t$ ” to obtain values at a previous time  $t + \Delta t$  :

$$\left. \begin{aligned}
 \Delta s &= -\left( V\Delta t + \frac{1}{2} \frac{dV}{dt} \Delta t^2 \right) \\
 V &\leftarrow V + \frac{dV}{dt} \Delta t \\
 x &\leftarrow x + \Delta s \cos(-\gamma) \\
 z &\leftarrow z + \Delta s \sin(-\gamma)
 \end{aligned} \right\} \quad (C.3)$$

where,  $\Delta t$  is negative,  $V$  is positive and  $dV/dt$  is negative for deceleration. Note that within any segment, the above equations hold for values of  $\Delta t$  that need not necessarily be small. In the present analysis a  $\Delta t$  corresponding to the negative of a rotor revolution period is assumed.  $\alpha_{TPP}$  is updated using the Quasi-Static equation. The trajectories considered, as mentioned before, consist of segments with constant flight path angle and either constant speed or small decelerations (up to  $-0.1\text{ g}$ ). Performance states  $(\mu, \alpha_{TPP})$  vary gradually along each segment. However, large discontinuous jumps in  $\alpha_{TPP}$  between two contiguous performance states may occur at segment-interfaces i.e. the beginning and end of deceleration and at the transition from level flight to descent mode (Fig. C.6). The transient performance states, corresponding to, for instance, the aircraft speeding up to a constant deceleration, which may be important acoustically even though they last for a short period of time, have not been modeled at this stage.

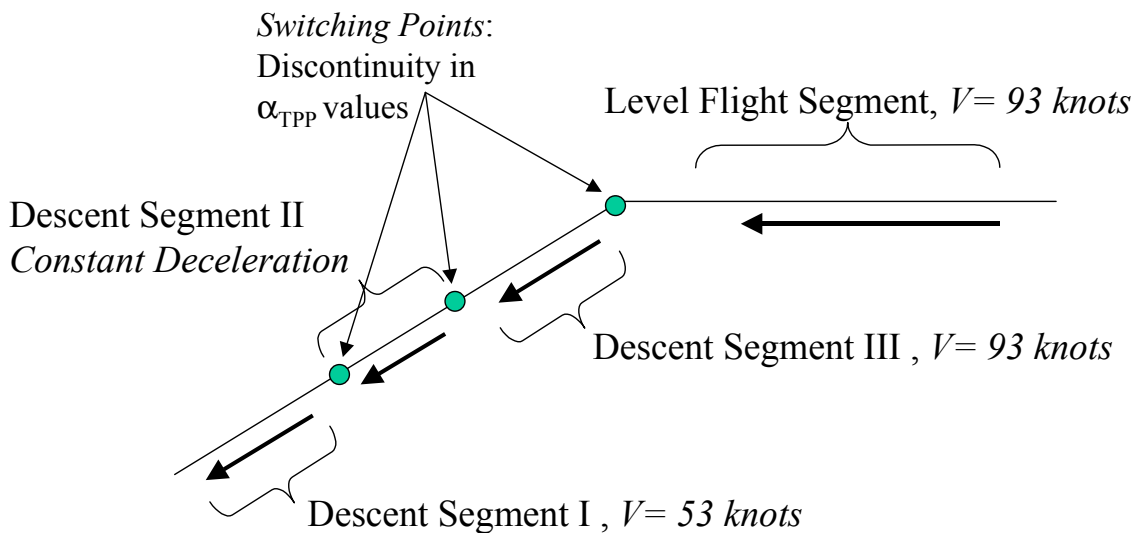


Figure C.6 Trajectory segments, segment interfaces and “switching points”.

## The Sphere Selection module

For each control point along the trajectory, an acoustic sphere that corresponds to the performance state  $(\mu, \alpha_{TPP})$  for that element is selected from the previously computed matrix of acoustic spheres tabulated for the entire spectrum of  $\mu, \alpha_{TPP}$  combinations of interest to the BVI problem. Interpolation is used when the required aerodynamic/performance state is intermediate to known computed states. Energy values corresponding to each one-third octave band at each  $\psi$ - $\theta$  location on the radiation sphere at the required state are obtained by interpolating between appropriate spheres. The code for the Q-SAM method can perform both 1-D linear and 2-D linear interpolation. The assumption here is that for reasonably “small” changes in  $\alpha_{TPP}$  and  $V$  (Fig. C.7), the acoustic amplitudes at any  $\theta, \psi$  location on the radiation sphere vary linearly.

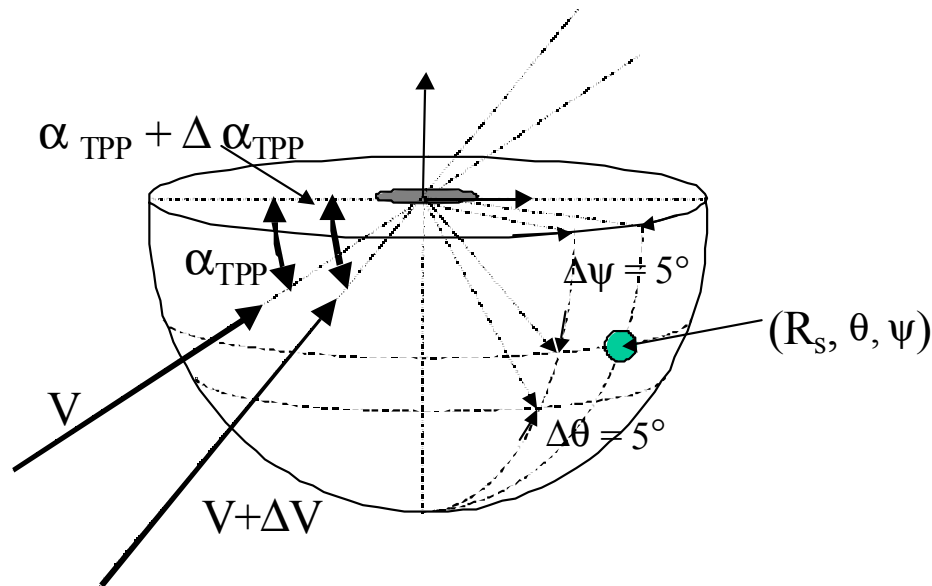


Figure C.7 Linear Interpolation over small changes in  $V$  and  $\alpha_{TPP}$

The performance equation defines characteristic parabolic curves of operation in the  $\mu$ - $\alpha_{TPP}$  plane, for segments with uniform deceleration, or a constant  $\gamma_{eff}$  in general. Linear 1-D interpolation is carried out along these physical  $\mu$ - $\alpha_{TPP}$  curves to obtain radiation spheres for aerodynamic states intermediate to those computed directly from the BVI equations. Linear interpolation has also been performed along constant flight path angle and constant advance ratio curves. In general however, a 2-D linear interpolation scheme is used on a rectangular grid over the  $\mu$ - $\alpha_{TPP}$  axes (Fig. C.8).

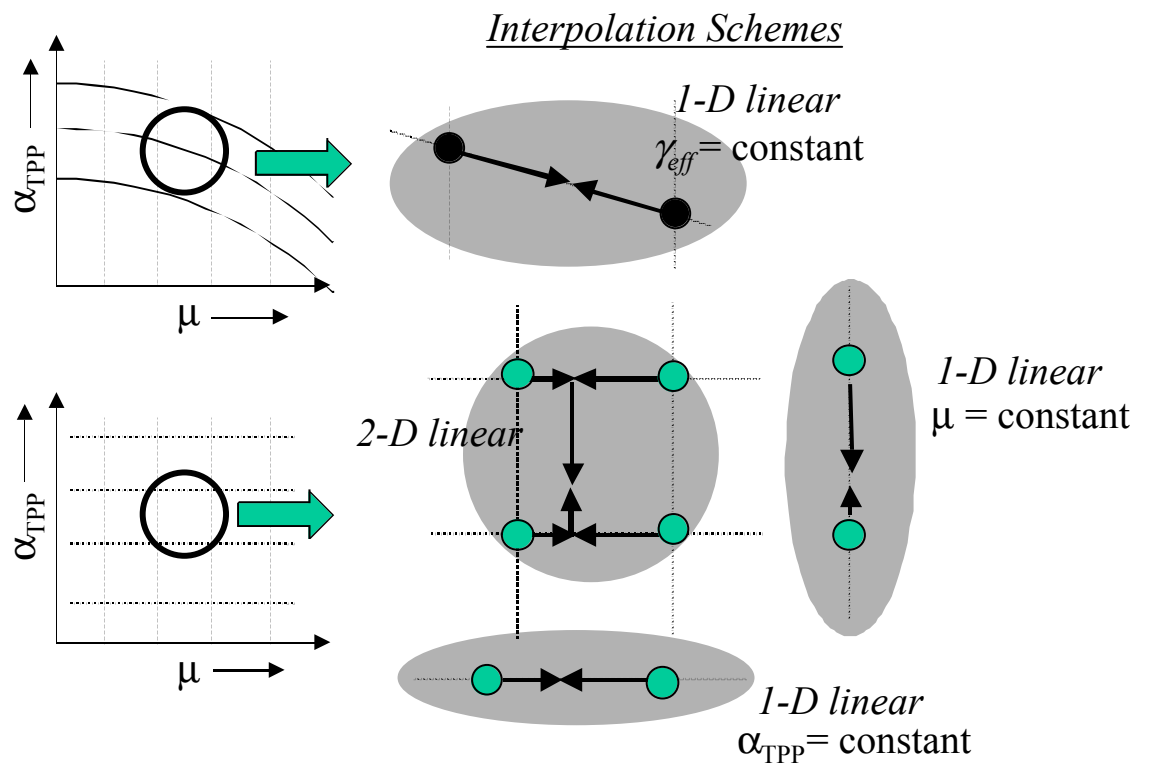


Figure C.8 Interpolation Schemes used in the sphere selection module

## Ground Noise Module

The Ground Noise module essentially makes use of all previous modules, implicitly or explicitly, to estimate various noise and annoyance metrics on the observer plane. The measurement architecture over the observer plane is currently specified as a simplified horizontal rectangular grid of observer locations or ground microphones. The effect of ground reflection is ignored. In general a realistic observer plane with detailed surface topography and reflection/absorption coefficients/properties, and detailed microphone positions, may require a separate module that describes these specifications.

The Ground Noise module begins with the specification of the observer plane relative to the inertial reference frame  $R_F$ . It then reads in the appropriate trajectory file, which specifies a sequence of control points relative to the ground plane. This defines the trajectory under consideration with respect to the ground or the space-fixed coordinate system.

The trajectory is stepped through, point by point, in reverse time, i.e. from the end to the beginning of the trajectory. For each control point or element along the trajectory, the sphere selection module is invoked and an appropriate radiation sphere is obtained. The following procedure is then used to map the acoustic energy to the ground:

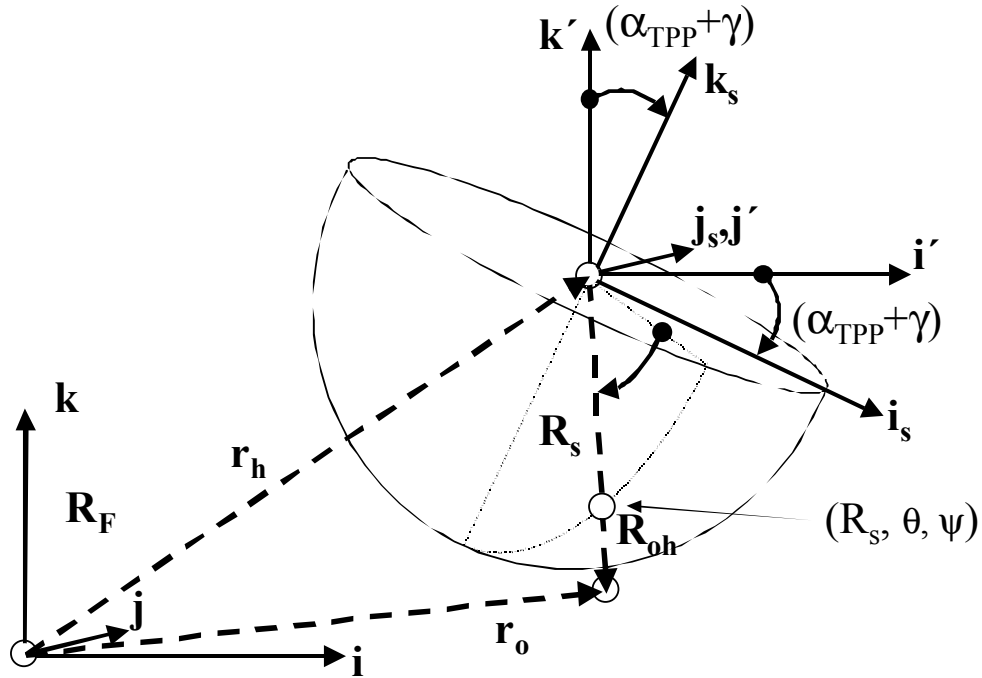


Figure C.9 Correct positioning and orientation of the radiation sphere, along with propagation geometry.

The sphere is first positioned and oriented in space relative to the ground observer plane. It is centered at the mid-interval hub location (i.e. at the  $x, y, z$  coordinates of the control point) for each trajectory element and the median plane ( $\theta = 0^\circ$ ) of the sphere is oriented in the direction of the tip-path-plane for that performance state. This corresponds to rotating the sphere about its  $y$ -axis by an angle  $\gamma + \alpha_{TPP}$  with respect to the horizon (Fig. C.9). Thus,

$$\begin{aligned}
\vec{i}_s &= \cos(\gamma + \alpha_{TPP})\vec{i}' - \sin(\gamma + \alpha_{TPP})\vec{j}' \\
\vec{j}_s &= \vec{j}' \\
\vec{k}_s &= \sin(\gamma + \alpha_{TPP})\vec{i}' + \cos(\gamma + \alpha_{TPP})\vec{j}'
\end{aligned} \tag{C.4}$$

For the purpose of propagation to the far-field, the sphere center is assumed to be the center of noise propagation. This idealized compact source assumption holds for observers that are sufficiently in the far field. Thus, the three-dimensional spread of noise sources about the hub trajectory over each element is collapsed to a conceptual compact source located at the mid-interval hub location for that rotor revolution.

Acoustic information is mapped to each ground observer by first identifying the portion of the sphere that radiates noise to it. A straight line joining the sphere center to the observer ( $\mathbf{R}_{oh}$ ) represents the ray along which noise propagates from the helicopter ( $\mathbf{r}_h$ ) to the observer ( $\mathbf{r}_o$ ). The position vectors  $\mathbf{r}_h$  and  $\mathbf{r}_o$  are specified with respect to the ground based reference frame  $R_F$ , and  $\mathbf{R}_{oh}$  is the position vector of the observer in the reference frame whose origin is at the sphere center (Fig. C.9). The straight-line propagation is a simplifying assumption to the real bending of acoustic rays due to wind and temperature gradients and other atmospheric effects. The point  $(\psi, \theta)$  at which this line intersects the sphere defines the relative orientation of the observer with respect to the helicopter tip-path plane (averaged over one rotor revolution). These coordinates are found using vector algebra as follows:

$$\left. \begin{aligned} \tan \psi &= \frac{\vec{R}_{oh} \cdot \vec{j}_s}{\vec{R}_{oh} \cdot \vec{i}_s} \\ \sin \theta &= \frac{\vec{R}_{oh} \cdot \vec{k}_s}{\|\vec{R}_{oh}\|} \end{aligned} \right\} \quad (C.5)$$

$$\vec{R}_{oh} = \vec{r}_o - \vec{r}_h$$

A 2-D linear interpolation is carried out along the  $\psi$  and  $\theta$  directions on the radiation sphere to obtain one-third octave band energies (SPL-dB values) at this point on the sphere. These interpolated values are then propagated to the observer location. The above geometry and process is summarized in Fig. C.10.

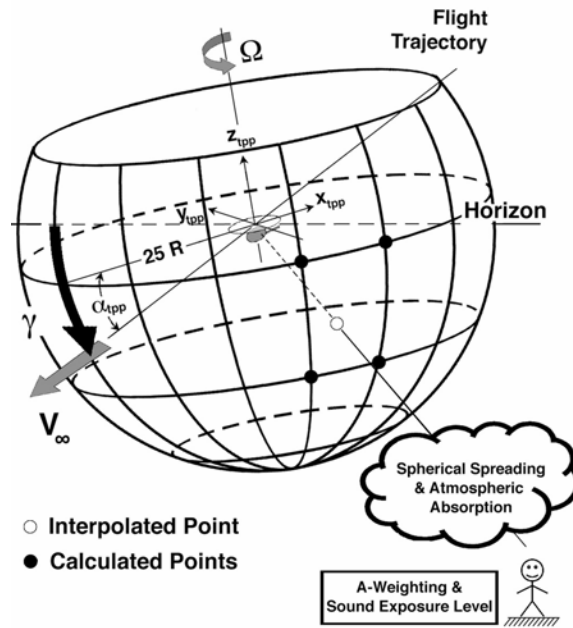


Figure C.10 Acoustics mapping in the Q-SAM method.

The acoustic energies in each one-third octave band are spherically spread using a far-field 1/R geometric spreading law.

$$\Delta dB = 20 \log \left( \frac{R_s}{\|\vec{R}_{oh}\|} \right) \quad (C.6)$$

An atmospheric absorption model based on the ANSI Standard for noise absorption is used:

$$\Delta dB = -C_f \|\vec{R}_{oh}\| \quad (C.7)$$

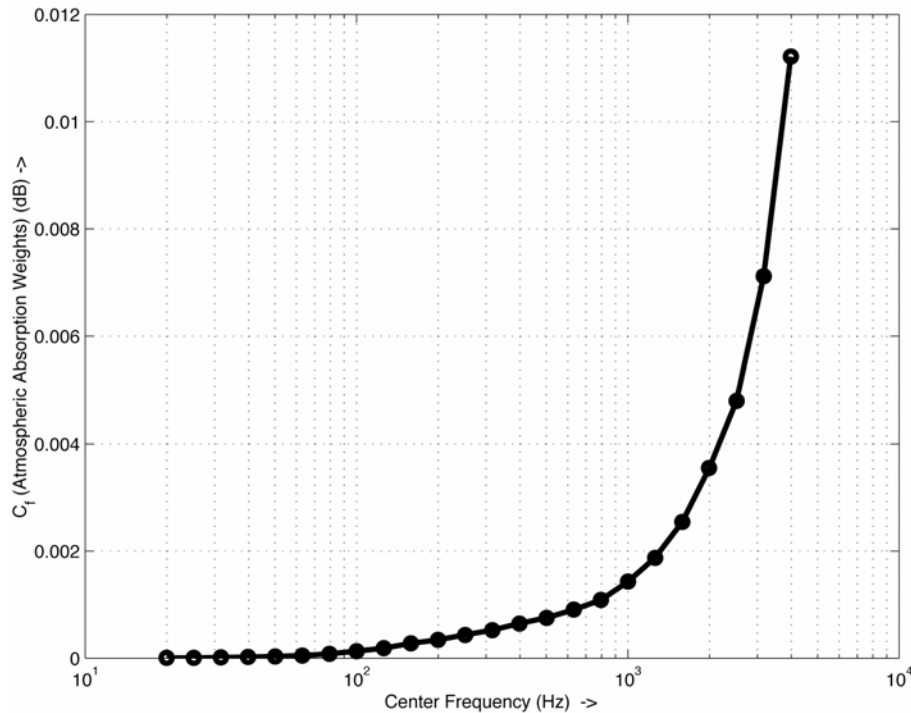


Figure C.11 Atmospheric absorption mapping factors as a function of one-third octave band center-frequencies.

where  $C_f$ , in  $dB/ft$ , is a non-decreasing function. A humidity of 40% is nominally assumed. Figure C.11 shows the variation of  $\Delta dB/ft$  as a function of one-third octave band center-frequency. Attenuation in dB is directly proportional to the distance of propagation,  $R_{oh}$ , and it is higher at higher frequencies. Hence, for large distances of propagation, the atmosphere absorbs a significant portion of the higher frequency energy content.

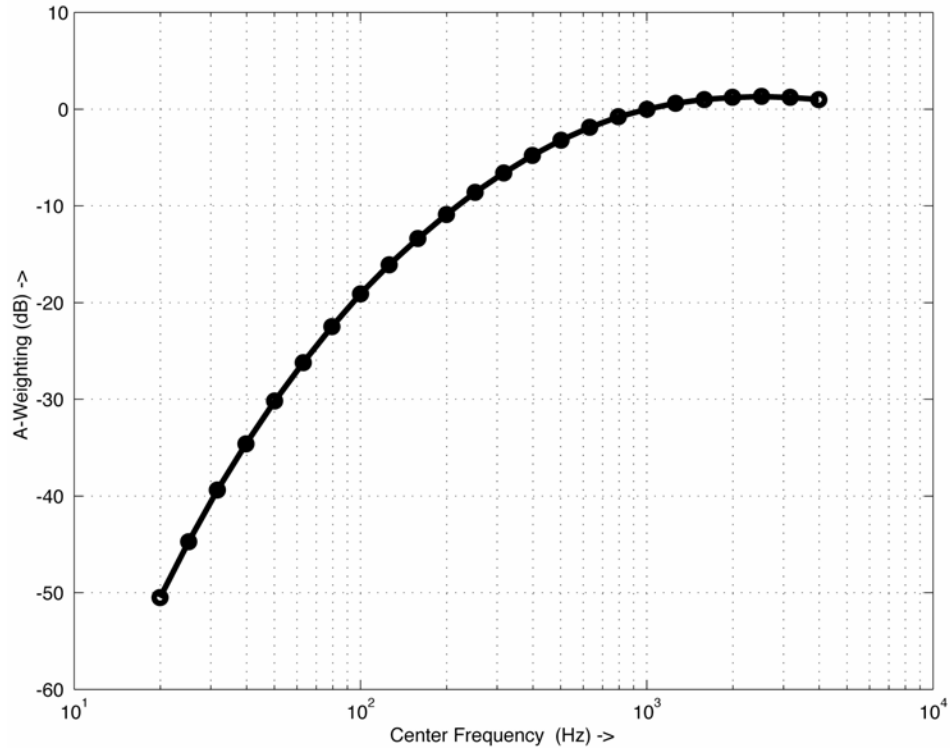


Figure C.12 A-weighting filter factors as a function of one-third octave band center-frequencies.

The acoustic energies at the ground observer are A-weighted and summed up over all the one-third octave bands to obtain an A-weighted acoustic dB value (SLA) corresponding to each trajectory element at the given observer. A-weighting modifies SPL values to reflect human annoyance to mid- and high-frequency levels and de-emphasizes low-frequency component of noise. The A-weighting filter is shown in Fig. C.12.

The arrival time,  $t_{obs}$ , of the BVI acoustic energy is also kept track of through the retarded time equation. The mid-interval time for each element (the value of “ $t$ ” corresponding to each control point) is taken to represent the average time at which the one-rotor revolution acoustic energy is radiated by the compact source. This time “ $t$ ” is represented by  $\tau_{source}$ , or the source time, in the equation below.

$$t_{obs} = \tau_{source} + \frac{R_{obs}}{a_0} \quad (C.8)$$

The trajectory is stepped through, control point by control point, in reverse time order and this entire process of mapping noise to the ground is repeated for all ground observer locations and for all control points along the trajectory. An SLA (in dBA) time-history is thus obtained at all selected observer locations (Fig. C.13). These time-histories are stored in data-files where the columns represent the acoustic time-histories of individual ground observer, specified in a particular order. Owing to differences in times of propagation, SLA time-histories for different observers are available at different  $t_{obs}$  values and ranges. Cubic interpolation is used to map time

intervals for all observers to a common interval divided uniformly into a specific number of time steps. At each time step, the SLA values over the observer plane are presented as contours plots. An animation of the entire dBA contour time-history is also developed for several contours. These time snap-shots indicate noise annoyance levels on the entire plane as a function of time.

The SEL (Sound Exposure Level) is used as a metric to express the effect of time exposure to noise annoyance at each ground observer location. The SEL noise metric is calculated from the observer time history using a continuous time integration formulation. A contour plot of SEL over the ground observer plane determines the relative “noisiness” of the associated trajectory. It is instructive to derive metrics from the SEL distribution over the observer plane, which can then be used to easily quantify the “noisiness” of each trajectory, thus simplifying comparison, though possibly at the cost of loss of detailed information. One such metric is obtained by area-averaging SEL values over the bounded ground plane, on an energy basis. This proposed noise metric represents an average value for exposure to A-weighted acoustic energies over the plane. This is referred to as  $SEL_{av}$  and expressed in dBA.

$$SEL_{av} = 10 \log \left( \sum \frac{10^{\frac{SEL}{10}} \Delta A_i}{A_i} \right) \quad (C.9)$$

While this very simple integrated annoyance metric does not account for annoyance sensitivity due to land use and many other factors, it does represent the total relative

annoyance measured on the ground for selected combinations of flight path and control parameters. As such, it can be used to qualitatively judge the “goodness” of one flight path over another. This new metric, introduced in Reference [72], was devised to give an indication of the integrated effect of the spatial distribution of noise exposure on the ground.

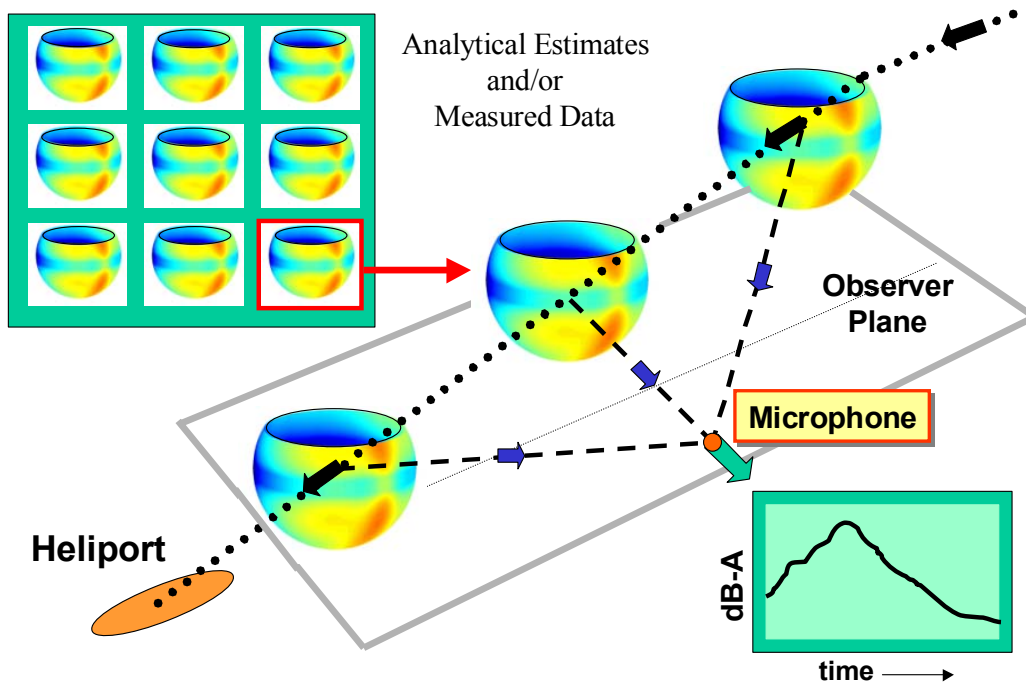


Figure C.13 A schematic representation of noise extrapolation from the sphere to the ground.

## Appendix D

### Development of Approach Trajectories that Minimize BVI Noise Exposure on the Ground

Using *Q-SAM*, it is possible to specify a helicopter flight path (acceleration and flight path angle) time history and calculate the effective radiation spheres along the trajectory, as well as the resulting Sound Pressure Level (*SPL*) time history and the Sound Exposure Level (*SEL*) at any “far-field” observer location. Typically, the results are presented as an *SEL* contour plot over a ground plane. The average value of *SEL* over this plane computed on an energy basis is referred to as  $SEL_{av}$ . The objective of this section is to use the  $SEL_{av}$  metric as a cost function in gradient-based optimization techniques for determining acceptable approach trajectories [105].  $SEL_{av}$  is defined as:

$$F = SEL_{av} = 10 \log_{10} \sum_n^{Ground\ Plane} \left( \sum_i^{Trajectory\ Elements} 10^{SPL_{dB,i,n}/10} \frac{\Delta t_{i,n}}{T_o} \right) \frac{\Delta A_n}{A_o} \quad (D.1)$$

In the above expression “*n*” refers to a spatial location on the observer plane and “*i*” refers to an element along the trajectory. By reversing the order of summation over

the spatial and temporal dimensions, the area-average SEL over the ground plane can be approximated as the time-summation of the area-average SPL over the ground plane associated with each element along the flight trajectory:

$$F \approx 10 \log_{10} \sum_i^{\text{Trajectory Elements}} 10^{\text{SPL}_{\text{av,dB}}^{\text{Ground}}(z_i, \mu_i, \alpha_{\text{TPP},i})/10} \frac{\Delta t_i}{T_o} \quad (\text{D.2})$$

where:

$$\text{SPL}_{\text{av,dB}}^{\text{Ground}}(z, \mu, \alpha_{\text{TPP}}) = 10 \log_{10} \sum_n^{\text{Ground Plane}} 10^{\text{SPL}_{\text{dB},n}/10} \frac{\Delta A_n}{A_o} \frac{\Delta t_n}{T}$$

where,  $\text{SPL}_{\text{dB},n}$  refers to the sound pressure level received at an observer, denoted by the index  $n$ .  $\Delta A_n$  represents the area element associated with the observer location.  $\Delta t_n$  refers to the difference between the arrival times of the noise signal from the two endpoints of the element.  $T$  is the time period associated with a trajectory element, typically one rotor revolution period.  $A_o$  refers to the area of the ground observer plane.  $T_o$  refers to a reference duration, taken as 1 second.

The pre-computed trends of the average SPL on the ground plane, shown in Fig. D.1 for different advance ratios in the range 0.12 and 0.21, are curve-fit to a semi-empirical model that is based on the physics of the BVI noise generation process. For a fixed height  $z$  above the ground, this trend is expressed as:

$$\text{SPL}_{\text{av,dB}}^{\text{Ground}} = \text{SPL}_{\text{o,dB}} - 20 \log_{10} \left( 1 + I_2 \mu^2 \left( \alpha_{\text{TPP},0,\text{eff}} - \alpha_{\text{TPP}} \right)^2 \right) \quad (\text{D.3})$$

where,

$$I_{2,1} = \begin{cases} I_{2,1}, & \text{if } (\alpha_{\text{TPP}} < \alpha_{\text{TPP},0,\text{eff}}) \\ I_{2,2}, & \text{if } (\alpha_{\text{TPP}} > \alpha_{\text{TPP},0,\text{eff}}) \end{cases}$$

This model is based on the physics of individual BVI and extended to the overall trend of BVI noise radiation as a function of advance ratio and tip-path plane angle. Its application to ground noise trends is based on the previous observation that the variation of the average BVI sound pressure levels on the ground plane closely follows the average BVI sound pressure levels radiated by the helicopter over a radiation sphere. The resulting curve-fit is compared with analytical data in Figure D.2 for an advance ratio of 0.165, which corresponds to a flight velocity of about 70 knots for the AH-1 helicopter. Equation D.3 correlates with trends corresponding to higher advance ratios better than lower advance ratios. The overall correlation is reasonable for the purpose of this study, over the entire range of advance ratios. Typically, at a fixed advance ratio, as the flight path angle is varied from zero degrees in level flight to steeper approach angles, the average radiated sound power associated with BVI noise increases to a maximum value and then begins to reduce again. This variation of the average BVI ground noise radiation with tip-path-plane angle corresponds to the wake effectively operating below the disk at small tip-path-

plane angles and shallow flight path angles, cutting through or operating near the rotor disk at intermediate tip-path-plane angles, and finally being pushed above the rotor disk for steep descent flight conditions which correspond to higher tip-path-plane angles.

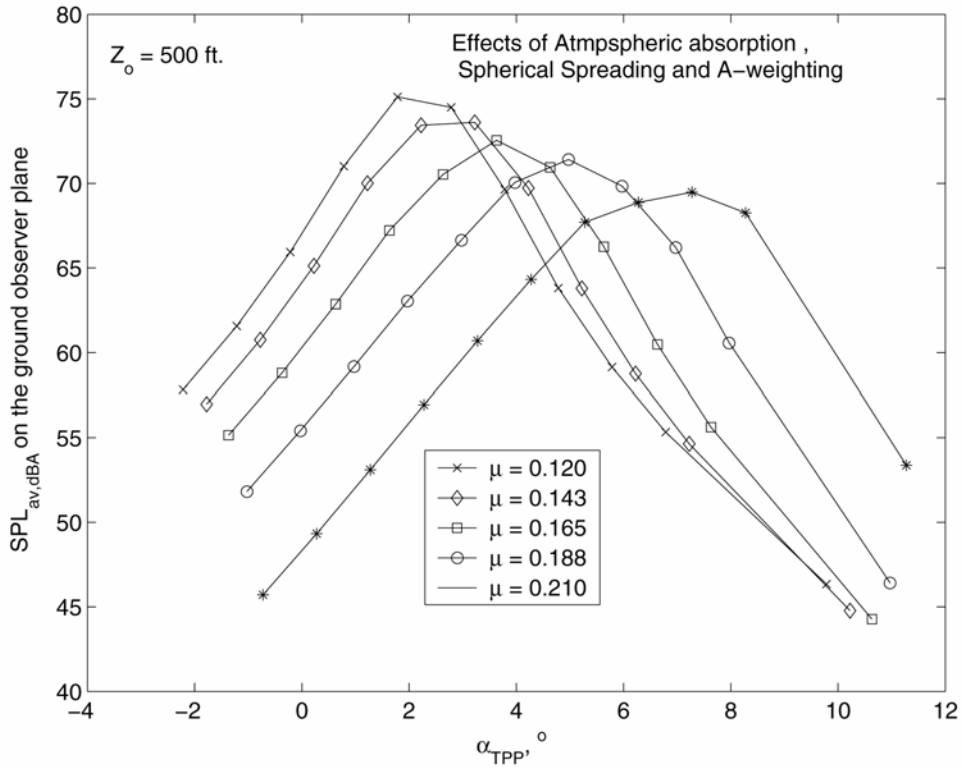


Figure D.1 SPL<sub>av</sub> over the ground plane for steady flight conditions as a function of tip-path plane angle for advance ratios 0.12, 0.143 0.165, 0.188 and 0.21.

The effect of atmospheric absorption on the noise levels as a function of propagation distance is, in general, a function of the power spectrum or frequency content of the noise signature, and therefore of the flight condition. For the data set used however, it is observed that the variation with  $z$ , of average A-weighted noise levels for any flight

condition is independent of flight condition, within an error bound of about 1 dB. Therefore, in the current model, the variation of average radiated noise levels as a function of height above the ground plane is assumed to be independent of flight conditions. The dependence of average radiated noise on the ground on the height  $z$  of the helicopter above the ground is estimated as below (Fig. D.3):

$$SPL_{av,dB}^{Ground}(z, \mu, \alpha_{TPP}) = SPL_{av,dB}^{Ground}(z_o, \mu, \alpha_{TPP}) + \Delta SPL(z, z_o) \quad (D.4)$$

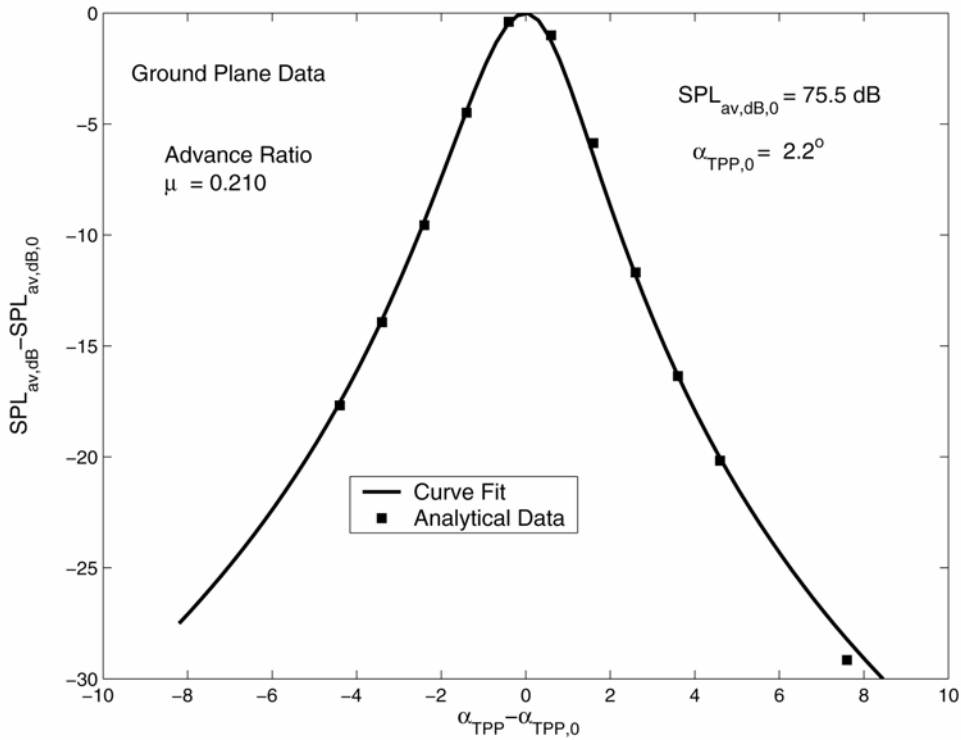


Figure D.2 Curve-fit for the average radiated BVI sound power on the ground plane, as a function of main-rotor tip-path plane angle, for advance ratio 0.165.

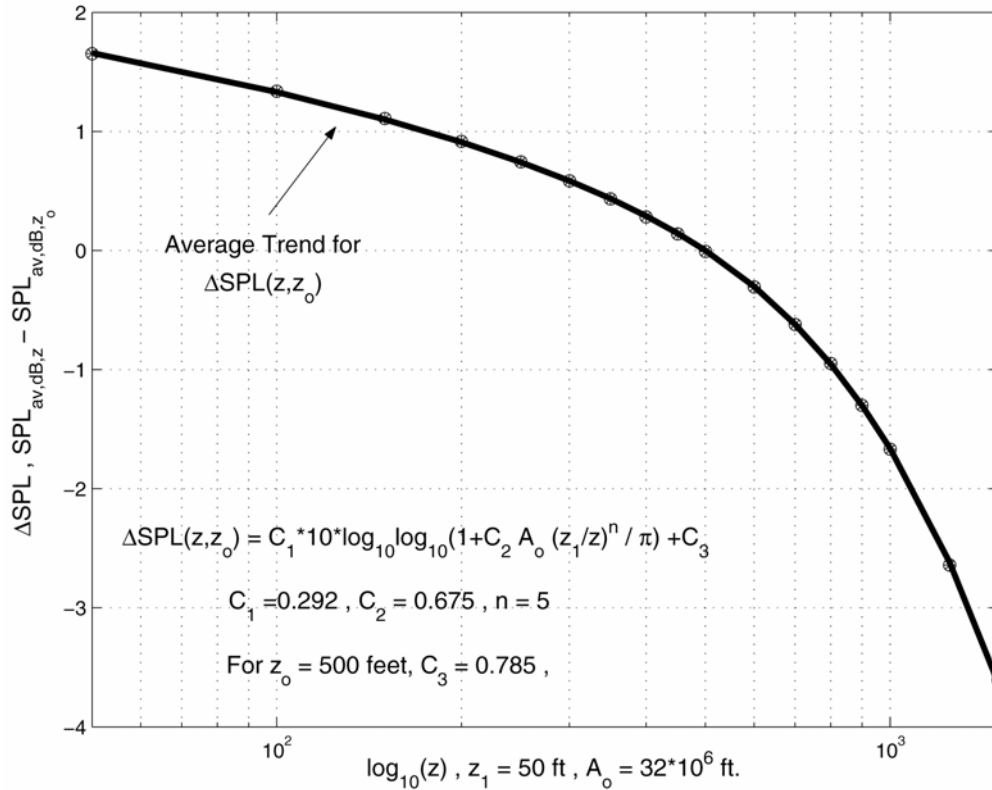


Figure D.3 The variation of the mean-trend for the radiated main-rotor BVI sound power averaged over a representative ground plane plotted as a function of height above the ground plane center.

**Optimization Problem Statement:**

Based on the objective function F, described above in Eq. D.2, the task of finding an optimal longitudinal approach trajectory, in terms of the minimum associated BVI noise annoyance, can be expressed mathematically as follows:

Find the functions  $z(t)$ ,  $\mu(t)$  and  $\alpha_{TPP}(t)$  that, subject to a set of specified initial and final conditions, minimize the function:

$$\begin{aligned}
F &= 10 \log_{10} \int_{t_{\text{initial}}}^{t_{\text{final}}} 10^{\text{SPL}_{\text{av,dB}}^{\text{Ground}}(z, \mu, \alpha_{\text{TPP}}) / 10} \frac{dt}{T_o} \\
&= 10 \log_{10} \int_{t_{\text{initial}}}^{t_{\text{final}}} f(z, \mu, \alpha_{\text{TPP}}) dt
\end{aligned} \tag{D.5}$$

where

$$\dot{z} = V \sin \gamma$$

$$\mu = \frac{V}{\Omega R}$$

$$\alpha_{\text{TPP}} = -\frac{D_{\text{eff}}}{W} - \gamma - \frac{\dot{V}}{g}.$$

It is assumed that the main rotor tip-speed is held approximately constant during nominal approach trajectories and that the effective drag of the helicopter is primarily a function of the flight velocity. Using the relations above, the optimization problem statement can now be posed as:

Find the functions  $\dot{V}(t)$  and  $\gamma(t)$  that minimize the function:

$$F = 10 \log_{10} \int_{t_{\text{initial}}}^{t_{\text{final}}} f(z(t), V(t), \gamma(t) + \frac{\dot{V}(t)}{g}) dt \tag{D.6}$$

where,

$$z(t) = z_{\text{initial}} + \int_{t_{\text{initial}}}^t V \sin \gamma dt$$

$$V(t) = V_{initial} + \int_{t_{initial}}^t \dot{V} dt$$

The acceleration along the flight path and the flight path angle along the trajectory are treated as the “controls” of the problem. The focus of the current project is on nominal descent approach conditions. Therefore, instead of modeling the flight dynamics of the helicopter from first-principles, certain key aspects of the performance characteristics of the helicopter can be expressed in terms of bounds on the behavior of functions  $\gamma$  and  $V$  and their derivatives, and an idealized approximation to an approach trajectory profile is developed. It is first assumed that the flight path angle is restricted to climbs and descents no steeper than  $9^\circ$  at all flight speeds. A bound is also imposed on the maximum acceleration or deceleration parallel to the flight path. Based on passenger comfort this value is selected as  $0.05g$ . The flight velocity  $V$  is restricted to lie between 40 knots and 100 knots, a typical range for nominal approach procedures. The height  $z$  of the helicopter is also bound between 50 feet and 2000 feet.

The small angle assumption made for the flight path angle and the consideration of only longitudinal trajectories impose a condition of strict monotonicity on  $x(t)$ . The objective function can therefore be cast as an integral over  $x$  rather than time. The initial and final  $x$  locations become the bounds of  $x$ . The objective is to find functions  $z(x)$  and  $V(x)$  that minimize the function  $F$  subject to the boundary conditions, and the problem constraints. For travel in the reverse  $x$  direction:

$$\begin{aligned}
F &= 10 \log_{10} \int_{x_{\text{initial}}}^{x_{\text{final}}} f(z(x), V(x), \gamma(x) + \dot{V}(x)/g) \frac{dx}{-V(x)} \\
&\equiv 10 \log_{10} \int_{x_{\text{initial}}}^{x_{\text{final}}} f(z(x), V(x), 1/g \frac{\partial E}{\partial x}) \frac{dx}{-V(x)} \tag{D.7}
\end{aligned}$$

where,

$$\gamma \approx \frac{\partial z}{\partial x} \quad \text{and} \quad \dot{V} \approx \frac{\partial}{\partial x} \frac{V^2(x)}{2}$$

$$1/g \frac{\partial E}{\partial x} = \gamma(x) + \dot{V}(x)/g = \gamma(x) + \frac{\partial}{\partial x} \frac{V^2(x)}{2g} \quad \text{and} \quad E = gz(x) + \frac{V^2(x)}{2}.$$

The term  $E(x)$  represents the sum of the specific kinetic and potential energies associated with the helicopter. The flight path angle is equivalent to the gradient of the potential energy of the helicopter along the trajectory, while the acceleration along the flight path is equivalent to the gradient of kinetic energy. The objective function therefore depends only on  $z(x)$  and  $V(x)$  and their derivatives as a function of  $x$ . While  $z(x)$  completely specifies the trajectory geometry,  $V(x)$  imposes a dynamic character to the trajectory in terms of a velocity profile. It should be noted that the objective function, based on the BVI noise radiation characteristics of the helicopter, couple the choice of the functions  $z(x)$  and  $V(x)$ , preempting the possibility of selecting them independently.

During a nominal approach to a landing, a helicopter pilot typically executes a small number of constant glide-slope segments before the final stages of flare and touch down. The very last stages of descent are usually close enough to the heliport to not exert a significant acoustic impact on noise sensitive areas. Typically these

longitudinal approach trajectories consist of a series of constant flight path angle segments with constant acceleration along the flight path. Therefore, for trajectories under consideration, each constituent segment is characterized by a constant flight path angle, a uniform acceleration along the flight path and a segment length. The functions  $z$  and  $V^2/2$ , which represent the potential and kinetic energies of the helicopter respectively, are further idealized to be piecewise-linear continuous functions along the trajectory:

$$\begin{aligned} z_{i,i-1}(x) &\approx z_{i-1} - \gamma|_{i,i-1}[x - x_{i-1}] \\ V_{i,i-1}^2(x)/2 &\approx V_{i-1}^2/2 - \dot{V}|_{i,i-1}[x - x_{i-1}] \end{aligned}$$

The sequence  $\{x_i, z_i, V_i\}$  that constitute the end points of these piecewise linear functions are called waypoints or node points of the trajectory. Such a trajectory is uniquely defined by the sequence  $\{x_i, z_i, V_i\}$ , representing the values of  $x$ ,  $z$  and  $V$  at each waypoint. The boundary conditions for such a trajectory with  $n$  segments, and  $n-1$  waypoints between the specified boundary points, are expressed as  $\{x_o, z_o, V_o\}$  and  $\{x_n, z_n, V_n\}$ . The objective function for this discretized system, can be expressed as:

$$\begin{aligned} F &= 10 \log_{10} \sum_{i=1}^n \int_{x_{i-1}}^{x_i} f(z_{i,i-1}(x), V_{i,i-1}(x), \gamma_{i,i-1} + \frac{\dot{V}_{i,i-1}}{g}) \frac{dx}{-V_{i,i-1}(x)} \\ &= 10 \log_{10} \sum_{i=1}^n \int_{x_{i-1}}^{x_i} f(z_{i,i-1}(x), V_{i,i-1}(x), \frac{1}{g} \frac{E_i - E_{i-1}}{x_{i-1} - x_i}) \frac{dx}{-V_{i,i-1}(x)} \end{aligned} \quad \text{(D.8)}$$

where,

$$\gamma_{i,i-1} \approx \frac{z_i - z_{i-1}}{x_{i-1} - x_i}$$

$$\dot{V}_{i,i-1} \approx \frac{V_i^2 - V_{i-1}^2}{2(x_{i-1} - x_i)}$$

$$E_i = gz_i + \frac{V_i^2}{2}$$

This idealization of the trajectory may introduce discontinuities in  $dz/dx$  and  $dv/dx$  at the node points. Transient maneuvers like changes in flight path angle and changes in the acceleration along the flight path are governed by the vehicle dynamics, performance and stability and control equations, and in turn affect the noise characteristics of the helicopter. Therefore constraints on the variation of acceleration and flight path angle along such a segmented trajectory should also be introduced to represent the physics of these transient unsteady phenomena. At the initial stage, these transient effects have not been modeled.

### **Trajectory Optimization Using Gradient Descent**

An  $n$ -segmented approach trajectory is assumed to consist of a series of “ $n-1$ ” waypoints, which, along with the two boundary points, divide the trajectory into  $n$  segments. For a specified set of boundary conditions, the waypoint locations and the associated waypoint flight velocity specifications completely specify the entire trajectory. Therefore, for a trajectory composed of “ $n-1$ ” waypoints:

$$X = [x_1, z_1, v_1, \dots, x_i, z_i, v_i, \dots, x_{n-1}, z_{n-1}, v_{n-1}]:$$

Design Vector

$$X_{\text{initial}} = [x_0, z_0, v_0]$$

$$X_{\text{final}} = [x_n, z_n, v_n]:$$

Boundary Conditions

(Initial and Final Approach Fixes)

$F(X)$ : Objective Function

$X_{\text{LB}} \leq X \leq X_{\text{UB}}$  : Lower and Upper Bounds on  $X$

$$g(X) = [\dot{V}_{i,i-1} - \dot{V}_{\text{max}}, -\dot{V}_{i,i-1} + \dot{V}_{\text{min}},$$

$$\gamma_{i,i-1} - \gamma_{\text{max}}, -\gamma_{i,i-1} + \gamma_{\text{min}}] \leq 0:$$

Non - linear constraints (Bounds on acceleration and flight path angle)

Starting with a relatively small number of segments, an optimal solution is sought.

The characteristic nature of BVI noise allows for non-unique locally optimal solutions under nominal approach conditions. By varying the initial value of the design vector  $X_0$ , potentially, several local minima can be found for a given set of boundary conditions. By introducing one new waypoint along any segment of the set of local minimum solutions for an  $n$ -segmented trajectory, possibly the segment with the highest contribution to the objective function, initial values for the design vector of an  $n+1$ -segmented trajectory are generated. This process is repeated till a trajectory with an acceptable value for the objective function is obtained. Depending on the nature of the objective and constraint functions as well as the bounds on the problem variables, arriving at the global minimum value of the objective function may

potentially require a very large number of segments. But such a trajectory may be unrealistic in terms of its actual implementation by pilots and air-traffic controllers. It may be of interest to find the minimum noise trajectory for an approach consisting of a small number of segments, for a given set of conditions and constraints. In effect, this would yield the most acoustically efficient  $n$ -segmented trajectory.

Figure D.4 shows some solution trajectories for a range of 50,000 feet and a constant flight velocity of 70 knots. The boundary values were chosen as  $x = 0 \text{ ft}$ ,  $z = 50 \text{ ft}$  and  $x = 50,000 \text{ ft}$ ,  $z = 1000 \text{ ft}$ . The  $z$  dimension was bound by 50 ft and 1500 ft. Flight path angles were constrained to lie between climbs and descents of  $9^\circ$  and accelerations were constrained to be 0. Starting at  $n=1$ , it is observed that simply joining the two boundary points actually yields a feasible solution, a shallow approach trajectory, which is one of the local minima of this problem. This trajectory is associated with an  $SEL_{av}$  of about 86 dB. By placing one waypoint along this trajectory,  $n$  is increased to 2, and the optimization procedure is performed. The solution converges to a very similar trajectory with a flight path angle close to  $-1^\circ$ . By choosing other feasible initial conditions, two other minimum noise solutions are obtained. One minimum solution is a steep descent followed by a very shallow approach to the final point. This trajectory is associated with an  $SEL_{av}$  of about 84 dB. The other minimum solution, the global minimum for a two-segmented trajectory for the specified conditions and constraints, starts with a climb to 1500 feet followed by a steep descent to the final point. This trajectory corresponds to an  $SEL_{av}$  of about 78 dB. When climbs are restricted, the minimum-noise solution consists of level flight

followed by a steep descent. The two maximum-noise trajectories are also shown in Fig. D.4. These trajectories consist of a  $5^\circ$  approach either preceded or followed by level flight. Such a trajectory corresponds to an  $SEL_{av}$  of about 92 dB.

D.5 shows similar trajectories for a horizontal range of 20000 feet. Because trajectories last for a shorter duration, the average annoyance levels associated with the corresponding trajectories are lower when compared to Fig. D.4.

This relatively simple model is used to obtain low noise trajectories for a small number of segments. The choice of a suitable initial design vector to represent an initial choice of the trajectory is critical to the success of this method, especially when the design vector becomes large in size. This method is also extendable to three dimensions in space, at the cost of design vector size. It is to be noted that because of the approximations made in arriving at the analytical form of the objective function, care must be taken when trying to arrive at the global minimum solution. Also it is of greater interest to arrive at a range of segment parameters that correspond to a low value of the objective function, rather than a single trajectory that corresponds to the minimum associated value of  $SEL_{av}$ .

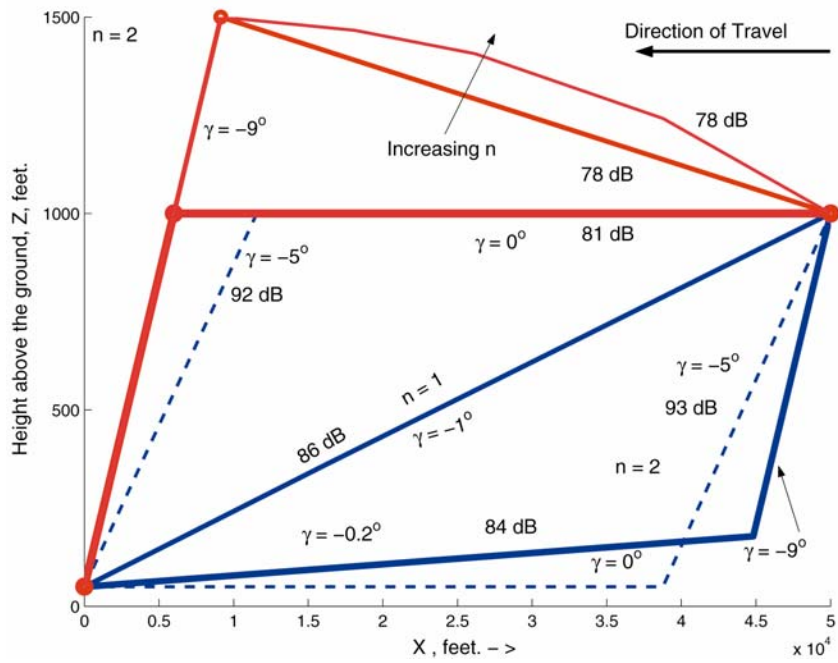


Figure D.4 Several low-noise solutions for a 2-segmented trajectory with a range of 50000 feet, obtained using gradient descent. The maximum noise trajectories corresponding to  $5^\circ$  approaches are also shown for comparison.

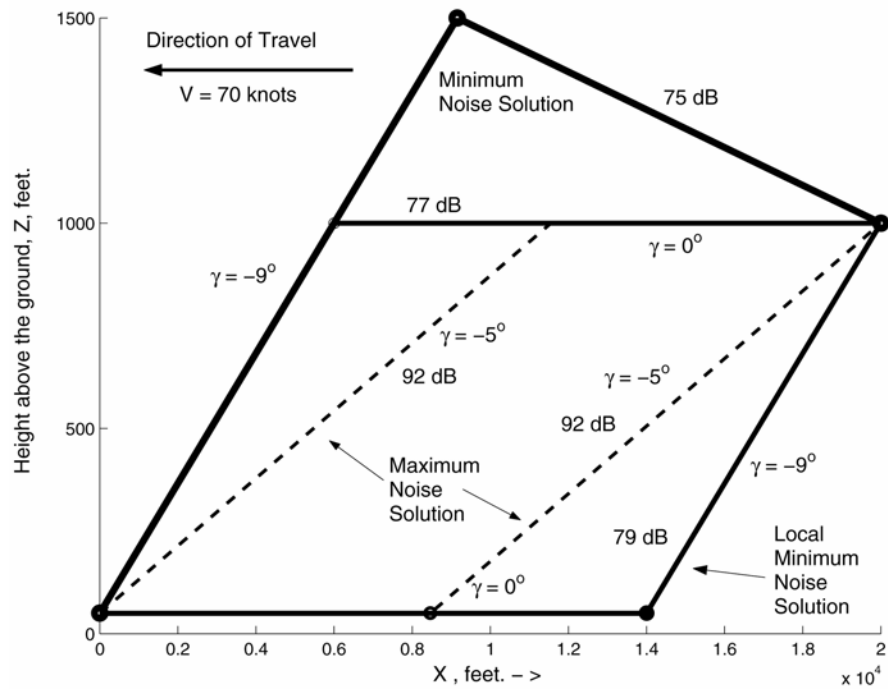


Figure D.5 Several low-noise solutions for a 2-segmented trajectory with a range of 20000 feet, obtained using gradient descent. The maximum noise trajectories corresponding to  $5^\circ$  approaches are also shown for comparison.

## BIBLIOGRAPHY

- [1] George, A. R., "Helicopter Noise: State-of-the-Art," *Journal of Aircraft*, Vol. 15, pp. 707-715, 1978.
- [2] Cox, C. R., Subcommittee chairman's report to membership on aerodynamic sources of rotor noise, AHS 28<sup>th</sup> Annual Forum, May, 1972.
- [3] Schmitz, F.H., "Rotor Noise," *Aeroacoustics of Flight Vehicles, Theory and Practice, Vol. 1: Noise Sources*, (book authored by Hubbard, H. H.), Published for the Acoustical Society of America through the American Institute of Physics, Chapter 2, 1995.
- [4] Lowson, M. V., "Progress Towards Quieter Civil Helicopters", *Aeronautical Journal*, Vol. 96, pp. 209-223, 1992.
- [5] Brentner, K. S. and Farassat, F., "Modeling Aerodynamically Generated Sound of Helicopter Rotors", *Progress in Aerospace Sciences*, Vol. 39, pp. 83-120, 2003.
- [6] Newman, D. and Wilkins, R., "Rotorcraft Integration into the Next Generation NAS," Proceedings of the American Helicopter Society (AHS) 54<sup>th</sup> Annual Forum, Washington, DC, May, 1998.

- [7] Pike, A. C. and Leverton, J. W., "Understanding Helicopter Noise - Implications of Design and Operation," Proceedings of the 24<sup>th</sup> European Rotorcraft Forum, Marseilles, France, September, 1998.
- [8] Bennet, R. L. and Pearsons, K. S., "Handbook of Aircraft Noise Metric," NASA CR-3406, 1981.
- [9] Schmitz, F. H. and Yu, Y. H., "Helicopter Impulsive Noise: Theoretical and Experimental Status", *Journal of Sound and Vibration*, Vol. 109, No. 3, pp. 361-422, 1986.
- [10] Schmitz, F. H. and Yu, H. Y., "Theoretical Modeling of High-Speed Impulsive Noise," Proceedings of the Third European Rotorcraft and Powered Lift Aircraft Forum, Aix-en-Provence, France, September, 1977.
- [11] Yu, Y. H., Caradonna, F. X. and Schmitz, F. H., "The Influence of the Transonic Flow Field on High-Speed Impulsive Noise," Proceedings of the Fourth European Rotorcraft and Powered Lift Aircraft Forum, Stresa, Italy, 1978.
- [12] Brentner, S. B., "Modeling Aerodynamically Generated Sound: Recent Advances in Rotor Noise Prediction," Proceedings of the 38<sup>th</sup> Aerospace Sciences Meeting and Exhibit, Reno, NV, January, 2000.

- [13] Yu, Y., "Rotor Blade-Vortex Interaction Noise," *Progress in Aerospace Sciences*, Vol. 36, pp. 97-115, 2000.
- [14] Boxwell, D. A., Schmitz, F. H., Spletstoesser, W. R. and Schultz, K. J., "Helicopter Model Rotor-Blade Vortex Interaction Impulsive Noise: Scalability and Parametric Variations", *Journal of the American Helicopter Society*, Vol. 32, No. 1, January, 1987.
- [15] Schmitz, F. H. and Boxwell, D. A., "In-flight Far-field Measurement of Helicopter Impulsive Noise", *Journal of the American Helicopter Society*, Vol. 21, pp. 2-16, 1976.
- [16] Boxwell, D. A. and Schmitz, F. H., "Full-Scale Measurements of Blade-Vortex Interaction Noise", *Journal of the American Helicopter Society*, Vol. 27, No. 4, pp. 11-27, 1982.
- [17] Cross, J. L. and Watts, M. E., "In-Flight Acoustic Testing Techniques Using the YO-3A Acoustic Research Aircraft", NASA TM-85895, February, 1984.
- [18] Burley, C. L. and Martin, R. M., "Tip-Path Plane Angle Effects on Rotor Blade-Vortex Interaction Noise Levels and Directivity", Proceedings of the 44<sup>th</sup>

Annual Forum of the American Helicopter Society, Washington, D.C., June, 1988.

[19] Martin, R. M., Spletstoeser, W. R., Elliot, J. W. and Schultz, K. J., "Advancing-Side Directivity and Retreating Side Interactions of Model Rotor Blade-Vortex Interaction Noise", NASA TP 2784, 1988.

[20] Yamauchi, G. K., Signor, D. B., Watts, M. E., Hernandez, F. J. and LeMasurier, P., "Flight Measurements of Blade Vortex Interaction Noise Including Comparisons with Full-Scale Wind Tunnel Data", Proceedings of the AHS 49<sup>th</sup> Annual Forum, St. Louis, Missouri, May, 1993.

[21] Signor, D. B., Watts, M. E., Hernandez, F. J., and Felker, F. F., "Blade-Vortex Interaction Noise: A Comparison of In-Flight, Full-Scale, and Small-Scale Measurements." American Helicopter Society Aeromechanics Specialists Conference, San Francisco, CA, January 1994.

[22] Kufeld, R., Balough, D. L., Cross, J. L., Studebaker, K. F., Jennison, C. D., and Bousman, W. G. "Flight Testing of the UH-60A Airloads Aircraft." 50th Annual Forum of the American Helicopter Society, Washington, D.C., May, 1994.

- [23] Lyrintzis, A. S., Koutsavdis, E. and Strawn, R. C., “Technical Note: A Comparison of Computational Aeroacoustic Prediction Methods”, *Journal of the American Helicopter Society*, Vol. 42, No. 1, pp. 54-57, 1997.
- [24] Lyrintzis, A. S., “Surface Integral Methods in Computational Aeroacoustics – From the (CFD) Near-Field to the (Acoustic) Far-Field”, *International Journal of Aeroacoustics*, Vol. 2, No. 2, pp. 95-128, 2003.
- [25] Lighthill, M. J., “On Sound Generated Aerodynamically – 1: General Theory”, *Proceedings of the Royal Society*, A211, pp. 564-587, 1952.
- [26] Ffowcs Williams, J. E. and Hawkings, D. L., “Sound Generation by Turbulence and Surfaces in Arbitrary Motion”, *Philosophical Transactions of the Royal Society of London*, A264, pp. 321-342, 1969.
- [27] Farassat, F., “Linear Acoustic Formulas for Calculation of Rotating Blade Noise,” *AIAA Journal*, Vol. 19, No. 9, pp. 1122-1130, 1981.
- [28] Brooks, T. F., Boyd, Jr., D. D., Burley, C. L. and Jolly, Jr., J. R., “Aeroacoustics Codes for Rotor Harmonic and BVI Noise – CAMRAD.Mod1/HIRES”, 2<sup>nd</sup> AIAA/CEAS Aeroacoustics Conference, State College, PA, May, 1996.

- [29] Brentner, K. S., “Prediction of Helicopter Discrete Frequency Rotor Noise – A Computer Program Incorporating Realistic Blade Motions and Advanced Acoustic Formulation”, NASA TM 87721, October, 1986.
- [30] Caradonna, F., Kitaplioglu, C., McCluer, M., Baeder, J., Leishman, J. G., Berezin, C., Visintainer, J., Bridgeman, J., Burley, C., Epstein, R., Lyrantzis, A., Koutsavdis, E., Rahier, G., Delrieux, Y., Rule, J. and Bliss D., “Methods for the Prediction of Blade-Vortex Interaction Noise”, Proceedings of the American Helicopter Society Technical Specialists’ Meeting for Rotorcraft Acoustics and Aerodynamics, Williamsburg, VA, October, 1997.
- [31] Kitaplioglu, C. and Caradonna, F., “A Study of Blade-Vortex Interaction Aeroacoustics utilizing an Independently Generated Vortex”, AGARD Symposium, Berlin, Germany, October, 1994.
- [32] Hassan, A. A., Taghichi, H. and Charles, B. D., “Aerodynamics and Acoustics of Three-Dimensional Blade-vortex Interactions”, NASA CR 182009, April, 1990.
- [33] Johnson, W., “*CAMRAD/JA A Comprehensive Analytical Model of Rotorcraft Aerodynamics and Dynamics*,” Johnson Aeronautics, Palo Alto, CA, 1988.

- [34] Lim, J. W., Yu, Y. H. and Johnson, W., “Calculation of Rotor Blade-Vortex Interaction Using a Multiple-Trailer Free-Wake”, *Journal of Aircraft*, Vol. 40, No. 6, pp. 1123-1130, November, 2003.
- [35] Jobard, N., Costes, M. and Beaumier, P., “Three Dimensional BVI Simulation on Aeroelastic Blades Using a New Deforming Grid Approach Coupled to a Free-Wake Analysis”, Proceedings of the 52<sup>nd</sup> Annual Forum of the American Helicopter Society, Washington, D.C., June, 1996.
- [36] Nakamura, Y., “Prediction of blade-vortex interaction noise from measured blade pressures”, Seventh European Rotorcraft and Powered Lift aircraft Forum, Garmisch-Partenkirchen, Germany, 1981.
- [37] Joshi, M. and Liu, S., “Prediction of Blade-Vortex Interaction Noise using Measured Blade Pressures”, NASA CR 181640, July, 1988.
- [38] Schultz, K. J. and Spletstoeser, W. R., “Measured and Predicted Impulsive Noise Directivity Characteristics”, Proceedings of the 13<sup>th</sup> European Rotorcraft Forum, Arles, France, 1987.
- [39] Ziegenbien, P. R. and Oh, B. K., “Blade Vortex Interaction Noise Predictions Using Measured Blade Pressures”, Proceedings of AHS Specialists Meeting on Aerodynamics and Aeroacoustics, Arlington TX, February, 1987.

- [40] Visintainer, J. A., Marcolini, M. A., Burley, C. L. and Liu, S., “Acoustic Predictions Using Measured Pressures from a Model Rotor in the DNW”, *Journal of the American Helicopter Society*, Vol. 38, No. 3, pp. 35-44, July, 1993.
- [41] Tung, C., Kube, R., Brooks, T, F. and Rahier, G., “Prediction and Measurement of Blade-Vortex Interaction,” *Journal of Aircraft*, Vol. 35, No. 2, pp. 260-266, 1998.
- [42] Allongue, M., Marze, H. J. and Potdevin, F., “The quiet Helicopter – From Research to Reality”, Proceedings of the 55<sup>th</sup> Annual Forum of the American Helicopter Society, Montreal, Canada, May, 1999.
- [43] Niesl, G. and Arnaud, G., “Low Noise Design of the EC 135 Helicopter”, Proceedings of the 52<sup>nd</sup> Annual Forum of the American Helicopter Society, Washington, DC, May, 1996.
- [44] Baeder, J. D., “Passive Design for Isolated Blade-Vortex Interaction Noise Reduction”, Proceedings of the 53<sup>th</sup> Annual Forum of the American Helicopter Society, Virginia Beach, May, 1997.
- [45] Charles, B., Taghichi, H. and Hassan, A., “Higher Harmonic Actuation of Trailing-Edge Flaps for Rotor BVI Noise Control”, Proceedings of the 52<sup>nd</sup>

- Annual Forum of the American Helicopter Society, Washington, D.C., June, 1996.
- [46] Yu, Y. H., Gmelin, B., Heller, H., Phillipe, J., Mercker, E. and Preisser, J. S, “HHC Aeroacoustics Rotor Test at the DNW – The Joint German/French/US HART Project”, Proceedings of the 20<sup>th</sup> European Rotorcraft Program at Amsterdam, The Netherlands, October, 1994.
- [47] Swanson, S. M., Jacklin, S. A., Blaas, A., Kube, R. and Niesl, G. , “Individual Blade Control Effects on Blade-Vortex Interaction Noise”, Proceedings of the 50<sup>th</sup> Annual Forum of the American Helicopter Society, Washington, D.C., May, 1994.
- [48] Chen, P. C., Baeder, J. D., Evans, R. A. D. and Niemczuk, J., “Blade-Vortex Interaction Noise Reduction with Active Twist Smart rotor Technology”, *Smart Materials and Structures*, Vol. 10, No. 1, pp. 77-85, February, 2001.
- [49] Schmitz, F. H. ”Reduction of Blade-Vortex Interaction (BVI) Noise through X-Force Control”, NASA TM-110371, April, 1995.
- [50] Hawles, D. R., “Flight Operations to Minimize Noise,” Proceedings of the American Helicopter Society-AIAA-University of Texas at Arlington Joint

- Symposium on Environmental Effects of VTOL Designs, Arlington, Texas, November, 1970.
- [51] Helicopter Association International (HAI) Fly Neighborly Committee, "Fly Neighborly Guide," February, 1971.
- [52] Yoshikami, S., "Flight Operations: Noise Tests of Eight Helicopters", Federal Aviation Authority, US Department of Transportation, Report No. FAA-EE-85-7, August, 1985.
- [53] Hindson, W. S. and Chen, R. T., "Operational Tests for Noise Abatement Approaches for Rotorcraft Using Differential GPS for Guidance," *Journal of the American Helicopter Society*, Vol. 43, Number 4, October, 1998.
- [54] Lappos, N., Arnold, J., Erway, P., and McConkey, E., "The Development of a Decelerating Helicopter Instrument Landing system Using Differential GPS", Proceedings of the American Helicopter Society 56<sup>th</sup> Annual National Forum, Virginia Beach, VA, May 2-4, 2000.
- [55] Chen, R. T. F., Hindson, W. S. and Mueller, A. W., "Acoustic Flight Tests of Rotorcraft Noise-Abatement Approaches Using Local Differential GPS Guidance," Proceedings of the American Helicopter Society Specialists

- Conference on Rotorcraft Aeromechanical Technologies, Fairfield County, Conn.,  
October 11-13, 1995.
- [56] Gopalan, G., Schmitz, F. H., and Sim, B. W., “Flight Path Management and Control Methodology to Reduce Helicopter Blade-Vortex (BVI) Noise,” Proceedings of the American Helicopter Society Vertical Lift Aircraft Design Conference, San Francisco, CA, January, 2000.
- [57] Schmitz, F. H.; Stepniewski, W. Z.; Gibs, J.; Hinterkeuser, E.: “A Comparison of Optimal and Noise-Abatement Trajectories of a Tilt-Rotor Aircraft”. NASA CR-2034, May, 1972.
- [58] Stepniewski, W.Z.; Schmitz, F. H.: “Possibilities and Problems of Achieving Community Noise Acceptance of VTOL Aircraft”, *The Aeronautical Journal of Great Britain*, Vol. 77, No. 730, pp. 311-326, June, 1973.
- [59] Schmitz, F. H.; Stepniewski, W.Z.: “Reduction of VTOL Operational Noise through Flight Trajectory Management”, *Journal of Aircraft*, Vol. 10, No. 7, pp. 385-394, July, 1973.
- [60] Lucas, M. J., and Marcolini, M. A., “Rotorcraft Noise Model”, AHS Technical Specialists Meeting for Rotorcraft Acoustics & Aerodynamics, Williamsburg, VA, October 1997.

- [61] Conner, D. A. and Page, J., “A Tool for Low Noise Procedures Design and Community Noise Impact Assessment: the Rotorcraft Noise Model (RNM)”, Proceedings of the AHS International Meeting on “Advance Rotorcraft Technology and Life Saving Activities”, Heli Japan, Japan, November, 2002.
- [62] Page, J. and Plotkin, K., “Acoustic Repropagation Technique, Version 2,” Wyle research Report, WR 01-04, January, 2001.
- [63] Janikaram, R. D. and Khan, H., “Prediction and Validation of Helicopter Descent Flyover Noise,” Proceedings of the American Helicopter Society 56<sup>th</sup> Annual Forum, Virginia Beach, VA, May 2-4, 2000
- [64] Theodore, C. R. and Celi R., “Flight Dynamic Simulation with Refined Aerodynamics and Flexible Blade Modeling”, Proceedings of the American Helicopter Society 56<sup>th</sup> Annual National Forum, Virginia Beach, VA, May 2-4, 2000.
- [65] Bagai, A., Leishman, J. G. and Park, J., “Aerodynamic Analysis of a Helicopter in Steady Maneuvering Flight Using a Free-Vortex Wake Model”, Proceedings of the AHS Technical Specialist’s Meeting on Rotorcraft Acoustics and Aerodynamics, Williamsburg, VA, 1997.

- [66] Spence, A. M. and Celi, R., “Coupled Rotor Fuselage Dynamics and Aeroelasticity in Turning Flight”, Proceedings of the 33<sup>rd</sup> AIAA/ASME/ASCE/AHS/ASC Structures, Structural Dynamics, and Materials Conference, Dallas, April, 1992.
- [67] Pitt, D. M. and Peters, D. A., “Theoretical Predictions of Dynamic Inflow Derivatives”, *Vertica*, Vol. 5, No. 1, pp. 21-34, 1981.
- [68] Keller, J. D., “An Investigation of Helicopter Dynamic Coupling Using an Analytical Model”, Proceedings of the 21<sup>st</sup> European Rotorcraft Forum, St. Petersburg, Russia, August, 1995.
- [69] Chen, H., Brentner, K. S., Lopes, L. V. and Horn, J. F., “A Study of Rotorcraft Noise Prediction in Maneuvering Flight”, Proceedings of the 42<sup>nd</sup> Aerospace Sciences Meeting and Exhibit, Reno, NV, January, 2004.
- [70] Brentner, K. S. and Jones, H. E., “Noise Prediction for Maneuvering Rotorcraft,” AIAA-2000-2031, Proceedings of the 6<sup>th</sup> AIAA/CEAS Aeroacoustics Conference, Lahaina, Hawaii, June 12-14, 2000.
- [71] Brentner, K. S., Perez, G. and Bres, G. A., “Towards a Better Understanding of Maneuvering Rotorcraft Noise”, Proceedings of the AHS 58<sup>th</sup> Annual Forum, Montreal, June, 2002.

- [72] Schmitz, F. H., Gopalan, G. and Sim, B. W., “Flight Trajectory Management to Reduce Helicopter Blade-Vortex Interaction (BVI) Noise with Head/Tailwind Effects”, Proceedings of the 26<sup>th</sup> European Rotorcraft Forum, The Hague, The Netherlands, September 26-29, 2000.
- [73] Sim, B. W., and Schmitz, F. H., “Acoustic Phasing and Amplification Effects of Single Rotor Helicopter Blade-Vortex Interactions,” Proceedings of the American Helicopter Society 55<sup>th</sup> Annual Forum, Montreal, Canada, May, 1999.
- [74] Leishman, J. G., *Principles of Helicopter Aerodynamics*, Cambridge University Press, 2000.
- [75] Lawson, M. V., “Focusing of Helicopter BVI Noise,” *Journal of Sound & Vibration*, Vol. 190, pp. 477-494, 1996.
- [76] Widnall, S. E., “Helicopter Noise due to Blade-Vortex Interaction,” *Journal of the Acoustical Society of America*, Vol. 50, No. 1 (Part 2), pp. 354-365, 1971.
- [77] Ringler, T. D., George, A. R. and Steele, J. B., “A Study of Blade-Vortex Interaction Sound and Directivity”, AHS/RAES Meeting on Rotorcraft Acoustics, Philadelphia, 1991.

- [78] Sim, B. W., George, A. R. and Yen, S. J., "Blade-Vortex Interaction Noise Directivity Studies Using Trace Mach Number," Proceedings of the American Helicopter Society Aeromechanics Specialist Meeting, Connecticut, October, 1995.
- [79] Leishman, J. G., "Acoustic Focusing Effects Generated by Parallel and Oblique Blade Vortex Interactions", AHS Technical Specialist Meeting on Rotorcraft Acoustics and Aerodynamics, Virginia Beach, October 1997.
- [80] Leishman, J. G., "Sound Directivity Generated by Helicopter Rotors Using Wave Tracing Concepts," *Journal of Sound and Vibration*, Vol. 221, No. 3, pp. 415-441, 1999.
- [81] Schmitz, F. H. and Sim, B. W., "Radiation and Directionality Characteristics of Advancing Side Blade-Vortex Interaction (BVI) Noise," Proceedings of the 6<sup>th</sup> AIAA/CEAS Aeroacoustics Conference, Lahaina, Hawaii, June, 2000.
- [82] Beddoes, T. S., "A Wake Model for High Resolution Airloads", International Conference on Rotorcraft Basic Research, North Carolina, February 1985.
- [83] Prouty, R., Helicopter *Performance, Stability and Control*, Kreiger Publishing Co., Florida, 1995.

- [84] Gessow, A. and Myers, G. C., 1952, *Aerodynamics of the Helicopter*, Macmillan Co. (Republished by Frederick Ungar Publishing), New York, 1967.
- [85] Johnson, W., *Helicopter Theory*, Princeton University Press, Princeton, New Jersey, 1980.
- [86] Gopalan, G. and Schmitz, F. H., “A Sensitivity Analysis of the Quasi-Static Acoustic Mapping of Helicopter Blade-Vortex Interaction (BVI) Noise during Slowly Maneuvering Flight”, Proceedings of the 9<sup>th</sup> AIAA/CEAS Aeroacoustics Conference, Hilton Head, South Carolina, May 2003.
- [87] Panandikar, N. G., *Computational Fluid Dynamics Analysis of Blade-Vortex Interaction for a Rotor*, Master of Science Thesis, University of Maryland, 2000.
- [88] Yu, Y. H. and Tung, C., “Blade Aeroelastic Effect of Rotor Blade-Vortex Interaction (BVI) Noise”, 52<sup>nd</sup> Annual AHS Forum, Washington, DC, June, 1996.
- [89] Farassat, F., “Theory of Noise Generation from Moving Bodies with an Application to Helicopter Rotors”, NASA Technical Report TR R-451, 1975.
- [90] Scully, M. P., “Computation of Helicopter Rotor Wake Geometry and its Effect on Rotor Harmonic Airloads”, Massachusetts Institute of Technology, ASRL TR 178-1, 1975.

- [91] Martin, P. B., Leishman, J. G., Pugliese, G. J., and Anderson, S. L., “Stereoscopic PIV Measurement in the Wake of a Hovering Rotor,” Proceedings of the American Helicopter Society 56<sup>th</sup> Annual Forum, Virginia Beach, VA, May, 2000.
- [92] Heineck, J. T., Yamauchi, G. K., Wadcock, A. J., Lourenco, L. and Abrego, A. I., “Application of the Three-Component PIV to a Hovering Rotor Wake,” Proceedings of the American Helicopter Society 56<sup>th</sup> Annual Forum, Virginia Beach, VA, May, 2000.
- [93] Farassat, F. and Succi, G., “The Prediction of Helicopter Rotor Discrete Frequency Noise”, *Vertica*, Vol. 7, No. 4, pp. 309-320, 1983.
- [94] Lawson, M. V., “The Sound Field for Singularities in Motion”, *Proceedings of the Royal Society*, Vol. A286, pp. 559-572, 1965.
- [95] Colin, R. T., *Helicopter Flight Dynamics Simulation with Refined Aerodynamic Modeling*, Ph.D. Thesis, Department of Aerospace Engineering, University of Maryland at College Park, 2000.
- [96] Celi, R., *Helicopter Stability and Control - Lecture Notes*, Department of Aerospace Engineering, University of Maryland at College Park, 2000.

- [97] Perkins, C. D. and Hage, R. E., *Airplane Performance, Stability and Control*, John Wiley and Sons, New York, 1949.
- [98] Bramwell, A. R. S., *Helicopter Dynamics*, John Wiley and Sons, New York, 1976.
- [99] Stepniewsky, W. Z. and Keys, C. N., *Rotary Wing Aerodynamics*, Dover Publications, New York, 1981.
- [100] Padfield, G. D., *Helicopter Flight Dynamics – The Theory and Applications of Flying Qualities and Simulation Modeling*, AIAA Education Series, 1996.
- [101] Mehrotra, K., Mohan, C. K. and Ranka, S., *Elements of Artificial Neural Networks*, The MIT Press, Cambridge, Massachusetts, 1997.
- [102] ANSI S1.26-1978, Acoustical Society of America, American National Standard, “Method for the Calculation of the Absorption of Sound by the Atmosphere”, 1978.
- [103] VanGaasbeek, J. R., “Rotorcraft Flight Simulation Computer Program C81 with DATAMAP Interface”, USAAVRADCOM-TR-D-38A, October 1981.

- [104] Talbot, P. D., Tinling, B. E., Decker, W. B. and Chen, R. T. N., “A Mathematical Model of a Single Rotor Helicopter for Piloted Simulation”, NASA TM 84281, September, 1982.
- [105] Gopalan, G., Xue, M., Atkins, E. and Schmitz, F. H., “Longitudinal-Plane Simultaneous Non-Interfering Approach Trajectory Design for Noise Minimization”, Presented at the 59<sup>th</sup> AHS International Forum and Technology Display, Phoenix, Arizona, May, 2003.